

# UC Berkeley

## UC Berkeley Electronic Theses and Dissertations

### Title

Detecting and Characterizing Small Planets in Diverse Environments

### Permalink

<https://escholarship.org/uc/item/91h146hh>

### Author

Mayo, Andrew

### Publication Date

2024

Peer reviewed|Thesis/dissertation

Detecting and Characterizing Small Planets in Diverse Environments

by

Andrew W. Mayo

A dissertation submitted in partial satisfaction of the

requirements for the degree of

Doctor of Philosophy

in

Astrophysics

in the

Graduate Division

of the

University of California, Berkeley

Committee in charge:

Professor Courtney Dressing, Chair

Professor Eugene Chiang

Professor Joshua S. Bloom

Spring 2024

Detecting and Characterizing Small Planets in Diverse Environments

Copyright 2024  
by  
Andrew W. Mayo

## Abstract

## Detecting and Characterizing Small Planets in Diverse Environments

by

Andrew W. Mayo

Doctor of Philosophy in Astrophysics

University of California, Berkeley

Professor Courtney Dressing, Chair

Our ability to detect and characterize small planets in diverse environments is expanding rapidly with the development and continued improvement of the transit and radial velocity methods. Better models, instruments, and telescopes are producing greater planet yields and tighter planetary radius and mass constraints, which in turn provide new targets for atmospheric characterization and produce new insights on planet composition, formation, and evolution. In this thesis, I present work on the characterization and mass determination of small planets with the radial velocity method, the detection of new planets via the transit method, and the study of a planet's atmosphere through transmission spectroscopy and its implications for planet formation and planet population features.

First, I report on mass estimation and characterization of the long-period exoplanet Kepler-538b. This sub-Neptune with a period of  $P = 81.7$  days is the only planet known to be orbiting its Sun-like star ( $0.892 M_{\odot}$ ). Simultaneously modeling Kepler photometry and radial velocities (RVs) yields a semi-amplitude of  $1.68 \pm 0.39 \text{ m s}^{-1}$  and a planet mass of  $10.6 \pm 2.5 M_{\oplus}$ , which made Kepler-538b the smallest planet beyond  $P = 50$  days with an RV mass measurement at the time of publication. Precise mass measurements on long-period planets will not only directly address questions about the long-period planet population, but also draw comparisons and shed light on aspects of the short-period planet population like the planetary radius occurrence gap and the impact of high stellar irradiation on exoplanet compositions and atmospheres.

Next, I discuss K2-136c, a sub-Neptune with a period of  $P = 17.3$  days and the largest of three transiting planets orbiting a late-K dwarf ( $0.742 M_{\odot}$ ) in the young Hyades open cluster ( $650 \pm 70 \text{ Myr}$ ). Collecting and analyzing RV data from the HARPS-N and ESPRESSO spectrographs jointly with photometry from the K2 and TESS space telescopes yielded an RV semi-amplitude of  $5.46 \pm 0.45 \text{ m s}^{-1}$  for K2-136c, corresponding to a mass of  $18.0 \pm 1.7 M_{\oplus}$ . K2-136c is now the smallest planet to have a measured mass in an open cluster and one of the youngest planets ever with a mass measurement. As a result, this system adds an important

new window into young small planet compositions, atmospheric mass loss constraints around young active stars, and planetary evolution at relatively unexplored ages.

I then present the TATER planet detection pipeline and apply it to high-cadence photometry of 914 known planet systems observed during TESS Cycle 3. This work has led to the new validation of 4 short-period planets. This study provides independent modeling and vetting of hundreds of planet candidates while also expanding the known planet population and providing updated transit ephemerides and planet radii.

Finally, I report on the atmospheric characterization of WASP-166b, a short-period super-Neptune ( $P = 5.44$  d,  $M_p = 32.1 \pm 1.6 M_\oplus$ ,  $R_p = 7.1 \pm 0.3 R_\oplus$ ). WASP-166b is located near the edge of the Hot Neptune Desert, a sparse region of exoplanet parameter space at high stellar irradiation and intermediate planet radii. Using transmission spectroscopy of WASP-166b (two transit observations with the James Webb Space Telescope), initial analyses show evidence of  $\text{H}_2\text{O}$  and  $\text{CO}_2$ ; no evidence of  $\text{SO}_2$ ,  $\text{NH}_3$ , or a cloud deck; constraints on planetary metallicity and the C/O ratio; and a plausible formation pathway that includes planetesimal accretion followed by core erosion or photoevaporation. This in turn points to mechanisms that can create substellar or stellar C/O ratios and superstellar metallicities, like photoevaporation and core erosion, as feasible components of the formation of the Hot Neptune Desert.

# Contents

<b>Contents</b>	<b>i</b>
<b>List of Figures</b>	<b>iii</b>
<b>List of Tables</b>	<b>v</b>
<b>1 Introduction</b>	<b>1</b>
<b>2 An 11 Earth-Mass, Long-Period Sub-Neptune Orbiting a Sun-like Star</b>	<b>12</b>
2.1 Introduction . . . . .	13
2.2 Observations . . . . .	14
2.3 Stellar Characterization . . . . .	16
2.4 Data Analysis . . . . .	19
2.5 Results and Discussion . . . . .	31
2.6 Summary and Conclusions . . . . .	38
<b>3 Hyades Member K2-136c: The Smallest Planet in an Open Cluster with a Precisely Measured Mass</b>	<b>40</b>
3.1 Introduction . . . . .	41
3.2 Observations . . . . .	42
3.3 Stellar Characterization . . . . .	44
3.4 Data Analysis . . . . .	50
3.5 Results and Discussion . . . . .	70
3.6 Summary and Conclusions . . . . .	76
<b>4 Detecting and Validating New Short-Period <i>TESS</i> Planets with TATER and TRICERATOPS</b>	<b>78</b>
4.1 Introduction . . . . .	78
4.2 Sample & Observations . . . . .	80
4.3 Stellar Characterization . . . . .	80
4.4 Analysis . . . . .	82
4.5 Results & Discussion . . . . .	92
4.6 Conclusion . . . . .	98

<b>5</b>	<b>Detection of H<sub>2</sub>O and CO<sub>2</sub> in the Atmosphere of the Hot Super-Neptune WASP-166b with JWST</b>	<b>100</b>
5.1	Introduction . . . . .	100
5.2	Observations . . . . .	101
5.3	Analysis . . . . .	104
5.4	Atmospheric Modeling and Retrieval Methods . . . . .	120
5.5	Discussion . . . . .	124
5.6	Conclusion . . . . .	128
<b>6</b>	<b>Future Work</b>	<b>129</b>
	<b>Bibliography</b>	<b>132</b>

# List of Figures

1.1	Insolation flux versus planet mass, with the Hot Neptune Desert labeled on the left. . . . .	10
2.1	Transit plot of Kepler-538b. . . . .	20
2.2	Stellar activity and corresponding Gaussian process regression of Kepler-538 (with planetary signal removed). . . . .	24
2.3	Periodograms of the window function (computed from observation times), RV, $\log R'_{HK}$ , CCF FWHM, and CCF BIS the Kepler-538 system. . . . .	25
2.4	Scatter plots of RV vs. $\log R'_{HK}$ , BIS, and FWHM for Kepler-538. . . . .	29
2.5	Kepler-538 RVs (with stellar activity subtracted) as a function of the orbital phase of Kepler-538b. . . . .	30
2.6	Mass-radius diagram of transiting planets with fractional mass and radius uncertainties less than 50%. . . . .	32
2.7	Orbital period versus planet radius for all transiting exoplanets with $P > 50$ days and RV or transit timing variation (TTV) mass measurements. . . . .	35
2.8	A simulated transmission spectrum of Kepler-538b with five transits observed with <i>JWST</i> . . . . .	37
3.1	Periodograms of RV, CCF FWHM, CCF BIS, and $S_{HK}$ for the K2-136 system. . . . .	51
3.2	Scatter plots of $S_{HK}$ , BIS, and FWHM against RV for the K2-136 system. . . . .	52
3.3	Transit plot of K2-136. . . . .	58
3.4	K2-136 observations and model fits for RVs (and fit residuals). . . . .	59
3.5	Phased RV plots and mass posteriors for all three K2-136 planets. . . . .	62
3.6	Planet mass v. radius, planet mass v. density, and planet insolation flux v. density for transiting planets with fractional mass and radius uncertainties less than 50%. . . . .	63
3.7	Mg II surface flux as a function of stellar rotation period for K star Hyades members. . . . .	67
3.8	X-ray spectra of K2-136 from the XMM pn, MOS1, and MOS2 EPIC cameras. . . . .	68
3.9	Age-radius diagram for all planets smaller than Jupiter, younger than 5 Gyr, and with radius and age uncertainties both smaller than 25%. . . . .	72
3.10	Simulation of <i>JWST</i> transmission spectra for K2-136c using JET. . . . .	75



4.1	Histograms and a scatter plot of stellar and planetary properties for our 914 target systems. . . . .	81
4.2	Histogram of the period distribution of the 1814 unique TCEs detected in our target sample with SDE > 8. . . . .	86
4.3	Example TATER periodogram of TIC 281575427 identifying a TCE with period of 4.252986 d. . . . .	89
4.4	Example TATER transit model and residuals for the phased light curve of TIC 281575427. . . . .	90
4.5	Example output of vetting for TIC 281575427 (TOI-205) with the planet vetting Python package <code>LEO-vetter</code> . . . . .	91
4.6	Phased light curves for TIC 281575427. . . . .	92
4.7	Phased light curves for TIC 183593642. . . . .	92
4.8	Phased light curves for TIC 305424003. . . . .	95
4.9	Phased light curves for TIC 421894914. . . . .	95
4.10	Period versus radius for all signals vetted or validated in this work. . . . .	96
4.11	Period v. radius for all TCEs detected (or otherwise detectable) with TATER. . . . .	97
5.1	Insolation flux versus planet mass, with the Hot Neptune Desert labeled on the left. . . . .	102
5.2	NIRISS SOSS first (index 0) <code>refpix</code> integration frame for group 2 before and after the background subtraction step is applied. . . . .	106
5.3	Median image of our NIRISS SOSS F277W integrations. . . . .	107
5.4	Comparison of the NIRISS SOSS CRDS spectral trace, the <code>pastasoss</code> -derived spectral trace, and the <code>pastasoss</code> trace shifted by 10 pixels. . . . .	107
5.5	NIRISS SOSS raw white light curve for the 30 pixel width <code>nirHiss</code> box extraction. . . . .	109
5.6	NIRISS SOSS extracted 1D stellar spectra (flux versus wavelength) overplotted for all integrations. . . . .	109
5.7	The measured, smoothed, and integer-rounded relative position of the NIRSpec spectral trace on the detector determined with the <code>Eureka!</code> atmospheric reduction pipeline. . . . .	113
5.8	The NIRSpec aligned spectral trace and residual background. . . . .	114
5.9	NIRSpec 1-D spectrum, with flux versus absolute pixel position for Integration 2. . . . .	115
5.10	NIRSpec broadband (white) light curve for WASP-166b. . . . .	118
5.11	WASP-166b transmission spectrum from POSEIDON free chemistry retrieval, based on an early NIRISS data reduction, and later stage NIRSpec reduction. . . . .	121

# List of Tables

2.1	Kepler-538 RV observations and activity indicators. . . . .	16
2.2	Stellar parameters of Kepler-538 . . . . .	17
2.3	Transit and RV parameters of Kepler-538b . . . . .	21
3.1	Stellar parameters of K2-136. . . . .	44
3.2	Kepler-136 RV observations and activity indicators. . . . .	48
3.3	K2-136 transit and planetary parameters. . . . .	60
3.4	K2-136 RV model parameters. . . . .	61
3.5	Model Evidence Comparisons for K2-136 Planet Configurations. . . . .	61
3.6	X-ray Spectral Fit Parameters of K2-136 . . . . .	69
4.1	Stellar parameters for 854 stars with sufficient reported stellar parameters . . . .	82
4.2	Table of all TCEs detected with TATER . . . . .	93
4.3	Table of all vetted TOIs detected with TATER . . . . .	94
4.4	Table of all planets we validate with TRICERATOPS . . . . .	94
5.1	System parameters used in this paper. . . . .	103
5.2	Key parameter priors for the WASP-166b NIRSPEC light curve fits with <i>Eureka!</i> (using <i>dynesty</i> for fitting). . . . .	117
5.3	Model parameters and prior distributions used in the atmospheric retrievals of WASP-166b. . . . .	122
5.4	Retrieved free parameter posterior median values from POSEIDON for selected cases.	125
5.5	Detection significance of various atmospheric constituents based on POSEIDON with free chemistry. . . . .	126

## Acknowledgments

Chapters 2-3 of this work correspond to published articles with several collaborators, and Chapters 4-5 of this work correspond to draft articles that will soon be published with several collaborators. I would like to thank all of these collaborators for their valuable contributions, and refer readers to each respective article for additional acknowledgments of funding sources.

I am indebted and grateful to my primary doctoral research advisor Dr. Courtney Dressing and my secondary doctoral research advisor Dr. Lars Buchhave; without their guidance and expertise this thesis could not have been completed. Additional thanks and gratitude to the other members of my Berkeley thesis committee: Dr. Eugene Chiang and Dr. Joshua Bloom; the members of my University of Copenhagen thesis committee assessing my double PhD degree program: Dr. Troels Haugbølle, Dr. Enric Palle, and Dr. Hans Kjeldsen; as well as my University of Copenhagen academic advisor: Dr. Jes Jørgensen. I also wish to thank my undergraduate mentor, Dr. Andrew Vanderburg, for nurturing my interest in exoplanets and providing more than a decade of guidance, advice, and friendship.

I would also like to acknowledge and thank the staff, students, and faculty of the UC Berkeley Astronomy Department for building and maintaining a vibrant, collaborative academic community. The hard work and dedication of the department staff, past and present - Amber Banayat, Bill Boyd, Brianna Franklin, Cara-Lyn Giovannello, Mark Hayden, Brandye Johnson, Maria Kies, Yasasha Ridell, Nina Ruymaker, and Lochland Trotter - cannot be overstated; their work not only keeps the department running, it also serves as one of the most vital and direct sources of support available to undergraduate and graduate astronomy students. I also extend my sincere thanks to Steven Giacalone, Jordan Fleming, Charles Fortenbach, Emma Turtelboom, Caleb Harada, and all the other fellow members of Dr. Courtney Dressing's PALS research group; their collaboration, assistance, advice, and help made this thesis possible.

My deepest thanks and love to my entire family, especially my dad, my sister Sarah, and my mom who first taught me about the stars. Thank you to Jill, Ronnie, Austin, Izzy, and Nana for all their love and support over these last seven years. To all my friends who have helped me get to this moment - Sami, Gwyn, Alex, Tas, Michelle, Helen, René, Noemí, and Julia - thank you so very much for all that you've done.

The work in this thesis was supported by numerous grants and funding sources including the NSF Graduate Research Fellowship award No. DGE 1752814 (awarded to Andrew Mayo), NASA K2 Guest Observer program grant 80NSSC19K0099 (awarded to Dr. Courtney Dressing), the Hellman Family Faculty Fellowship (awarded to Dr. Courtney Dressing), the Alfred P. Sloan Foundation Grant FG-2019-11662 (awarded to Dr. Courtney Dressing), and the David & Lucile Packard Foundation Grant 2019-69648 (awarded to Dr. Courtney Dressing).

This work includes data collected by the *Kepler* mission. Funding for the *Kepler* mission was provided by the NASA Science Mission Directorate. This work is based on observations made with the NASA/ESA/CSA JWST.

This work also uses the Exoplanet Follow-up Observation Program and NASA Exoplanet Archive websites, which are operated by the California Institute of Technology, under contract with NASA under the Exoplanet Exploration Program.

This work includes data collected with the TESS mission, obtained from the Mikulski Archive for Space Telescopes (MAST) data archive at the Space Telescope Science Institute (STScI). Funding for the TESS mission is provided by the NASA Explorer Program. STScI is operated by the Association of Universities for Research in Astronomy, Inc., under NASA contract NAS5-26555. Support for MAST for non-*Hubble Space Telescope* data is provided by the NASA Office of Space Science via grant NNX13AC07G and by other grants and contracts. I acknowledge the use of public TESS Alert data from pipelines at the TESS Science Office and TESS Science Processing Operations Center.

This work has made use of data from the European Space Agency (ESA) mission *Gaia* (<https://www.cosmos.esa.int/gaia>), processed by the *Gaia* Data Processing and Analysis Consortium (DPAC, <https://www.cosmos.esa.int/web/gaia/dpac/consortium>). Funding for the DPAC has been provided by national institutions, in particular the institutions participating in the *Gaia* Multilateral Agreement.

Some of the data presented herein were obtained at the W. M. Keck Observatory (which is operated as a scientific partnership among Caltech, UC, and NASA). The authors wish to recognize and acknowledge the very significant cultural role and reverence that the summit of Mauna Kea has always had within the indigenous Hawaiian community. We are most fortunate to have the opportunity to conduct observations from this mountain.

Based on observations made with the Italian *Telescopio Nazionale Galileo* (TNG) operated by the *Fundación Galileo Galilei* (FGG) of the *Istituto Nazionale di Astrofisica* (INAF) at the *Observatorio del Roque de los Muchachos* (La Palma, Canary Islands, Spain).

The HARPS-N project has been funded by the Prodex Program of the Swiss Space Office (SSO), the Harvard University Origins of Life Initiative (HUOLI), the Scottish Universities Physics Alliance (SUPA), the University of Geneva, the Smithsonian Astrophysical Observatory (SAO), and the Italian National Astrophysical Institute (INAF), the University of St Andrews, Queen's University Belfast, and the University of Edinburgh.

# Chapter 1

## Introduction

To date more than 5600 exoplanets have been detected (NASA Exoplanet Archive<sup>1</sup>; accessed 2024 Apr 25) and the number continues to grow rapidly. The vast majority of these detections arise from one of two primary methods: transits (e.g. Deeg and Alonso 2018) and radial velocities (RVs; e.g. Hara and Ford 2023). These two methods are responsible not only for the majority of exoplanet detections but also the majority of the work presented within this thesis. These results comprise contributions to the field of exoplanets via the transit method, the RV method, and atmospheric characterization through transmission spectroscopy. This thesis describes effective methods for detecting exoplanets smaller than Jupiter, places the findings into the context of the current state of the field and the known exoplanet population, and argues how these results and similar work are crucial for understanding planets.

In order to continue finding more exoplanets, astronomers push our planet detection limits to smaller and longer-period regimes, each year finding planets more similar to our own. With the development of larger telescopes, more precise spectrographs, and more comprehensive modeling techniques, multiple Earth analogs may be detected, confirmed, and characterized. This in turn will allow us to more tightly constrain the occurrence rate of Earth twins and study their atmospheres to possibly even search for the presence of biosignatures, molecules and atmospheric features unexplainable without biotic (i.e. living) processes.

These are the context and goals within which this thesis is presented. As described in detail, each of the discussed projects push one or another method of detecting and characterizing exoplanets toward smaller and more Earth-like planets. Chapter 1 provides background and context on the radial velocity and transit methods, explains the process of vetting planet candidates and statistically validating planets, details the transmission spectroscopy method of exoplanet atmospheric characterization, and discusses planet formation and evolution in the context of young planets in open clusters and highly irradiated planets in the Hot Neptune Desert. Chapter 2 presents the RV mass determination of the sub-Neptune Kepler-538b through simultaneous modeling of RVs and stellar activity indices via a joint Gaussian process. This work led to the smallest RV mass measurement of an exoplanet beyond an orbital

---

<sup>1</sup><https://exoplanetarchive.ipac.caltech.edu/>

period of 50 days, extending the RV method to smaller planets and longer orbital periods. Chapter 3 describes the RV analysis of the K2-136 system in the young Hyades open cluster, applying similar methods as Chapter 2 in order to measure the mass of K2-136c. This analysis yielded the smallest planet with a mass measurement in any open cluster, helping expand RV mass detection to smaller regimes for young planets. Chapter 4 details the development of the TATER transit detection pipeline and the use of the TRICERATOPS statistical validation pipeline to validate four new short-period exoplanets. New transit detection pipelines like TATER help expand the known planet population to smaller planets and longer periods while identifying individual targets that present valuable research opportunities through additional characterization. Chapter 5 presents a state-of-the-art example of follow-up characterization through an atmospheric analysis of the hot Neptune WASP-166b using transmission spectroscopy from the James Webb Space Telescope (*JWST*). As the most powerful space-based telescope ever launched, *JWST* has opened the field of exoplanet atmospheric analysis to smaller planets than ever before. Analysis of the atmosphere of WASP-166b reveals the presence of H<sub>2</sub>O and CO<sub>2</sub> and points to planetesimal accretion with photoevaporation or core erosion as plausible mechanisms for the formation of WASP-166b and as potential components of the origin of the Hot Neptune Desert. Chapter 6 is a review of all presented results that reiterates the contribution of each project in pushing our detection and characterization limits to smaller and more Earth-like planets and discusses interesting research questions and opportunities for future work.

## The RV Method

The RV method, sometimes colloquially referred to as the wobble method, is used to measure the gravitational tug of a planet as it orbits its host star. Observers can collect stellar spectra and analyze spectral absorption features to measure a Doppler wavelength shift in the host star spectrum, either a blueshift or a redshift, via the star’s velocity toward or away from observers. Planets induce a typically sinusoidal RV signal as their full orbital motion is projected onto the radial component and observed (hence the name “radial” velocity). This sinusoid approximation holds for circular orbits but must be modified to account for eccentricity.

The period, phase, and amplitude of an RV signal reveal the orbital period of a planet, the time of inferior conjunction, and its minimum mass  $M_p \sin(i)$ . The latter quantity can only be derived from RVs by estimating the stellar mass (e.g. via spectroscopy) and calculating planetary mass via Kepler’s Third Law. Note that RVs only directly measure *minimum* mass because they only capture the *radial* velocity component of motion. Without also measuring orbital inclination (via e.g. transits) to tell the difference, a brown dwarf or stellar binary in a nearly face-on orbit can induce a similar RV semi-amplitude to a low-mass planet in a nearly edge-on orbit.

When the planet mass is significantly smaller than the stellar mass, the scaling relations become very simple:  $K \sim M_p \sin(i) M_*^{-1} P^{-1/3}$ , where  $K$  is the RV semi-amplitude,  $M_p$  is the planet mass,  $i$  is the orbital inclination,  $M_*$  is the stellar mass, and  $P$  is the orbital period.

In other words, RV signals are strongest for massive planets orbiting low-mass stars with short-period, edge-on orbits.

Measuring planet masses via the RV method allows astronomers to better understand a planet’s density and composition, especially if the planet radius has also been estimated. This in turn reveals and provides insights on exoplanet population-level features. Further, measuring the planet mass breaks the degeneracy between mass and bulk metallicity in atmospheric characterization studies (both high mass and high bulk metallicity can lead to a compressed atmosphere with low scale height). As a result, mass constraints are an important prerequisite before detailed atmospheric analysis is possible; for example Batalha et al. (2019) finds that better than 20% mass constraints are recommended for detailed atmospheric analysis.

The RV method has been used widely and regularly for decades to characterize stellar binary systems. The idea of detecting exoplanets via their RV signature on the host star was first proposed by Struve (1952) as an extension of stellar binary mass characterization. But the first successful detection of an exoplanet via the RV method was not until 1995 with the discovery of 51 Pegasi b (Mayor and Queloz 1995).

Since this first detection of 51 Pegasi b, with a measured RV semi-amplitude of  $59 \pm 3$  m s<sup>-1</sup>, the RV detection threshold has dramatically improved. To date (NASA Exoplanet Archive, accessed 1 May 2024), there are more than 1000 exoplanets that have been first discovered via RVs and more than 2000 have been characterized via RVs. But in 2000, there were only 43 planets detected through RVs, none with an RV signal below 10 m s<sup>-1</sup> and only one with an RV signal below 20 m s<sup>-1</sup>: epsilon Eridani b ( $19.0 \pm 1.7$  m s<sup>-1</sup>; Hatzes et al. 2000). By 2010 these numbers had dramatically grown, with 468 RV planet detections, including 19 RV detections below 10 m s<sup>-1</sup> and 12 RV detections below 5 m s<sup>-1</sup>. Continuing into 2020, the RV method had proven regularly effective at detecting planet signals below the 1 m s<sup>-1</sup> level: out of 1534 total RV planet detections, 233 were below 5 m s<sup>-1</sup> and 20 were below 1 m s<sup>-1</sup>. Although we are now pushing below 1 m s<sup>-1</sup> sensitivity, this performance is still limited to only a handful of ground-based extreme-precision spectrographs, including HIRES (Vogt et al. 1994), HARPS (Mayor et al. 2003), HARPS-N (Cosentino et al. 2012), HPF (Mahadevan et al. 2012), NEID (Schwab et al. 2016), CARMENES (Quirrenbach et al. 2020), EXPRES (Brewer et al. 2020), ESPRESSO (Pepe et al. 2021), MAROON-X (Seifahrt et al. 2022), and KPF (Rubenzahl et al. 2023).

However, while instrumental precision is necessary to detect small planetary RV signals it is not nearly sufficient; there are numerous sources of stellar activity that induce spurious and complex noise into RV observations.

Starspots on a stellar surface, being cooler than surrounding stellar material, appear very dark and introduce asymmetries on the stellar surface. This manifests as a net redshift when a spot is on the approaching (blueshifted) side, since the redshifted side is emitting more cumulative flux. As the star rotates and the spot crosses over to the receding (redshifted) side of the stellar surface, it induces an inverse, blueshift effect. Thus, starspots and other localized stellar phenomena all induce correlated RV noise on the timescale of the stellar rotation period (Roettenbacher 2021). This also includes other magnetically induced features

like plage and faculae, bright spots formed by coalescences of magnetic flux tubes in the stellar chromosphere and photosphere, respectively. Additionally, there are a host of other short term effects like p-mode oscillations (resonant standing waves ringing through the stellar interior) that propagate on second to minute timescales (Chaplin et al. 2019) and long term effects like the stellar magnetic activity cycle (powered by an internal stellar dynamo) that operate on timescales of years (Deming et al. 2024).

Reliable planet detection and characterization with the RV method must either mitigate or model all of these effects appropriately. Dumusque et al. (2011) found all these effects tend to introduce stellar jitter on the order of a few meters per second when the star is chromospherically quiet. They also reported that short term effects like p-mode oscillations can be effectively mitigated by integrating over 15 minutes or longer in a given night. As for long-term, multi-year magnetic activity cycles, they are also often negligible on the day to month timescale of the orbital period of most detected planets. In order to mitigate the medium-timescale jitter effects modulated by the stellar rotation period (i.e. starspots, faculae, and plage), several approaches are commonly employed including: direct modeling of stellar surface inhomogeneities (Dumusque et al. 2014); principal component analysis (Cretignier et al. 2022); and Gaussian processes for modeling quasi-periodic activity variations with unknown functional forms (Mayo et al. 2018; Rajpaul et al. 2015). Further discussion of the RV method and procedures for mitigating stellar activity and measuring planet masses are presented in Chapters 2 and 3.

## The Transit Method

An exoplanet transit occurs when a planetary orbital plane is coincidentally aligned with observers and the planet appears to pass across the face of its host star, casting a shadow and causing a temporary (and periodic) dip in light. If stellar properties are known (especially stellar radius), studying a transiting exoplanet reveals the physical size of the planet (i.e. radius), the orbital period, and the orbital inclination. Exoplanet transits can also sometimes help place constraints on planetary eccentricity.

Transits are crucial for understanding the exoplanet population. By revealing a planet's radius and period, transits provide a wealth of information about planetary habitability (by inferring orbital separation and equilibrium temperature from orbital period, stellar mass, stellar luminosity, and planetary assumptions like albedo). If the planet mass is also known, combining it with a radius estimate yields insights into the planet's composition (i.e. rocky v. gaseous). Further, detecting a planet through RVs or another method in addition to transits serves as confirmation of a planet or planet candidate, an important step in verifying the existence and planethood of a transit signal. Without confirmation, the transit signal must instead be subjected to a process called statistical validation, in order to quantify the false positive probability (FPP) and validate planet candidates with a sufficiently low FPP.

The first confirmed transit detection of an exoplanet was made by Charbonneau et al. (2000) who detected a transit of HD 209458 b, a hot Jupiter orbiting its host star every 3.5 days. The transit method yielded a slow trickle of additional detections over the following



decade. According to the NASA Exoplanet Archive (accessed 2024 Apr 25), there were 2 transit detections in 2000-2002, 6 transit detections in 2003-2005, and 39 transit detections in 2006-2008.

But the field truly took off with the start of the Kepler mission. The first planet-hunting spacecraft built by NASA, Kepler was launched in 2009 and operated until 2013. The Kepler probe was designed to look for transiting planets in a field of  $\sim 100000$  stars, a single patch of sky 115 square degrees in size (about the size of an outstretched hand, or  $\sim 1/400$ th of the night sky). Its importance to the field of exoplanets cannot be overstated. According to the NASA Exoplanet Archive (accessed 2024 Apr 25), Kepler alone is responsible for approximately half of all exoplanets detected to date ( $2774/5612 = 49.4\%$ ).

After the second of four reaction wheels on the Kepler spacecraft broke in 2013, the probe could no longer observe its intended field of view and the mission was ended. However, the probe was revamped as the K2 mission to look at new fields of view along the ecliptic plane, discovering more than 500 additional planets before the spacecraft exhausted its fuel reserves in 2018 (NASA Exoplanet Archive; accessed 2024 Apr 25).

Since the Kepler/K2 era, the primary instrument to hunt transiting planets has been TESS, the Transiting Exoplanet Survey Satellite (Ricker et al. 2015). Successor to Kepler and K2, TESS forgoes Kepler's narrow and deep field with a long temporal baseline in favor of a full-sky survey of bright stars conducted in 27 day sectors. This approach was designed with the TESS primary mission goal in mind: detecting at least 50 sub-Neptunes orbiting stars bright enough to allow spectroscopic mass determination and atmospheric characterization.

TESS easily met its primary mission goal, providing *JWST* with dozens to hundreds of targets for follow-up atmospheric characterization. According to the NASA Exoplanet Archive (accessed 2024 Apr 25), TESS is responsible for detecting 440 confirmed, transiting exoplanets thus far. Of those, 237 are smaller than Neptune and 63 of those planets orbit host stars brighter than  $J = 8$  (and are thus potential *JWST* atmospheric targets). This success is due in part to the longevity of TESS operations. Although the TESS primary mission lasted only 2 years, larger than expected fuel reserves may optimistically allow operations to continue into the 2030s. The extended missions will be crucial for detecting additional planets, particularly at longer orbital periods, as well collecting further observations necessary to characterize and validate currently detected planets. In addition to 440 confirmed planets, TESS has detected an additional 4614 planet candidates that have yet to be confirmed or classified as false positives (NASA Exoplanet Archive, accessed 25 Apr 2024).

## Planet Vetting and Validation

A transiting planet signal must pass through several stages to become a confirmed planet. At the earliest stage, a planet-search algorithm will identify a periodic dip in light that passes a certain threshold of detection significance in order to be classified as a threshold crossing event (TCE).

TCEs must next be subjected to various vetting tests designed to identify instrumental false alarms and astrophysical false positives. TCEs passing all relevant vetting tests are upgraded to planet candidates and may then be subjected to statistical validation. Validation is only appropriate after the vetting stage, it should be not applied to pre-vetted TCEs. To illustrate some common vetting tests for identifying astrophysical false positives, here are descriptions of how the odd-even test and the secondary eclipse test are performed:

- Odd-even test: For a reference transit signal observed at  $t_0$  with period  $P$ , define even and odd transits as those occurring at  $t_0 + 2nP$  and  $t_0 + (2n + 1)P$ , respectively, for any integer  $n$ . If the transit depth of only the odd transits versus only the even transits is significantly different, it suggests the signal may be due to an eclipsing stellar binary. The odd transits are due to Star A eclipsing Star B while the even transits are due to Star B eclipsing Star A, and therefore odd and even transits look distinct unless both stars are nearly identical.
- Secondary eclipse test: If there is evidence of a deep secondary eclipse (when the proposed planet passes *behind* its host star), the signal may be due to an eclipsing stellar binary for which the detected transits are actually Star A eclipsing Star B while the secondary eclipses are due to Star B eclipsing Star A. Only the largest planets have detectable secondary eclipses, and small eclipses at that, so a large secondary eclipse is a strong indicator of a false positive.

Planet candidates are then subjected to statistical validation, a process by which a false positive probability (FPP) can be calculated in order to quantitatively assess the likelihood of the transiting planet scenario versus various eclipsing binary scenarios. Validation is typically conducted by constructing a large ensemble of synthetic stellar systems consistent with observed stellar properties (e.g.  $M_*$ ,  $R_*$ ,  $T_{\text{eff}}$ ), local field star distribution, and transit signal properties (e.g. transit depth and duration). Once the ensemble is conditioned on these input properties, the fraction of ensemble systems capable of matching observations via any kind of off-target or eclipsing binary scenario constitutes the FPP.

Statistical validation of an exoplanet is the bare minimum necessary to declare a “planet detection” or “planet discovery.” However, it is important to note that a planet can additionally be confirmed via any alternative detection method such as RVs or transit timing variations. Validation and confirmation can operate independently, meaning a planet discovery may be due to validation, confirmation via another method, or both. An application of planet detection, vetting, and validation methods is presented in Chapter 4 with the validation of 4 new exoplanets that may be amenable to follow-up observations.

## Transmission Spectroscopy

While the transit method itself is fundamental for exoplanet detection, it also allows for a crucial method of atmospheric characterization called transmission spectroscopy. This

method is conducted by collecting sequential spectra before, during, and after transit. Astronomers then analyze this time series of spectra in order to construct transit light curves as a function of wavelength. Observers can model these transits and assess the apparent size of the planet *and* its atmosphere in any observed wavelength bin. Because transit radius is a proxy for atmospheric opacity, this analysis yields a transmission spectrum of the planet's atmosphere.

Because different molecules absorb at unique wavelengths, modeling this transmission spectrum allows observers to identify and constrain individual atmospheric constituents. Exoplanet atmospheres reveal a vast amount of information about the planets they encompass. The atmospheric makeup of a planet can help differentiate between various planetary formation and evolution pathways as the planet locally accretes gas and solids of a particular mix during its formation phase that are later detectable in the atmosphere. The same estimates of atmospheric composition, by helping constrain bulk metallicity, also yield insights into interior planet composition. Atmospheric characterization is also vital for habitability studies, in order to contextualize what classes of habitable-zone planets are most promising for biosignature searches. Overall, studying planet atmospheres helps us to identify patterns between planets, their atmospheres, and the properties of their host star and planetary siblings.

Transmission spectroscopy has been successfully performed with both ground and space-based instruments. The first successful use of this technique was also the first detection of any molecule in any exoplanet atmosphere, via transmission spectroscopy or otherwise. This was the detection of sodium in the atmosphere of HD 209458 from four transit observations (Charbonneau et al. 2002). Since 2002, the use and capability of the transmission spectroscopy method has only expanded. According to the NASA Exoplanet Archive atmospheric spectroscopy table (accessed 2024 Apr 25), there are currently 324 spectra (of 5 or more data points) for 100 planets. 259 of those 324 spectra (80%) were collected via transmission spectroscopy corresponding to 92 of those 100 planets. All 65 remaining spectra were collected via emission spectroscopy (observing emitted planetary flux before, during, and after secondary eclipse). This corresponds to 31 of the 100 planets with atmospheric spectra of 5 or more data points (23 planets have both transmission and emission spectroscopy). In other words, transmission spectroscopy is currently by far the most popular and effective method of studying an exoplanet's atmosphere.

This is thanks in no small part to the rise in space based facilities capable of making these observations. Of the 324 planetary spectra with 5 or more points, the largest shares were due to the Hubble Space Telescope (*HST*) with 193 planetary spectra (60%) and *JWST* with 45 planetary spectra (14%). That number is expected to rise quickly and dramatically for *JWST* in particular, as the world's most powerful space-based telescope with multiple onboard instruments capable of exoplanet atmospheric observations. Consulting the planetary spectrum publication record (again, only for spectra with 5 or more data points), since 2022 there have been 93 newly published planetary spectra from *HST*; meanwhile, given that *JWST* launched on 25 Dec 2021, all 45 planetary spectra have been published since 2022. Thus far, these new observations have yielded several exciting results, including

detections of several molecules in new planets including H<sub>2</sub>O (Fu et al. 2022), CO<sub>2</sub> (JWST Transiting Exoplanet Community Early Release Science Team et al. 2023a), SO<sub>2</sub> (Dyrek et al. 2024; Powell et al. 2024), CH<sub>4</sub> (Madhusudhan et al. 2023) as well as the first transmission and emission spectra of terrestrial planet atmospheres, which thus far are essentially featureless (Greene et al. 2023; Zhang et al. 2024; Zieba et al. 2023).

In Chapter 5, we present an application of transmission spectroscopy with *JWST* to study the atmosphere of the hot super-Neptune WASP-166b.

## Exoplanet Demographics and Evolution

In this section, we discuss exoplanet demographics and how planet formation and evolution mechanisms like in-situ formation and migration directly inform the nature of the entire planet population. We describe how planetary evolution and photoevaporation may be studied by observing young planets in open clusters for which the stellar ages are tightly constrained. We also detail the nature and properties of the Hot Neptune Desert and how atmospheric characterization can probe evolution pathways for planets in and near this demographic feature.

### Young Stars: Planetary Evolution Laboratories

Young stars are excellent for studying planetary evolution. Studying them is akin to taking a baby photo, capturing planetary evolution processes (like photoevaporation) while they are ongoing. The timescales for stellar and planetary formation are significantly shorter than the timescale for most main sequence stars, meaning that on a cosmic scale planets formed at almost the same time as their host stars. Therefore, the age of the host star serves as an effective proxy for the age of the planet.

Unfortunately, host star ages are typically difficult to constrain well. This can be avoided by studying stars in open clusters, loose gravitationally bound associations of young stars and interstellar gas remaining from that initial star formation phase. Open clusters are essentially star nurseries, and they form when a gas cloud collapses and fragments under gravitational instability.

This formation method means the stars in an open cluster have essentially identical ages (and distances to observer), so a simple isochrone fit to the brightnesses and colors of the stellar population can place tight age constraints on the entire open cluster.

So why are young stars not observed more to study planet evolution? Essentially, many of the stellar activity issues that plague middle-aged main-sequence stars are compounded for young stars. Young stars tend to spin faster and exhibit greater magnetic activity, causing higher emissions of X-ray and UV radiation that impact RV and photometric detectability while also directly affecting or even stripping the planet's atmosphere (Lammer et al. 2014). This has resulted in a relatively small open cluster planet population. Among over 5000 planets discovered, only dozens have been detected within open clusters: (Nardiello et al. 2021) searched the literature and found 33 existing open cluster planet candidates. They

also analyzed *TESS* Cycle 2 photometry and reported on another 23 open cluster planet candidates with  $R_p < R_J$ , of which they estimated 60% are likely false positives. We discuss planet detection and characterization within open clusters in further detail in Chapter 3.

### The Hot Neptune Desert

The Hot Neptune Desert serves as an excellent example of a planet population feature that we can better understand through cutting-edge atmospheric studies. The Hot Neptune Desert denotes a region of planetary parameter space at very high instellation fluxes that excludes planets of intermediate planetary radii. Hot Neptunes, as they are called, are highly uncommon in comparison to hot, Earth-sized planets and hot, Jupiter-sized planets (Mazeh et al. 2016). As can be seen in Fig. 1.1, the Hot Neptune Desert does not have a simple upper or lower envelope. Mazeh et al. (2016) empirically measures its boundaries with an upper envelope power law and a separate lower envelope power law in period-radius space. Even as they report their empirical relations, they acknowledge that although these two power laws intersect at approximately 10 days in both period-radius space and period-mass space, they still observe that the actual Hot Neptune Desert extends out only to approximately 5 days. As WASP-166b has an orbital period of 5.44 days, these approximate boundaries situate the planet near the edge of the desert.

Numerous Hot Neptune Desert formation processes have been proposed. For example, Mazeh et al. (2016) suggests mechanisms to strip Neptunes and shrink their radii to below the Hot Neptune Desert lower envelope, including photoevaporation or Roche lobe overflow (when the planet expands beyond its gravitational sphere of influence and the host star begins accreting its atmosphere). Neptunes that migrate inward to shorter orbital periods and enter the Hot Neptune Desert are thus quickly stripped of their atmospheres and simply become hot Earths. Mazeh et al. (2016) also suggests an inner disk gap that halts accretion and prevents further migration to even shorter periods. They suggest that some property of the host star, perhaps its magnetic field, creates an inner radius gap or underdensity that disallows further inward planet migration; studies of young systems with protoplanetary disks could more directly probe such a connection. All of these proposed methods only explain the upper envelope of the Hot Neptune Desert. The lower desert boundary could be the result of planet cores forming after protoplanetary disk gas has dispersed (Helled et al. 2016; Lee and Chiang 2016; Rogers et al. 2011). If small (Earth or super-Earth sized) planet cores form after disk gas has dispersed, no runaway growth is possible, forming a lower Hot Neptune Desert boundary of rocky Earths and super-Earths.

Alternatively, there are Hot Neptune Desert origin theories that can explain the upper and lower desert boundaries simultaneously. Matsakos and Königl (2016) propose high-eccentricity tidal migration, whereby planets undergo high-eccentricity migration followed by tidal circularization near their Roche limit. Because the mass-radius relationship differs for small and large planets, the Roche limit increases with increasing mass for small planets, but then the trend reverses and the Roche limit decreases with increasing mass for large planets. This nonlinear behavior for the Roche limit can create a scarcity of intermediate-

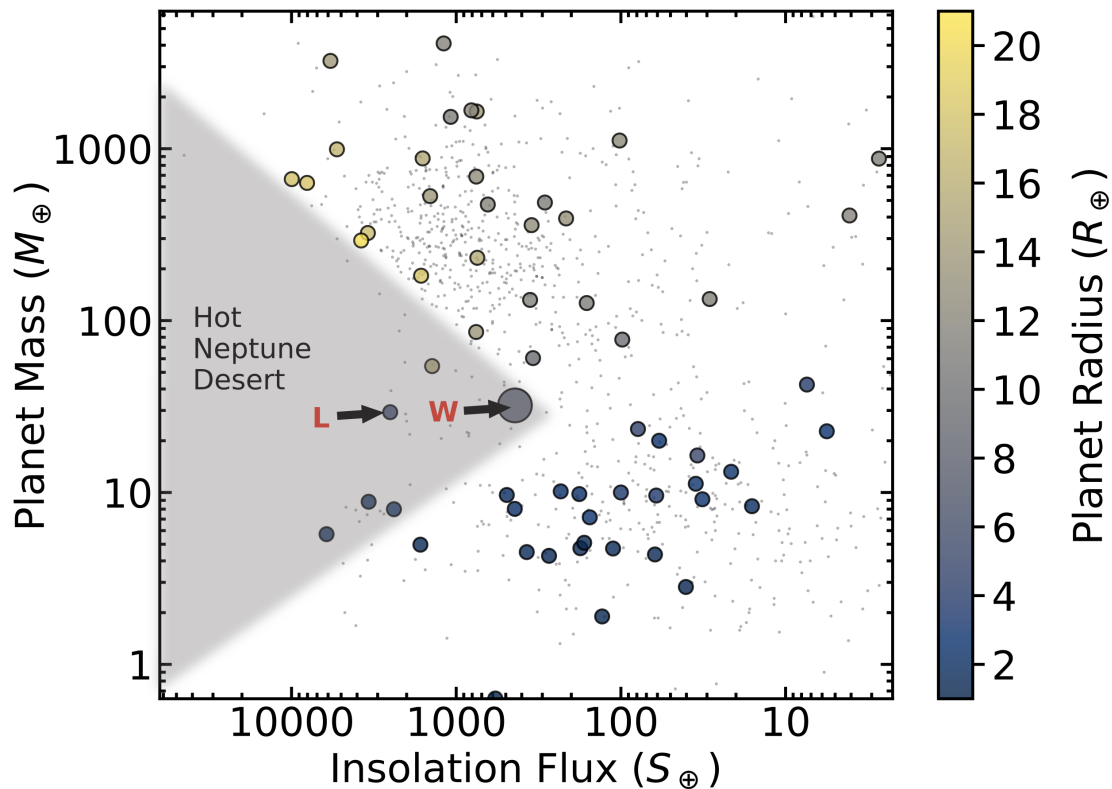


Figure 1.1: Insolation flux versus planet mass, with the approximate extent of the Hot Neptune Desert labeled and shaded in gray on the left. Small black dots are confirmed exoplanets; large dots colored by planet radius are confirmed planets with mass and radius uncertainties  $< 10\%$  and bright host stars ( $J < 9$ ). Our target WASP-166b (“W”) is plotted as well as LTT 9779b (“L”), another hot Neptune with atmospheric characterization from Jenkins et al. (2020) discussed further in Chapter 5.

sized planets able to reach short semimajor axes through tidal circularization, thus forming the Hot Neptune Desert as we know it.

Meanwhile, Batygin et al. (2016) suggested that in situ hot super-Earth formation can lead to runaway gas accretion and create hot Jupiters, with hot Neptunes only forming under fine-tuned accretion conditions. In this formation process, short-period planet cores that form early enough encounter runaway growth to hot Jupiters as they accrete protoplanetary gas, while planet cores formed after disk gas dispersal have no more local material to accrete and remain small and rocky. Only in the fine-tuned circumstance that the planet formation timescale and disk evolution timescale are comparable will the runaway gas accumulation cease midway and result in a hot Neptune, thus creating a paucity of hot planets with intermediate radii.

Each of these formation pathways for the Hot Neptune Desert rely on either planetary migration from the outer system inward or in-situ formation, by which the planet is born and grows with little or no change in orbital separation throughout the planetary evolution process. These distinct formation pathways imprint distinct planetary atmosphere compositions. The broadest implication is that planets forming in-situ near their host star should exhibit a stellar or substellar carbon-to-oxygen (C/O) ratio and superstellar bulk metallicity (Madhusudhan et al. 2014), whereas planets forming further out will tend to have a superstellar C/O ratio, especially if they form beyond the CO<sub>2</sub> snow line (Öberg et al. 2011). Now that *JWST* allows us to probe Hot Neptune atmospheres, we can begin to place constraints on formation pathways for individual hot Neptunes and build a larger picture of the evolutionary processes that are most impactful on Hot Neptune formation.

A study of the atmosphere of the hot Neptune WASP-166b is presented in Chapter 5, including discussion of the Hot Neptune Desert and the implications of this study on its formation mechanisms.

## Chapter 2

# An 11 Earth-Mass, Long-Period Sub-Neptune Orbiting a Sun-like Star

An earlier version of this article was published as: Mayo, A. W., Rajpaul, V. M., Buchhave, L. A., Dressing, C. D., Mortier, A., Zeng, L., Fortenbach, C. D., Aigrain, S., Bonomo, A. S., Cameron, A. C., Charbonneau, D., Coffinet, A., Cosentino, R., Damasso, M., Dumusque, X., Martinez Fiorenzano, A. F., Haywood, R. D., Latham, D. W., López-Morales, M., Malavolta, L., Micela, G., Molinari, E., Pearce, L., Pepe, F., Phillips, D., Piotto, G., Poretti, E., Rice, K., Sozzetti, A., Udry, S., 2019, *The Astronomical Journal*, 158, 165M.

Although several thousands of exoplanets have now been detected and characterized, observational biases have led to a paucity of long-period, low-mass exoplanets with measured masses and a corresponding lag in our understanding of such planets. In this paper we report the mass estimation and characterization of the long-period exoplanet Kepler-538b. This planet orbits a Sun-like star ( $V = 11.27$ ) with  $M_* = 0.892_{-0.035}^{+0.051} M_\odot$  and  $R_* = 0.8717_{-0.0061}^{+0.0064} R_\odot$ . Kepler-538b is a  $2.215_{-0.034}^{+0.040} R_\oplus$  sub-Neptune with a period of  $P = 81.73778 \pm 0.00013$  days. It is the only known planet in the system. We collected radial velocity (RV) observations with the High Resolution Echelle Spectrometer (HIRES) on Keck I and High Accuracy Radial velocity Planet Searcher in North hemisphere (HARPS-N) on the Telescopio Nazionale Galileo (TNG). We characterized stellar activity by a Gaussian process with a quasi-periodic kernel applied to our RV and cross-correlation FWHM observations. By simultaneously modeling *Kepler* photometry, RV, and FWHM observations, we found a semi-amplitude of  $K = 1.68_{-0.38}^{+0.39} \text{ m s}^{-1}$  and a planet mass of  $M_p = 10.6_{-2.4}^{+2.5} M_\oplus$ . Kepler-538b is the smallest planet beyond  $P = 50$  days with an RV mass measurement. The planet likely consists of a significant fraction of ices (dominated by water ice), in addition to rocks/metals, and a small amount of gas. Sophisticated modeling techniques such as those used in this paper, combined with future spectrographs with ultra high-precision and stability will be vital for yielding more mass measurements in this poorly understood exoplanet regime. This in turn will improve our understanding of the relationship between planet composition and insolation flux and how the rocky to gaseous transition depends on planetary equilibrium temperature.



## 2.1 Introduction

To date, more than 5600 exoplanets have been discovered, but roughly three quarters of them orbit their host star with periods of less than 50 days (NASA Exoplanet Archive<sup>1</sup>; accessed 2024 April 29). However, this is the result of observational biases rather than a feature of the underlying exoplanet population. Bias to short periods is especially strong for the transit method, the most common method of exoplanet detection. Nevertheless, Petigura et al. (2018) finds that from 1 to 24  $R_{\oplus}$ , the planet occurrence rate either increases or plateaus as a function of period out to many hundreds of days. Therefore, despite the estimated abundance of long-period planets (i.e. planets with periods longer than 50 days<sup>2</sup>), our understanding of them is still very incomplete. Relative to the short-period population, there are very few long-period exoplanets (particularly in the low-mass regime) with precise and accurate densities and compositions, and even fewer with atmospheric characterization.

Thus, a larger sample of masses for long-period planets would allow us to address a number of interesting questions. For example, it would allow us to study the rocky to gaseous planet transition and how it depends on stellar flux. We could also investigate planet compositions in or near the habitable zone of Sun-like stars.

Another interesting feature to study would be the planet radius occurrence gap detected by Fulton et al. (2017) and Fulton and Petigura (2018). Owen and Wu (2017) and Van Eylen et al. (2018) have proposed that photoevaporation strips planets near their host stars down to the core, thus creating the gap. Lopez and Rice (2018) have investigated the period dependence of the gap position and Zeng et al. (2017) have analyzed the relationship between gap position and stellar type. More long-period planets, with or without planet masses, would provide new insights into the nature and cause of this radius occurrence gap.

In this paper, we characterize the long-period exoplanet Kepler-538b, the only known planet in the Kepler-538 system, first validated by Morton et al. (2016). There is a possible second transiting planet candidate with a period of 117.76 days, but its existence is very much in question; we briefly discuss this candidate in Section 2.5. We determine the properties of the host star, a G-type star slightly smaller than the Sun. We also determine properties of the exoplanet including the orbital period, mass, radius, and density by modeling transit photometry, radial velocity (RV) data, and stellar activity indices. We find that Kepler-538b is the smallest long-period planet to date with both a measured radius and RV mass.

The format of this paper is as follows. In Section 2.2, we detail our photometric and spectroscopic observations of the planet and its host star. We then discuss stellar parameterization in Section 2.3 and modeling of photometry and spectroscopy in Section 2.4. Our results are then presented and discussed in Section 2.5. Finally, we summarize and conclude our paper in Section 2.6.

---

<sup>1</sup><https://exoplanetarchive.ipac.caltech.edu/>

<sup>2</sup>We define long-period planets as exoplanets with periods greater than 50 days. This may seem short relative to planets in our own solar system or many of the multi-year period exoplanets already found, but we think it is appropriate, given the relative scarcity of such planets in the known, low-mass planet population.

## 2.2 Observations

Photometric observations of the Kepler-538 system were collected with the *Kepler* spacecraft (Borucki et al. 2008) across 17 quarters beginning in 2009 May and ending in 2013 May. *Kepler* collected both long-cadence and short-cadence observations of this system. Short-cadence observations (in quarters 3, 7 – 12 and 17) were collected every 58.89 s, and long-cadence observations (in all other quarters) were collected every 1765.5 s ( $\sim 29.4$  minutes). In particular, we used pre-search data conditioning (PDC) light curves from these quarters downloaded from the Mikulski Archive for Space Telescopes.

Although Kepler-538 was not validated until Morton et al. (2016), it was flagged as a *Kepler* Object of Interest well before that. As a result, we have conducted a great deal of spectroscopic follow-up on Kepler-538 since it was identified as a candidate host star by the *Kepler* mission.

First, we collected two spectra with the Tillinghast Reflector Echelle Spectrograph, i.e. TRES (Fűrész 2008), an  $R = 44,000$  spectrograph on the 1.5 m Tillinghast reflector at the Fred Lawrence Whipple Observatory (located on Mt. Hopkins, Arizona). These spectra were collected on the nights of 2010 May 28 and 2010 July 5 and had exposure times of 12 and 15 minutes respectively.

We also downloaded RVs from 26 spectra collected with the HIRES instrument (Vogt et al. 1994) at the Keck I telescope from 2010 July 25 to 2014 July 11. These spectra were originally collected as part of the *Kepler* Follow-up Observing Program. The standard California Planet Search setup was used (Howard et al. 2010) and the C2 decker was utilized to conduct sky subtraction. Exposure times averaged 1800 s.

Finally, we gathered 83 spectra with the High Accuracy Radial velocity Planet Searcher in North hemisphere (HARPS-N) instrument (Cosentino et al. 2012, 2014), on the 3.6 m Telescopio Nazionale Galileo (TNG) on La Palma. These observations were made from 2014 June 20 to 2015 November 7, all with exposure times of 30 minutes. They were collected as part of the HARPS-N Collaboration’s Guaranteed Time Observations (GTO) program. Using the technique described in Malavolta et al. (2017), we confirmed that none of these spectra suffered from Moon contamination.

BJD	RV (m s <sup>-1</sup> )	RV Error (m s <sup>-1</sup> )	FWHM (km s <sup>-1</sup> )	BIS (km s <sup>-1</sup> )	log <sub>10</sub> ( $R'_{HK}$ )	log <sub>10</sub> ( $R'_{HK}$ ) Error	Instrument
2455402.854339	-8.78	1.32	...	...	-5.078	...	HIRES
2455414.971547	-1.24	1.33	...	...	-5.003	...	HIRES
2455486.859621	-0.83	1.50	...	...	-4.985	...	HIRES
2455544.719659	-5.95	2.14	...	...	-4.971	...	HIRES
2455760.087400	4.58	1.39	...	...	-4.982	...	HIRES
2455796.934228	-3.56	1.25	...	...	-4.974	...	HIRES
2455797.920566	-1.33	1.22	...	...	-4.972	...	HIRES
2455799.056115	-5.98	1.48	...	...	-5.005	...	HIRES
2456114.931149	-6.02	1.27	...	...	-4.944	...	HIRES
2456133.896429	-2.53	1.31	...	...	-4.933	...	HIRES
2456147.919325	0.44	1.31	...	...	-4.967	...	HIRES
2456163.912379	6.63	1.31	...	...	-4.922	...	HIRES
2456164.801818	-0.23	1.30	...	...	-4.924	...	HIRES
2456166.047782	1.05	1.37	...	...	-4.927	...	HIRES
2456166.759374	-2.55	1.44	...	...	-4.913	...	HIRES

2456167.990464	-3.55	1.51	...	...	-4.912	...	HIRES
2456451.100822	2.47	1.48	...	...	-4.953	...	HIRES
2456483.086583	5.47	1.94	...	...	-4.943	...	HIRES
2456486.833662	0.39	1.31	...	...	-4.938	...	HIRES
2456488.822611	7.76	1.19	...	...	-4.926	...	HIRES
2456494.987645	5.79	1.29	...	...	-4.926	...	HIRES
2456506.780605	1.27	1.21	...	...	-4.931	...	HIRES
2456507.968496	-0.32	1.23	...	...	-4.947	...	HIRES
2456532.877110	2.73	1.14	...	...	-4.940	...	HIRES
2456830.887055	-0.74	1.39	...	...	-4.962	...	HIRES
2456850.049952	2.59	1.26	...	...	-4.954	...	HIRES
2456828.616553	-37327.64	6.07	6.63443	-0.02220	-4.9522	0.0699	HARPS-N
2456828.651774	-37320.76	1.50	6.66839	-0.03107	-4.9819	0.0106	HARPS-N
2456829.664594	-37319.24	1.56	6.66376	-0.03206	-4.9788	0.0111	HARPS-N
2456830.665375	-37319.62	1.83	6.67197	-0.03353	-4.9882	0.0146	HARPS-N
2456831.690035	-37319.77	1.70	6.66691	-0.03495	-4.9634	0.0128	HARPS-N
2456832.615999	-37314.68	1.80	6.66854	-0.03182	-4.9975	0.0150	HARPS-N
2456833.672301	-37322.65	2.12	6.67240	-0.03957	-4.9553	0.0182	HARPS-N
2456834.581042	-37315.83	2.01	6.66876	-0.03718	-4.9764	0.0169	HARPS-N
2456834.677908	-37321.70	1.98	6.66877	-0.03961	-4.9768	0.0169	HARPS-N
2456835.587887	-37318.54	2.07	6.65839	-0.02603	-5.0090	0.0197	HARPS-N
2456845.576470	-37322.26	1.44	6.66668	-0.03079	-4.9739	0.0097	HARPS-N
2456846.662015	-37327.96	2.10	6.65639	-0.02891	-4.9885	0.0184	HARPS-N
2456847.656794	-37321.88	2.67	6.65969	-0.03820	-4.9938	0.0273	HARPS-N
2456848.652903	-37327.73	1.68	6.66082	-0.03667	-4.9900	0.0131	HARPS-N
2456849.657878	-37326.37	2.17	6.66712	-0.02913	-4.9558	0.0182	HARPS-N
2456850.660745	-37324.98	2.17	6.66481	-0.03397	-4.9575	0.0182	HARPS-N
2456851.654237	-37323.89	1.66	6.66590	-0.03297	-4.9625	0.0121	HARPS-N
2456852.655703	-37316.98	2.55	6.67237	-0.03670	-4.9994	0.0260	HARPS-N
2456853.657053	-37318.56	1.62	6.67355	-0.03209	-4.9818	0.0122	HARPS-N
2456865.684262	-37320.32	1.67	6.66629	-0.02961	-4.9818	0.0130	HARPS-N
2456866.681774	-37323.10	3.48	6.66279	-0.04100	-4.9629	0.0388	HARPS-N
2456883.639193	-37324.45	1.89	6.65864	-0.03904	-5.0004	0.0164	HARPS-N
2456884.647365	-37324.61	1.84	6.66539	-0.02953	-4.9982	0.0166	HARPS-N
2456885.644031	-37322.71	1.86	6.66503	-0.03266	-4.9753	0.0159	HARPS-N
2456886.642561	-37346.88	11.81	6.66764	-0.08202	-5.0609	0.2193	HARPS-N
2456887.651622	-37322.33	1.83	6.67033	-0.03390	-4.9883	0.0152	HARPS-N
2456888.580937	-37321.19	2.74	6.65114	-0.02926	-4.9577	0.0266	HARPS-N
2456889.585275	-37324.05	2.15	6.65998	-0.03761	-4.9716	0.0189	HARPS-N
2456903.541993	-37318.65	1.41	6.66569	-0.03568	-4.9851	0.0095	HARPS-N
2456919.514886	-37322.96	2.44	6.66569	-0.03738	-4.9735	0.0224	HARPS-N
2456922.547287	-37323.20	1.67	6.65621	-0.04098	-5.0131	0.0146	HARPS-N
2456923.501548	-37320.74	1.62	6.66346	-0.03370	-5.0026	0.0127	HARPS-N
2456924.510113	-37318.66	2.43	6.65831	-0.03765	-4.9763	0.0237	HARPS-N
2456936.514073	-37326.01	1.72	6.65525	-0.03770	-4.9864	0.0143	HARPS-N
2456939.418861	-37323.19	1.36	6.65561	-0.03499	-4.9986	0.0093	HARPS-N
2456969.402685	-37323.75	3.10	6.65044	-0.03308	-5.0094	0.0377	HARPS-N
2457106.734166	-37320.49	2.77	6.66677	-0.03337	-4.9801	0.0289	HARPS-N
2457116.717298	-37324.15	1.51	6.64918	-0.03136	-5.0282	0.0120	HARPS-N
2457118.706394	-37327.91	1.87	6.64875	-0.03660	-5.0338	0.0181	HARPS-N
2457121.726137	-37324.71	1.61	6.64485	-0.03692	-5.0174	0.0141	HARPS-N
2457153.685174	-37323.84	2.87	6.64814	-0.04127	-5.0063	0.0321	HARPS-N
2457156.714776	-37324.15	12.94	6.66453	-0.05998	-4.9161	0.1624	HARPS-N
2457159.642662	-37323.22	2.14	6.65282	-0.03562	-4.9989	0.0202	HARPS-N
2457160.638323	-37320.99	2.03	6.65589	-0.04059	-5.0130	0.0185	HARPS-N
2457161.626357	-37324.63	1.70	6.65201	-0.04164	-5.0095	0.0140	HARPS-N
2457180.658376	-37322.50	1.60	6.64953	-0.03798	-5.0160	0.0127	HARPS-N
2457181.686408	-37322.02	1.75	6.65033	-0.03871	-5.0016	0.0146	HARPS-N
2457182.670828	-37322.60	1.58	6.64797	-0.03663	-5.0014	0.0122	HARPS-N
2457183.652886	-37321.34	1.81	6.64944	-0.03550	-4.9890	0.0145	HARPS-N
2457184.643705	-37324.94	2.35	6.65649	-0.03450	-5.0265	0.0237	HARPS-N
2457185.662466	-37324.52	1.51	6.65258	-0.03701	-5.0096	0.0115	HARPS-N
2457186.662672	-37325.81	1.52	6.65510	-0.03815	-5.0237	0.0118	HARPS-N

2457188.679310	-37328.26	1.58	6.65099	-0.03864	-5.0010	0.0123	HARPS-N
2457189.672084	-37322.40	2.63	6.64860	-0.03852	-5.0649	0.0316	HARPS-N
2457190.685669	-37325.59	1.61	6.64984	-0.03343	-5.0211	0.0135	HARPS-N
2457191.685746	-37323.07	1.57	6.65434	-0.03606	-5.0243	0.0128	HARPS-N
2457192.684342	-37324.65	1.67	6.65251	-0.03217	-5.0374	0.0147	HARPS-N
2457193.684869	-37323.90	1.44	6.65760	-0.03912	-5.0097	0.0107	HARPS-N
2457195.594752	-37318.06	1.65	6.65239	-0.03455	-4.9930	0.0132	HARPS-N
2457221.626801	-37324.84	1.37	6.64834	-0.04333	-5.0237	0.0101	HARPS-N
2457222.569536	-37324.99	1.78	6.65155	-0.04076	-4.9982	0.0150	HARPS-N
2457223.579194	-37322.72	3.17	6.63767	-0.04077	-5.0049	0.0375	HARPS-N
2457225.522395	-37319.94	3.63	6.64970	-0.03534	-5.0279	0.0478	HARPS-N
2457226.582966	-37317.08	3.17	6.66790	-0.02615	-5.0750	0.0424	HARPS-N
2457226.606265	-37321.98	2.58	6.65109	-0.03404	-5.0105	0.0277	HARPS-N
2457227.627333	-37316.52	1.67	6.66113	-0.03348	-5.0084	0.0136	HARPS-N
2457228.630703	-37320.68	2.72	6.66677	-0.02712	-4.9272	0.0251	HARPS-N
2457229.584812	-37316.53	2.51	6.65780	-0.02953	-5.0054	0.0266	HARPS-N
2457230.528273	-37320.18	3.34	6.66154	-0.02550	-4.9889	0.0385	HARPS-N
2457254.631919	-37325.16	2.41	6.66627	-0.03812	-5.0093	0.0260	HARPS-N
2457256.398580	-37314.12	2.36	6.64870	-0.04351	-4.9894	0.0239	HARPS-N
2457257.413714	-37315.46	1.88	6.65391	-0.03681	-4.9651	0.0149	HARPS-N
2457267.435503	-37324.84	2.04	6.64591	-0.03502	-5.0136	0.0193	HARPS-N
2457268.492540	-37322.86	2.21	6.64810	-0.04496	-5.0215	0.0224	HARPS-N
2457269.418733	-37320.32	1.69	6.65385	-0.03696	-5.0211	0.0145	HARPS-N
2457270.407599	-37321.14	1.36	6.65014	-0.03809	-5.0301	0.0099	HARPS-N
2457271.408119	-37325.01	1.44	6.65177	-0.03459	-5.0336	0.0110	HARPS-N
2457273.426969	-37326.84	1.46	6.64860	-0.04486	-5.0183	0.0109	HARPS-N
2457301.384627	-37319.51	1.47	6.65573	-0.03632	-5.0121	0.0111	HARPS-N
2457302.383904	-37318.58	1.79	6.65019	-0.03970	-5.0308	0.0159	HARPS-N
2457321.426080	-37318.14	2.40	6.64231	-0.03293	-5.0135	0.0243	HARPS-N
2457330.417736	-37318.77	1.89	6.65257	-0.03583	-5.0053	0.0167	HARPS-N
2457334.397358	-37321.22	1.64	6.65030	-0.04224	-5.0085	0.0131	HARPS-N

Table 2.1: Kepler-538 RV observations and activity indicators collected with the HIRES and HARPS-N spectrographs, determined from the DRS.

## 2.3 Stellar Characterization

Stellar atmospheric parameters (effective temperature, metallicity, and surface gravity) were determined in two different ways. First, we combined the two TRES spectra and used the Stellar Parameter Classification tool, SPC, (Buchhave et al. 2012). SPC compares an input spectrum against a library grid of synthetic spectra from Kurucz (1992), interpolating over the library to find the best match as well as uncertainties on the relevant stellar parameters. This method provides a measure for the rotational velocity as well.

Second, we used ARES+MOOG on the combination of our 83 HARPS-N spectra. More details about this method, based on equivalent widths (EWs), are found in Sousa (2014) and references therein. In short, ARESv2 (Sousa et al. 2015) automatically calculates the EWs of a set of neutral and ionized iron lines (Sousa et al. 2011). These are then used as input in MOOG<sup>3</sup> (Snedden 1973), assuming local thermodynamic equilibrium and using a grid of ATLAS plane-parallel model atmospheres (Kurucz 1993). Following Sousa et al.

<sup>3</sup>2017 version: [http://www.as.utexas.edu/~sim\\$chris/moog.html](http://www.as.utexas.edu/~sim$chris/moog.html)

Table 2.2: Stellar parameters of Kepler-538

Parameter	Unit	SPC	ARES+MOOG	Combined
<i>Stellar parameters</i>				
Effective temperature $T_{\text{eff}}$	K	$5547 \pm 50$	$5522 \pm 72$	...
Surface gravity $\log g$	$\text{g cm}^{-2}$	$4.51 \pm 0.10$	$4.55 \pm 0.12$	...
Metallicity $[m/\text{H}]$	dex	$-0.03 \pm 0.08$	...	...
Metallicity $[\text{Fe}/\text{H}]$	dex	...	$-0.15 \pm 0.05$	...
Radius $R_*$	$R_{\odot}$	$0.8707^{+0.0063}_{-0.0060}$	$0.8727^{+0.0063}_{-0.0062}$	$0.8717^{+0.0064}_{-0.0061}$
Mass $M_*$	$M_{\odot}$	$0.925^{+0.034}_{-0.036}$	$0.870 \pm 0.024$	$0.892^{+0.051}_{-0.035}$
Density $\rho_*$	$\rho_{\odot}$	$1.404^{+0.061}_{-0.068}$	$1.31 \pm 0.052$	$1.349^{+0.089}_{-0.0716}$
Distance	pc	$156.67^{+0.71}_{-0.70}$	$156.65^{+0.70}_{-0.68}$	$156.66^{+0.71}_{-0.69}$
Age	Gyr	$3.8^{+2.1}_{-2.0}$	$6.7^{+1.8}_{-1.6}$	$5.3^{+2.4}_{-3.0}$
Projected rotational velocity $v \sin i$	$\text{km s}^{-1}$	$1.1 \pm 0.5$	...	...

(2011), we added systematic errors in quadrature to our errors. The value for surface gravity was corrected for accuracy following Mortier et al. (2014). The results from SPC and ARES+MOOG agreed well within uncertainties.

We then estimated stellar mass, radius, and thus density with the `isochrones` package, a Python routine for inferring model-based stellar properties from known observations (Morton 2015). We supplied the spectroscopic effective temperature, metallicity, the *Gaia* DR2 parallax (Gaia Collaboration et al. 2016, 2018), and multiple photometric magnitudes ( $B$ ,  $V$ ,  $J$ ,  $H$ ,  $K$ ,  $W1$ ,  $W2$ ,  $W3$ , and  $G$ ) as input. Note that we did not use the surface gravity as an input parameter as this parameter is not well determined spectroscopically, e.g. Mortier et al. (2014). We ran `isochrones` four times, using the two different sets of spectroscopic parameters and two sets of isochrones, Modules for Experiments in Stellar Astrophysics (MESA) Isochrones and Stellar Tracks (MIST) and Dartmouth<sup>4</sup>.

All four results were consistent, so we followed Malavolta et al. (2018) and derived our final set of parameters and uncertainties from the 16th, 50th, and 84th percentile values of the combined posteriors, minimizing systematic biases from using different spectroscopic methods or isochrones. The results of this analysis are listed in Table 2.2.

As a useful check, we find that our estimates of stellar effective temperature, stellar radius, and distance are all within  $1\sigma$  of the *Gaia* DR2 revised *Kepler* stellar parameters (Berger et al. 2018).

## Consistency with Stellar Activity and Gyrochronology

As will be discussed in more detail in later sections, RV observations with both HIRES and HARPS-N yielded  $\log R'_{HK}$ , an indicator of stellar activity. Although  $\log R'_{HK}$ , like stellar

<sup>4</sup>The Dartmouth isochrones did not use the  $G$  magnitude.

activity, is time variable, taking an average or median over time is still a useful metric of the general activity level of the star. The median  $\log R'_{HK}$  with HIRES and HARPS-N was  $-4.946 \pm 0.035$  and  $-5.001 \pm 0.027$ , respectively. The overall  $\log R'_{HK}$  across both datasets was  $-4.990 \pm 0.034$ .

We used this  $\log R'_{HK}$  value and the  $B - V$  color index<sup>5</sup> to estimate the stellar rotation period via Noyes et al. (1984), finding a value of  $32.0 \pm 1.0$  days. Our full model (described in Sections 2.4 and 2.4) included the rotation period as a free parameter, which we estimated to be  $25.2^{+6.5}_{-1.2}$  days, in agreement with the stellar activity predicted rotation period to within  $1\sigma$ . Further, during our processing of photometric data (see Section 2.4), we produced a periodogram and an auto-correlation function of the photometry. We found signals near 22 and 32 days in the former as well as a weak, broad signal around 20 – 25 days in the latter, all of which are near the activity-inferred rotation period or the rotation period estimated from our model.

We also checked that our estimate of stellar age was consistent with gyrochronology. We found a gyrochronological age for Kepler-538 first by determining the convective turnover timescale from Barnes and Kim (2010) using the  $B - V$  color index. Then we used the gyrochronological relation in Barnes (2010) to calculate age from the convective turnover timescale and the rotation period (calculated from our full model). In this way, we determined a stellar age of  $3.40^{+1.86}_{-0.29}$  Gyr, consistent within  $1\sigma$  of our isochrone-derived age of  $5.3^{+2.4}_{-3.0}$  Gyr.

## Possible Binarity of Kepler-538

In order to investigate whether Kepler-538 may be a binary star or have a companion, either of which could have an effect on the dynamics or nature of Kepler-538b, we downloaded all adaptive optics (AO) and speckle data uploaded to <https://exofop.ipac.caltech.edu/k2/> for the star before 2019 July 30. The Palomar High Angular Resolution Observer (PHARO) on the Palomar-5 m telescope collected AO observations on 2010 July 1 in  $J$  and  $Ks$  band; no companions were found between  $2''$  and  $5''$  down to 19th magnitude. The Differential Speckle Survey Instrument (DSSI) on the WIYN-3.5 m telescope collected speckle observations on 23 October 2010 in  $r$  and  $v$  band; no companions were found between  $0.2''$  and  $1.8''$  down to a contrast of  $\Delta m = 3.6$ . Finally, the Robo-AO instrument on the Palomar-1.5 m telescope collected an AO observation on 2012 July 28 in the  $i$  band; no companions were found between  $0.15''$  and  $2.5''$  down to a contrast of  $\Delta m \approx 6$ . In short, there is no evidence of a close stellar companion in any of the AO or speckle data.

However, it is worth noting that there is a faint comoving object  $17''$  from Kepler-538, which *Gaia* found at approximately the same distance of 157 pc (Gaia Collaboration et al. 2016, 2018). This means if the two stars are at the same distance, they are separated by  $2700 \pm 12$  au, a large enough separation to negligibly affect the planet. Both objects have good astrometric solutions with *Gaia* (Lindgren et al. 2018), and their relative motion given

<sup>5</sup>determined from <https://exofop.ipac.caltech.edu/>; accessed 2019 July 29

by *Gaia* proper motions is  $0.408 \pm 0.510 \text{ km s}^{-1}$ . However, this relative motion is so slight that we were unable to meaningfully constrain orbital motion.

We estimated the mass of the comoving object to be  $0.1169 \pm 0.0075 M_{\odot}$  by applying the photometric relation in Mann et al. (2019) to the Two Micron All-Sky Survey (2MASS)  $K_s$  magnitude (Cutri et al. 2003), which gives a total system mass of  $1.009 \pm 0.044 M_{\odot}$ . With this mass and separation, a circular face-on orbit would have a total relative velocity of  $0.576 \pm 0.013 \text{ km s}^{-1}$ . Thus, both the velocity of a face-on circular orbit and zero velocity are within  $1\sigma$  of the measured relative velocity. With such weak constraints from *Gaia* DR2, we cannot rule out a circular orbit at wide separation nor a highly eccentric orbit, currently observed at apastron, which brings the companion close enough in to potentially affect the planet.

## 2.4 Data Analysis

Our analysis of photometric and spectroscopic data included a simultaneous fit to both data types. Therefore, we first describe the data reduction process and model components of photometry and spectroscopy separately, then discuss the combined model afterward.

### Photometric Data

We cleaned and reduced the photometric *Kepler* data using the `lightkurve` Python package (Barentsen et al. 2019). Each quarter was cleaned and reduced separately. For a given quarter, observation times without a corresponding flux were removed. Then, a crude light curve model based on the exoplanet parameters reported in the NASA Exoplanet Archive<sup>10</sup> (accessed 2019 February 16) was subtracted from the light curve so that in-transit data would not be clipped or flattened out in the next steps. Next, we flattened the light curve using the `lightkurve` `flatten` function, which uses a Savitzky-Golay filter. A window length of 615 or 41 was selected (i.e. 615 or 41 consecutive data points) for short-cadence and long-cadence data respectively, which is approximately three times the ratio between the transit duration and the observation cadence. Then, we clipped outlier data points discrepant from the median flux by more than  $5\sigma$ . Lastly, we added the transit model from the earlier step back to the light curve. The reduced data can be seen in Fig. 2.1, plotted in time and also phase-folded to the period of Kepler-538b.

We modeled the light curve with the `BATMAN` Python package (Kreidberg 2015a), which is based on the Mandel and Agol (2002) transit model. The model included a baseline offset parameter, a white noise parameter (to allow for instrumental and systematic noise in the data), two quadratic limb-darkening parameters using the Kipping (2013a) parameterization, the transit time (i.e. reference epoch), orbital period, planet radius relative to stellar radius, transit duration, impact parameter, eccentricity, and longitude of periastron.

<sup>10</sup><https://exoplanetarchive.ipac.caltech.edu/>

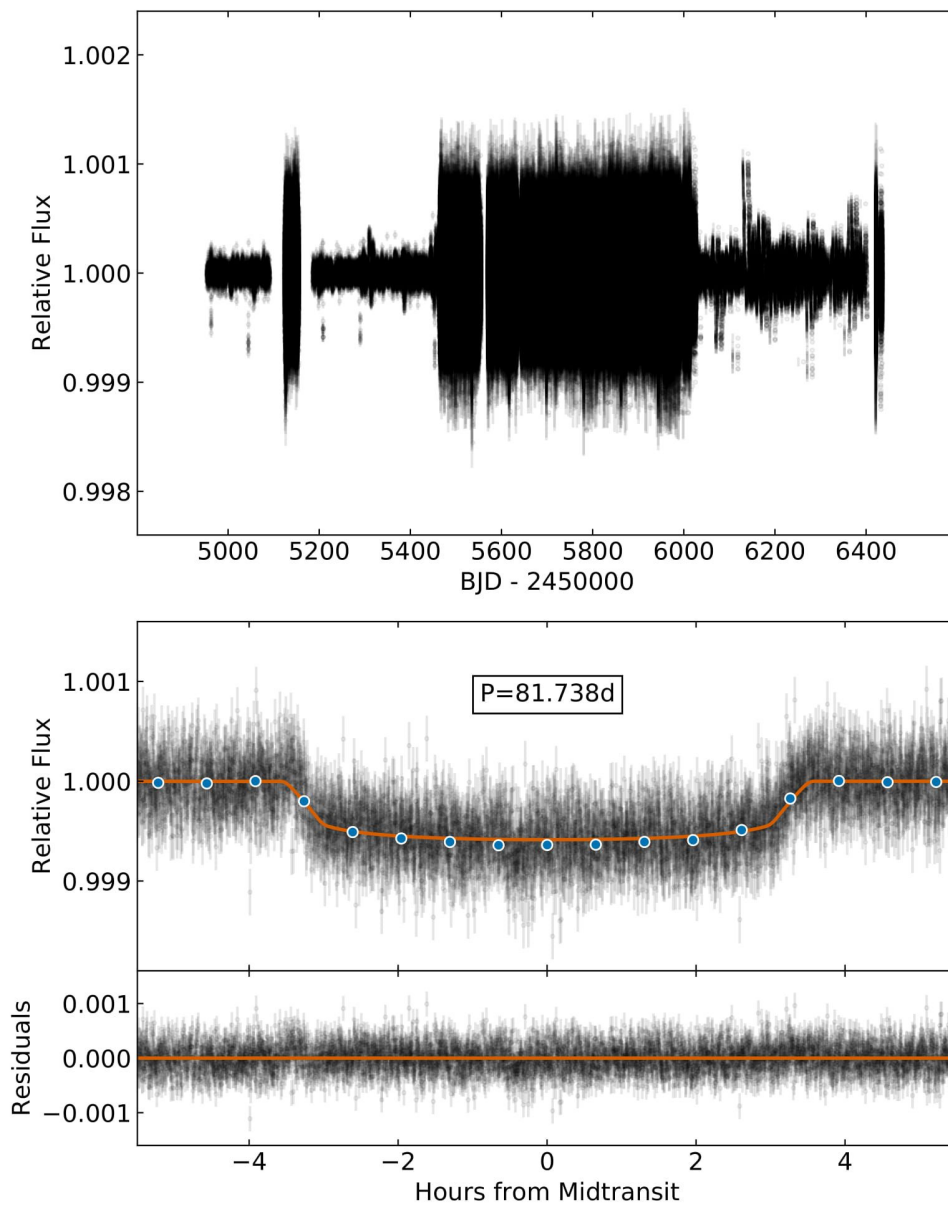


Figure 2.1: Transit plot of Kepler-538b. The top subplot is the pre-search data conditioning (PDC) *Kepler* photometry. The top panel of the bottom subplot shows the phase-folded photometry in and near the transit of Kepler-538b, with the best-fit transit model in orange and binned data in blue. The bottom panel of the bottom subplot shows the photometric residuals after subtracting the best-fit transit model.



Table 2.3: Transit and RV parameters of Kepler-538b

Parameter	Unit	This Paper	Priors
<i>Transit parameters</i>			
Period $P$	day	$81.73778 \pm 0.00013$	Unif(81.73666,81.73896)
Time of first transit	BJD-2454833	$211.6789^{+0.0010}_{-0.0011}$	Unif(211.6671,211.6901)
Orbital eccentricity $e$	...	$0.041^{+0.034}_{-0.029} (< 0.11)^6$	Beta(0.867,3.03) <sup>7,8</sup>
Longitude of periastron $\omega$	degree	$140^{+140}_{-90}$	Unif(0,360)
Impact parameter $b$	...	$0.41^{+0.10}_{-0.21}$	Unif(0,1)
Transit duration $t_{14}$	hr	$6.62^{+0.21}_{-0.13}$	Unif(0,24)
Radius ratio $R_p/R_*$	...	$0.02329^{+0.00039}_{-0.00033}$	Jeffreys(0.001,1)
Quadratic limb-darkening parameter $q_1$	...	$0.164^{+0.067}_{-0.042}$	Unif(0,1)
Quadratic limb-darkening parameter $q_2$	...	$0.74^{+0.16}_{-0.22}$	Unif(0,1)
Normalized baseline offset	ppm	$-2.1^{+2.7}_{-2.8}$	Unif(-100,100)
Photometric white noise amplitude	ppm	$112.2^{+2.5}_{-2.4}$	ModJeffreys(1,1000,234)
<i>RV parameters</i>			
Semi-amplitude $K$	$\text{m s}^{-1}$	$1.69^{+0.39}_{-0.38}$	ModJeffreys(0.01,10,2.1)
HIRES RV white noise amplitude	$\text{m s}^{-1}$	$3.25^{+0.56}_{-0.48}$	ModJeffreys(0,10,2.1)
HARPS-N RV white noise amplitude	$\text{m s}^{-1}$	$2.24^{+0.29}_{-0.27}$	ModJeffreys(0,10,2.1)
HARPS-N FWHM white noise amplitude	$\text{m s}^{-1}$	$6.71^{+0.52}_{-0.46}$	Jeffreys(0.01,10)
HIRES RV offset amplitude	$\text{m s}^{-1}$	$-0.50^{+0.78}_{-0.87}$	Unif(-5,5)
HARPS-N RV offset amplitude	$\text{m s}^{-1}$	$-37322.07^{+0.58}_{-0.73}$	Unif(-37330,-37315)
HARPS-N FWHM offset amplitude	$\text{m s}^{-1}$	$6655.4^{+7.5}_{-8.6}$	Unif(6600,6700)
GP RV convective blueshift amplitude $V_c$	$\text{m s}^{-1}$	$0.86^{+0.75}_{-0.54}$	ModJeffreys(0,15,2.1)
GP RV rotation modulation amplitude $V_r$	$\text{m s}^{-1}$	$4.0^{+5.7}_{-3.0}$	ModJeffreys(0,15,2.1)
GP FWHM amplitude $F_c$	$\text{m s}^{-1}$	$13.3^{+5.9}_{-4.9}$	Jeffreys(0.01,25)
GP stellar rotation period $P_*$	day	$25.2^{+6.59}_{-1.2}$	Unif(20,40)
GP inverse harmonic complexity $\lambda_p$	...	$5.2^{+2.8}_{-2.5}$	Unif(0.25,10)
GP evolution time-scale $\lambda_e$	day	$370^{+200}_{-140}$	Jeffreys(1,1000)
<i>Derived parameters</i>			
Planet radius $R_p$	$R_\oplus$	$2.215^{+0.040}_{-0.034}$	...
System scale $a/R_*$	...	$87.5^{+1.5}_{-1.6}$	...
Planet semi-major axis $a$	au	$0.3548^{+0.0066}_{-0.0068}$	...
Orbital inclination $i$	degree	$89.73^{+0.14}_{-0.06}$	...
Planet mass $M_p$	$M_\oplus$	$10.6^{+2.5}_{-2.4}$	...
Planet mean density $\rho_p$	$\rho_\oplus$	$0.98 \pm 0.23$	...
Planet mean density $\rho_p$	$\text{g cm}^{-3}$	$5.4 \pm 1.3$	...
Planet insolation flux $S_p$	$S_\oplus$	$5.19^{+0.31}_{-0.28}$	...
Planet eq. temp. $T_{eq}$ (albedo = 0.3)	K	380	...
Planet eq. temp. $T_{eq}$ (albedo = 0.5)	K	350	...

We assumed uniform, Jeffreys, or modified Jeffreys priors for most of the parameters in this model, which are listed in Table 2.3. A Jeffreys prior is less informative than a uniform prior when the prior range is large and the scale of the parameter is unknown. A modified Jeffreys prior has the following form (Gregory 2007):

$$p(X) = \frac{1}{X + X_0} \frac{1}{\ln\left(\frac{X_{\max} + X_0}{X_{\min} + X_0}\right)}$$

where  $X_{\min}$  and  $X_{\max}$  are the minimum and maximum prior value and  $X_0$  is the location of a knee in the prior. A modified Jeffreys prior behaves like a Jeffreys prior above the knee at  $X_0$  and behaves like a uniform prior below the knee; this is useful when the prior includes zero (creating an asymptote for a conventional Jeffreys prior). A Jeffreys prior is simply a modified Jeffreys prior with the knee at  $X_0 = 0$ .

The only parameter with a different prior was orbital eccentricity. We applied a beta prior to orbital eccentricity using the values recommended by Kipping (2013b); we also truncated the prior to exclude  $e > 0.95$ .

Additionally, we also applied a stellar density prior. This was done given the fact that stellar density can be measured in two distinct ways: from photometry for a transiting exoplanet and from a stellar spectrum combined with stellar evolutionary tracks (we used the latter method in Section 2.3). Specifically, stellar density can be calculated via the following equation (Seager and Mallén-Ornelas 2003; Sozzetti et al. 2007):

$$\rho_* = \frac{3\pi}{GP^2} \left(\frac{a}{R_*}\right)^3 \quad (2.1)$$

where the orbital period ( $P$ ) and the normalized semi-major axis ( $a/R_*$ ) are exoplanet properties that can be derived from the light curve. We applied a Gaussian prior to the exoplanet-derived stellar density using the density (and corresponding uncertainties) derived from spectra and stellar evolutionary tracks.

## RV Data

Our RV analysis of Kepler-538b included not only the RV values determined from our HIRES and HARPS-N spectra, but also a number of indicators of stellar activity estimated from these spectra. For HARPS-N, these included the cross-correlation function (CCF) bisector span inverse slope (hereafter BIS), the CCF full width at half maximum (FWHM), and  $\log R'_{HK}$ . Our data reduction was performed with the data reduction software (DRS) 3.7 HARPS-N pipeline which applied a G2 stellar type mask. For HIRES, RVs are estimated with an iodine cell rather than cross correlation, so  $\log R'_{HK}$  was calculated but not BIS or FWHM.

The RV and FWHM observations (and the corresponding model fit) can be seen in Fig. 2.2. Additionally, all RV, FWHM, BIS, and  $\log R'_{HK}$  values are listed in Table 2.1. There is a clear long-term trend in the FWHM observations (and to a lesser extent in the

BIS and  $\log R'_{HK}$  observations). However, we could not determine whether these trends have a stellar or instrumental origin, nor why there are no similar trends in the RV observations. On the one hand, when we checked three standard stars observed by HARPS-N during the same period of time, only one showed a similar FWHM trend. On the other hand, a FWHM trend in HARPS-N observations was also reported by Benatti et al. (2017) due to a defocusing problem, but that issue was corrected in 2014 March, before our first HARPS-N observations began. Still, perhaps a similar but slower and smaller drift affected our observations.

We first analyzed our observations with a periodogram, then with a correlation plot, and then constructed a model for our spectroscopic data.

### Periodogram Analysis

Before modeling our spectroscopic observations, we first investigated the frequency structure of our data. We made a generalized Lomb-Scargle periodogram (Scargle 1982; Zechmeister and Kürster 2009) of  $\log R'_{HK}$ , BIS, FWHM, RV, and the window function of the observation time series, all of which can be seen in Fig. 2.3.  $\log R'_{HK}$ , BIS, and FWHM are indicators of stellar activity (Queloz et al. 2001); also see Haywood (2015) and references therein. The window function shows how the signals are modified by the time sampling of the measurements.

The HARPS-N RV periodogram shows a clear peak at 82 days, the orbital period of Kepler-538b; the HIRES RV periodogram shows a weaker signal at the same period. None of the other periodograms show a similar feature, lending credence to the RV detection of Kepler-538b. The RV periodograms also exhibit two larger peaks near  $0.03 - -0.04 \text{ days}^{-1}$ , interpreted as the rotational frequency. Indeed, as our model fit discussed later in Section 2.4 and the results in Table 2.3 will show, both peaks fall within the  $1\sigma$  confidence region of the stellar rotation period. (See Section 2.4 for a description of our rotation period estimation.) We also find that the long-term trends observed in the activity indices, combined with the spectral window, affect the periodograms, since a long-term trend is clearly noticeable (see Fig. 2.2 and Table 2.1). We removed these trends and found the resulting periodograms show a peak at the rotational period, but nothing at the orbital period.

### Correlation Analysis

We also examined correlations between the RV observations and the other stellar activity indices. As can be seen in Fig. 2.4, there is a slightly stronger correlation between RV and FWHM than between RV and BIS or  $\log R'_{HK}$ . However, there may also be useful information in the correlations between RV and BIS or  $\log R'_{HK}$ . In order to test this, we cross-checked results that included BIS and  $\log R'_{HK}$  in the modeling against those that did not and found consistent results. For this reason, and for the sake of simplicity, in this paper we only report our analysis of RVs in conjunction with FWHM observations.

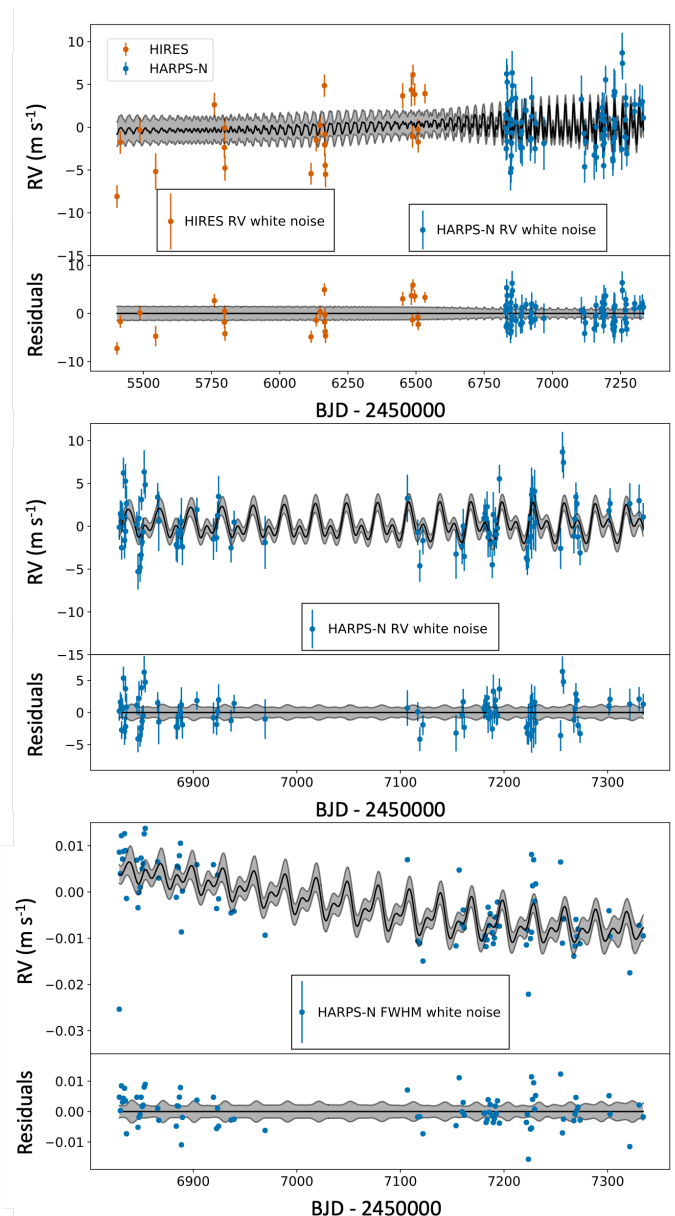


Figure 2.2: Stellar activity and corresponding Gaussian process regression of Kepler-538 (with planetary signal removed). The top subplot shows the HIRES (orange) and HARPS-N (blue) mean-subtracted RV observations and corresponding model fit in the top panel, with residuals in the bottom panel. The black line is the model fit and the gray region is the  $1\sigma$  confidence interval (drawn from the full posterior distribution). The data points in boxes correspond to the white noise amplitude modeled for each dataset. The middle subplot is a zoom in of the top subplot to the latter two campaigns of observations (only the HARPS-N data). The bottom subplot shows the mean-subtracted FWHM times from HARPS-N (matching the time series of the middle panel) and the corresponding model fit in the top panel, residuals in the bottom panel. Note: two RV data points with error bars greater than  $5 \text{ m s}^{-1}$  were removed from the plots (but not the underlying model fit).

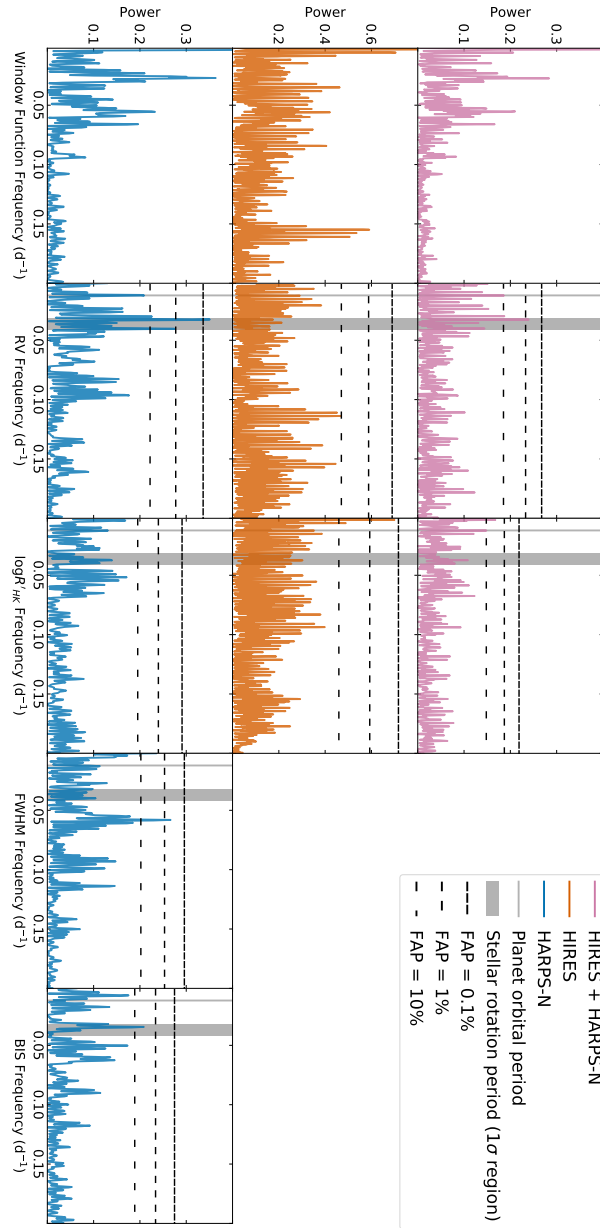


Figure 2.3: Periodograms of the window function (computed from observation times), RV,  $\log R'_{HK}$ , CCF FWHM, and CCF BIS the Kepler-538 system. Subplots in blue are based on HARPS-N observations, subplots in orange are based on HIRES observations, and subplots in pink are based on both HARPS-N and HIRES. The gray region is the  $1\sigma$  confidence interval of the rotation period of Kepler-538 (a stellar activity parameter we estimated in our full model). The gray line is the orbital period of Kepler-538b ( $P = 81.74$  days). Lastly, the dashed black lines correspond to various false alarm probabilities. (Note the different y-axis scalings for HIRES.)

## General RV Modeling Approach

In order to model our RV and FWHM observations, we followed the method described in Rajpaul et al. (2015), hereafter R15, which establishes a method to characterize stellar activity that uses simultaneous regression of distinct data types (with potentially distinct time series). Here we briefly discuss Gaussian process (GP) regression and the novel approach to GPs used by R15.

In brief, a GP is a stochastic process that captures the covariance between observations and allows for the modeling of correlated noise (Rasmussen and Williams 2006). A GP is specified by a covariance matrix in which the diagonal elements are the individual observation variances and each off-diagonal element describes the covariance between two observations. The values of the off-diagonal elements are determined by a kernel function, which describes the nature of the correlated noise. GPs provide a great deal of flexibility that has made them an effective tool to account for stellar activity (Haywood et al. 2014). R15 recommended characterizing stellar activity with a quasi-periodic (QP) kernel, which balances physical motivation with simplicity. The QP kernel uses four parameters (commonly called hyperparameters) and defines the covariance matrix as follows:

$$K_{\text{QP}}(t_i, t_j) = h^2 \exp \left( - \frac{\sin^2(\pi(t_i - t_j)/P_*)}{2\lambda_p^2} - \frac{(t_i - t_j)^2}{2\lambda_e^2} \right), \quad (2.2)$$

where  $t_i$  and  $t_j$  are observations made at any two times,  $h$  is the amplitude hyperparameter (though not a *true* amplitude, as it incorporates some multiplicative constants),  $P_*$  is the period of the variability (i.e. the rotation period in the case of stellar activity),  $\lambda_p$  is the inverse harmonic complexity (a smoothness factor that acts as a proxy for the number of turning points and inflection points per rotation period), and  $\lambda_e$  is an exponential decay factor (scaling with, though not exactly equal to, the decay timescale of the spots on the star).

One of the key insights of R15 is the way in which they related multiple GPs to one another. GP regression can be used on multiple datasets by constructing a covariance matrix that describes the covariances between two observations of any type. In our case, this means any possible pairing of RV–RV, RV–FWHM, or FWHM–FWHM data points. The following equations (based on equations 13 and 14 from R15) relate RV and FWHM:

$$\Delta RV = V_c G(t) + V_r \dot{G}(t) \quad (2.3)$$

$$FWHM = F_c G(t) \quad (2.4)$$

Here,  $G(t)$  is an underlying GP directly quantifying stellar activity, and  $V_c$ ,  $V_r$ , and  $F_c$  are amplitude parameters corresponding to the RV convective blueshift suppression effect, RV rotation modulation, and FWHM signal amplitude (note that this means there are three amplitude parameters instead of the single  $h$  parameter expressed in Equation 2.2). Because RVs and FWHMs respond differently to the underlying stellar activity, this approach

allows for more rigorous characterization of the stellar activity than methods using only RV observations, which improves the separation of the stellar and planetary signals.

We followed R15 and simultaneously modeled the HIRES RV data as well as the HARPS-N RV and FWHM data. This included a separate offset parameter and noise parameter (added in quadrature to the uncertainties) for both RV datasets and the FWHM dataset (for a total of three offset parameters and three white noise parameters). Finally, the RV reflex motion due to the planet was characterized by a simple five-parameter orbital model: reference epoch, orbital period, reflex motion semi-amplitude, eccentricity, and longitude of periastron.

Because we conducted a joint fit to both photometry and spectroscopy, all orbital parameters except for reflex motion semi-amplitude are simultaneously used in our photometric model. In other words, reference epoch, orbital period, eccentricity, and longitude of periastron are used in both the photometric and spectroscopic components of our full model.

For all of the parameters used in the spectroscopic portion of the model, we assumed uniform, Jeffreys, or modified Jeffreys priors. The specific types and bounds of the priors are all listed in Table 2.3.

## Parameter Estimation

Overall, our full model included a photometric baseline offset parameter, a photometric white noise parameter, two quadratic limb-darkening parameters, the impact parameter, the transit duration, the planet radius relative to the stellar radius, the reference epoch, the orbital period, eccentricity, longitude of periastron, the reflex motion semi-amplitude, three spectroscopic offset parameters and three spectroscopic white noise parameters (for HIRES RV, HARPS-N RV, and HARPS-N FWHM), and six GP hyperparameters (two corresponding to the two RV semi-amplitudes and one corresponding to the FWHM semi-amplitude in Equations 2.3 and 2.4, as well as the stellar rotation period, a smoothness factor, and an exponential decay factor). This yielded a total of 24 parameters, all of which are also listed in Table 2.3. (Note: because we only modeled the detrended and flattened photometry, our estimation of the stellar rotation period was derived solely from our spectroscopic data.)

We estimated model parameters using `MultiNest` (Feroz et al. 2009; Feroz et al. 2019), a Bayesian inference tool for parameter space exploration, especially well suited for multimodal distributions. We used the following `MultiNest` settings for our parameter estimation: constant efficiency mode, importance nested sampling mode, multimodal mode, sampling efficiency = 0.01, 1000 live points, and evidence tolerance = 0.1.

Our full results from this analysis are presented in Table 2.3 and discussed in Section 2.5. Further, the best-fit transit model is plotted against the photometric data in Fig. 2.1 and the phase-folded, stellar-activity-removed RV observations and model are presented in Fig. 2.5. We find Kepler-538b to have a mass of  $M_p = 10.6_{-2.4}^{+2.5} M_\oplus$ , a radius of  $R_p = 2.215_{-0.034}^{+0.040} R_\oplus$ , a mean density of  $\rho_p = 0.98 \pm 0.23 \rho_\oplus$ , and negligible eccentricity (consistent with zero,  $< 0.11$  at 95% confidence). Notably, thanks to the *Gaia* parallax, our uncertainty on the planetary radius is less than 2%. For context, the average uncertainty,  $0.037 R_\oplus$ , is only

236 km, approximately the distance between Portland and Seattle<sup>11</sup>. Finally, we also note that our estimates of transit parameters are all within  $1\sigma$  of those reported in the original Kepler-538b validation paper (Morton et al. 2016).

## Model Tests

In order to confirm the validity of the results from our RV analysis, we conducted a number of tests designed to verify both our method of analysis and its output. These tests included removing our prior knowledge (obtained via transit photometry) of the transit time and period, injecting and recovering synthetic planet signals into the RV data, and removing the GP to model only the planet signal.

### Removing the Transit Prior

The first test we conducted was to repeat our analysis without any photometric observations, thereby removing the strong photometric constraints on the transit time and orbital period. We refit our model with a prior of  $\text{BJD}-2453833 = \text{Unif}(172,252)$  on transit time,  $P = \text{Jeffreys}(40,120)$  on orbital period, and the same priors on all other parameters that we previously used in our full analysis. We fit against only RV and FWHM observations, so we did not have any photometric parameters. Our choice of transit time prior was large enough to be naive, but small enough to exclude other transit times modulo some number of orbital periods. Similarly, our choice of orbital period prior was large enough to be naive, but small enough (on the lower end) to prevent overlap with the stellar rotation period of 25 – 30 days.

The results were consistent with the full simultaneous fit to spectroscopy and photometry. Of course, the posterior distributions on transit time and orbital period were much wider, which is to be expected. Specifically, the transit time was found to be  $t_0$  (BJD–2454833) =  $203_{-13}^{+14}$  and the period was found to be  $P = 82.25_{-0.74}^{+0.62}$  days. However, all parameters agreed within  $1\sigma$  of those from the full, simultaneous fit results. Further, all uncertainties (other than those of transit time, period, and eccentricity) were of a similar scale to those from the full model.

### Injection Tests

The next test we conducted was to introduce a  $1.7 \text{ m s}^{-1}$ , non-eccentric, sinusoidal planetary signal into the RV data at various periods to see whether the signal could be recovered, whether the measured RV semi-amplitude was accurate, and whether the uncertainties were similar to those for Kepler-538b. We ran four separate model fits with a synthetic planetary signal introduced at 60 days, 70 days, 90 days, and 100 days respectively. For each dataset, we modeled Kepler-538b and the synthetic signal simultaneously, including eccentricity in the model for both planets. To reduce computational expenses, we did not model the *Kepler*

---

<sup>11</sup><https://www.distancecalculator.net/from-portland-to-seattle>



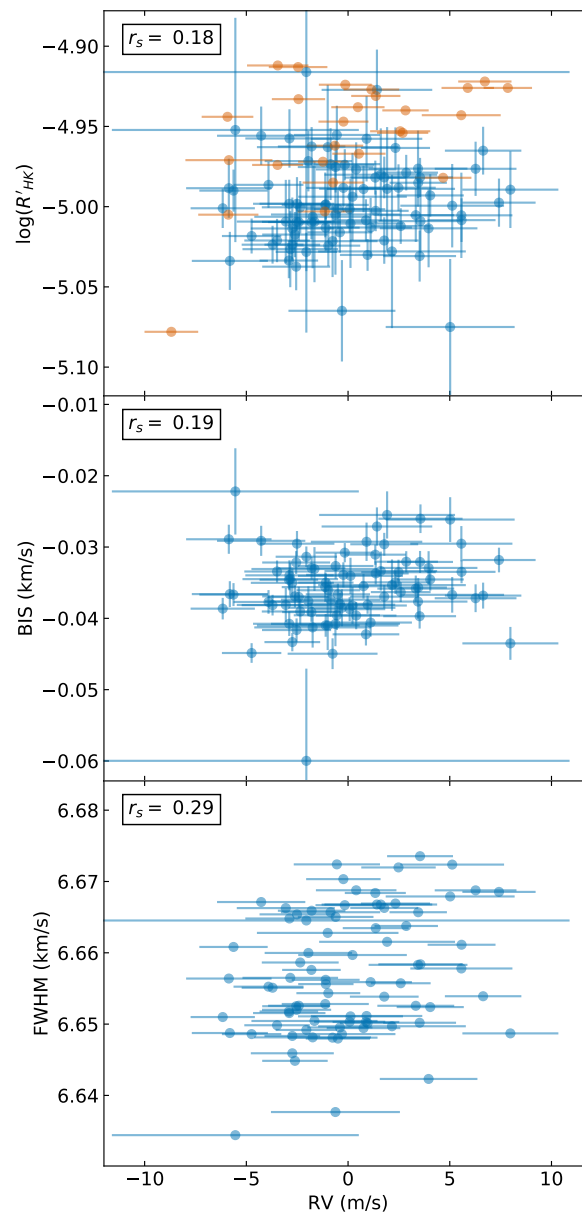


Figure 2.4: Scatter plots of RV vs.  $\log R'_{HK}$ , BIS, and FWHM for Kepler-538. The RVs have been mean-subtracted and plotted against the other three data types. Blue data points correspond to HARPS-N observations, orange data points to HIRES. In the top left corner of each panel is the Spearman correlation coefficient between the two datasets, an indicator of nonlinear, monotonic correlation. (The coefficients were calculated using the observation values but not their uncertainties.)

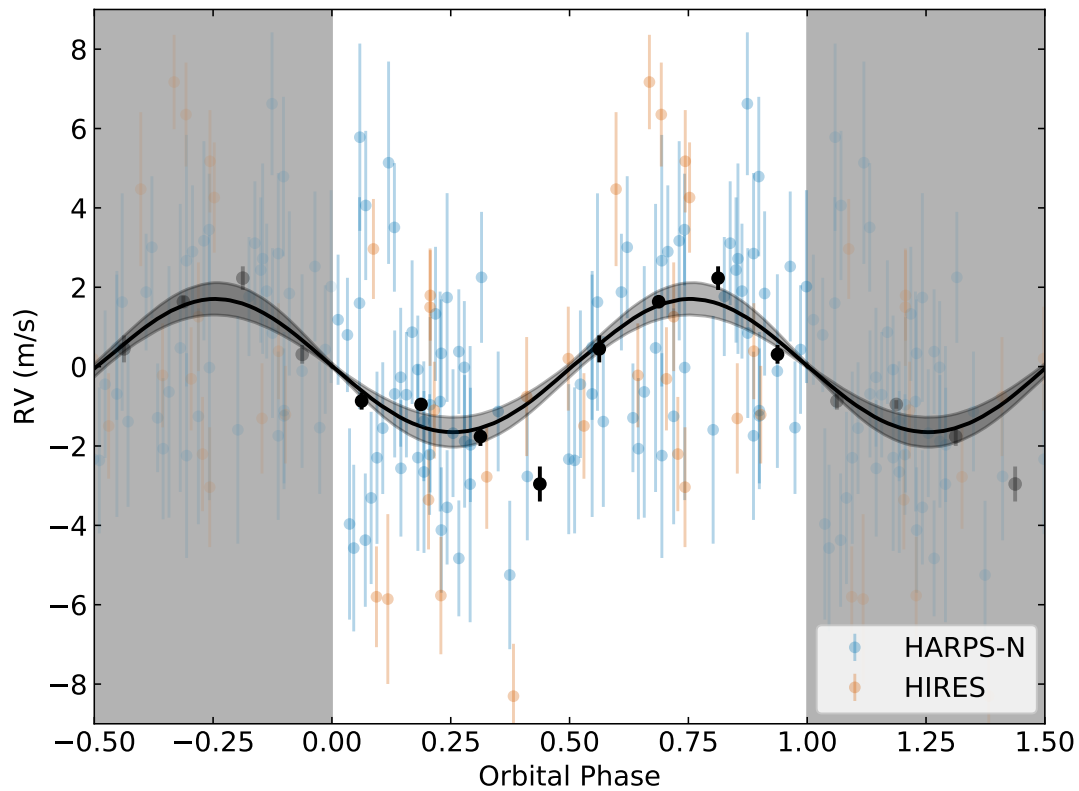


Figure 2.5: Kepler-538 RVs (with stellar activity subtracted) as a function of the orbital phase of Kepler-538b. Observations from HARPS-N and HIRES are plotted in blue and orange respectively, and binned data points are plotted in black. Data in the gray regions on each side of the plot are duplicates of the data in the white region. The median model and  $1\sigma$  confidence interval are plotted as a black line and gray region respectively. Note: two RV data points with error bars greater than  $5 \text{ m s}^{-1}$  were removed from the plot (but not the underlying model fit).

photometry for these tests, instead we applied Gaussian priors to the orbital period and transit time of Kepler-538b based on the values from our main results (see Table 2.3). As for our injected signal, we applied Gaussian priors to transit time and orbital period, centered respectively on the transit time and orbital period of the injected signal, with the same variance on transit time and same fractional variance on orbital period as for Kepler-538b. Finally, priors on semi-amplitude, eccentricity, and longitude of periastron were identical to those for Kepler-538b.

In all four model fits, we recovered the semi-amplitude of the injected signal to within  $1\sigma$  of  $1.7 \text{ m s}^{-1}$  (except for the 60d injection test, for which we found a semi-amplitude that was less than  $1.7 \text{ m s}^{-1}$  by  $1.1\sigma$ ). Further, the recovered semi-amplitude uncertainty of the injected planets were all on the order of  $0.4 - -0.5 \text{ m s}^{-1}$ , similar to the error bars on the semi-amplitude of Kepler-538b. Finally, in all four cases, the measured eccentricity of the injected planet was consistent with zero to within  $2\sigma$ .

### Fitting without a GP

Another important test we conducted was trying to model the RVs of Kepler-538b without accounting for the stellar activity at all. We did this by simply running the analysis without the GP. If the GP regression adequately accounted for the stellar activity (rather than subsume and weaken the planetary signal), we would expect to recover a similar RV semi-amplitude for the planet when the GP is excluded, as well as either comparable or larger uncertainties.

And this is indeed what we find. Without a GP, we found an RV semi-amplitude of  $K = 2.06_{-0.46}^{+0.49} \text{ m s}^{-1}$ , within  $1\sigma$  of the semi-amplitude found when a GP was included. Similarly, all other parameters in common between the two model fits agreed to within  $1\sigma$ , adding confidence to our results.

This particular test illustrates that our choice to use a GP to account for stellar activity was sufficient for this system and dataset, though not strictly necessary. This may be due to the long evolution time scale of the stellar activity and the large difference in periods between stellar rotation and planetary orbital period. However, we cannot rely on favorable stellar features in general, therefore it is best to err on the side of caution and use a sufficiently sophisticated method (e.g. GP regression) to characterize stellar activity signals.

## 2.5 Results and Discussion

The results of our stellar characterization and light curve, RV, and FWHM modeling can be found in Tables 2.2 and 2.3.

After conducting our model fits and running the requisite follow-up tests, we found the mass of Kepler-538b to be  $M_p = 10.6_{-2.4}^{+2.5} M_\oplus$ . Combining this with the planetary radius of  $R_p = 2.215_{-0.034}^{+0.040} R_\oplus$  resulted in a planetary density of  $\rho_p = 0.98 \pm 0.23 \rho_\oplus$ , or  $5.4 \pm 1.3 \text{ g cm}^{-3}$ .

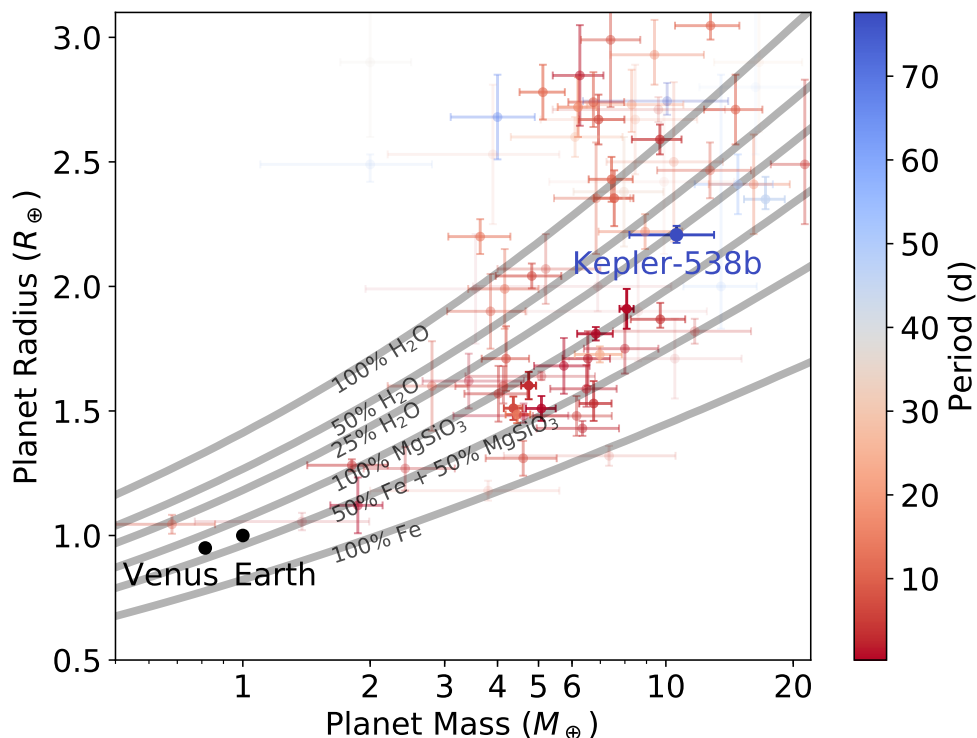


Figure 2.6: Mass-radius diagram of transiting planets with fractional mass and radius uncertainties less than 50%. Planet colors correspond to orbital period, with short periods in red and long periods (such as Kepler-538b) in blue. Further, except for Kepler-538b, planets with larger fractional mass and radius uncertainties are fainter. Venus and Earth are also labeled and plotted in black for reference. Gray lines correspond to planetary compositions (from top to bottom) of 100%  $H_2O$ , 50%  $H_2O$ , 25%  $H_2O$ , 100%  $MgSiO_3$ , 50%  $MgSiO_3$  + 50% Fe, and 100% Fe, respectively (Zeng and Sasselov 2013; Zeng et al. 2016a). Kepler-538b lies closest to the 25%  $H_2O$  composition line. The planet likely consists of a significant fraction of ices (dominated by water ice), in addition to rocks/metals, and a small amount of gas.

Owing to its long orbital period, and its location on the mass-radius diagram, Kepler-538b likely consists of a significant fraction of ices (dominated by water ice), in addition to rocks/metals, and a small amount of gas (Zeng et al. 2018). Its host star is slightly less massive than our own Sun. Because the luminosity of a main-sequence star is a strong function of its mass (typically to the power of 3 or 4), the luminosity of the host star Kepler-538 is somewhat less than the Sun. Therefore, the snowline in the disk when this system was formed was closer in, increasing the likelihood for Kepler-538b to accrete ices during its formation.

The estimated bulk density of Kepler-538b is comparable to that of the Earth. However, this high mean density is partly due to its high mass resulting in more compression of materials under self-gravity. Its uncompressed density, as revealed by the mass-radius curves (Zeng and Sasselov 2013; Zeng et al. 2016a) in Fig. 2.6, is consistent with a composition somewhat less dense than pure-rocky and/or Earth-like rocky (1:2 iron/rock mixture). One ready explanation is that Kepler-538b is an icy core, which for some reason had not accreted as much gas as our own Uranus or Neptune (both are estimated to have a few up to ten perfect mass of gas).

The eccentricity of Kepler-538b is small (less than 0.11 with 95% confidence). However, the planet may still have arisen from a dynamical origin, that is, inward planet migration due to planet-planet gravitational interactions (Raymond et al. 2009). Some planet formation theories have suggested the formation of multiple icy cores in relatively adjacent space near the snowline around a host star, increasing the likelihood of dynamical interactions among them and resulting in inward scatterings for some of them. If Kepler-538b were scattered inward, then its orbital eccentricity could have been higher initially, and then damped to its current value through interactions with the disk when the disk was still around. Alternatively, inward migration through planet-disk interactions may be a more likely scenario, since a disk would always keep the planet orbital eccentricity low (Chambers 2018; Morbidelli 2018) and would probably be required to damp any eccentricity from scattering.

In summary, Kepler-538b is only the “tip of a huge iceberg”, likely representing a class of planets common in our Galaxy, but which are not found in our own solar system. The absence of planets in between the size of the Earth and Neptune (about four Earth radii) is linked to the formation/presence of a gas giant – Jupiter (Barbato et al. 2018; Izidoro et al. 2015), and vice versa.

To date, very few exoplanets have been found on long-period orbits that also have any kind of mass measurements. In fact, according to the NASA Exoplanet Archive<sup>12</sup> (accessed 2019 July 31), there are only 10 transiting exoplanets (excluding Kepler-538b) with an RV mass measurement and an orbital period greater than 50 days. If we look at other common methods of mass measurement (specifically transit timing variations and dynamical mass measurements of circumbinary planets), that number only increases to 37.

<sup>12</sup><https://exoplanetarchive.ipac.caltech.edu/>. This number was determined by constraining orbital period > 50 days, planet mass < 11 $M_{\text{Jup}}$ , planet mass limit flag = 0 (to remove upper limit results), planet circumbinary flag = 0, planet transit flag = 1, and planet RV flag = 1.

Further, most of those planets are quite large, more similar to Jupiter or Saturn in mass and radius than Neptune or Earth. Fig. 2.7 demonstrates where Kepler-538b fits into this sparse region of parameter space. Kepler-538b is one of the very few small, low-mass planets well characterized to date.

As the sample of small, long-period planets with precisely determined masses and densities grows, we will be able to address a number of fundamental questions. For example, what effect does stellar incident flux have on the size and composition of exoplanets? Since most known exoplanets have periods shorter than that of Mercury, it is difficult to analyze exoplanet composition and size for incident fluxes comparable to or less than that of Earth. Similarly, is there a relationship between the location or depth of the planet radius occurrence gap detected by Fulton et al. (2017) and a planet’s mass or composition? Further characterization of this gap at longer periods would help confirm (or refute) the photoevaporation explanation of the gap and therefore provide insights about exoplanet formation.

## Detection of Kepler-538b with Other Methods

As methods of detecting exoplanets become more sensitive, regions of parameter space accessible to multiple detection methods will grow, and with them the opportunity to more rigorously characterize the planet population and calibrate detection methods against one another. Kepler-538b pushes RV characterization further into the low-mass, long-period planet regime. As a result, it is interesting to explore whether other methods might also be able to characterize such a planet.

To begin with, there is no possibility of detecting an astrometric signal of Kepler-538b. Perryman et al. (2014), which analyzed the expected planet yield from *Gaia* astrometry, found that the expected along-scan accuracy per field of view for *Gaia* would be  $\sigma_{\text{fov}} = 34.2\mu\text{as}$  for a star like Kepler-538 ( $G = 11.67$ ). While they required an astrometric signal of  $3\sigma_{\text{fov}}$  for a detection, the astrometric signal of Kepler-538b is only  $0.095 \pm 0.022\mu\text{as}$ , over 1000 times smaller than this detection threshold.

Similarly, a planet like Kepler-538b is very unsuitable for direct imaging. According to the NASA Exoplanet Archive<sup>13</sup> (accessed 2019 July 28), there are no directly imaged planets less massive than  $2M_{\text{Jup}}$  or closer to their host star than 2 au, both of which disqualify Kepler-538b. Further, direct imaging is well suited for young stars which still host self-luminous planets, but the median estimated age of Kepler-538 is 3.8 Gyr, older than nearly every host star of a directly imaged planet on the NASA Exoplanet Archive (there are only two exceptions, WISEP J121756.91+162640.2 A and Oph 11).

Unlike astrometry and direct imaging, Penny et al. (2019) determined that a planet with the mass and semi-major axis of Kepler-538b would be just inside the microlensing sensitivity curve of the *Wide Field Infrared Survey Telescope (WFIRST)*. They estimated that if every star hosted a planet like Kepler-538b, we could expect *WFIRST* to detect a microlensing

<sup>13</sup><https://exoplanetarchive.ipac.caltech.edu/>

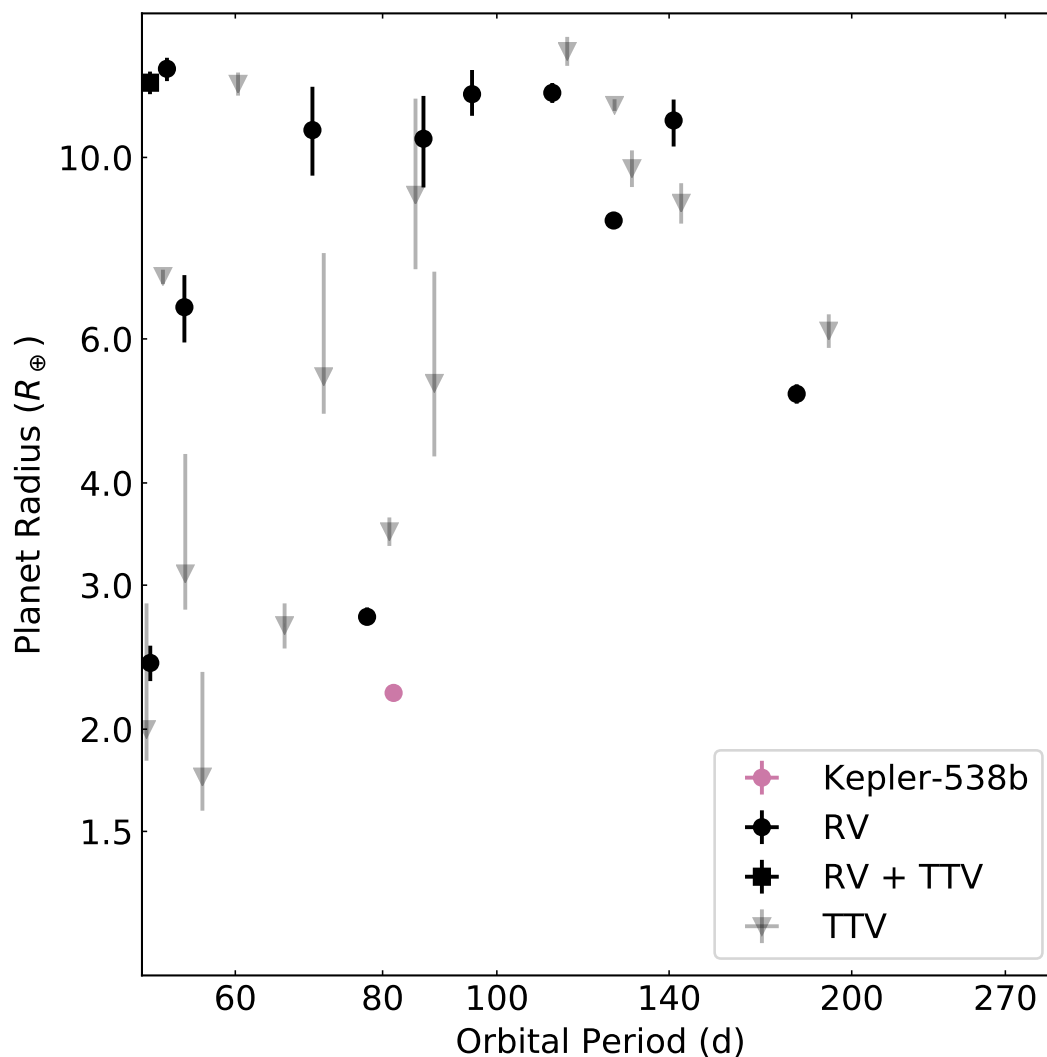


Figure 2.7: Orbital period versus planet radius for all transiting exoplanets with  $P > 50$  days and RV or transit timing variation (TTV) mass measurements. Data for all planets besides Kepler-538b were retrieved from the NASA Exoplanet Archive (accessed 2019 February 16). Kepler-538b is plotted as a pink circle, all other exoplanets with RV mass measurements are plotted as black circles, one exoplanet (Kepler-117c) has a jointly derived mass from RV and TTV measurements and is plotted as a black square, and exoplanets with only TTV mass measurements are plotted as gray triangles. (Period and radius uncertainties are plotted for all planets, including Kepler-538b, but are smaller than the data points in many cases.) At long periods ( $P > 50$  days), Kepler-538b is the smallest transiting exoplanet with an RV mass measurement, and Kepler-20d is the only such planet with a lower mass (by  $0.5M_{\oplus}$ ). Overall, there are very few mass measurements for planets in the long-period, small-radius regime of Kepler-538b.

signal from roughly 10 – 30 such planets during the course of the full mission; see Fig. 9 from Penny et al. (2019).

## Potential for Atmospheric Characterization

One interesting question to ask about Kepler-538b is whether or not it may be amenable to atmospheric characterization via transmission spectroscopy. The *James Web Space Telescope*, *JWST*, (Deming et al. 2009; Gardner et al. 2006; Kalirai 2018) will devote a significant portion of its mission to the characterization of exoplanet atmospheres. The spectra shown in Fig. 2.8 for the atmosphere of Kepler-538b were generated by the *JWST* Exoplanet Targeting (JET) code (Fortenbach and Dressing 2020) assuming five observed transits. This code first takes the observed planet and system parameters ( $R_p$ , period, insolation flux,  $R_*$ ,  $T_{eff}$ , and  $J$ -band magnitude) and then derives other key parameters (semi-major axis,  $T_{eq}$ , planet surface gravity, planet mass, and transit duration). In this case we used the planet mass already determined in this paper. We also assumed an optimistic low-metallicity (five times solar) planetary atmosphere with no clouds. JET then used *Exo-Transmit* (Kempton et al. 2017) to generate model transmission spectra and used *Pandexo* (Batalha et al. 2017) to generate simulated instrument spectra. We focused on the Near InfraRed Imager and Slitless Spectrograph (NIRISS) SOSS-Or1 and NIRSpec G395M instruments/modes since they are, according to Batalha and Line (2017), best suited for exoplanet transmission spectroscopy. Finally, the JET code performed a statistical analysis for multiple transits and determined if the simulated instrument spectra fit the model well enough to confirm a detection. Given current estimates of the precision (noise floor) of these *JWST* instruments (as well as visual inspection of the simulated spectra after five transits in Fig. 2.8), it would likely be very difficult to detect the Kepler-538b atmosphere even with a large number of transit observations with *JWST*.

Perhaps other next-generation observatories such as the Thirty Meter Telescope (Sanders 2013), the Extremely Large Telescope (Udry et al. 2014), the Giant *Magellan* Telescope (Johns et al. 2012), or the *Large UV/Optical/IR Surveyor* (The *LUVOIR* Team 2018) will be able to make such a project feasible.

## Possibility of a Second Planet in the System

Some early versions of the *Kepler* catalog included a weak transit signal at 117.76 days and labeled it as a planet candidate (K00365.02). However, one early catalog instead labeled it as a false positive (Mullally et al. 2015) and the final *Kepler* DR25 catalog (Thompson et al. 2018) did not detect a candidate at that period at all (or even a threshold crossing event, the broadest detection category in the *Kepler* pipeline). Further, the *Kepler* False Positive Working Group (Bryson et al. 2017) investigated K00365.02 and could not determine a final disposition; they did however flag the candidate with a “Transit Not Unique False Alarm”



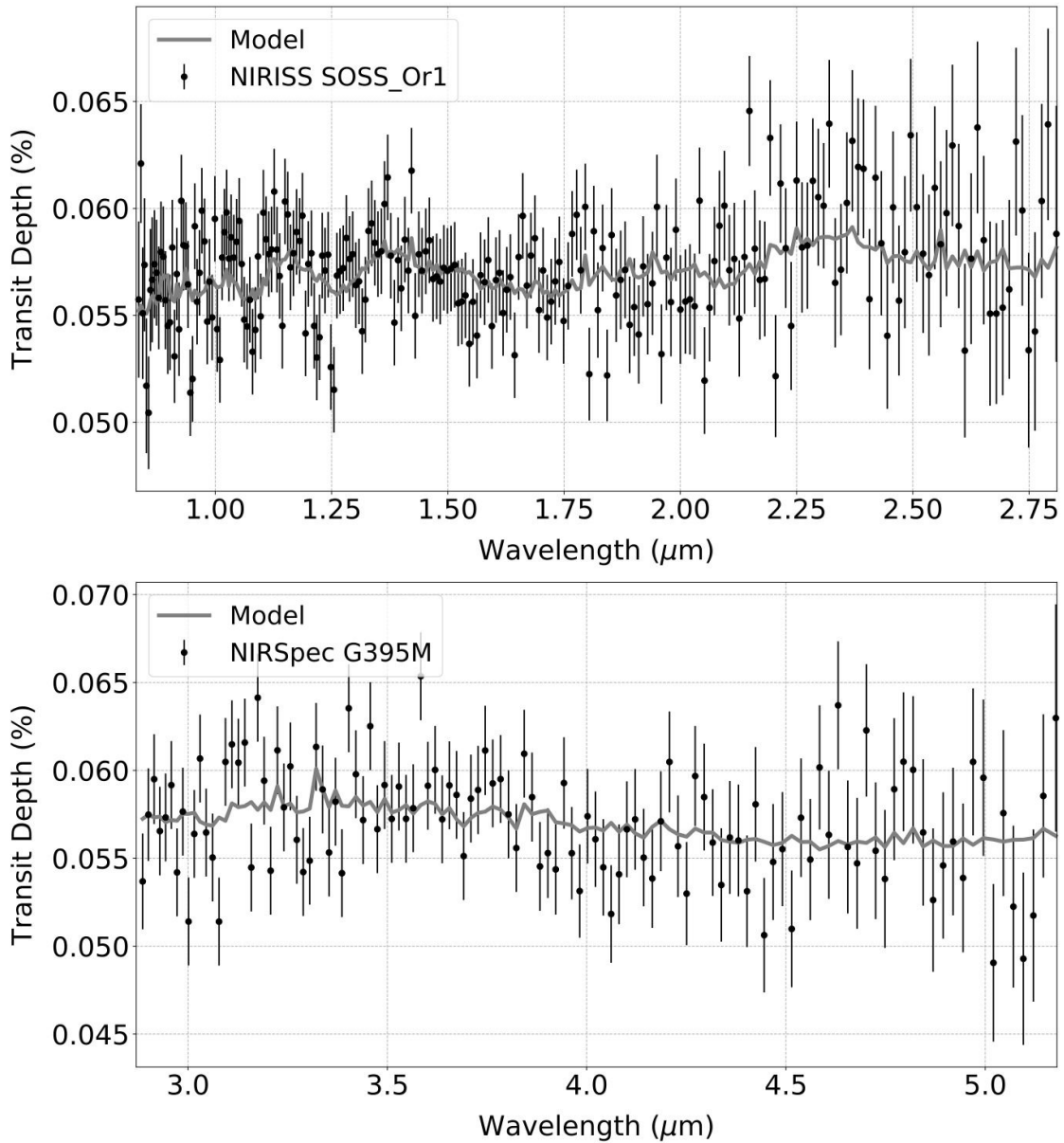


Figure 2.8: A simulated transmission spectrum of Kepler-538b with five transits observed with *JWST*. The model spectrum, with low metallicity (five times solar) and no clouds, is shown as a gray line. The black data points are the simulated instrument spectra, using NIRISS SOSS-Or1 (0.81 – 2.81  $\mu\text{m}$ ) and NIRSpec G395M (2.87 – 5.18  $\mu\text{m}$ ).

flag, meaning “the detected transit signal is not obviously different from other signals in the flux light curve.”<sup>14</sup>

The radius of K00365.02 was reported on the NASA Exoplanet Archive as  $0.62_{-0.03}^{+0.10} R_{\oplus}$ . Assuming a pure iron composition and using Zeng and Sasselov (2013) and Zeng et al. (2016a) yields an upper limit mass of  $0.37_{-0.05}^{+0.25} M_{\oplus}$  and an upper limit semi-amplitude of  $5.3_{-0.8}^{+3.4} \text{ cm s}^{-1}$ , well below the detection threshold for HARPS-N, HIRES, or any other spectrograph. However, for the sake of rigor, we also ran a two planet model for Kepler-538b and K0035.02 on our RV and FWHM data (similar to our main model). Instead of jointly modeling photometry, we applied period and transit time priors on Kepler-538b and K00365.02 (the former based on our final results, the latter determined from the NASA Exoplanet Archive<sup>15</sup>; accessed 31 July 2019). Our results showed an RV semi-amplitude at 117.76 days of  $K = 0.26_{-0.18}^{+0.28} \text{ m s}^{-1}$ , negligible and consistent with zero at less than  $1.5\sigma$ .

Additionally, the periods of Kepler-538b and K00365.02 are not in or near a first-order mean motion resonance (or second-order, for that matter), so we do not expect a large, detectable transit timing variation (TTV) signal on Kepler-538b either (Lithwick et al. 2012). Indeed, the NASA Exoplanet Archive (accessed 31 July 2019) does not report a TTV flag for Kepler-538b. As a result, with an unverified transit signal, a negligible RV signal, and an apparently negligible TTV signal, the existence of K00365.02 remains inconclusive.

## 2.6 Summary and Conclusions

In this paper, we analyze the Kepler-538 system in order to determine the properties of Kepler-538b, the single, known exoplanet in the system. Kepler-538 is a  $0.924 M_{\odot}$ , G-type star with a visual magnitude of  $V = 11.27$ . We model the *Kepler* light curve and determine the orbital period of Kepler-538b to be  $P = 81.74$  days and the planetary radius to be  $R_p = 2.215_{-0.034}^{+0.040} R_{\oplus}$  (for reference,  $0.037 = 236$  km, approximately the distance between Portland and Seattle<sup>16</sup>). These results are in agreement with previous transit fits. We also determine the planetary mass by accounting for stellar activity via a GP regression that uses information from the FWHM and RV observations simultaneously. Our model fit yields a mass estimate for Kepler-538b of  $M_p = 10.6_{-2.4}^{+2.5} M_{\oplus}$ . Combined, these results show the planet to have a density of  $\rho_p = 0.98 \pm 0.23 \rho_{\oplus} = 5.4 \pm 1.3 \text{ g cm}^{-3}$ . This suggests a composition and atmosphere somewhere between that of Earth and Neptune, with a significant fraction of ices (dominated by water ice), in addition to rocks/metals, and a small amount of gas (Zeng et al. 2018).

To date, there have been very few precise and accurate mass measurements of long-period exoplanets. Beyond 50 days, Kepler-538b is only the 11th transiting exoplanet with an RV

<sup>14</sup>[https://exoplanetarchive.ipac.caltech.edu/\docs/API\\_fpwg\\_columns.html](https://exoplanetarchive.ipac.caltech.edu/\docs/API_fpwg_columns.html)

<sup>15</sup><https://exoplanetarchive.ipac.caltech.edu/>

<sup>16</sup><https://www.distancecalculator.net/from-portland-to-seattle>

mass measurement (NASA Exoplanet Archive<sup>17</sup>; accessed 2019 May 4). Additional, well-constrained mass measurements of long-period planets will improve our understanding of the long-period exoplanet population. Beyond that, they will also help to answer questions about the short-period planet population, such as the nature of the planetary radius occurrence gap (Fulton et al. 2017) and the effect of stellar flux on exoplanet compositions and atmospheres.

With new, next-generation spectrographs such as HPF (Mahadevan et al. 2010, 2014), KPF (Gibson et al. 2016, 2018), EXPRES (Jurgenson et al. 2016), ESPRESSO (Mégévard et al. 2010), and NEID (Schwab et al. 2016) coming online now or in the near future, our ability to characterize long-period exoplanets will only improve. Better data will require more advanced analysis methods to extract as much information as possible. The methods used in this paper, such as GP regression, injection tests, and simultaneous modeling of RV observations and stellar activity indices, are valuable tools that strengthen the analysis of spectroscopic data, improve exoplanet characterization, and therefore better our understanding of the exoplanet population as a whole.

---

<sup>17</sup><https://exoplanetarchive.ipac.caltech.edu/> This number was determined by constraining Orbital Period > 50 days, Planet Mass < 11 $M_{\text{Jup}}$ , Planet Mass Limit Flag = 0 (to remove upper limit results), Planet Circumbinary Flag = 0, Planet Transit Flag = 1, and Planet RV Flag = 1.

## Chapter 3

# Hyades Member K2-136c: The Smallest Planet in an Open Cluster with a Precisely Measured Mass

An earlier version of this article was published as: Mayo, A. W., Dressing, C. D., Vanderburg, A., Fortenbach, C. D., Lienhard, F., Malavolta, L., Mortier, A., Núñez, A., Richey-Yowell, T., Turtelboom, E. V., Bonomo, A. S., Latham, D. W., López-Morales, M., Shkolnik, E., Sozzetti, A., Agüeros, M. A., Borsato, L., Charbonneau, D., Cosentino, R., Douglas, S. T., Dumusque, X., Ghedina, A., Gibson, R., Granata, V., Harutyunyan, A., Haywood, R. D., Lacedelli, G., Lorenzi, V., Magazzù, A., Martinez Fiorenzano, A. F., Micela, G., Molinari, E., Montalto, M., Nardiello, D., Nascimbeni, V., Pagano, I., Piotto, G., Pino, L., Poretti, E., Scandariato, G., Udry, S., Buchhave, L. A., 2023, *The Astronomical Journal*, 165, 235M.

K2-136 is a late-K dwarf ( $0.742 \pm 0.039 M_{\odot}$ ) in the Hyades open cluster with three known, transiting planets and an age of  $650 \pm 70$  Myr. Analyzing *K2* photometry, we found that planets K2-136b, c, and d have periods of 8.0, 17.3, and 25.6 days and radii of  $1.014 \pm 0.050 R_{\oplus}$ ,  $3.00 \pm 0.13 R_{\oplus}$ , and  $1.565 \pm 0.077 R_{\oplus}$ , respectively. We collected 93 radial velocity measurements (RVs) with the HARPS-N spectrograph (TNG) and 22 RVs with the ESPRESSO spectrograph (VLT). Analyzing HARPS-N and ESPRESSO data jointly, we found K2-136c induced a semi-amplitude of  $5.49 \pm 0.53 \text{ m s}^{-1}$ , corresponding to a mass of  $18.1 \pm 1.9 M_{\oplus}$ . We also placed 95% upper mass limits on K2-136b and d of 4.3 and  $3.0 M_{\oplus}$ , respectively. Further, we analyzed HST and XMM-Newton observations to establish the planetary high-energy environment and investigate possible atmospheric loss. K2-136c is now the smallest planet to have a measured mass in an open cluster and one of the youngest planets ever with a mass measurement. K2-136c has  $\sim 75\%$  the radius of Neptune but is similar in mass, yielding a density of  $3.69^{+0.67}_{-0.56} \text{ g cm}^{-3}$  ( $\sim 2 - 3$  times denser than Neptune). Mass estimates for K2-136b (and possibly d) may be feasible with more RV observations, and insights into all three planets' atmospheres through transmission spectroscopy would be challenging but potentially fruitful. This research and future mass measurements of young planets are critical for investigating the compositions and characteristics of small exoplanets

at very early stages of their lives and providing insights into how exoplanets evolve with time.

### 3.1 Introduction

The timescales on which planets and planetary systems evolve are far longer than any feasible timescale of scientific observations. The only way to learn about how planets form and evolve is to collect snapshots at different stages of their development and assemble these snapshots into a cohesive framework. This is where open clusters prove particularly useful. Open clusters, close collections of young, recently formed stars, are excellent laboratories for studying the early lives of stars, because all of the stars in an open cluster, regardless of size, temperature, metallicity, or location, have a shared formation history, and therefore the ages of the stars can be very tightly constrained. This logic can also be applied to planets; if they form very quickly after the coalescence of their host star (Raymond and Morbidelli 2022), it is possible to determine the age of a planet orbiting an open cluster star, thereby capturing one of the early snapshots required to assemble the framework of a planet’s evolution.

In this paper we characterize K2-136c, a sub-Neptune planet in the Hyades open cluster. Orbiting a late K dwarf, this planet is one of the three known, transiting planets in the system. The system was originally observed in *K2* Campaign 13 for 80 days (2017 March 8 - 2017 May 27) and was proposed for observation by seven guest observer teams: GO13008, GO13018, GO13023, GO13049, GO13064, GO13077, and GO13090. All three planets were originally discovered by Mann et al. (2018) (hereafter M18) and Ciardi et al. (2018) (a parallel analysis published simultaneously). Shortly thereafter a subsequent analysis was completed by Livingston et al. (2018). All three papers are in broad agreement regarding stellar and planetary parameters, but M18 established the tightest constraints on orbital period for all three planets.

In their analysis, M18 found an Earth-sized planet ( $0.99_{-0.04}^{+0.06} R_{\oplus}$ ) at  $P = 8.0$  days (K2-136b), a sub-Neptune-sized planet ( $2.91_{-0.10}^{+0.11} R_{\oplus}$ ) at  $P = 17.3$  days (K2-136c, the focus of this paper), and a super-Earth-sized planet ( $1.45_{-0.08}^{+0.11} R_{\oplus}$ ) at  $P = 25.6$  days (K2-136d). They also determined a host star mass of  $0.74 \pm 0.02 M_{\odot}$  and a stellar radius of  $0.66 \pm 0.02 R_{\odot}$ .

As for the stellar age, there are a number of estimates available. Perryman et al. (1998) found the Hyades open cluster to be  $625 \pm 50$  Myr. Gossage et al. (2018) found an age of  $\sim 680$  Myr while Brandt and Huang (2015) determined a slightly older age of  $750 \pm 100$  Myr. The age we use throughout this paper comes from Martín et al. (2018), who determined the Hyades to be  $650 \pm 70$  Myr old. We thus assume that K2-136 and the three orbiting planets share that approximate age. We chose this age because it is a relatively recent result, it compares and combines results using both old (Burrows et al. 1997) and new (Baraffe et al. 2015) standard evolutionary models, and it also agrees broadly with other, previous estimates. The young age of the system was our primary reason for pursuing K2-136c as a target: there are very few young, small planets with mass measurements. According to the NASA Exoplanet Archive (NASA Exoplanet Science Institute 2020), accessed 2023 Mar 12,

there are only 13 confirmed exoplanets with  $R_p < 4 R_\oplus$ , a host star age  $< 1$  Gyr, and a mass measurement (not an upper limit): HD 18599b (Desidera et al. 2023), HD 73583b and c (Barragán et al. 2022); K2-25b (Stefansson et al. 2020); L 98-59b, c, and d (Demangeon et al. 2021); Kepler-411b and Kepler-411d (Sun et al. 2019); Kepler-462b (Masuda and Tamayo 2020); Kepler-289b and Kepler-289d (Schmitt et al. 2014); and K2-100b (Barragán et al. 2019). Of these, only the Kepler-411, K2-100, HD 73583, K2-25, and HD 18599 systems have an age constraint tighter than 50% (Barragán et al. 2019, 2022; Desidera et al. 2023; Stefansson et al. 2020; Sun et al. 2019).

We analyzed photometry of the K2-136 system in order to measure the radii, ephemerides, and other transit parameters of each planet. We also collected spectra of the K2-136 system and measured radial velocities (RVs) as well as stellar activity indices. Then, by modeling these RVs following Rajpaul et al. (2015), we determined the mass of K2-136c and placed upper limits on the masses of the other two planets. We used this system to investigate the nature, environment, and evolution of young, small exoplanets.

This paper is organized as follows. In Section 3.2 we discuss our observations. Then we detail our method of stellar characterization in Section 3.3. Next, in Section 3.4 we describe our RV and photometry models, data analysis, model comparison, and parameter estimation. In Section 3.5 we present and discuss our results. Finally, we summarize and conclude in Section 3.6.

## 3.2 Observations

### *K2*

Photometric observations of the K2-136 system were collected with the *Kepler* spacecraft (Borucki et al. 2008) through the *K2* mission during Campaign 13 (2017 Mar 08 to 2017 May 27). *K2* collected long-cadence observations of this system every 29.4 minutes.

### *TESS*

Photometric observations of the K2-136 system were also collected with the *TESS* spacecraft (Ricker et al. 2015) during Sector 43 (2021 Sep 16 to 2021 Oct 10) and Sector 44 (2021 Oct 12 to 2021 Nov 06). *TESS* collected long-cadence full frame image observations of this system every 10 minutes in Sector 43 and short-cadence observations every 20 seconds in Sector 44.

### *HARPS-N*

We collected 93 RV observations using the HARPS-N spectrograph (Cosentino et al. 2012, 2014) on the Telescopio Nazionale Galileo (TNG). The first 88 spectra were collected between 2018 August 11 and 2019 February 7 (programs A37TAC.24 and A38TAC.27, PI: Mayo), and the final 5 spectra were collected between 2020 September 18 and 2020 October 31 by

the HARPS-N Guaranteed Time Observation program. RVs and additional stellar activity indices were extracted using a K6 stellar mask and version 2.2.8 of the Data Reduction Software (DRS) adapted from the ESPRESSO pipeline. Spectra had an average exposure time of 1776.5 seconds and the average SNR in the order around 550 nm was 51.1. The RV standard deviation was  $6.9 \text{ m s}^{-1}$  and the RV median uncertainty was  $1.6 \text{ m s}^{-1}$ . Stellar activity indices also extracted and reported in this paper include the cross-correlation function (CCF) bisector span inverse slope (hereafter BIS), the CCF full width at half maximum (FWHM), and  $S_{HK}$  (which measures chromospheric activity via core emission in the Ca II H and K absorption lines). The observation dates, velocities, and activity indices are provided in Table 3.2.

## ESPRESSO

We collected 22 RV observations using the ESPRESSO spectrograph (Pepe et al. 2021) on the Very Large Telescope (VLT) between 2019 November 1 and 2020 February 27 (program 0104.C-0837(A), PI: Malavolta). RVs and additional stellar activity indices were extracted using a K6 stellar mask and the same pipeline as the HARPS-N observations (DRS version 2.2.8). Typical exposure time for spectra was 1800 seconds and the average SNR at Order 111 (central wavelength = 551nm) was 79.9. The RV standard deviation was  $7.8 \text{ m s}^{-1}$  and the RV median uncertainty was  $0.70 \text{ m s}^{-1}$ . These observations and indices are also provided in Table 3.2.

## Hubble Space Telescope

Near-ultraviolet (NUV) observations of K2-136 were taken as part of a broader *Hubble Space Telescope* (*HST*) program observing the Hyades (GO-15091, PI: Agüeros). The target was exposed for 1166.88 seconds on 2019 September 13 using the photon-counting Cosmic Origins Spectrograph, COS, (Green et al. 2012) in the G230L filter and had no data quality flags.

After initial data reduction through the CALCOS pipeline version 3.3.10, we additionally confirmed that the star was not flaring during observations by integrating the background-subtracted flux by wavelength over 1 and 10 second time intervals in the time-tagged data. No flares above  $3\sigma$  were identified.

## XMM-Newton

K2-136 was the target of an *XMM-Newton* (*XMM*) 43 ksec observation on 2018 September 11 (Obs. ID: 0824850201, PI: Wheatley). The observation was processed using the standard Pipeline Processing System (PPS version 17.56\_20190403.1200; Pipeline sequence ID: 147121). The source detection corresponding to K2-136 was detected by both the pn and MOS cameras, for a total of 800 source counts in the 0.2 – 12.0 keV energy band. The X-ray source has a data quality flag `SUM_FLAG=0` (i.e. good quality). No variability or pileup were detected for this X-ray source.

Parameter	Unit	Value			Reference
EPIC	-	247589423			-
2MASS	-	J04293897+2252579			-
$\alpha$ R.A.	J2016.0	04:29:39.1			GAIA DR3 <sup>1</sup>
$\delta$ Dec	J2016.0	+22:52:57.2			GAIA DR3 <sup>1</sup>
$\mu_\alpha$	mas yr <sup>-1</sup>	82.778 ± 0.021			GAIA DR3 <sup>1</sup>
$\mu_\delta$	mas yr <sup>-1</sup>	-35.541 ± 0.015			GAIA DR3 <sup>1</sup>
Parallax	mas	16.982 ± 0.019			GAIA DR3 <sup>1</sup>
Distance	pc	58.752 <sup>+0.061</sup> <sub>-0.072</sub>			b
Age	Myr	650 ± 70			c
B mag	-	12.48 ± 0.01			UCAC4 <sup>4</sup>
V mag	-	11.20 ± 0.01			UCAC4 <sup>4</sup>
J mag	-	9.096 ± 0.022			2MASS <sup>5</sup>
H mag	-	8.496 ± 0.020			2MASS <sup>5</sup>
K mag	-	8.368 ± 0.019			2MASS <sup>5</sup>
W1 mag	-	8.263 ± 0.023			WISE <sup>6</sup>
W2 mag	-	8.349 ± 0.020			WISE <sup>6</sup>
W3 mag	-	8.312 ± 0.030			WISE <sup>6</sup>
Fractional X-ray luminosity $L_X/L_*$	-	(1.97 ± 0.30) × 10 <sup>-5</sup>			This work
Parameter	Unit	SPC	ARES+MOOG	Combined <sup>7</sup>	Reference
Effective temperature $T_{\text{eff}}$	K	4517 ± 49	4447 ± 149	4500 <sup>+125</sup> <sub>-75</sub>	This work
Surface gravity $\log g$	g cm <sup>-2</sup>	4.68 ± 0.10	4.82 ± 0.43	-	This work
Microturbulence	km s <sup>-1</sup>	-	< 1.1 <sup>8</sup>	-	This work
Metallicity [Fe/H]	dex	-	0.05 ± 0.10	-	This work
Metallicity [M/H]	dex	-0.02 ± 0.08	-	-	This work
Radius $R_*$	R <sub>⊙</sub>	0.6764 <sup>+0.0039</sup> <sub>-0.0033</sub>	0.6770 <sup>+0.0050</sup> <sub>-0.0038</sub>	0.677 ± 0.027	This work
Mass $M_*$	M <sub>⊙</sub>	0.7413 <sup>+0.0033</sup> <sub>-0.0056</sub>	0.7430 <sup>+0.0126</sup> <sub>-0.0070</sub>	0.742 <sup>+0.039</sup> <sub>-0.038</sub>	This work
Density $\rho_*$	$\rho_\odot$	2.397 <sup>+0.017</sup> <sub>-0.018</sub>	2.397 <sup>+0.018</sup> <sub>-0.019</sub>	2.40 ± 0.31	This work
Luminosity $L_*$	L <sub>⊙</sub>	0.1682 <sup>+0.0043</sup> <sub>-0.0035</sub>	0.1664 <sup>+0.0038</sup> <sub>-0.0035</sub>	0.1673 <sup>+0.0053</sup> <sub>-0.0049</sub>	This work
Projected rot. velocity $v \sin i$	km s <sup>-1</sup>	< 2	-	-	This work

Table 3.1: Stellar parameters of K2-136

### 3.3 Stellar Characterization

In order to characterize the star, we started by combining all of our collected HARPS-N spectra (from 2018-2019) into a single, stacked spectrum with S/N  $\sim$  300, based on signal divided by scatter on continuum segments near 6000 Å; see Section 3.1 of Mortier et al. (2013) for more details. Then we ran the ARESv2 package (Sousa et al. 2015) to obtain equivalent widths for a standard set of neutral and ionized iron lines (Sousa et al. 2011).

<sup>1</sup>Babusiaux et al. (2023), Gaia Collaboration and Vallenari (2022), and Gaia Collaboration et al. (2016, 2021a)

<sup>2</sup>Bailer-Jones et al. (2021)

<sup>3</sup>Martín et al. (2018)

<sup>4</sup>Zacharias et al. (2013)

<sup>5</sup>Cutri et al. (2003) and Skrutskie et al. (2006)

<sup>6</sup>Wright et al. (2010)

<sup>7</sup>Systematic uncertainties added in quadrature (Tayar et al. 2022)

<sup>8</sup>Value is poorly constrained, 1 $\sigma$  upper limit reported instead



We refer to Mortier et al. (2013), Sousa (2014), and Sousa et al. (2015) for our choice of typical model parameters. Afterward, we calculated stellar parameters using MOOG<sup>1</sup> (Snedden 1973) with ATLAS plane-parallel model atmospheres (Kurucz 1993) assuming local thermodynamic equilibrium. A downhill simplex minimization procedure (Press et al. 1992) was used to determine the stellar photospheric parameters; see e.g. Mortier et al. (2013) and references therein. We determined that the stellar temperature was less than 5200 K, so we reran the minimization procedure with a sublist of lines designed for cooler stars (Tsantaki et al. 2013); we also constrained our line list to those with equivalent widths between 5 and 150 milliAngstroms (mÅ), removing 5 lines above 150 mÅ and 1 line below 5 mÅ (lines within this range tend to be sufficiently strong and well-described by a Gaussian). Finally, we corrected for  $\log g$  and re-scaled errors following Torres et al. (2012), Mortier et al. (2014), and Sousa et al. (2011). The resulting effective temperature, surface gravity, microturbulence, and metallicity are reported in Table 3.1.

Then we determined the same stellar parameters from the same spectra with a different, independent tool: the Stellar Parameter Classification tool, SPC (Buchhave et al. 2012). SPC interpolates across a synthetic spectrum library from Kurucz (1992) to find the best fit and uncertainties on an input spectrum. In addition to the stellar parameters calculated from ARES+MOOG, this tool also estimated rotational velocity. All atmospheric stellar parameters from ARES+MOOG and SPC were in good agreement (within  $1\sigma$ ). Like ARES+MOOG, all SPC parameter estimates can be found in Table 3.1.

We then took our estimated effective temperature and metallicity from ARES+MOOG and SPC, the *Gaia* Data Release 3 (DR3) parallax (Gaia Collaboration and Vallenari 2022; Gaia Collaboration et al. 2016, 2021a), and numerous photometric magnitudes (B, V, J, H, K, W1, W2, and W3) and input them into the `isochrones` Python package (Morton 2015). This package used two different sets of isochrones: Dartmouth (Dotter et al. 2008) and Modules for Experiments in Stellar Astrophysics (MESA) Isochrones and Stellar Tracks, MIST (Choi et al. 2016; Dotter 2016). Comparing two standard, independent models is useful for mitigating systematic errors and revealing discrepancies or issues in the resulting parameter estimates. We used `MultiNest` (Feroz et al. 2009; Feroz et al. 2019) for parameter estimation, assuming 600 live points and otherwise standard `MultiNest` settings: importance nested sampling mode, multimodal mode, constant efficiency mode disabled, evidence tolerance = 0.5, and sampling efficiency = 0.8. As stated earlier, K2-136 is a member of the Hyades and therefore has a very tight age constraint of  $650 \pm 70$  Myr (Martín et al. 2018). We applied a much broader age prior of  $475 - -775$  Myr, a  $3\sigma$  range on the  $625 \pm 50$  Hyades age estimate from Perryman et al. (1998), which was more than sufficient to achieve convergence. This yielded posterior distributions from both input atmospheric parameter sets (ARES+MOOG and SPC) as well as both isochrone sets (Dartmouth and MIST), for a total of four sets of posterior distributions (based on all combinations of input parameters and isochrones).

The posteriors were then combined together (i.e. the posterior samples were appended together) to yield a single posterior distribution for each parameter. Lastly, systematic

---

<sup>1</sup>2017 version: <http://www.as.utexas.edu/~chris/moog.html>

uncertainties determined by Tayar et al. (2022) were added in quadrature to the combined posteriors to yield final parameters and uncertainties. Specifically, we added 4% uncertainty to  $R_{\odot}$ , 5% uncertainty to  $M_{\odot}$ , 2% uncertainty to  $L_{\odot}$ , and 13% uncertainty to  $\rho_{\odot}$  (propagated from  $R_{\odot}$  and  $M_{\odot}$  uncertainties). The input *Gaia* DR3 parallax, distance, photometric magnitudes, and the resulting stellar radius, mass, density, and luminosity are all reported in Table 3.1.

BJD	RV	$\sigma_{RV}$	CCF BIS	$\sigma_{BIS}$	CCF FWHM	$\sigma_{FWHM}$	$S_{HK}$	$\sigma_{SHK}$	Instrument
(TDB)	(m s <sup>-1</sup> )	(m s <sup>-1</sup> )	(m s <sup>-1</sup> )	(m s <sup>-1</sup> )	(m s <sup>-1</sup> )	(m s <sup>-1</sup> )			
2458341.70618026	39498.9	1.8	6901.1	3.7	63.8	3.7	1.191	0.022	HARPS-N
2458345.70159539	39516.8	1.4	6920.6	2.7	63.4	2.7	1.198	0.014	HARPS-N
2458346.70175761	39515.5	2.0	6948.0	4.0	70.2	4.0	1.274	0.025	HARPS-N
2458361.71645940	39513.6	2.9	6945.1	5.7	75.3	5.7	1.234	0.039	HARPS-N
2458363.75019615	39514.0	1.4	6942.8	2.8	69.2	2.8	1.222	0.013	HARPS-N
2458364.69673319	39516.3	1.4	6941.9	2.8	74.6	2.8	1.251	0.014	HARPS-N
2458365.69775405	39515.1	1.3	6949.1	2.7	71.9	2.7	1.238	0.013	HARPS-N
2458366.72988568	39504.4	1.7	6932.3	3.3	83.8	3.3	1.212	0.018	HARPS-N
2458378.65078445	39517.9	2.2	6947.9	4.4	72.8	4.4	1.294	0.027	HARPS-N
2458379.66372361	39514.4	1.4	6945.1	2.8	80.4	2.8	1.249	0.014	HARPS-N
2458380.65930503	39510.6	1.2	6930.6	2.4	77.3	2.4	1.294	0.012	HARPS-N
2458381.66442355	39504.7	1.2	6921.7	2.3	86.1	2.3	1.251	0.011	HARPS-N
2458382.66425283	39501.7	1.6	6913.0	3.2	78.8	3.2	1.243	0.018	HARPS-N
2458383.66210025	39495.8	2.3	6902.9	4.5	75.2	4.5	1.172	0.029	HARPS-N
2458384.71464839	39498.4	2.2	6896.4	4.4	67.9	4.4	1.160	0.027	HARPS-N
2458385.66982781	39500.0	1.4	6900.7	2.8	63.5	2.8	1.162	0.014	HARPS-N
2458386.73771712	39499.1	1.5	6910.7	3.1	59.3	3.1	1.165	0.016	HARPS-N
2458388.70001017	39504.0	1.4	6916.2	2.9	62.5	2.9	1.213	0.015	HARPS-N
2458390.75891115	39507.6	1.5	6923.3	3.0	66.3	3.0	1.194	0.016	HARPS-N
2458391.74334211	39509.3	1.5	6907.4	2.9	65.3	2.9	1.203	0.015	HARPS-N
2458410.64445231	39506.1	2.2	6903.3	4.3	82.2	4.3	1.165	0.027	HARPS-N
2458410.73761710	39506.9	2.7	6904.2	5.4	81.5	5.4	1.143	0.037	HARPS-N
2458415.61383639	39507.7	2.4	6905.6	4.8	66.5	4.8	1.130	0.028	HARPS-N
2458415.72038413	39504.5	1.4	6916.4	2.9	68.7	2.9	1.163	0.015	HARPS-N
2458421.64508561	39500.0	1.4	6937.6	2.8	74.8	2.8	1.240	0.014	HARPS-N
2458421.72295016	39497.8	4.0	6953.8	8.0	67.1	8.0	1.317	0.062	HARPS-N
2458424.69841781	39505.2	4.4	6922.8	8.8	63.0	8.8	1.255	0.068	HARPS-N
2458424.76629848	39502.2	2.9	6916.1	5.7	69.5	5.7	1.247	0.041	HARPS-N
2458448.58055249	39506.0	1.2	6911.5	2.3	63.8	2.3	1.137	0.010	HARPS-N
2458448.71120394	39506.1	1.8	6917.5	3.6	75.5	3.6	1.160	0.020	HARPS-N
2458449.42303120	39518.1	5.9	6925	12	81	12	1.17	0.11	HARPS-N
2458449.69543641	39507.7	2.3	6903.0	4.5	63.2	4.5	1.158	0.029	HARPS-N
2458451.47509484	39511.7	1.6	6923.5	3.2	69.2	3.2	1.164	0.017	HARPS-N
2458451.61304290	39512.1	1.5	6917.5	2.9	68.5	2.9	1.184	0.015	HARPS-N
2458453.60424787	39495.9	1.6	6922.3	3.3	79.5	3.3	1.242	0.019	HARPS-N
2458453.70820393	39493.9	1.6	6914.4	3.3	78.0	3.3	1.173	0.019	HARPS-N
2458454.46507987	39492.6	1.5	6902.0	3.1	75.7	3.1	1.155	0.017	HARPS-N
2458454.55426377	39488.9	1.5	6907.1	3.0	77.3	3.0	1.180	0.015	HARPS-N
2458456.47471787	39499.7	1.5	6895.0	3.0	68.5	3.0	1.198	0.016	HARPS-N
2458462.64638556	39509.7	1.7	6915.3	3.4	60.7	3.4	1.237	0.021	HARPS-N
2458473.54081960	39494.9	1.3	6911.9	2.5	73.2	2.5	1.092	0.011	HARPS-N
2458473.63947550	39492.6	1.3	6909.0	2.7	74.8	2.7	1.068	0.012	HARPS-N
2458474.47139808	39494.1	1.3	6913.1	2.7	76.0	2.7	1.067	0.012	HARPS-N
2458474.56083109	39491.6	1.1	6911.6	2.2	66.0	2.2	1.1493	0.0099	HARPS-N
2458477.50294855	39506.5	2.9	6915.2	5.8	70.1	5.8	1.164	0.039	HARPS-N
2458477.60820837	39503.8	3.4	6950.6	6.7	64.1	6.7	1.120	0.048	HARPS-N
2458478.43374093	39504.7	1.9	6914.6	3.8	66.9	3.8	1.164	0.021	HARPS-N
2458478.55045568	39502.0	1.3	6917.9	2.7	72.5	2.7	1.250	0.013	HARPS-N
2458479.54013997	39497.3	1.1	6919.3	2.2	65.9	2.2	1.223	0.010	HARPS-N
2458479.59583870	39498.3	1.2	6908.3	2.4	69.5	2.4	1.235	0.012	HARPS-N

*HYADES MEMBER K2-136c: THE SMALLEST PLANET IN AN OPEN CLUSTER WITH A  
PRECISELY MEASURED MASS*

2458480.49811363	39498.5	1.6	6904.6	3.3	80.0	3.3	1.164	0.017	HARPS-N
2458480.61833460	39500.4	3.3	6922.6	6.5	74.6	6.5	1.182	0.049	HARPS-N
2458481.52056002	39494.5	1.9	6896.6	3.8	74.5	3.8	1.150	0.022	HARPS-N
2458481.61815376	39500.0	1.5	6893.8	2.9	74.9	2.9	1.174	0.016	HARPS-N
2458482.47714376	39502.2	1.4	6893.7	2.8	68.9	2.8	1.127	0.014	HARPS-N
2458482.57623761	39502.2	1.2	6888.0	2.4	67.9	2.4	1.135	0.011	HARPS-N
2458483.48217046	39506.5	1.4	6892.5	2.8	66.2	2.8	1.120	0.013	HARPS-N
2458483.57932245	39507.8	1.3	6886.6	2.6	70.6	2.6	1.118	0.012	HARPS-N
2458484.45739679	39506.9	1.8	6894.0	3.6	61.6	3.6	1.160	0.020	HARPS-N
2458484.56221664	39507.2	1.5	6892.7	2.9	71.3	2.9	1.127	0.015	HARPS-N
2458486.56813502	39505.3	2.0	6905.7	4.1	75.7	4.1	1.221	0.027	HARPS-N
2458487.44451438	39500.6	1.4	6899.3	2.8	69.1	2.8	1.192	0.015	HARPS-N
2458487.55454800	39501.7	1.4	6901.2	2.8	69.6	2.8	1.170	0.015	HARPS-N
2458488.41884010	39497.3	1.2	6901.9	2.5	66.8	2.5	1.138	0.012	HARPS-N
2458488.52873713	39499.6	1.9	6900.0	3.9	66.3	3.9	1.206	0.024	HARPS-N
2458489.43534717	39496.3	1.8	6899.7	3.6	70.6	3.6	1.193	0.021	HARPS-N
2458489.58136198	39492.8	1.6	6908.5	3.1	67.7	3.1	1.166	0.018	HARPS-N
2458502.38887026	39505.0	1.7	6903.9	3.3	66.2	3.3	1.123	0.018	HARPS-N
2458502.53993777	39505.4	2.5	6896.3	5.0	77.0	5.0	1.120	0.032	HARPS-N
2458503.37914022	39506.8	1.5	6904.6	2.9	71.5	2.9	1.183	0.015	HARPS-N
2458503.50487143	39505.3	1.2	6903.0	2.5	74.4	2.5	1.170	0.012	HARPS-N
2458504.43989909	39509.9	2.4	6912.6	4.8	81.1	4.8	1.114	0.029	HARPS-N
2458504.55233098	39503.5	2.1	6915.0	4.2	70.0	4.2	1.102	0.025	HARPS-N
2458505.38129467	39500.6	1.7	6905.6	3.3	72.6	3.3	1.200	0.019	HARPS-N
2458505.49840229	39498.6	2.3	6909.7	4.7	77.7	4.7	1.118	0.030	HARPS-N
2458506.36962284	39493.9	3.6	6916.2	7.1	66.2	7.1	1.243	0.055	HARPS-N
2458506.50672836	39488.8	2.9	6899.0	5.8	71.8	5.8	1.171	0.041	HARPS-N
2458518.37653154	39508.5	2.2	6909.8	4.3	66.3	4.3	1.193	0.027	HARPS-N
2458518.45830362	39515.6	4.3	6932.0	8.7	73.9	8.7	1.278	0.072	HARPS-N
2458518.47977117	39509.4	2.8	6914.6	5.5	76.9	5.5	1.203	0.040	HARPS-N
2458519.35187655	39498.8	3.8	6910.8	7.7	74.4	7.7	1.120	0.061	HARPS-N
2458519.45005233	39502.4	3.5	6921.3	7.0	84.8	7.0	1.213	0.055	HARPS-N
2458520.35461693	39497.1	1.5	6893.9	2.9	74.7	2.9	1.142	0.015	HARPS-N
2458520.45526091	39494.5	1.8	6914.5	3.5	72.8	3.5	1.157	0.021	HARPS-N
2458521.40212719	39499.0	2.2	6889.8	4.5	71.3	4.5	1.183	0.029	HARPS-N
2458521.48828747	39498.2	2.1	6899.6	4.2	71.1	4.2	1.147	0.027	HARPS-N
2458522.35495354	39499.9	1.2	6887.3	2.4	65.3	2.4	1.132	0.011	HARPS-N
2458522.43817942	39500.6	1.4	6892.8	2.8	67.9	2.8	1.130	0.015	HARPS-N
2458788.78775712	39499.17	0.89	6953.5	1.8	43.7	1.8	1.1403	0.0020	ESPRESSO
2458804.67601741	39480.32	0.67	6965.9	1.3	65.6	1.3	1.2545	0.0013	ESPRESSO
2458806.80347928	39484.42	0.79	6928.5	1.6	56.1	1.6	1.0794	0.0016	ESPRESSO
2458808.76852035	39504.65	0.83	6941.7	1.7	41.2	1.7	1.0573	0.0018	ESPRESSO
2458820.76166121	39489.22	0.46	6928.21	0.91	48.14	0.91	1.18743	0.00067	ESPRESSO
2458825.59389775	39492.79	0.71	6962.1	1.4	60.4	1.4	1.1525	0.0014	ESPRESSO
2458833.58700359	39486.65	0.70	6934.8	1.4	54.4	1.4	1.1807	0.0013	ESPRESSO
2458839.65413441	39493.99	0.63	6955.9	1.3	54.1	1.3	1.2941	0.0011	ESPRESSO
2458840.58619720	39501.76	0.70	6967.2	1.4	41.1	1.4	1.3193	0.0013	ESPRESSO
2458848.60085991	39501.35	0.49	6942.72	0.98	43.38	0.98	1.17686	0.00075	ESPRESSO
2458849.56597102	39505.53	0.69	6955.6	1.4	38.6	1.4	1.1913	0.0013	ESPRESSO
2458850.58225768	39494.9	1.8	6972.4	3.5	46.6	3.5	1.2761	0.0044	ESPRESSO
2458850.60464655	39497.81	0.92	6955.0	1.8	34.1	1.8	1.2108	0.0019	ESPRESSO
2458851.58865177	39493.17	0.79	6953.3	1.6	57.3	1.6	1.2570	0.0016	ESPRESSO
2458853.68186920	39502.19	0.57	6968.8	1.1	58.0	1.1	1.3340	0.0010	ESPRESSO
2458864.55947341	39502.03	0.65	6954.6	1.3	44.6	1.3	1.2129	0.0012	ESPRESSO
2458864.64168610	39502.17	0.77	6944.7	1.5	53.7	1.5	1.2462	0.0017	ESPRESSO
2458865.59784818	39505.73	0.94	6978.3	1.9	38.7	1.9	1.3126	0.0024	ESPRESSO
2458869.61564757	39488.28	0.56	6996.3	1.1	63.6	1.1	1.2687	0.0011	ESPRESSO
2458886.57544506	39481.55	0.69	6924.4	1.4	52.8	1.4	1.2086	0.0013	ESPRESSO
2458887.57037120	39487.19	0.61	6925.7	1.2	45.6	1.2	1.1117	0.0011	ESPRESSO
2458906.52291945	39500.21	0.67	6988.0	1.3	45.9	1.3	1.2254	0.0012	ESPRESSO
2459110.65183858	39492.2	2.7	6957.0	5.3	66.3	5.3	1.251	0.033	HARPS-N
2459111.66733900	39505.2	1.2	6956.5	2.5	67.6	2.5	1.401	0.011	HARPS-N
2459112.66195511	39508.2	1.9	6955.8	3.8	64.1	3.8	1.294	0.020	HARPS-N

2459120.71102749	39512.7	1.3	6979.6	2.7	70.1	2.7	1.339	0.013	HARPS-N
2459153.51589766	39502.7	2.4	6939.2	4.7	67.1	4.7	1.216	0.026	HARPS-N

Table 3.2: Kepler-136 RV observations and activity indicators

## Stellar Rotation Period

One parameter of special interest is the stellar rotation period, which we include as a parameter in our RV model (see Section 3.4). M18 conducted a Lomb-Scargle periodogram on the *K2* light curve and reported a rotation period of  $15.04 \pm 1.01$  days. Ciardi et al. (2018) analyzed the same light curve and found a rotation period of  $15.2 \pm 0.2$  days through a Lomb-Scargle periodogram and  $13.8 \pm 1.0$  days through an autocorrelation function. Livingston et al. (2018) conducted a Gaussian process (GP) regression, a Lomb-Scargle periodogram, and an autocorrelation function on the light curve and found a corresponding rotation period of  $13.5^{+0.7}_{-0.4}$  d,  $15.1^{+1.3}_{-1.2}$  d, and  $13.6^{+2.2}_{-1.5}$  d, respectively. Note: Given an offset and uncertainties in the photometric data set, a generalized Lomb-Scargle periodogram would be preferred (Zechmeister and Kürster 2009); however, it is not clear from the referenced papers whether this generalized method was used or just a basic Lomb-Scargle periodogram (Scargle 1982).

Notably, the estimates via a Lomb-Scargle periodogram are longer than estimates with other methods. All results are broadly consistent with our findings from our full model results ( $13.37^{+0.13}_{-0.17}$  days; see Table 3.4), except the  $15.2 \pm 0.2$  day result from the Lomb-Scargle analysis by Ciardi et al. (2018). They also have the smallest uncertainties of any rotation period estimate, so it is possible that their value is reasonable but the uncertainties are overly optimistic.

A possible explanation of this discrepancy could be differential rotation. Regardless of activity level, starspots, plage, and other activity may be more prominent at different stellar latitudes when the *K2* photometry and our HARPS-N spectroscopy were conducted. This hypothesis is also mentioned by Ciardi et al. (2018) to explain a larger than expected  $v \sin i$ . Following Barnes et al. (2005) and Kitchatinov and Olemskoy (2012), they estimate that the equatorial rotation period of K2-136 could be faster than higher latitudes by  $\sim 1$  day. Then again, Aigrain et al. (2015) found that claims of differential rotation should be treated with caution even for long baselines of photometry. We may simply be seeing different starspots at different longitudes creating phase modulation, combined with greater or fewer numbers of starspots leading to better or worse constraints on rotation period.

## Binarity of K2-136

One of the planet discovery papers, Ciardi et al. (2018), reported a binary companion to K2-136. In addition to their *K2* photometric analysis, they collected spectra from the SpeX spectrograph (Rayner et al. 2003; Rayner et al. 2004) at the 3-m NASA Infrared Telescope Facility and the HIRES spectrograph (Vogt et al. 1994) at the Keck I telescope, as well as AO observations with the NIRC2 instrument at the Keck II telescope and the P3K AO system and PHARO camera (Hayward et al. 2001) on the 200" Hale Telescope at Palomar

Observatory. The AO observations at both facilities detected an M7/8V star separated from the primary star by  $\sim 0.7''$ , corresponding to a projected separation of  $\sim 40$  AU; the spectroscopic observations did not detect this companion, and no further companions were found by any of the above observations. (Notably, this angular separation is more than enough for HST to resolve; see Sections 3.4 and 3.2.)

Gaia DR3 did not detect the binary companion, leaving the issue of boundedness unresolved. However, Ciardi et al. (2018) compared the current position of K2-136 against observations from the 1950 Palomar Observatory Sky Survey (POSS I) and noted that the star had moved  $6''$  in the intervening time with no evidence of background stars. These POSS I observations show that the stellar companion is likely bound.

Further, Gaia DR3 reported K2-136 to have an astrometric excess noise of  $96 \mu\text{as}$  and a Renormalised Unit Weight Error (RUWE) of 1.23, a mild departure from a good single-star model. At the separation and brightness of the companion, this excess variability in the astrometry is unlikely to be due to pollution from its light contribution: at  $\sim 0.7''$  separation a companion can be detected only with a G magnitude difference of  $\lesssim 2$  (Gaia Collaboration et al. 2021b). There is therefore a mild indication of astrometric variability due to unmodeled orbital motion. Using the formalism of Torres (1999), at the distance of the system, given its angular separation, and for the mass range of an M7/8 star, the median astrometric acceleration is expected to be  $\sim 25 \mu\text{as yr}^{-2}$ , with maximum value close to  $40 \mu\text{as yr}^{-2}$ , indicating that in addition to simple astrometric noise, the bulk of the astrometric variability could be caused by the detection of the acceleration due to the companion.

It is worth considering whether flux from the companion could bias the measured RVs of the primary K dwarf. Both the HARPS-N and ESPRESSO band passes are approximately 380nm – 690nm and centered on the V band. According to Ciardi et al. (2018), the M dwarf companion is at least 10 magnitudes fainter than the primary in the V-band. We can use  $\Delta m = 10$  as a worst-case scenario and similarly assume the companion star was well-centered on the fiber for all observations (because the companion and primary are separated by  $0.7''$ , the companion would not be well-centered and the actual flux contamination from the companion would be less). Cunha et al. (2013) explored the RV impact of flux contamination from a stellar companion: for a K5 dwarf and an M dwarf (M3 or later) with  $\Delta m = 10$ , the maximum impact on RVs is  $< 10 \text{ cm s}^{-1}$ , and therefore negligible for our level of RV precision.

Ciardi et al. (2018) explored whether the transit signals may originate from the M dwarf. They found that in order to match the observed transit depth of K2-136c, the M dwarf would have to be a binary system itself that exhibits significant and detectable secondary eclipses, which have not been observed. Further, the transit duration of K2-136c is inconsistent with a transit of an M dwarf. Finally, K2-136c has already been validated by Ciardi et al. (2018) and all three planets have been independently validated by M18 and Livingston et al. (2018). Therefore, it is very unlikely that the planets are false positive signals or planetary signals from the M dwarf.

However, in the *Kepler* band pass, the companion M dwarf is 6.5 magnitudes fainter, which leads to a very small dilution effect on the planet transit depths. Following Ciardi et

al. (2015), we include this effect for the sake of robustness in our final planet radius estimates (which enlarges each planet by  $\sim 0.13\%$ ).

This binary companion may also cause a long-term RV trend, which we discuss further in Section 3.4 and test in Section 3.4.

## 3.4 Data Analysis

We analyzed the RV data in conjunction with a number of other common stellar activity indices that are calculated with the ESPRESSO DRS 2.2.8 pipeline, specifically the CCF BIS, CCF FWHM, and  $S_{HK}$ . In this section, we first explore the data set by generating a periodogram and conducting a correlation analysis between the RVs and other data types. Then we discuss the transit and RV components of our model, the parameter estimation process, and how we compare our models. Finally, we conduct tests on our results and discuss the implications of a binary companion in the system.

### Periodogram Analysis

In order to investigate periodic signals in our data (planetary or otherwise), we created Generalized Lomb-Scargle periodograms (Scargle 1982; Zechmeister and Kürster 2009) of our RVs and our stellar activity indices. As a point of reference, we also included the window function of our data (built from constant, non-zero values at each of the timestamps of our observations). It is used to determine the regular patterns in the periodograms due to the sampling and gaps in the time series. These periodograms are presented in Fig. 3.1.

To ascertain the robustness of any apparent signals, we also estimated each periodogram’s False Alarm Probability (FAP), the likelihood that an apparent signal of a given strength will be detected when no underlying signal is actually present. The FAP was estimated with the bootstrap method: sampling the observations randomly with replacement while maintaining the same timestamps. We repeat this process 100000 times, each time constructing a periodogram and determining the maximum peak. This reveals how often a given signal strength will appear due only to noise, from which the FAP is calculated.

The strongest RV signals in our combined periodogram (both HARPS-N and ESPRESSO) are at the orbital period of K2-136c, the rotation period of the star, and near  $0.017 \text{ d}^{-1}$  (i.e. half the length of the ESPRESSO data baseline of 117.7 days), although none are significant at the 1% level. Among the stellar activity periodograms, the strongest signals are the rotation period signal in the ESPRESSO FWHM power and a long-period signal in the HARPS-N FWHM power which can be attributed to the window function. Also, the strongest peak in the (combined data) window function periodogram above  $0.01 \text{ days}^{-1}$  (near  $0.03 \text{ days}^{-1}$ ) does not correspond to any significant signals or aliases in any of the four data types. As for low-frequency signals  $< 0.01 \text{ days}^{-1}$ , we discuss possible long-term trends in Sections 3.3 and 3.4. All of this indicates that K2-136c has a more detectable RV signal than the other two planets, as expected given its size.

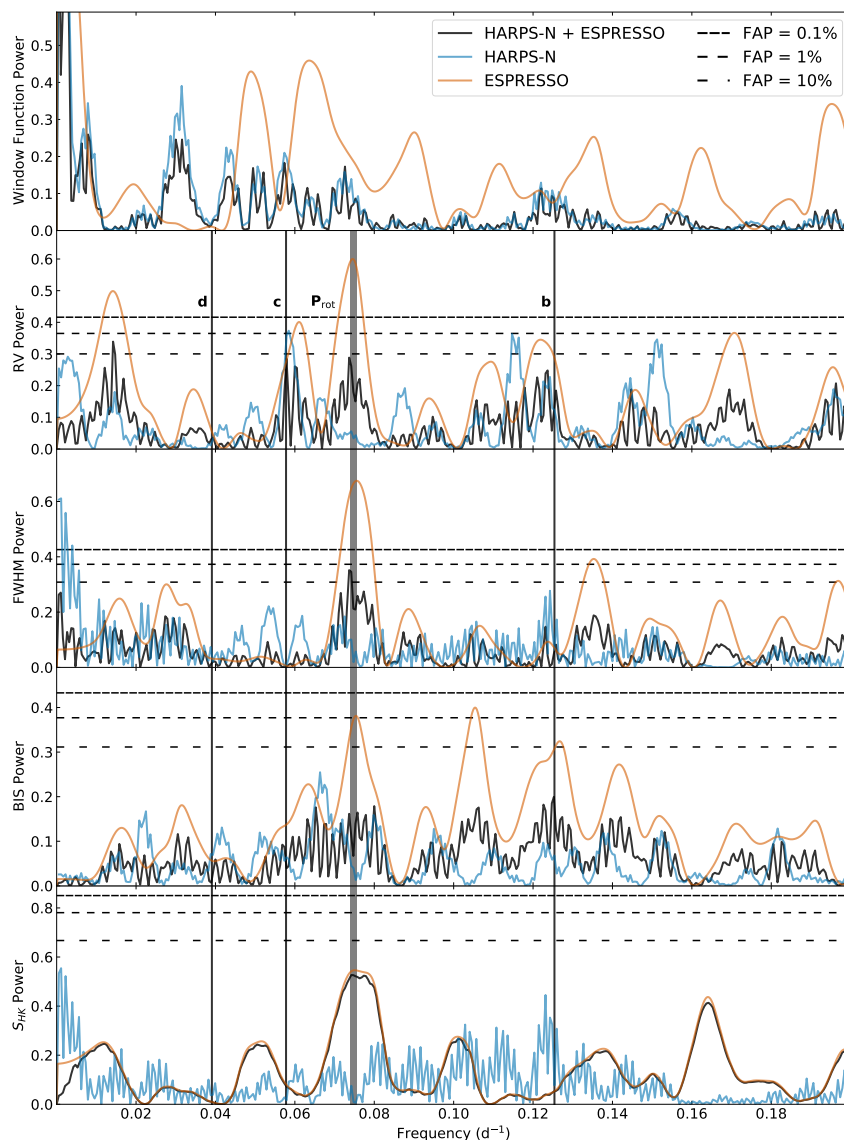


Figure 3.1: Periodograms of RV, CCF FWHM, CCF BIS, and  $S_{HK}$  for the K2-136 system. In the top panel is the window function (computed from observation times only). Each subplot has the periodogram of HARPS-N and ESPRESSO combined (black), HARPS-N alone (blue), and ESPRESSO alone (orange). The gray region corresponds to the  $1\sigma$  confidence interval of the stellar rotation period (as determined from our model results); the three vertical, black lines correspond to the orbital periods of K2-136b, c, and d. Finally, the horizontal dashed lines refer to different false alarm probabilities (for HARPS-N and ESPRESSO combined).

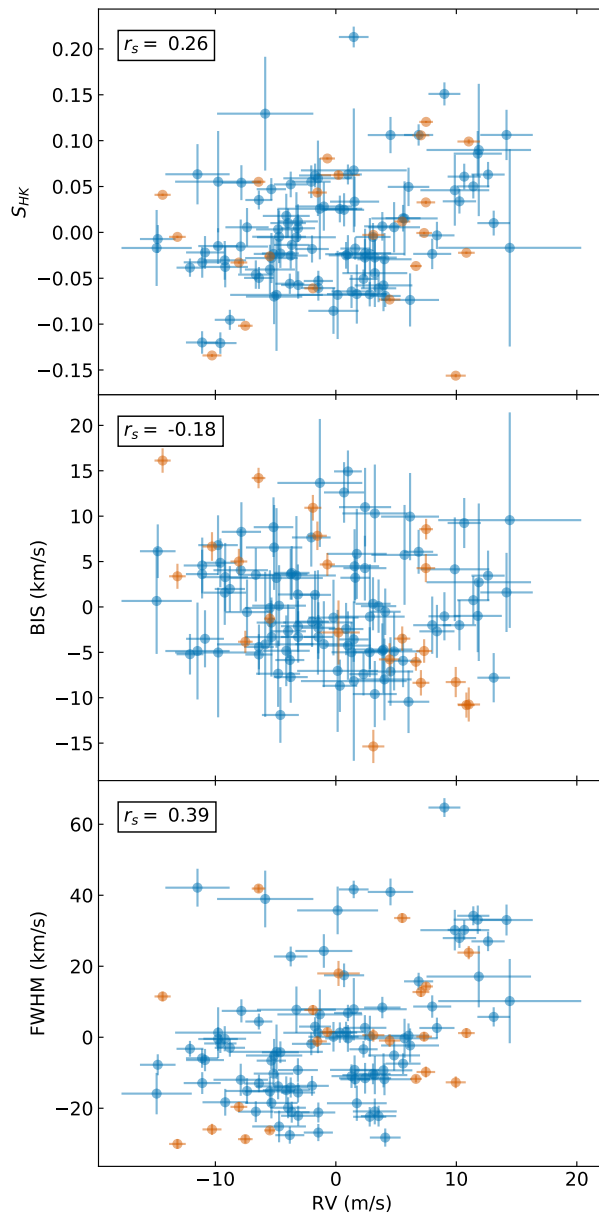


Figure 3.2: Scatter plots of  $S_{HK}$ , BIS, and FWHM against RV for the K2-136 system. All HARPS-N and ESPRESSO data have been separately offset shifted according to the median model offsets listed in Table 3.4. Blue data points correspond to HARPS-N observations, orange data points to ESPRESSO. In the top-left corner of each subplot is the Spearman correlation coefficient, which can capture nonlinear, monotonic correlations. (Coefficients were calculated with data values but not uncertainties.)



## Correlation Analysis

We also examined the relationship between RVs and our stellar activity indices. Because RVs are measured from small shifts in spectral absorption lines, and stellar activity can change the shape of absorption lines, stellar activity can significantly affect RV observations, e.g. Haywood (2015), Queloz et al. (2001), and Rajpaul et al. (2015). Scatter plots between RVs and all three activity indices are presented in Fig. 3.2. At least in the case of  $S_{HK}$  and FWHM, there are notable correlations with RVs according to the p-values for the Spearman correlation coefficient (which captures nonlinear, monotonic correlations and uses the same  $-1$  to  $1$  range as the Pearson correlation coefficient). According to the Spearman coefficient, there is a correlation of 0.26 between RV and  $S_{HK}$ , a negative correlation of  $-0.18$  between RV and BIS, and the strongest correlation of 0.39 between RV and FWHM. For a data set of this size, these coefficients correspond to p-values of 0.004 for RV and  $S_{HK}$ , 0.052 for RV and BIS, and  $\ll 0.001$  for RV and FWHM. Therefore, for RV and  $S_{HK}$  and especially RV and FWHM, there appears to be a statistically significant correlation. In other words, there is good reason to believe that this data set includes correlated and structured stellar activity. In fact, the Spearman correlation coefficient is likely an underestimate of the correlation between RVs and stellar activity indices, since there can be a phase shift in the amplitude variation from one data type to another (Collier Cameron et al. 2019; Santos et al. 2014).

## K2 Transit Photometry

We cleaned and flattened the photometric data from *K2* using the exact same procedure as was used originally in M18. Their procedure follows the self-flat-fielding (SFF) method developed in Vanderburg and Johnson (2014) to perform a rough removal of instrumental variability followed by a simultaneous fit to a model consisting of Mandel and Agol (2002) transit shapes for the three planets, a basis spline in time to describe the stellar variability, and splines in *Kepler*'s roll angle to describe the systematic photometric errors introduced by the spacecraft's unstable pointing (Vanderburg et al. 2016). After performing the fit, they removed the best-fit systematics and stellar variability components, isolating the transits for further analysis. The interested reader should refer to M18 for additional detail of the full procedure.

We modeled the flattened and cleaned M18 light curve with the **BATMAN** Python package (Kreidberg 2015a), based on the Mandel and Agol (2002) transit model. Our model included a baseline offset parameter and white noise parameter for our *K2* Campaign 13 photometry as well as two quadratic limb-darkening parameters parameterized using Kipping (2013a). Each planet was modeled with five parameters: the transit time, orbital period, planet radius relative to stellar radius, transit duration, and impact parameter. All parameters were modeled with either uniform, Gaussian, Jeffreys, or modified Jeffreys priors (Gregory 2007). Only the photometric white noise parameters used modified Jeffreys priors, with a knee located at the mean of the photometric flux uncertainty for that particular campaign or sector. All priors are listed in Table 3.3. The raw and flattened data can be seen in Fig. 3.3.

We also applied a Gaussian prior on stellar density by comparing the spectroscopically derived stellar density to the stellar density found via the following equation (Seager and Mallén-Ornelas 2003; Sozzetti et al. 2007):

$$\rho_* = \frac{3\pi}{GP^2} \left( \frac{a}{R_*} \right)^3 \quad (3.1)$$

where orbital period ( $P$ ) and the semi-major axis ( $a/R_*$ ) are derived directly from the light curve model.

All together, our full transit model includes 15 planetary parameters (5 per planet: time of transit, orbital period, ratio of planet radius to stellar radius, transit duration, and impact parameter), 2 quadratic limb darkening parameters, 1 photometric noise parameter, and 1 photometric baseline offset parameter for a total of 19 parameters.

The only parameters in common between our transit model and our RV model (as explained in further detail below) are transit times and orbital periods.

## ***TESS* Transit Photometry**

No pre-processed light curves were available for the *TESS* Sector 43 observation of K2-136, so we extracted the photometry from the full frame image (FFI) pixel level. Following Vanderburg et al. (2019), we constructed 20 different apertures (10 circular, 10 shaped like the *TESS* point spread function) and selected the one that best minimized photometric scatter. As for *TESS* Sector 44 observations, we used the simple aperture photometry (SAP) light curve produced by the Science Processing Operations Center (SPOC) pipeline (Jenkins et al. 2016). Light curves from both sectors were then flattened in the same way: a basis spline fit was performed iteratively on the photometry (with breakpoints every 0.3 days in order to adequately model stellar variability) and  $3\sigma$  outliers were removed until convergence; this too, aside from the breakpoint length, follows Vanderburg et al. (2019). Finally, we conducted a simultaneous fit of the low-frequency variability and the transits in order to determine the best-fit low-frequency variability.

*TESS* photometry is not incorporated into our final photometric model, although we did run exploratory joint transit models on *K2* and *TESS* photometry simultaneously. The transit signals of the two smaller planets, K2-136b and d were too small to reliably detect in the *TESS* photometry: individual transits were indistinguishable in depth and quality from temporally adjacent stellar activity. However, the transits of K2-136c were easily identifiable individually in *TESS* photometry, so we ran a joint transit model on all *K2* photometry and *TESS* photometry to explore the resulting improvements in the parameters of K2-136c. This joint transit model included all parameters listed in Section 3.4 as well as additional baseline offset and white noise parameters for the two *TESS* Sectors (43 and 44) and two additional quadratic limb-darkening parameters for *TESS* photometry for six additional parameters total. The fit resulted in consistent values for all planet and system parameters as well as a dramatically more precise ephemeris for K2-136c:  $P_c = 17.307081^{+0.000014}_{-0.000013}$  days and

$t_{0,c} = 8678.07179^{+0.00067}_{-0.00063}$  (BJD-2450000). For comparison, this period and transit time have uncertainties that are both approximately 15x tighter than those resulting from *K2* transit modeling alone (see Table 3.3). We report these values here to minimize ephemeris drift and facilitate planning of future transit observations of K2-136c.

## RV Model

We modeled the RV signal of the orbiting planets and the stellar activity simultaneously. We assumed non-interacting planets with Keplerian orbits. We used *RadVel* (Fulton et al. 2018) to model the RV signal from each planet with 5 parameters: reference epoch, orbital period, RV semi-amplitude, eccentricity, and argument of periastron. The latter two parameters, eccentricity and longitude of periastron, were parameterized as  $\sqrt{e} \cos w$  and  $\sqrt{e} \sin w$ . As explained in Eastman et al. (2013), this reparameterization avoids a boundary condition at zero eccentricity that may lead to eccentricity estimates that are systematically biased upward. We conducted trial simulations with circular versus eccentric orbits for all three planets and found excellent agreement in all parameters (less than  $1\sigma$ ). We opted to keep eccentricity and argument of the periastron as parameters in order to constrain or place upper limits on each planet’s eccentricity. Additionally, we prevented system configurations that would lead to orbit crossings of any two planets, as well as overlaps of planetary Hill spheres. For each planet’s reference epoch and orbital period, we applied a Gaussian prior based on the transit parameters determined from M18. We analyzed the *K2* transit photometry with and without *TESS* photometry and verified these M18 values (see Table 3.3).

We also applied additional prior limits on the eccentricities of K2-136b and K2-136d. Based on preliminary modeling of all three planets with uninformed prior eccentricity constraints (and everything else identical to our final model), we found that we could determine the eccentricity of K2-136c but not its siblings. Thus, we decided to set eccentricity constraints by using the Stability of Planetary Orbital Configurations Klassifier, *SPOCK* (Tamayo et al. 2020), an N-body simulator that employs machine learning to improve performance. We input into *SPOCK* our stellar mass posterior and our orbital period posteriors for all three planets (from our preliminary simulations). We also input the mass, eccentricity, and argument of the periastron posteriors for K2-136c (again, from our early simulations). Lastly, we input uniform distributions for mass, eccentricity, and argument of the periastron for K2-136b and K2-136d. Planet mass ranged from 0 up to that of approximately 100% iron planet composition:  $3 M_{\oplus}$  for K2-136b and  $30 M_{\oplus}$  for K2-136d (Fortney et al. 2007). Eccentricity ranged from 0 to 0.6 and argument of the periastron ranged from 0 to 360 degrees. We took the subset of our sample that had a  $> 90\%$  chance of surviving for  $> 10^9$  orbits (of the innermost planet) and then determined the  $3\sigma$  upper limit on the eccentricities of K2-136b and K2-136d for that subset. We then used those values,  $e_{b,\max} = 0.35$  and  $e_{d,\max} = 0.37$ , as eccentricity upper limit priors in all subsequent simulations.

Given the M dwarf companion to our host star (Ciardi et al. 2018), we wanted to include the potential for an RV trend caused by this companion. For further discussion of binarity

and linear trends, see Section 3.3. Our planetary RV signals and the RV trend therefore take the following form:

$$RV = \sum_{i \in \{b, c, d\}} K_i \left( \cos(\omega_i + f_i) + e_i \cos \omega_i \right) + mt \quad (3.2)$$

$$f = 2 \arctan \left( \sqrt{\frac{1+e}{1-e}} \tan \frac{E}{2} \right) \quad (3.3)$$

$$M = E - e \sin E \quad (3.4)$$

$$M = nt = \frac{2\pi(t - \tau)}{P} \quad (3.5)$$

where  $K$  is the induced RV semi-amplitude,  $\omega$  is the argument of the periastron,  $f$  is the true anomaly,  $e$  is the eccentricity,  $m$  is the slope of the RV trend,  $t$  is the observation time,  $E$  is the eccentric anomaly,  $M$  is the mean anomaly,  $n$  is the mean motion,  $\tau$  is the time of periastron passage (as calculated from transit time, orbital period, eccentricity, and argument of the periastron), and  $P$  is the orbital period.

The stellar activity was handled via a GP on RVs. We first used a simultaneous model of stellar activity on four different data types: RV, FWHM (a measure of the width of absorption lines), BIS (a measure of line asymmetry), and  $S_{HK}$  (an estimate of chromospheric magnetic activity via emission in the cores of the Ca II H & K lines). However, we found that this approach forced the model to include unreasonable amounts of white noise into each data type via a white noise jitter parameter included in our model. Further, it did not lead to a notable improvement in our final parameter constraints. We conducted numerous tests exploring the excess white noise preferred by the model, including modeling different instruments, different numbers of planets, altering the data reduction pipeline, e.g. trying the ZLSD pipeline (Lienhard et al. 2022), and creating synthetic data sets to model against. The most reasonable hypothesis we could find is that for the K2-136, our data (especially for ESPRESSO) is of a sufficiently high quality, with small enough uncertainties, that the model we used from Rajpaul et al. (2015) to relate the stellar activity indices to each other and to the RVs was not complex enough to account for the correlated structure of the stellar activity of K2-136.

Our RV data and the final RV model fit can be seen in Fig. 3.4. Despite only modeling RVs without any stellar activity indices, a GP is still robust and allows us to separate planet-induced RVs from stellar activity to the extent that disentanglement is possible. We followed the method laid out in Rajpaul et al. (2015), but we constrained the model only to the portions relevant to RVs rather than additional stellar activity indices. They dictate that the RVs are related to the stellar activity as follows:

$$\Delta RV = V_c G(t) + V_r \dot{G}(t) \quad (3.6)$$

In this equation,  $G(t)$  corresponds to the underlying stellar activity GP, while  $V_c$  and  $V_r$  correspond to the RV amplitudes of the convective blueshift and rotation modulation effect, respectively. It is important to include both rotation modulation and convective blueshift for data types impacted by both, as one phenomenon may play a larger role than the other depending on the data type and star. In fact, our final results (see Table 3.4) show that for K2-136, rotation modulation has an outsized effect on RVs compared to convective blueshift; however, we retain both terms in our model since  $V_c$  is still inconsistent with zero. We follow Rajpaul et al. (2015) further by using a quasi-periodic kernel to establish the covariance matrix of our GP. A quasi-periodic kernel is a good choice to capture the stellar variability of a star because quasi-periodicity describes well the variability exhibited by a rotating star with starspots that come and go. Following Giles et al. (2017), we find a predicted starspot lifetime for K2-136 of  $38_{-13}^{+20}$  days (versus a rotation period of 13.37 days); this estimate is consistent with our GP evolution time-scale result ( $48_{-11}^{+19}$  days, see Table 3.4). In other words, stellar activity during the time frame of a single rotation period is likely to look similar (though not identical) to stellar activity during the previous and subsequent stellar rotation periods, since the starspots for K2-136 are likely to be longer lived than the stellar rotation period. Thus, the quasi-periodic kernel is defined as follows:

$$K_{\text{QP}}(t_i, t_j) = h^2 \exp \left( - \frac{\sin^2(\pi(t_i - t_j)/P_*)}{2\lambda_p^2} - \frac{(t_i - t_j)^2}{2\lambda_e^2} \right), \quad (3.7)$$

where  $h$  is the GP amplitude (which is folded into the amplitude parameters described above),  $P_*$  is the stellar rotation period,  $\lambda_e$  is a decay timescale proportional to the starspot lifetime, and  $\lambda_p$  is a smoothness parameter that captures the level of variability within a single rotation period.  $t_i$  and  $t_j$  are any two times between which the covariance is being calculated; for a given time series of  $N$  observations, all  $N^2$  combinations of time pairs create the  $N \times N$  covariance matrix. This covariance matrix (plus a mean model) is a normal multivariate distribution;  $G(t)$  can be explored by sampling from this distribution. We refer the reader to Rajpaul et al. (2015) for a more detailed description of this method, as well as Mayo et al. (2019) for an application of this method to the sub-Neptune Kepler-538b.

Finally, we include a jitter parameter (added in quadrature to RV uncertainties) and a baseline offset parameter for each instrument (HARPS-N and ESPRESSO). All together, our full model includes 21 planetary parameters (5 per planet: time of transit, orbital period, RV semi-amplitude,  $\sqrt{e} \sin \omega$ , and  $\sqrt{e} \cos \omega$ ), 5 GP parameters (2 GP amplitudes corresponding to  $V_c$  and  $V_r$  from equation 3.6 as well as  $P_*$ ,  $\lambda_p$ , and  $\lambda_e$  from equation 3.7), 1 linear trend parameter, 2 RV noise parameters (1 per instrument) and 2 RV baseline offset parameters (1 per instrument), for a total of 25 parameters.

We used a uniform prior for the RV semi-amplitude for each planet. However, we conducted a trial simulation to compare a uniform versus log uniform prior for RV semi-amplitude and found no discernible difference in our results (all parameters agreed to within  $1\sigma$ ).

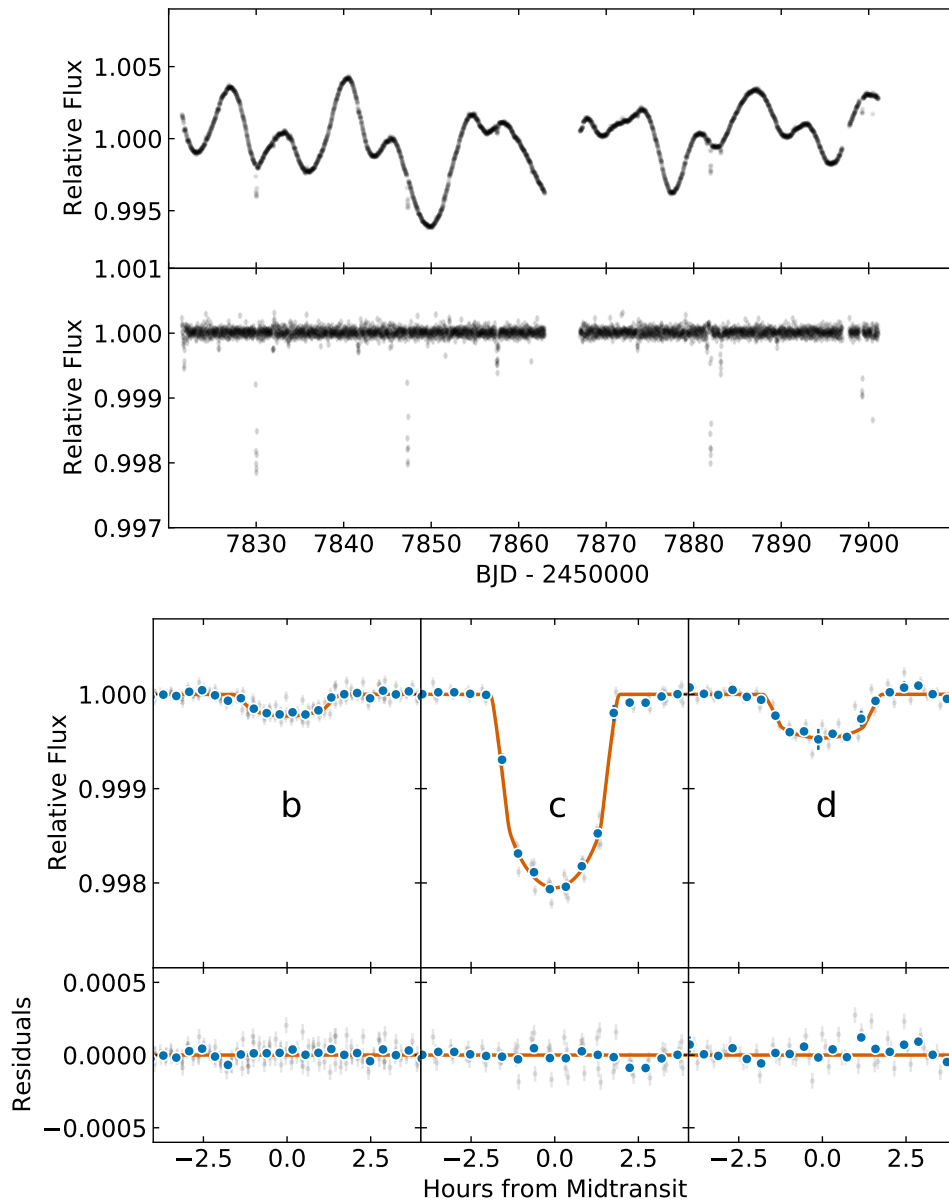


Figure 3.3: Transit plot of K2-136. The top and bottom subplots of the top plot are the raw and normalized *K2* photometry versus time from Campaign 13, respectively. In the top subplots of the bottom plot are the phase-folded light curves and transit model fits for K2-136b, c, and d. The gray points are the raw data. The best-fit transit model is the orange line and binning is represented by the blue points. The bottom subplots of the bottom plot are the residuals after the best-fit model has been subtracted.

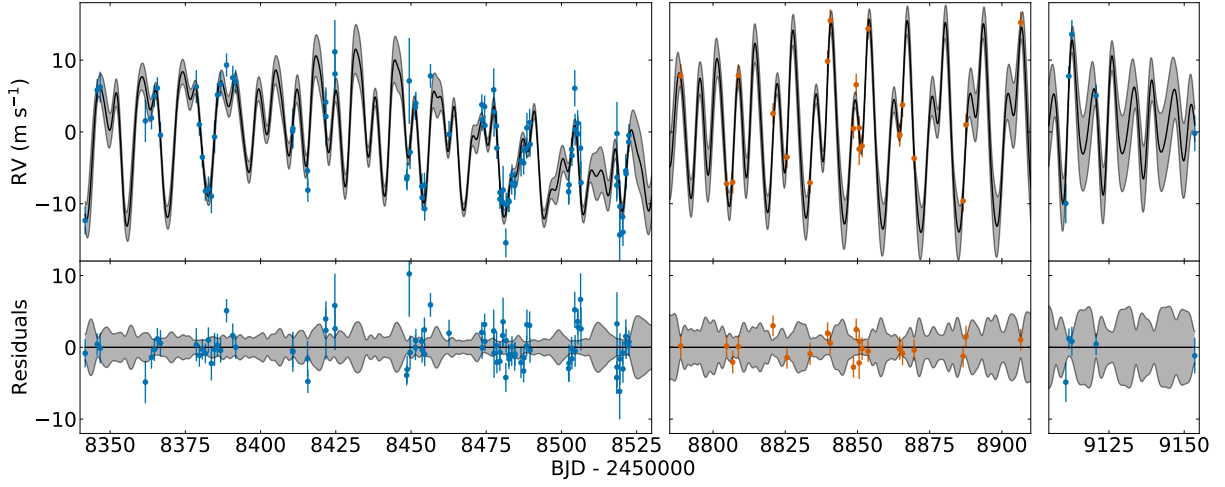


Figure 3.4: K2-136 observations and model fits for RVs (and fit residuals). In each panel, the blue points (HARPS-N) or orange points (ESPRESSO) are the observations while the black line and gray region are the model fit and  $1\sigma$  confidence interval, respectively. RVs have been mean-subtracted (corresponding to their respective instrument) and planet-induced reflex motion has been subtracted as well. RV errors have been inflated from their original values by adding the model-estimated RV jitter term in quadrature. Note the two time gaps between the first 88 HARPS-N observations, the 22 ESPRESSO observations, and the final 5 HARPS-N observations.

Parameter	Unit	This Paper	Priors
<i>Planet b</i>			
Period $P_b$	day	$7.97525 \pm 0.00073$	Unif(7.96529, 7.98529)
Time of transit $t_{0,b}$	BJD-2450000	$8679.083^{+0.075}_{-0.074}$	Unif(8678.58762, 8679.58762) <sup>1</sup>
Planet-star radius ratio $R_b/R_*$	-	$0.01370^{+0.00041}_{-0.00036}$	Jeffreys(0.001, 0.1)
Radius $R_b$	$R_\oplus$	$1.014^{+0.030}_{-0.049}$	...
Transit duration $T_{14,b}$	hr	$2.67^{+0.086}_{-0.084}$	Unif(0, 7.2)
Impact parameter $b_b$	-	$0.22^{+0.15}_{-0.14}$	Unif(0, 1)
Semi-major axis $a_b$	AU	$0.0707 \pm 0.0012$	...
Mean density $\rho_b$	$\rho_\oplus$	$< 2.8^2, < 4.4^3$	...
Mean density $\rho_b$	$\text{g cm}^{-3}$	$< 16^2, < 24^3$	...
Insolation flux $S_b$	$S_\oplus$	$33.5^{+1.6}_{-1.5}$	...
Equilibrium temperature $T_{eq,b}$ (albedo = 0.3)	K	610	...
Equilibrium temperature $T_{eq,b}$ (albedo = 0.5)	K	560	...
<i>Planet c</i>			
Period $P_c$	day	$17.30723^{+0.00019}_{-0.00020}$	Unif(17.30514, 17.30914)
Time of transit $t_{0,c}$	BJD-2450000	$8678.0792^{+0.0088}_{-0.0096}$	Unif(8677.0747, 8679.0747) <sup>1</sup>
Planet-star radius ratio $R_c/R_*$	-	$0.04064^{+0.00068}_{-0.00071}$	Jeffreys(0.001, 0.1)
Radius $R_c$	$R_\oplus$	$3.00 \pm 0.13$	...

<sup>1</sup> $t_0$  centered between *K2* and *TESS* photometry, so ephemeris drift is incorporated into  $t_0$  and  $P$ .

Transit duration $T_{14,c}$	hr	$3.449^{+0.039}_{-0.031}$	Unif(0, 7.2)
Impact parameter $b_c$	-	$0.31^{+0.11}_{-0.14}$	Unif(0, 1)
Semi-major axis $a_c$	AU	$0.1185^{+0.0020}_{-0.0021}$	...
Mean density $\rho_c$	$\rho_{\oplus}$	$0.67^{+0.12}_{-0.10}$	...
Mean density $\rho_c$	$\text{g cm}^{-3}$	$3.69^{+0.67}_{-0.56}$	...
Insolation flux $S_c$	$S_{\oplus}$	$11.91^{+0.57}_{-0.53}$	...
Equilibrium temperature $T_{eq,c}$ (albedo = 0.3)	K	470	...
Equilibrium temperature $T_{eq,c}$ (albedo = 0.5)	K	440	...
<hr/>			
<i>Planet d</i>			
Period $P_d$	day	$25.5750^{+0.0022}_{-0.0021}$	Unif(25.5551, 25.5951)
Time of transit $t_{0,d}$	BJD-2450000	$8675.936^{+0.072}_{-0.068}$	Unif(8675.4401, 8676.4401) <sup>1</sup>
Planet-star radius ratio $R_d/R_*$	-	$0.02119^{+0.00057}_{-0.00061}$	Jeffreys(0.001, 0.1)
Radius $R_d$	$R_{\oplus}$	$1.565^{+0.077}_{-0.076}$	...
Transit duration $T_{14,d}$	hr	$3.04^{+0.10}_{-0.09}$	Unif(0, 7.2)
Impact parameter $b_d$	-	$0.677^{+0.042}_{-0.049}$	Unif(0, 1)
Semi-major axis $a_d$	AU	$0.1538^{+0.0026}_{-0.0027}$	...
Mean density $\rho_d$	$\rho_{\oplus}$	$< 0.35^2, < 0.79^3$	...
Mean density $\rho_d$	$\text{g cm}^{-3}$	$< 1.9^2, < 4.3^3$	...
Insolation flux $S_d$	$S_{\oplus}$	$7.07^{+0.34}_{-0.32}$	...
Equilibrium temperature $T_{eq,d}$ (albedo = 0.3)	K	420	...
Equilibrium temperature $T_{eq,d}$ (albedo = 0.5)	K	380	...
<hr/>			
<i>System parameters</i>			
Kepler/K2 quadratic limb-darkening $q_{1,Kepler}$	-	$0.38^{+0.22}_{-0.13}$	Unif(0, 1)
Kepler/K2 quadratic limb-darkening $q_{2,Kepler}$	-	$0.56^{+0.24}_{-0.18}$	Unif(0, 1)
K2 Campaign 13 normalized baseline offset	ppm	$0.7^{+2.9}_{-3.0}$	Unif(-1000, 1000)
K2 Campaign 13 photometric white noise amp.	ppm	$53.9 \pm 1.8$	ModJeffreys(1, 1000, 0)

Table 3.3: K2-136 transit and planetary parameters

Parameter	Unit	This Paper	Priors
<hr/>			
<i>Planet b</i>			
Period $P_b$	day	$7.97520 \pm 0.00079$	Normal(7.97529, 0.00080) <sup>1</sup>
Time of transit $t_{0,b}$	BJD-2450000	$7817.7563^{+0.0046}_{-0.0048}$	Normal(7817.7563, 0.0048) <sup>1</sup>
Semi-amplitude $K_b$	$\text{m s}^{-1}$	$< 1.2^2, < 1.7^3$	Unif(0.001, 20)
Eccentricity $e_b$	-	$0.14^{+0.12}_{-0.11} (< 0.21^2, < 0.32^3)$	d, e
Argument of periastron $\omega_b$	degrees	$189^{+82}_{-132}$	d, e
Mass $M_b$	$M_{\oplus}$	$< 2.9^2, < 4.3^3$	...
<hr/>			
<i>Planet c</i>			
Period $P_c$	day	$17.30713 \pm 0.00027$	Normal(17.30714, 0.00027) <sup>1</sup>
Time of transit $t_{0,c}$	BJD-2450000	$7812.71770^{+0.00086}_{-0.00085}$	Normal(7812.71770, 0.00089) <sup>1</sup>
Semi-amplitude $K_c$	$\text{m s}^{-1}$	$5.49^{+0.54}_{-0.52}$	Unif(0.001, 20)
Eccentricity $e_c$	-	$0.047^{+0.062}_{-0.034} (< 0.074^2, < 0.16^3)$	d
Argument of periastron $\omega_c$	degrees	$124 \pm 99$	d
Mass $M_c$	$M_{\oplus}$	$18.1^{+1.9}_{-1.8}$	...
<hr/>			
<i>Planet d</i>			

<sup>1</sup>Mann et al. (2018)

<sup>2</sup>68% confidence limit

<sup>3</sup>95% confidence limit

<sup>4</sup>Unif(-1, 1) on  $\sqrt{e} \sin \omega$  and  $\sqrt{e} \cos \omega$ . See Eastman et al. (2013).

<sup>5</sup>K2-136b and K2-136d had additional eccentricity prior upper limits of 0.35 and 0.37, respectively; see Section 3.4.



Period $P_d$	day	$25.5750^{+0.0024}_{-0.0023}$	Normal( $25.5751, 0.0024$ ) <sup>1</sup>
Time of transit $t_{0,d}$	BJD-2450000	$7780.8117 \pm 0.0065$	Normal( $7780.8116, 0.0065$ ) <sup>1</sup>
Semi-amplitude $K_d$	m s <sup>-1</sup>	$< 0.36^2, < 0.78^3$	Unif(0.001, 20)
Eccentricity $e_d$	-	$0.071^{+0.063}_{-0.049}$ ( $< 0.10^2, < 0.16^3$ )	d, e
Argument of periastron $\omega_d$	degrees	$280^{+130}_{-110}$	d, e
Mass $M_d$	$M_{\oplus}$	$< 1.3^2, < 3.0^3$	...
<hr/> <i>System and GP parameters</i>			
RV slope	m s <sup>-1</sup> yr <sup>-1</sup>	$0.1 \pm 2.5$	Unif(-365, 365)
HARPS-N RV white noise amp.	m s <sup>-1</sup>	$0.83 \pm 0.52$	Unif(0, 20)
ESPRESSO RV white noise amp.	m s <sup>-1</sup>	$1.57^{+0.73}_{-0.62}$	Unif(0, 20)
HARPS-N RV offset amp.	m s <sup>-1</sup>	$39503.7^{+2.1}_{-1.9}$	Unif(39450, 39550)
ESPRESSO RV offset amp.	m s <sup>-1</sup>	$39494.7^{+3.5}_{-3.6}$	Unif(39450, 39550)
GP RV conv. blueshift amp. $V_c$	m s <sup>-1</sup>	$3.5^{+2.2}_{-1.2}$	Unif(0, 100)
GP RV rot. modulation amp. $V_r$	m s <sup>-1</sup>	$22.0^{+12.9}_{-8.0}$	Unif(0, 100)
GP stellar rotation period $P_*$	day	$13.37^{+0.13}_{-0.17}$	Unif(1, 20)
GP inverse harmonic complexity $\lambda_p$	...	$0.75^{+0.23}_{-0.16}$	Unif(0.1, 3)
GP evolution time-scale $\lambda_e$	day	$48^{+19}_{-11}$	Unif(1, 200)

Table 3.4: K2-136 RV model parameters

## Parameter estimation

We conducted parameter estimation of our model with the observed data using the Bayesian inference tool **MultiNest** (Feroz et al. 2009; Feroz et al. 2019). We set **MultiNest** to constant efficiency mode, importance nested sampling mode, and multimodal mode. We used a sampling efficiency of 0.01, 1000 live points, and an evidence tolerance of 0.1. Constant efficiency is typically off, but we turned it on since it allows for better exploration of parameter space in higher-dimensional models such as our own. Further, sampling efficiency is usually set to 0.8 and the number of live points is usually set to 400. Decreasing sampling efficiency and increasing the number of live points leads to more complete coverage of parameter space, at the cost of a typically longer simulation convergence time. Finally, the evidence tolerance is usually set to 0.8; reducing the evidence tolerance causes the simulation to run longer but increases confidence that the simulation has fully converged. In other words, the standard

Table 3.5: Model Evidence Comparisons for K2-136 Planet Configurations

Planets in model	$\Delta \log_{10}(\text{evidence})$	Interpretation
c	0	-
b,c	-1.10	Strongly disfavored
c,d	-2.06	Strongly disfavored
b,c,d	-3.23	Excluded
-	-5.54	Excluded
d	-7.00	Excluded
b	-7.78	Excluded
b,d	-9.17	Excluded

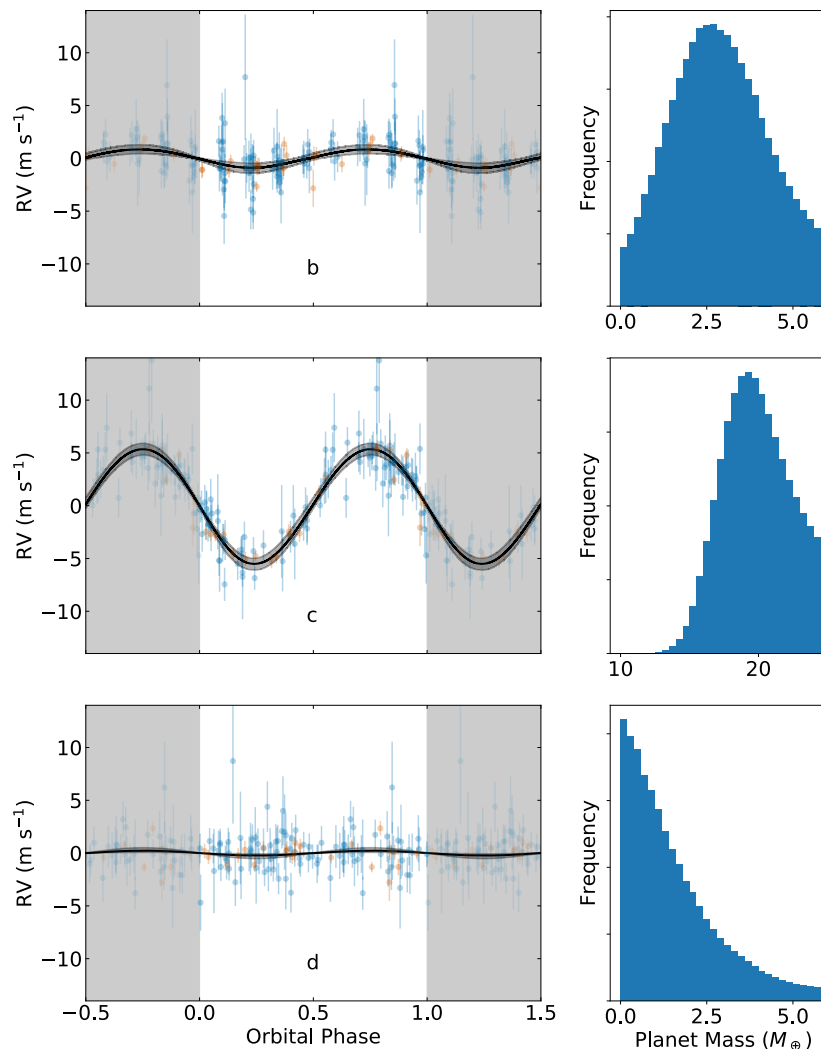


Figure 3.5: Left: Phased RV plots for all three K2-136 planets. For each subplot, we used our best fit model parameters to remove stellar activity and the presence of the other two planets. In each subplot, blue data points (HARPS-N) and orange data points (ESPRESSO) are unbinned RV observations. The black line is the median fit and the gray region around that line is the  $1\sigma$  confidence interval. Right: Posterior mass distribution plots for all three K2-136 planets. It is visually apparent that while there is a strong mass detection for K2-136c ( $R_p = 3.00 \pm 0.13 R_{\oplus}$ ), there is at best only a marginal detection for K2-136b ( $R_p = 1.014 \pm 0.050 R_{\oplus}$ ) and no evidence of a detection for K2-136d ( $R_p = 1.565 \pm 0.077 R_{\oplus}$ ). Therefore, we report only place upper limits on the masses of K2-136b and K2-136d (see Table 3.4).

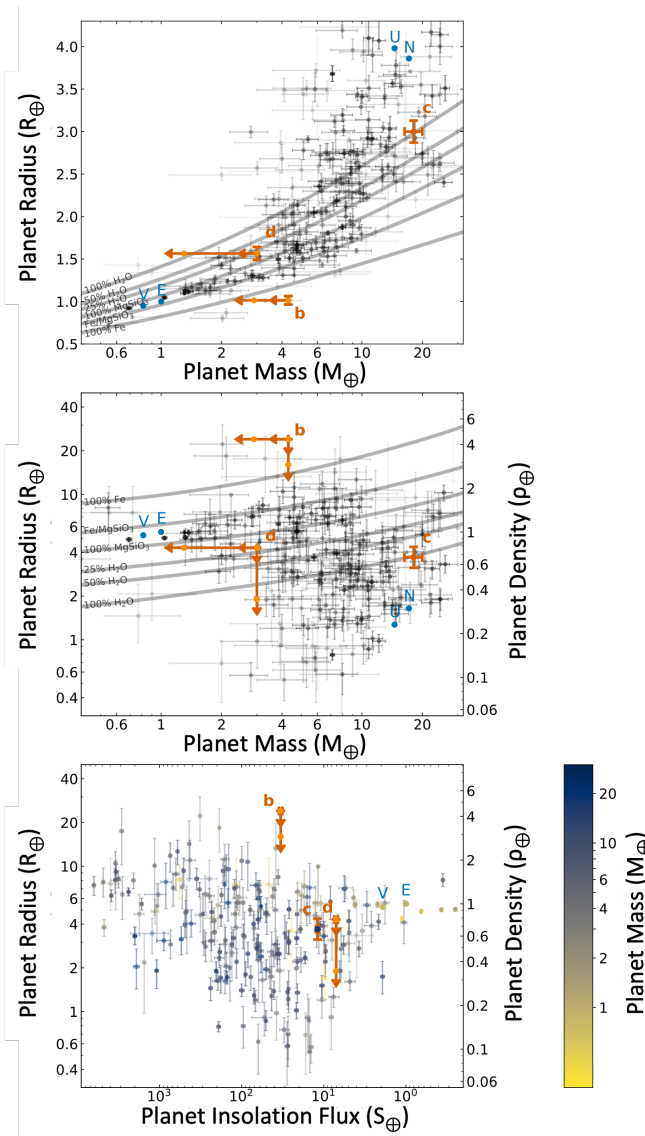


Figure 3.6: Top: mass-radius diagram of transiting planets with fractional mass and radius uncertainties less than 50%. K2-136b, c, and d are plotted in dark orange, with mass uncertainties on K2-136b and d as 68% and 95% upper limits denoted in light orange. Data collected from the NASA Exoplanet Archive (accessed 2023 Mar 22). Venus, Earth, Uranus, and Neptune are also labeled and plotted in blue for reference. Except for the K2-136 system, planets with larger fractional mass and radius uncertainties are fainter. Gray lines correspond to planetary compositions (from top to bottom) of 100% H<sub>2</sub>O, 50% H<sub>2</sub>O, 25% H<sub>2</sub>O, 100% MgSiO<sub>3</sub>, 50% MgSiO<sub>3</sub> + 50% Fe, and 100% Fe, respectively (Zeng and Sasselov 2013; Zeng et al. 2016b). Kepler-136c lies closest to the 100% H<sub>2</sub>O composition line, and is similar in mass to Uranus and Neptune although smaller and much more dense. Middle: the same sample plotted in mass versus planet density, with the same solar system references and composition lines (order inverted from top panel). Bottom: the same sample plotted in planet insolation flux versus planet density, with the color of all data points (except K2-136b and d) corresponding to planet mass.

`MultiNest` settings would likely lead to reliable results, but our choice of settings increases the trustworthiness of our parameter estimation and model evidence results.

## Model Evidence Comparison

One of the strengths of `MultiNest` is that it automatically calculates the Bayesian evidence of the selected model, making model comparison very easy. We compared the model evidence of eight different models (RV only, no photometry), based on all possible combinations of planets b, c, and d. The results of our model comparisons are listed in Table 3.5. We find that the most preferred model is the one that contains only planet c, and not planets b or d. In fact, using the Bayes factor interpretation of Kass and Raftery (1995), we find that almost every other combination of planets can be decisively ruled out (i.e. the Bayes factor of the planet c model to any other model is  $> 100$ ). The only exceptions are the model with planets b and c and the model with planets c and d, which are only strongly disfavored. This tells us that neither K2-136b nor K2-136d are unambiguously detected, so including either in the model quickly worsens the model evidence. However, it is notable that the model with planets b and c is better than the model with planets c and d, and is nearly in the more likely “Disfavored” category rather than “Strongly disfavored”. This makes sense, as K2-136b (unlike K2-136d) has a non-zero peak in its semi-amplitude posterior distribution (see Fig. 3.5). In fact, although only upper limits are reported for the mass of K2-136b in Table 3.4, the median mass is actually non-zero at the  $2.0\sigma$  level ( $M_b = 2.4 \pm 1.2 M_\oplus$ ).

Our results tell us that we can be confident that K2-136c has been detected in our observations. In contrast, the RV signals of K2-136b and K2-136d fall below the threshold of detection, at least given the quantity and quality of our specific data set. Continued radial velocity monitoring, particularly with high precision instruments and facilities may be able to measure their masses, especially K2-136b (which appears to already be near the threshold of detection with our current data set).

Although the model with only K2-136c is the most favored, we still use a model with all three planets as our canonical model for parameter estimation for three reasons. First, we already know from transit photometry that planets b and d exist. Accordingly, the goal of the model comparison exercise described above is not to question the existence of these planets but to examine whether the RV signals from each planet can be detected in our data set. By adopting the three-planet model, we incorporate the uncertainties introduced by the unknown masses and eccentricities of planets b and d. Second, using the three-planet model allows us to determine upper limits for the masses of planets b and d, which is useful for constraining planet compositions and providing guidance for any future attempts to constrain the mass of either planet. Third, both models agree very closely: all parameters are consistent at  $1\sigma$  or less, and all uncertainties on parameters are similar in scale. For the RV semi-amplitude of K2-136c, our key parameter of interest, our canonical model returned  $K_c = 5.49_{-0.52}^{+0.54}$  m s<sup>-1</sup> while the one-planet model returned  $K_c = 5.17_{-0.51}^{+0.56}$  m s<sup>-1</sup>.

## Model Reliability Tests

In order to rigorously assess the accuracy of our results, we conducted tests to analyze different components of our model. Specifically, we removed the GP portion of the model, and we also injected and recovered synthetic planets into the system to compare input and output RV semi-amplitudes.

For our test models we chose not to include planets b and d, as well as photometry, and we then compared against the model with only K2-136c (hereafter referred to as the “one-planet reference model”) rather than the three-planet model; this is despite already selecting the three-planet model as the canonical model to report our results (see Section 3.4). This was done for a few reasons. First, the one-planet model is the preferred model according to the Bayesian evidences, so it is a reasonable point of comparison. Second, as stated earlier, the one-planet reference model and the three-planet model agree very closely. Therefore, any test model parameters found to be highly consistent with the one-planet reference model results will also be highly consistent with the three-planet model results. Third, as a practical matter, including only K2-136c in our test models significantly reduced computational complexity, allowing us to test a wider variety of models.

### No GP

GPs are very versatile and can fit highly variable and correlated signals. Therefore, it is reasonable to ask whether a GP may, in the process of modeling stellar activity, “steal” part of the RV signal from a planet due to overfitting of the data. In order to address these concerns, we ran a model without a GP, and no alternative method to handle stellar activity. We found the resulting parameters were broadly consistent. The noise parameters for each data type in the no-GP model were notably larger, but that is to be expected given no mitigation of the stellar activity. All other parameters agreed with the one-planet reference model parameters to within  $1\sigma$ ; for the RV semi-amplitude of K2-136c, we determined a value of  $K_c = 5.92_{-0.91}^{+0.89} \text{ m s}^{-1}$  (compared to  $K_c = 5.17_{-0.51}^{+0.56} \text{ m s}^{-1}$  for the one-planet reference model). Finally, it is worth noting we also found that  $\Delta \log_{10}(\text{evidence}) = -18.1$  compared to the one-planet reference model, decisively ruling out the no-GP model (Kass and Raftery 1995). In other words, a GP accounts for the stellar activity satisfactorily, whereas ignoring stellar activity is clearly insufficient.

### Synthetic Planet Injections

We also conducted planet injection tests to determine how robustly we could recover the injected signals. Accurate recovery of such signals builds confidence in the accuracy of the RV signal recovered for K2-136c as well as the upper limits placed on K2-136b and K2-136d.

We ran four separate tests in which we injected a  $5.5 \text{ m s}^{-1}$  RV signal of a planet on a circular orbit with a period of 4, 12, 20, and 28 days.  $5.5 \text{ m s}^{-1}$  was chosen because it is approximately the same semi-amplitude as the signal induced by K2-136c, allowing us to directly test our confidence in the recovered RV signal of K2-136c specifically. Our set of

orbital periods was selected in order to 1) span the range of known periodic signals in the system (the orbital period of the three known planets and the stellar rotation period), 2) avoid close proximity to those signals (none are within 1.5 days of the injected signals), and 3) be equally spaced in order to uniformly test the encompassed period range.

All four of the recovered signals agree with the injected signal of  $5.5 \text{ m s}^{-1}$  to within  $1\sigma$ . In all four tests, the recovered signal of K2-136c also agrees with our one-planet reference model ( $K_c = 5.28 \pm 0.56 \text{ m s}^{-1}$ ) within  $1\sigma$ , lending further confidence to our results.

## High-Energy Observations

### *HST* NUV observations

To compare the UV quiescent activity of K2-136 with other K stars Hyades members, we measured the surface flux of the Mg II h ( $2796.35 \text{ \AA}$ ) and k ( $2808.53 \text{ \AA}$ ) lines. The Mg II lines are the strongest emission lines in the NUV and correlate strongly with the chromospheric activity of the star. For accurate emission measurements, we subtracted the NUV continuum by fitting the data outside of the Mg II integration region using the `astropy` module `specutils`. We then integrated over  $2792.0 - 2807.0 \text{ \AA}$  to measure the Mg II emission flux. To convert from observed flux to surface flux, we estimated the radii of the stars using the relationships between age, effective temperature, and radius given by Baraffe et al. (2015), except for K2-136, where we use the radius reported in this work.

Figure 3.7 shows the Mg II surface flux as a function of the rotation period for K2-136 and 13 other observed K star members of the Hyades from GO-15091. K2-136 has a surface Mg II flux of  $(8.32 \pm 0.17) \times 10^5 \text{ erg s}^{-1} \text{ cm}^{-2}$ , whereas the median of the sample is  $(9.66 \pm 0.24) \times 10^5 \text{ erg s}^{-1} \text{ cm}^{-2}$ .

Additionally, Richey-Yowell et al. (2019) measured the NUV flux densities of 97 K stars in the Hyades using archival data from the *Galaxy Evolution Explorer*, *GALEX* (Martin et al. 2005). The median NUV flux density of their sample of Hyades stars at a normalized distance of 10 pc was  $1.89 \times 10^3 \mu\text{Jy}$ . We measure a *GALEX* NUV magnitude for K2-136 of 19.51 mag, which corresponds to a flux density at 10 pc of  $1.52 \times 10^3 \mu\text{Jy}$ , well within the interquartiles of the total sample from Richey-Yowell et al. (2019).

### X-ray observations

We detected a total of 800 EPIC counts for K2-136 in the XMM observation and can therefore extract an X-ray spectrum for the star. We used a one-temperature APEC model to fit the spectrum, which is appropriate for representing the hot plasma in stellar coronae. We combined this model with the ISM absorption model `tbabs` using photoelectric cross-section from Balucinska-Church and McCammon (1992) to account for the neutral hydrogen column density  $N_{\text{H}}$ . We set  $N_{\text{H}}$  to  $5.5 \times 10^{18} \text{ cm}^{-2}$ , derived using  $E(B - V) = 0.001$  for Hyades (Taylor 2006),  $R_V = 3.1$ , and the relation  $N_{\text{H}}[\text{cm}^{-2}/A_v] = 1.79 \times 10^{21}$  (Predehl and Schmitt 1995); allowing  $N_{\text{H}}$  to float did not improve the fit. The spectra for each of the three XMM

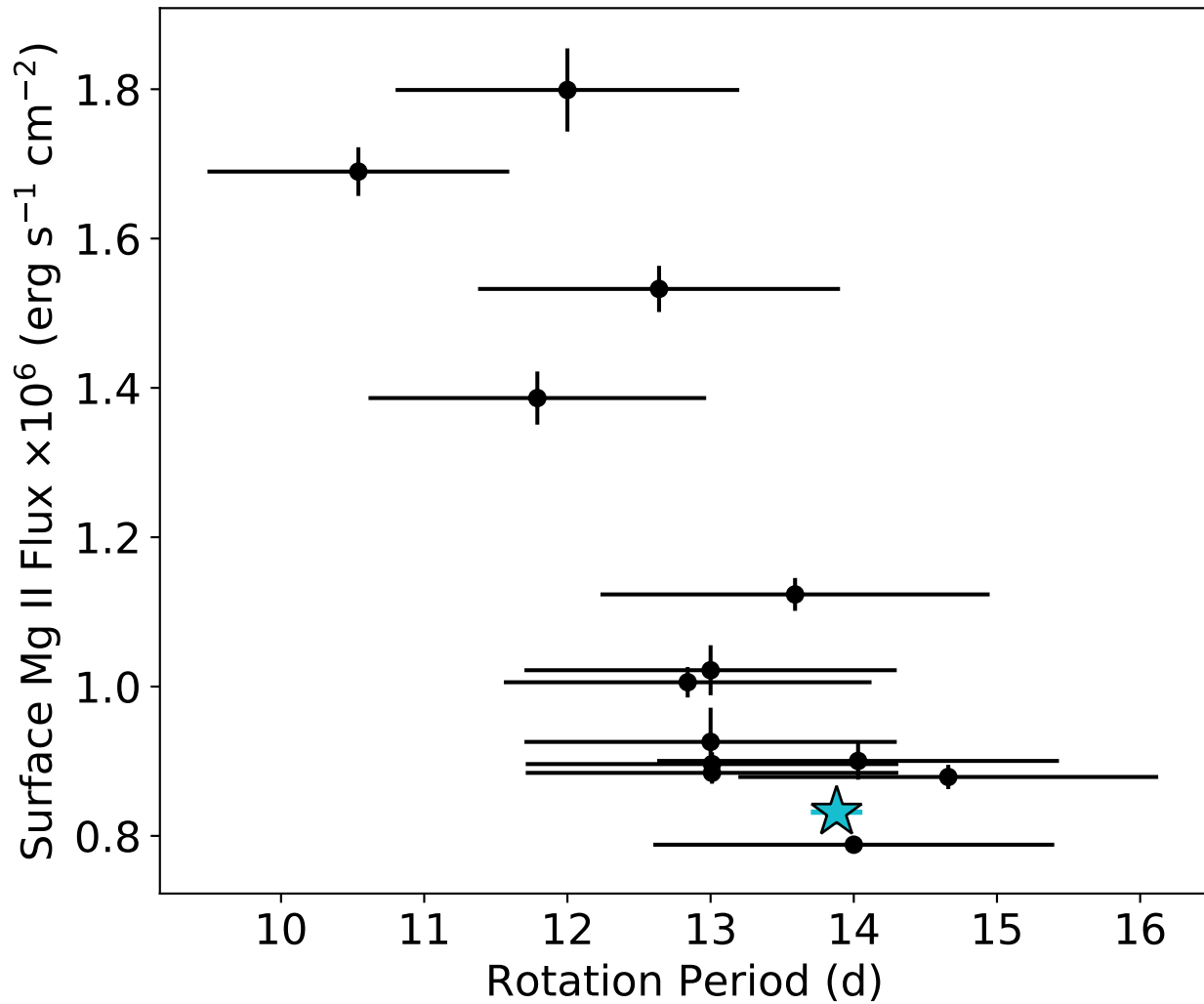


Figure 3.7: Mg II surface flux as a function of stellar rotation period for K star Hyades members. The blue star represents K2-136, and the black points are the 13 other K star Hyades observed in a broader HST program (GO-15091, PI: Agüeros). The rotation periods are from Douglas et al. (2019) and have assumed errors of 10%, except for K2-136, which we determined to be  $13.88^{+0.17}_{-0.18}$  d in this work. K2-136 does not show any distinct chromospheric activity or unique rotation period compared to the rest of the sample.

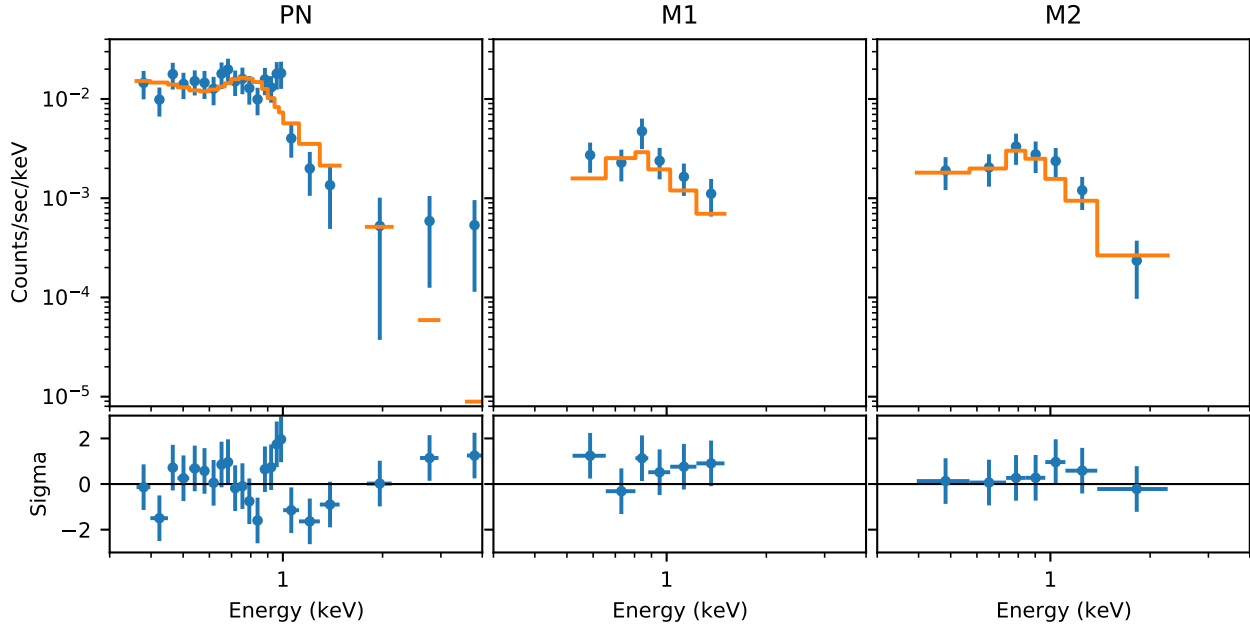


Figure 3.8: X-ray spectra of K2-136 from the XMM pn (left panel), MOS1 (center), and MOS2 (right) EPIC cameras. X-ray counts are binned by 20 in the pn camera, and 15 in the MOS cameras. The orange lines are the best fits using a one-temperature APEC model and assuming a fixed neutral hydrogen column density of  $5.5 \times 10^{18} \text{ cm}^{-2}$ , typical for Hyads (see Sec. 3.4). The residuals of each fit are shown in the bottom panels. The best-fit parameters are presented in Table 3.6.

cameras are shown in Figure 3.8 and the best-fit parameters, which are obtained from a simultaneous fit to the three, are provided in Table 3.6.

Using the total EPIC energy flux from the spectral best fit, we obtained an X-ray luminosity  $L_X = (1.26 \pm 0.19) \times 10^{28} \text{ erg s}^{-1}$  and  $L_X/L_* = (1.97 \pm 0.30) \times 10^{-5}$  (0.1 – 2.4 keV energy range). These values are within  $1\sigma$  of those found by Fernández Fernández and Wheatley (2022) using the same XMM observation<sup>4</sup>. For the sample of 89 K dwarfs with X-ray detections in the Hyades, the median values for  $L_X$  and  $L_X/L_*$  are  $4.5_{-3.3}^{+7.9} \times 10^{28} \text{ erg s}^{-1}$  and  $4.0_{-1.6}^{+20.8} \times 10^{-5}$ , respectively (Núñez et al. 2024). K2-136, therefore, appears somewhat less luminous in X-rays than most of its coeval K dwarf brethren. A narrower comparison, against late-K (K5 and later) dwarf Hyads, shows that the  $L_X$  and  $L_X/L_*$  values for K2-136 are within one standard deviation of the median for that cohort.

In addition to X-ray luminosity, we also estimated extreme ultraviolet (EUV) luminosity using stellar age and Equation 4 from Sanz-Forcada et al. (2011) and found  $L_{\text{EUV}} =$

<sup>4</sup>These authors performed spectral fitting (using a three-temperature APEC model) only to the EPIC pn detection to derive the X-ray energy flux for K2-136.



Table 3.6: X-ray Spectral Fit Parameters of K2-136

Parameter <sup>1</sup>	Value	Unit
Degrees of Freedom	33	
Reduced $\chi^2$	0.91	
Plasma Temperature	$0.65 \pm 0.07$	keV
Plasma Metal Abundance	$0.06 \pm 0.02$	Solar
pn Energy Flux	$3.12 \pm 0.68$	$10^{-14}$ erg s <sup>-1</sup> cm <sup>-2</sup>
MOS1 Energy Flux	$3.01 \pm 0.93$	$10^{-14}$ erg s <sup>-1</sup> cm <sup>-2</sup>
MOS2 Energy Flux	$3.02 \pm 0.88$	$10^{-14}$ erg s <sup>-1</sup> cm <sup>-2</sup>
EPIC <sup>2</sup> Energy Flux	$3.06 \pm 0.46$	$10^{-14}$ erg s <sup>-1</sup> cm <sup>-2</sup>

$(22.6_{-5.7}^{+7.8}) \times 10^{28}$  erg s<sup>-1</sup>. Combining  $L_X$  and  $L_{EUV}$  and using the semi-major axis of K2-136c, we are able to estimate the X-ray and UV flux incident on K2-136c to be  $F_{XUV} = (6.0_{-1.4}^{+2.0}) \times 10^3$  erg s<sup>-1</sup> cm<sup>-2</sup>. Then, using this incident flux value (along with  $M_c$  and  $R_c$ ) we estimate an atmospheric mass loss rate with Equation 1 from Foster et al. (2022). This yields a current atmospheric mass loss rate for K2-136c of  $\dot{M}_c = (3.4_{-0.9}^{+1.3}) \times 10^9$  g s<sup>-1</sup> =  $(17.8_{-5.0}^{+6.7}) \times 10^{-3}$   $M_\oplus$  Gyr<sup>-1</sup>. This rate is based on current values, so the mass loss rate in the past or future may differ. At this current rate, with a H<sub>2</sub>-He envelope mass fraction of  $\sim 5\%$ , it would take  $51_{-16}^{+23}$  Gyr to fully evaporate the atmosphere. Even the 95% lower limit evaporation time is still 28 Gyr, longer than the age of the universe. In other words, in  $\sim 4$  Gyr, when the K2-136 system is as old as the Solar System currently is, we expect K2-136c will have likely only lost 5 – 10% of its current atmosphere.

We also calculated the Rossby number  $R_o$  of K2-136, which is defined as the star’s rotation period  $P_*$  divided by the convective turnover time  $\tau$ . We used the  $(V - K_s)$ -log  $\tau$  empirical relation in Wright et al. 2018 (their equation 5) to obtain  $\tau = 22.3$  d for K2-136. Using our measured  $P_*$  value (see Sec. 3.3) gives  $R_o = 0.6$ . This  $R_o$  puts K2-136 well within the X-ray unsaturated regime, in which the level of magnetic activity decays follows a power slope as a function of  $R_o$ ; see Figure 3 in Wright et al. (2018). For the sample of 51 K dwarf rotators with X-ray detection in the Hyades, the median  $R_o = 0.46_{-0.08}^{+0.06}$  (Núñez et al. 2024), which suggests that the lower levels of X-ray emission from K2-136 relative to its fellow Hyades K dwarfs can be explained by its slower rotation rate.

In conclusion, K2-136 does not appear unusually active in either the NUV or the X-ray relative to its fellow Hyades K dwarfs.

## Considering the Nearby Stellar Companion

As discussed in Section 3.3, prior observations of this system revealed a likely bound M7/8V companion with a projected separation of approximately 40 AU. The presence of a nearby

stellar companion can easily cause a trend in RV observations. We wanted to estimate the range of possible trend amplitudes for our system using some reasonable assumptions. Using the distance of  $58.752^{+0.061}_{-0.072}$  pc from Bailer-Jones et al. (2021) and the projected angular separation of  $0.730 \pm 0.030''$  from adding in quadrature the R.A. and Dec separation components in Ciardi et al. (2018), we found a projected separation of  $42.9 \pm 1.7$  AU. We considered the possibility of additional radial separation by folding in a uniform distribution on radial separation between 0 and twice the median projected separation to estimate an overall separation (this broad range was chosen to include radial separations of approximately the same scale as the projected separation). As an approximation, we treat this overall separation as the semi-major axis.

Next, the stellar companion was reported in Ciardi et al. (2018) to have a spectral type consistent with M7/8 (we were unable to find uncertainties associated with this result, but nearby spectral types were never mentioned). Taking a conservative approach, we assumed a stellar companion mass between  $1 M_{\text{Jup}}$  (for a low-mass brown dwarf) and  $0.2 M_{\odot}$  (for a mid to late M dwarf).

Then, we combined our separation distribution and stellar mass distributions (primary and companion) via Kepler’s Third Law to get a broad orbital period estimate of  $520^{+320}_{-180}$  years. Including a wide range of eccentricities (Unif(0,0.9)), we estimated an RV semi-amplitude of  $490^{+340}_{-320}$  m s<sup>-1</sup>. On the timescale of our observations, this centuries-long sinusoidal signal would manifest as a linear trend, with a maximum (absolute) slope of  $5.3^{+7.5}_{-3.6}$  m s<sup>-1</sup> yr<sup>-1</sup>. This is a very rough estimate with many assumptions, but it serves to demonstrate that a drift of only a few m s<sup>-1</sup> each year or less is very reasonable. Indeed, from our model of the RV data we found an RV trend of  $0.1 \pm 2.5$  m s<sup>-1</sup> yr<sup>-1</sup>, highly consistent with both a zero trend as well as our estimate calculated here.

### 3.5 Results and Discussion

The results of our stellar and planet analyses are listed in Tables 3.1, 3.4, and 3.3. Phase plots of all three planets can be seen in Fig. 3.5. After conducting our analysis and tests, we find that K2-136c has a mass of  $18.1^{+1.9}_{-1.8} M_{\oplus}$  and a radius of  $3.00 \pm 0.13 R_{\oplus}$ . This radius is consistent with and slightly larger than the value estimated in M18 ( $2.91^{+0.11}_{-0.10} R_{\oplus}$ ). This is because we find a stellar radius value slightly larger than M18 (by about 3%).

Using planet mass and radius we find K2-136c has a density of  $3.69^{+0.67}_{-0.56}$  g cm<sup>-3</sup> (or  $0.67^{+0.12}_{-0.10} \rho_{\oplus}$ ). For comparison, Neptune<sup>2</sup> is roughly similar in mass ( $17.15 M_{\oplus}$ ) but larger in radius ( $3.883 R_{\oplus}$ ); as a result, K2-136c is more than twice as dense as Neptune ( $2.25^{+0.41}_{-0.34} \rho_{\text{Neptune}}$ ). Similarly, Uranus<sup>3</sup> is slightly less massive ( $14.54 M_{\oplus}$ ) but still larger in radius ( $4.007 R_{\oplus}$ ); thus, K2-136c is nearly three times as dense as Uranus ( $2.90^{+0.52}_{-0.44} \rho_{\text{Uranus}}$ ). This is visually apparent in Fig. 3.6, which shows K2-136c almost perfectly on the 100% H<sub>2</sub>O composition line. It is important to remember that mass and radius alone do not fully

<sup>2</sup><https://nssdc.gsfc.nasa.gov/planetary/factsheet/neptunefact.html>

<sup>3</sup><https://nssdc.gsfc.nasa.gov/planetary/factsheet/uranusfact.html>

constrain a planet’s composition. Although K2-136c may have a density similar to that of a large ball of water (an unrealistic reference composition), it is also consistent with a gaseous sub-Neptune with a massive core or metal-rich atmosphere.

Unfortunately, it is very difficult to determine compositional properties of a planet without atmospheric characterization, especially sub-Neptunes (since there are no analogs in our own Solar System). On the one hand, sub-Neptunes may include ocean worlds with H<sub>2</sub>O abundance fractions not seen in our Solar System (Mousis et al. 2020). And indeed, water vapor has already likely been detected in the atmosphere of the sub-Neptune exoplanet K2-18b (Benneke et al. 2019b). On the other hand, sub-Neptunes like K2-136c may instead be composed of a rocky, Earth-like core composition, very little water, and an atmosphere close to solar metallicity and thus primarily hydrogen and helium (Benneke et al. 2019a; Van Eylen et al. 2018).

As a valuable point of comparison, there are three confirmed planets that share a similar mass and radius to K2-136c to within 10%: Kepler-276c, Kepler-276d (Xie 2014), and TOI-824b (Burt et al. 2020). The masses of the planets in the Kepler-276 system were measured via transit timing variations (TTVs) in a TTV catalog paper. Unfortunately, because they were characterized alongside so many other systems, there is no discussion regarding the formation or composition of those two specific planets. TOI-824b, however, was characterized in a standalone paper that investigated the nature of the planet thoroughly. Unlike K2-136c, TOI-824b is near the hot-Neptune desert (Mazeh et al. 2016) with a very short orbital period (1.393 d). Despite its proximity to its host star, TOI-824b still retains a H<sub>2</sub>-He atmosphere, which the authors estimate has a mass fraction of  $\geq 2.8\%$ . They hypothesize that the larger than average mass of the planet (compared to planets of a similar radius) helps the planet retain its atmosphere. K2-136c, with a similar mass and radius and a lower insolation flux, would therefore be able to retain a H<sub>2</sub>-He atmosphere even more easily.

We can go further and form a picture of a reasonable composition for K2-136c. We may assume the planet has a rocky core surrounded by a gaseous H<sub>2</sub>-He envelope. Going a step further, we may also assume the rocky core is similar to that of Earth, namely a core-mass fraction (CMF) of 0.325, i.e. a rock-iron composition of 32.5% Fe and 67.5% MgSiO<sub>3</sub> (Seager et al. 2007). Following the theoretical models of Howe et al. (2014), we find that with an Earth-like rocky core and a H<sub>2</sub>-He envelope, the measured mass and radius of K2-136c are most consistent with a H<sub>2</sub>-He mass fraction of  $\sim 5\%$ .

With this rough envelope mass fraction estimate and the measured mass and radius of K2-136c, we wanted to investigate the potential for past or ongoing atmospheric mass loss. After consulting the theoretical models presented in Lopez et al. (2012), Lopez and Fortney (2013), Lopez and Fortney (2014), and Jin et al. (2014), we concluded that if there is any historical or contemporary mass loss for K2-136c, it is minimal: likely somewhere between 0 –  $-10\%$  loss of the H<sub>2</sub>-He envelope across the entire lifespan of the planet.

As suggested in Mann et al. (2016), young planets may be puffier than older planets due to an early-age atmospheric mass loss phase. And yet, K2-136c is not particularly puffy, in fact being notably denser than Uranus or Neptune. However, this planet may indeed have an extended atmosphere but also a lower atmospheric mass fraction than Uranus, Neptune, and

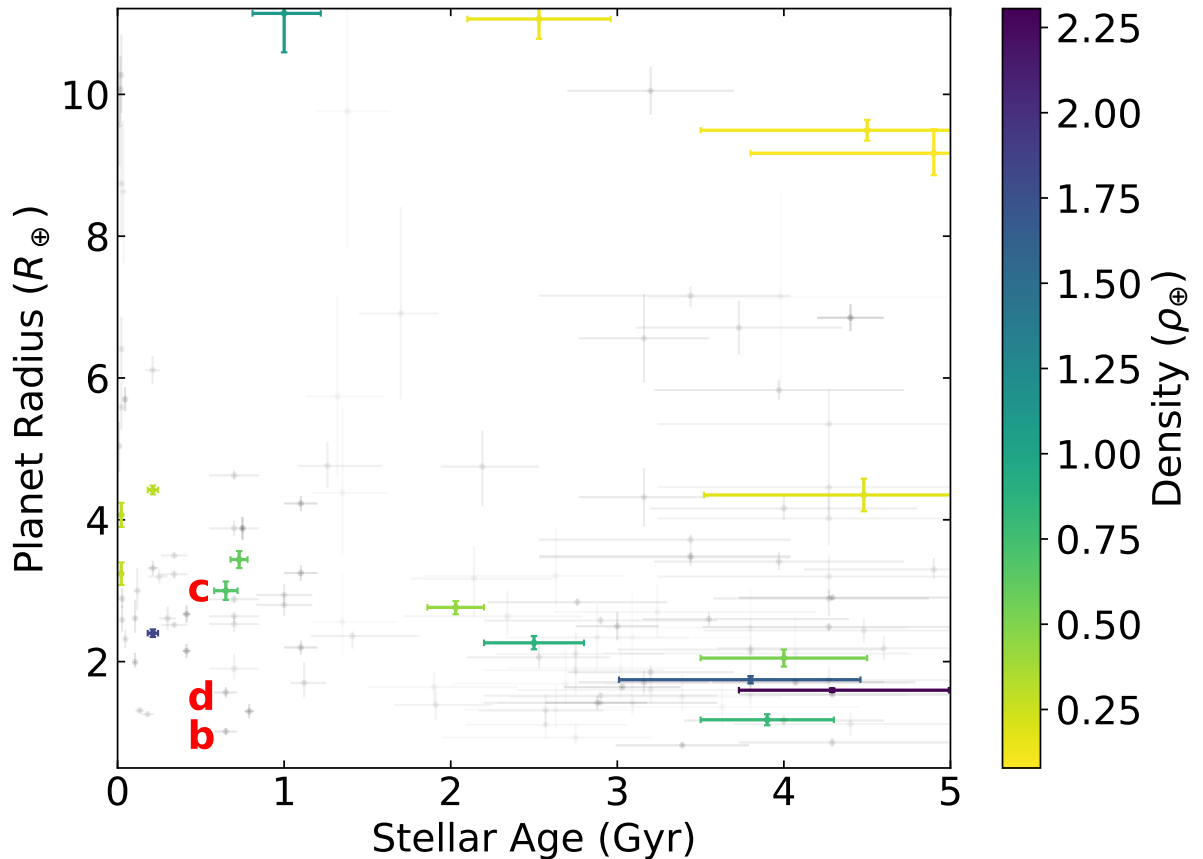


Figure 3.9: Age-radius diagram for all planets smaller than Jupiter, younger than 5 Gyr, and with radius and age uncertainties both smaller than 25%. Data point color corresponds to planet density for planets with mass uncertainties smaller than 25%. Data collected from the NASA Exoplanet Archive (NASA Exoplanet Science Institute 2020), accessed 2023 Mar 22. K2-136b, c, and d are labeled in red to the left of the planet symbol. There are only four planets in this figure with a stellar age younger than K2-136 and a mass measurement better than 25%: AU Mic b and c with stellar age =  $22 \pm 3$  Myr (Mamajek and Bell 2014) and Kepler-411 b and c with stellar age =  $212 \pm 31$  Myr (Sun et al. 2019). The only other plotted planet  $< 1$  Gyr with a mass measurement is the open cluster planet K2-25b (Stefansson et al. 2020), which is slightly larger than K2-136c.

other lower-density planets. In other words, as this system ages, the atmosphere of K2-136c may settle to some extent, reducing the planet radius and increasing planet density. Without atmospheric characterization, further insights into the planet’s composition are very limited.

Bayesian model comparison proved that we could not conclusively detect K2-136b or K2-136d in our data set (see Fig. 3.5). Even so, we also conduct similar analyses for K2-136b and K2-136d in order to report upper mass limits and corresponding upper density limits. With 95% confidence, K2-136b is no denser than  $24 \text{ g cm}^{-3}$  (a largely unhelpful limit, since that would be much more dense than pure iron) and K2-136d is no denser than  $4.3 \text{ g cm}^{-3}$ , corresponding to semi-amplitudes of  $1.7 \text{ m s}^{-1}$  and  $0.78 \text{ m s}^{-1}$ , respectively. Referring to Fig. 3.6, we can see that unlike the middle planet K2-136c, the other two planets K2-136b and K2-136d could have a wide variety of densities and compositions. K2-136d could range from a low-density gas planet to Earth composition. K2-136b has an even wider array of possible compositions and theoretically could range from very gaseous to pure iron.

The RV signals of K2-136b and K2-136d may be detectable with more data from next generation spectrographs. K2-136d would be particularly interesting, since its radius places it near the planet radius gap (Fulton et al. 2017). As for K2-136b, the peak of the planet mass posterior distribution is already non-zero, and a marginal detection may already be noted at the  $2.0\sigma$  level ( $2.4 \pm 1.2 M_{\oplus}$ ), suggesting a firm planet mass measurement may be within reach with further observations.

To check this, we followed the mass-radius relationship laid out in Wolfgang et al. (2016) and found predicted masses for K2-136b and K2-136d to be  $1.17_{-0.72}^{+0.79} M_{\oplus}$  and  $4.1_{-1.8}^{+1.9} M_{\oplus}$ , respectively. These correspond to densities of  $7.7_{-4.7}^{+3.7} \text{ g cm}^{-3}$  (i.e.  $1.40_{-0.85}^{+0.66} \rho_{\oplus}$ ) and  $8.4_{-3.7}^{+4.1} \text{ g cm}^{-3}$  (i.e.  $1.52_{-0.66}^{+0.74} \rho_{\oplus}$ ), respectively. We note that these mass and density estimates do not make use of the upper limits determined in this paper. By folding in our stellar mass, orbital period, and eccentricity posteriors as well as the orbital inclinations determined in M18, we found the estimated masses of K2-136b and K2-136d correspond to semi-amplitudes of  $0.5 \pm 0.3 \text{ m s}^{-1}$  and  $1.1 \pm 0.5 \text{ m s}^{-1}$ , respectively. The current RV upper limit on K2-136b ( $1.7 \text{ m s}^{-1}$ ) is much larger than the estimated semi-amplitude and therefore fully consistent. As for K2-136d, we acknowledge that the estimated semi-amplitude is smaller than the upper limit ( $0.80 \text{ m s}^{-1}$ ), which perhaps suggests K2-136d has a density on the lower end of the range predicted from the Wolfgang et al. (2016) relationship.

There are very few young and small exoplanets that also have measured masses. As can be seen in Fig. 3.9, the vast majority of young exoplanets do not have a firm mass measurement. There are some young planets with both robust radius measurements and notable upper mass limits, such as the low-density planet TS Duc A b (Benatti et al. 2021), which can be of interest for follow-up study and comparison. However, according to the NASA Exoplanet Archive (NASA Exoplanet Science Institute 2020), accessed 2023 Mar 12, there are only 13 known planets, excluding K2-136c, with  $R_p < 4 R_{\oplus}$ , a host star age  $< 1$  Gyr, and a mass measurement (not an upper limit): HD 18599b (Desidera et al. 2023), HD 73583b and c (Barragán et al. 2022); K2-25b (Stefansson et al. 2020); L 98-59b, c, and d (Demangeon et al. 2021); Kepler-411b and Kepler-411d (Sun et al. 2019), Kepler-462b (Masuda and Tamayo 2020), Kepler-289b and Kepler-289d (Schmitt et al. 2014), and

K2-100b (Barragán et al. 2019).

K2-136c is now the smallest exoplanet in an open cluster to have a mass measurement. It is also one of the youngest exoplanets to ever have a mass measurement. The only planets with firm age, radius, and mass measurements ( $< 25\%$  uncertainties) known to be younger are AU Mic b and c (Klein et al. 2021) as well as Kepler-411b and d (Sun et al. 2019), as can be seen in Fig. 3.9. In general, measuring the masses of young planets like K2-136c provides an interesting window into the early childhood of planetary systems, allowing us to probe how planet masses and compositions evolve over time.

## Atmospheric Characterization Prospects

To explore the suitability of the K2-136 system planets for atmospheric characterization, we calculated the transmission spectroscopy metric (TSM) defined in Kempton et al. (2018). K2-136c has a TSM of  $32.7^{+4.8}_{-4.1}$ , which is well below the recommended TSM of 90 for  $R_p > 1.5 R_\oplus$ . Because K2-136b and K2-136d have unconstrained masses, we followed Zeng et al. (2016b) and assumed an Earth-like CMF of 0.325 in order to predict planet masses of  $0.85^{+0.27}_{-0.21} M_\oplus$  and  $3.35^{+1.08}_{-0.84} M_\oplus$ , respectively. For K2-136b, this yields a TSM of  $4.20^{+0.42}_{-0.37}$ , well below the recommended TSM of 10 for  $R_p < 1.5 R_\oplus$ . As for K2-136d, its radius of  $R_d = 1.565 \pm 0.077 R_\oplus$  is very near  $1.5 R_\oplus$ , where the TSM metric includes a scale factor that jumps dramatically, thus creating a TSM bimodal distribution. Thus, for  $R_d < 1.5 R_\oplus$  we find a TSM of  $2.36^{+0.15}_{-0.13}$  and for  $R_d > 1.5 R_\oplus$  we find a TSM of  $13.6^{+1.0}_{-1.1}$ . In their respective radius ranges, these values are both well below the recommended TSM, so K2-136d is also probably not a good target for atmospheric characterization.

We also calculated the emission spectroscopy metric (ESM) for K2-136b and K2-136d as defined in Kempton et al. (2018) (the metric applies only to “terrestrial” planets with  $R_p < 1.5 R_\oplus$ , excluding K2-136c). We find K2-136b and K2-136d have ESM metrics of  $0.520^{+0.049}_{-0.047}$  and  $0.342^{+0.043}_{-0.041}$ , respectively, both below the recommended ESM of 7.5 or higher. Therefore, these planets do not appear to be particularly attractive targets for emission spectroscopy or phase curve detection.

The TSM analysis of K2-136c is not very favorable for atmospheric characterization, but we decided to conduct a more thorough transmission spectroscopy analysis. We used the JET tool (Fortenbach and Dressing 2020) to model atmospheric spectra and to simulate the performance of the *JWST* instruments for certain atmospheric scenarios. We opted for the broad wavelength coverage of combining NIRISS SOSS Order 1 ( $0.81 - 2.81 \mu\text{m}$ ) with NIRSpec G395M ( $2.87 - 5.18 \mu\text{m}$ ), as recommended by Batalha and Line (2017) to maximize the spectral information content. A single instrument, the NIRSpec Prism, can also cover this wavelength range, but brightness limits preclude its use here. We assumed pessimistic pre-launch instrumental noise values (Rigby et al. 2023), so a future *JWST* program for atmospheric characterization should outperform our conservative expectations.

The JET tool found that for an optimistic, cloudless, low-metallicity atmosphere (5x solar) we can meet a  $\Delta\text{BIC}$  detection threshold of 10 (corresponding to a  $\sim 3.6\sigma$  detection of the atmosphere compared to a flat line) with 5 free retrieval parameters (i.e. recon level) with

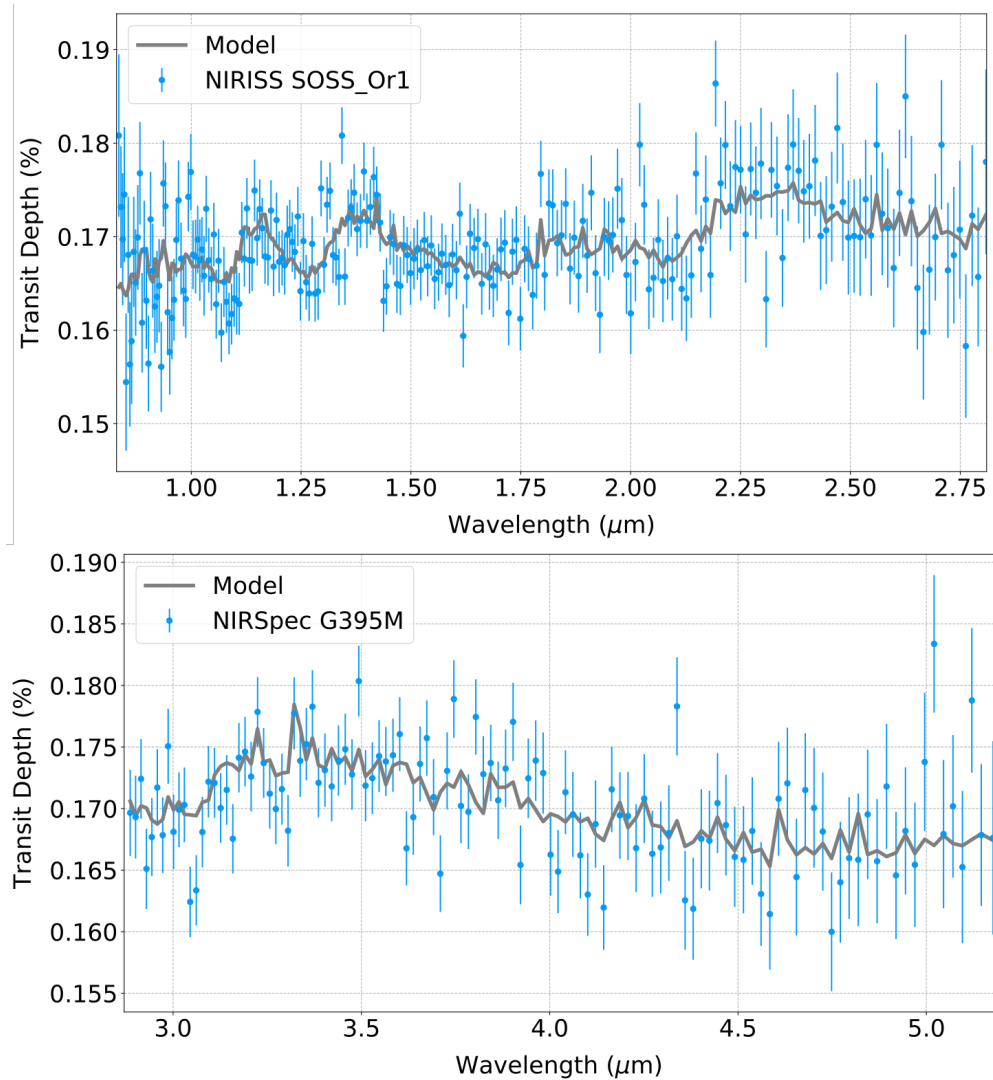


Figure 3.10: Simulation of *JWST* transmission spectra for K2-136c using JET (Fortenbach and Dressing 2020). The top and bottom panels correspond to the NIRISS SOSS-Or1 (0.81 – 2.81  $\mu\text{m}$ ) instrument, and the NIRSpec G395M (2.87 – 5.18  $\mu\text{m}$ ) instrument, respectively. The gray line in both panels is the modeled atmospheric spectrum assuming low metallicity (5x solar) and no clouds, while the blue data points are the simulated instrument spectra for one observed transit with NIRISS SOSS, and two observed transits with NIRSpec G395M, including the effects of photon noise, and instrument systematics.

only one transit for NIRISS SOSS and two transits for NIRSpec G395M. For a less optimistic, higher metallicity atmosphere (100x solar) with clouds at 100 mbar, we can meet the same detection threshold with two transits for NIRISS SOSS and five transits for NIRSpec G395M.

With 10 free retrieval parameters (a more typical number), and with the optimistic atmosphere, we can meet a  $\Delta\text{BIC}$  detection threshold of 10 with only one transit for NIRISS SOSS and three transits for NIRSpec G395M. For the less optimistic atmosphere, we can meet the detection threshold with three transits for NIRISS SOSS, but we show no detection for NIRSpec G395M for up to 50 transits considered. This analysis makes the conservative assumption that the instrument noise floor is not reduced by co-adding transits.

The resulting spectra for the low metallicity, cloudless, case are shown in Fig. 3.10. It seems that atmospheric characterization of K2-136c may be within reach (assuming a relatively low mean molecular weight/low metallicity atmosphere, and low cloud level), but could require a more significant investment of *JWST* resources if the actual atmospheric properties are less favorable.

It should be noted that given the on-sky position of K2-136, the ability to observe the system with *JWST* will be limited due to aperture position angle constraints. In addition, the very close ( $\sim 0.7''$ ) stellar companion may cause contamination of spectra from both instruments. This is a common issue for NIRISS since it is slit-less, but NIRSpec can usually isolate the primary target with its  $1.6''$  square aperture. For K2-136 the companion star is well inside this aperture boundary and will likely create some contamination. The companion is significantly fainter than the host star (J magnitude of 14.1 vs 9.1), which should mitigate the impact to a degree. It should also be possible to reduce the companion M-star's spectral contamination effect in post-processing.

The most enticing feature of K2-136 is the young age of the system; it could be argued that despite the potential difficulty in observing the planets' atmospheres, the rewards outweigh the risks for the chance to better understand the atmospheres of very young, relatively small planets. Observations of this system could help us construct a picture of the environment and evolution of young, low-mass planets.

### 3.6 Summary and Conclusions

In this paper, we analyzed K2-136, a young system in the Hyades open cluster. The star is a K dwarf with  $M_* = 0.742_{-0.038}^{+0.039} M_\odot$  and  $R_* = 0.677 \pm 0.027 R_\odot$ . It hosts three known, transiting planets with periods of 8.0, 17.3, 25.6 days, and radii of  $1.014 \pm 0.050 R_\oplus$ ,  $3.00 \pm 0.13 R_\oplus$ , and  $1.565 \pm 0.077 R_\oplus$ . We gathered RV observations with the TNG HARPS-N spectrograph and ESPRESSO VLT spectrograph in order to measure the masses of the three planets. We find that K2-136c, a sub-Neptune and the middle planet of the system, has a mass of  $18.0_{-1.6}^{+1.7} M_\oplus$ . This corresponds to a density of  $3.69_{-0.56}^{+0.67} \text{ g cm}^{-3}$  (or  $0.67_{-0.10}^{+0.12} \rho_\oplus$ ). K2-136c is thus similar in mass to Neptune and Uranus but more than twice as dense as Neptune and nearly three times as dense as Uranus. K2-136c has a density consistent with an ocean world; a rocky, Earth-like core with solar metallicity atmosphere; and many other compositions. However,



assuming an Earth-like rocky core and a H<sub>2</sub>-He envelope yields a H<sub>2</sub>-He mass fraction of  $\sim 5\%$ . K2-136b and K2-136d have RV signals too small to detect with our data set, but we have placed upper mass limits with 95% confidence of 4.3 and 3.0 M<sub>⊕</sub>, respectively. Atmospheric characterization of K2-136c (or its siblings, if a firm mass measurement can be made), would be difficult but not necessarily unfeasible, and is the most practical way to narrow the compositional parameter space for these planets.

K2-136c is the smallest planet in an open cluster to have a mass measurement, and one of the youngest planets found to date smaller than Neptune. There are very few young planets with precise mass measurements, and even fewer as small as K2-136c. As a result, this system provides an important view of planet composition and evolution at ages that are relatively unexplored.

## Chapter 4

# Detecting and Validating New Short-Period *TESS* Planets with TATER and TRICERATOPS

The Transiting Exoplanet Survey Satellite (*TESS*) has thus far detected hundreds of transiting exoplanets orbiting bright stars. We collected and analyzed 2-min and 20-sec cadence *TESS* Cycle 3 photometry of 914 host stars with known planets and candidates, exploring this and any additional Cycle 1 and 5 photometry to detect, vet, and validate new exoplanets. We developed the TATER planet detection pipeline to search for new planets. Using TATER we were able to detect 1814 threshold crossing events (TCEs, i.e. potential planetary transit signals) and recovered 89% of the previously detected *TESS* Objects of Interest (TOIs) in the Cycle 3 photometry. We vetted our TCEs using the LEO-*vetter* vetting package (Kunitomo 2024). Of the remaining TOIs we could not detect, only 13% are confirmed planets, while 83% are planet candidates and 4% have been identified as false positives. Finally, we subjected all identified candidates to statistical validation using the TRICERATOPS package (Giacalone and Dressing 2020; Giacalone et al. 2021) and validated 13 as planets. Of these, 4 are newly validated planets. Ranging in size from super-Earth to sub-Jovian ( $2.39 - 8.8 R_{\oplus}$ ), our 4 new validated planets have relatively short orbital periods ( $1.04 - 5.31$  d). Each of these 4 newly validated planets had been detected as solitary planet candidates in previous *TESS* sectors, and are still the only known planet in their respective systems. This work expands the known planet population and provides follow-up research and validation opportunities for these newly validated planets.

### 4.1 Introduction

To date, more than 5600 exoplanets have been detected, and over 40% of those planets are known to reside in multiplanet systems, according to the NASA Exoplanet Archive (NASA Exoplanet Science Institute 2020), accessed 15 Apr 2024. In fact, planets orbiting hot stars

( $T_{\text{eff}} > 6500$  K) have an average of 0.8 planetary siblings and planets orbiting cool stars ( $T_{\text{eff}} < 5000$  K) have an even higher average of 1.8 planetary siblings (Yang et al. 2020). The NASA Exoplanet Archive (accessed 15 Apr 2024) also reports a total of 948 multiplanet systems have been detected to date, comprising 2390 planets. Just as studying the properties of other bodies within our solar system informs our understanding of Earth’s history, the detection of multiple planets around other stars increases our ability to accurately situate exoplanets within the broader context of their environments. This advantage is particularly pronounced for systems of multiple transiting planets in which the radii, orbital periods, eccentricities, masses, bulk densities, and perhaps even atmospheric compositions can be studied in tandem.

The *TESS* mission (Ricker et al. 2015), a space-based, wide-field, all-sky planet hunting probe, has been crucial for detecting exoplanets that are amenable to follow-up observations. We analyzed high-cadence, 20-s photometry from *TESS* Cycle 3 (and Cycles 1 and 5 when available) in order to detect new planet candidates in known planetary systems. Of the known planets in multiplanet systems, the Kepler mission was responsible for detecting more than half: 1317 planets in 525 multiplanet systems, or  $\sim 55\%$  of all detected planets in multiplanet systems (NASA Exoplanet Archive, accessed 15 Apr 2024); by comparison, *TESS* has only detected 190 planets ( $\sim 8\%$  of total) in 95 multiplanet systems. However, the median visual brightness for the multiplanet hosts observed by Kepler was  $V = 14.6 \pm 1.4$  while for *TESS* it was  $V = 10.6 \pm 2.0$ , a full four magnitudes brighter on average. In other words, although the *TESS* mission has found far fewer planets in multiplanet systems, operating as an all-sky survey mission has allowed *TESS* to detect planets orbiting much brighter host stars that are far more amenable to follow-up observations including radial velocities (RVs) to measure planet masses and transmission spectroscopy to study planet atmospheres.

We collected high cadence photometry in Cycle 3 of *TESS* to detect new planet transit signals, which we then assess via planetary vetting tests followed by statistical validation. Planetary transits can be very short, shallow, and difficult to detect; transit signals can be made even more difficult to detect by photometric noise and activity from the host star. Further, certain astrophysical phenomena, especially eclipsing binary stars, can mimic and be easily confused with exoplanet transits (Morton et al. 2016). Therefore, detections of planet transits must be subjected to a suite of tests and analyses to distinguish true positives from false positives. For example, particular multi-star architectures can be photometrically indistinguishable from planet transits, such as an eclipsing binary with a nearby or bound star at small visual separation to wash out and minimize otherwise conspicuously deep binary occultations (Ciardi et al. 2015; Morton et al. 2016). As a result, it is crucial to subject planet candidates to either mass measurement or statistical validation, quantitatively assessing the likelihood of the transiting planet scenario in comparison to multiple false positive scenarios including eclipsing binaries.

We subject our target sample to a systematic planet transit search. Each planet signal we detect in *TESS* photometry is subjected to candidate vetting with the *LEO-vetter* Python package (Kunimoto 2024) and planet validation with the *TRICERATOPS* Python package (Giacalone and Dressing 2020; Giacalone et al. 2021) to determine which signals can be

upgraded to planet candidate and potentially fully validated as a planet.

In Section 4.2, we detail the observations collected for this work. Then, in Section 4.3, we explain our stellar parameter compilation procedure. Next, in Section 4.4, we present the TATER pipeline and our full strategy for planet signal detection and authentication. Then we present and discuss our results in Section 4.5. Finally, we summarize and conclude in Section 4.6.

## 4.2 Sample & Observations

Our sample comprises 914 target stars proposed for observations by *TESS* during Cycle 3 and collected through *TESS* Guest Investigator Program G03278 (PI: A. Mayo). We constructed our target list by querying the NASA Exoplanet Archive (NASA Exoplanet Science Institute 2020) and ExoFOP<sup>1</sup> to identify all known, transiting planets as well as all K2 and *TESS* planet candidates. We also constrained all planets and planet candidates to be smaller than  $20 R_{\oplus}$  to exclude likely false positives while retaining inflated Jupiters. We then used the WebTESSViewing Tool (now the *TESS*-point Web Tool<sup>2</sup>) provided by the *TESS* Guest Investigator Office to identify the subset of systems observable during Cycle 3 (Sectors 27 – 39).

All of our target stars already have at least one known planet or planet candidate. A detailed breakdown of our sample is shown in Fig. 4.1. From tables of stellar properties on the Mikulski Archive for Space Telescopes (MAST), ExoFOP-*TESS*, and the NASA Exoplanet Archive (see Section 4.3), we found that our host stars have a median radius of  $1.1^{+4.8}_{-0.8} R_{\odot}$  (95% confidence interval) and a median  $T_{\text{mag}}$  brightness of  $10.7^{+4.0}_{-3.1}$  (95% confidence interval). A total of 7% of our sample (65 systems) already had 2 or more known, transiting planets. As can be seen in Fig. 4.1, known planets in our sample had relatively short orbital periods ( $4.5^{+9.9}_{-2.9}$  d) but spanned a large range of radii ( $5.8^{+8.4}_{-3.7} R_{\oplus}$ ).

Observations were collected by the *TESS* mission during Cycle 3 (4 July 2020 to 6 June 2021). 61% of our targets were observed for a single sector in Cycle 3 and 16% were observed for two sectors. Only 13% were observed for more than half of Cycle 3 (7+ sectors) and only 4% were in the continuous viewing zone and observed for all 13 sectors of Cycle 3. All observations of our sample targets were collected at 20-s cadence.

## 4.3 Stellar Characterization

We compiled stellar characteristics for our target sample by retrieving  $M_*$ ,  $R_*$ ,  $T_{\text{eff}}$ ,  $\log(g)$ , and  $[\text{Fe}/\text{H}]$  from the MAST data archive operated by the Space Telescope Science Institute (STScI), specifically the *TESS* Science Processing Operations Center (SPOC) data products.

<sup>1</sup><https://exofop.ipac.caltech.edu/tess/>

<sup>2</sup>[https://heasarc.gsfc.nasa.gov/wsgi-scripts/TESS/TESS-point\\_Web\\_Tool/TESS-point\\_Web\\_Tool/wtv\\_v2.0.py/](https://heasarc.gsfc.nasa.gov/wsgi-scripts/TESS/TESS-point_Web_Tool/TESS-point_Web_Tool/wtv_v2.0.py/)

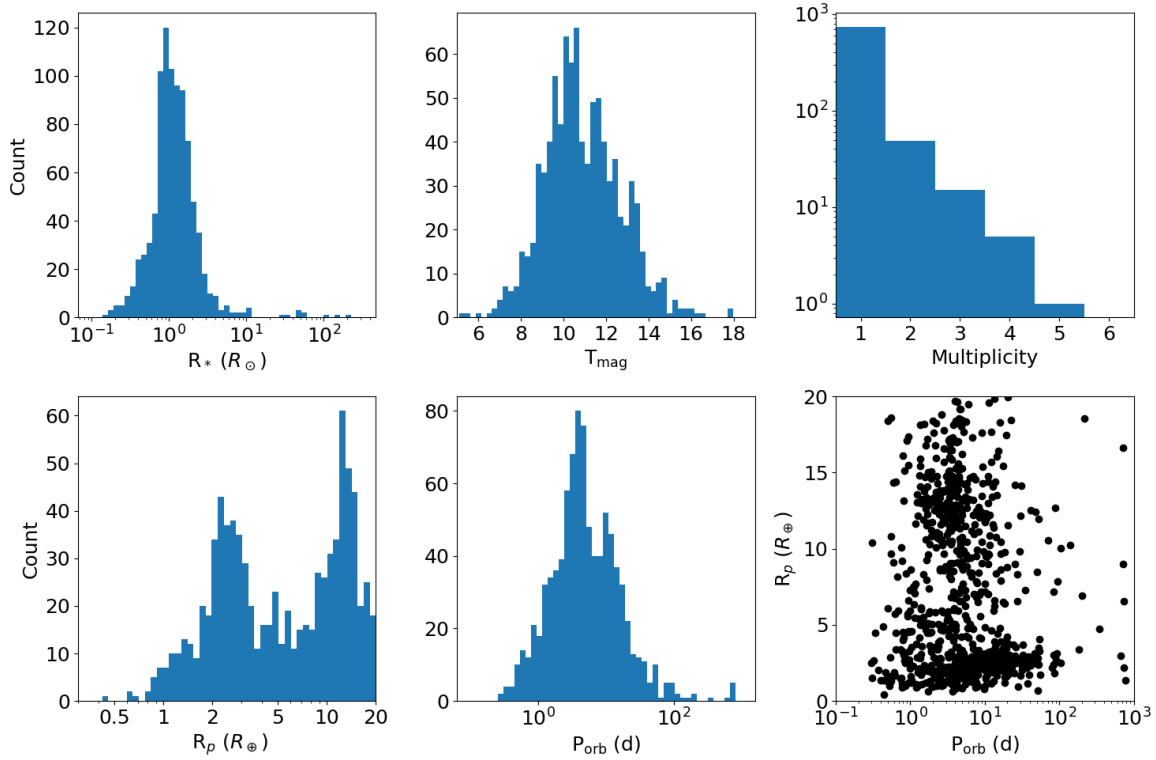


Figure 4.1: Histograms and a scatter plot of stellar and planetary properties for our 914 target systems. The top three panels display stellar radius, stellar  $TESS$  magnitude, and planetary multiplicity (left to right). The bottom three panels display planet radius, planet orbital period, and a scatter plot of orbital period versus planet radius.

This step was sufficient to identify 88% of target stellar masses (all but 112 stars), 94% of stellar radii (all but 55 stars), 95% of  $T_{eff}$  values (all but 46 stars), and 88% of  $\log(g)$  values (all but 112 stars).

For stars lacking any stellar parameters from MAST, we next retrieved parameters from the ExoFOP- $TESS$  website<sup>3</sup>. This step allowed us to determine stellar radii for an additional 23 stars (96% total, all but 32 stars),  $T_{eff}$  for an additional 32 stars (98% total, all but 14 stars), and  $\log(g)$  for an additional 41 stars (92% total, all but 71 stars).

After these steps, we then resolved additional missing parameters by consulting spectral energy distribution (SED) fits from EXOFASTv2 (Eastman 2017) that have been uploaded to ExoFOP<sup>4</sup> and described in Eastman et al. (2019). This step allowed us to determine stellar mass for an additional 32 stars (91% total, all but 80 stars), stellar radii for an additional 10

<sup>3</sup><https://exofop.ipac.caltech.edu/tess/>

<sup>4</sup>Uploaded 2019 May 31, ExoFOP tag 3993

stars (98% total, all but 22 stars),  $T_{\text{eff}}$  for an additional 3 stars (99% total, all but 11 stars), and  $\log(g)$  for an additional 19 stars (94% total, all but 52 stars).

Finally, we referred to the K2 table of the NASA Exoplanet Archive to fill in any remaining missing parameters. This step allowed us to determine stellar radii for an additional 4 stars (98% total, all but 18 stars) and  $\log(g)$  for an additional 1 star (94% total, all but 51 stars). Consulting the K2 table did not increase the number of stars with estimates of stellar mass or effective temperature.

If, at this stage,  $R_*$ , and  $\log(g)$  were determined but  $M_*$  remained unknown, we would calculate  $M_*$  directly from the former two quantities. Using this approach, we estimated the stellar mass for 23 target stars that had only stellar radius and  $\log(g)$  reported from other sources, allowing us to determine a cumulative 94% of stellar masses (all but 57 stars). Comparing all three parameters after this step shows excellent agreement, as expected; the root-mean-square scatter in disagreement between adopted  $\log(g)$  values and those inferred from  $M_*$  and  $R_*$  is 0.19 dex and the median disagreement is only 0.00092 dex.

We then proceeded with a TATER planet search if  $M_*$ ,  $R_*$ ,  $T_{\text{eff}}$ , and  $\log(g)$  were all determined for a given system. If  $[\text{Fe}/\text{H}]$  was not available, we assumed solar metallicity, as  $[\text{Fe}/\text{H}]$  only impacts limb darkening in our TATER search. We could not determine enough stellar parameters for 60 of our 914 target stars ( $\sim 6.6\%$ ), so they were excluded from the planet search.

TIC	Mass ( $M_{\odot}$ )	Mass Prov.	Radius ( $R_{\odot}$ )	Radius Prov.	$\log(g)$	$\log(g)$ Prov.	$T_{\text{eff}}$ (K)	$T_{\text{eff}}$ Prov.
1003831	$0.98 \pm 0.12$	MAST	$1.122 \pm 0.055$	MAST	$4.328 \pm 0.076$	MAST	$5550.0 \pm 117.0$	MAST
1129033	$0.99 \pm 0.12$	MAST	$0.934 \pm 0.043$	MAST	$4.493 \pm 0.073$	MAST	$5605.0 \pm 111.0$	MAST
1528696	0.74	MAST	0.78	MAST	4.52	MAST	$4669.0 \pm 122.0$	MAST
2527981	$0.635 \pm 0.026$	MAST	$0.660 \pm 0.030$	MAST	$4.601 \pm 0.022$	MAST	$3604.0 \pm 157.0$	MAST
2670610	$1.00 \pm 0.13$	MAST	$1.156 \pm 0.059$	MAST	$4.312 \pm 0.078$	MAST	$5640.0 \pm 125.0$	MAST
2760710	$0.212 \pm 0.020$	MAST	$0.2413 \pm 0.0074$	MAST	$4.998 \pm 0.015$	MAST	$3176.0 \pm 157.0$	MAST
4616072	$1.38 \pm 0.23$	MAST	$1.237 \pm 0.055$	MAST	$4.393 \pm 0.088$	MAST	$6600.0 \pm 134.0$	MAST
4646810	$0.800 \pm 0.094$	MAST	$0.744 \pm 0.056$	MAST	$4.598 \pm 0.099$	MAST	$4884.0 \pm 140.0$	MAST
5109298	$2.38 \pm 0.32$	MAST	$2.22 \pm 0.11$	MAST	$4.120 \pm 0.073$	MAST	$9385.0 \pm 207.0$	MAST
5772442	$1.04 \pm 0.12$	MAST	$2.55 \pm 0.18$	MAST	$3.644 \pm 0.085$	MAST	$5806.0 \pm 123.0$	MAST
5868998	0.53	MAST	0.78	MAST	4.37	MAST	$3644.0 \pm 122.0$	MAST

Table 4.1: Stellar parameters and provenances for 854 of our 914 target stars with reported stellar parameters. We searched each of these systems for planetary transits. (Not all stellar values have reported uncertainties, which is still sufficient to run the TATER pipeline.)

## 4.4 Analysis

We summarize each component of the TATER pipeline and our investigation of the *TESS* photometry in this section. In order to detect and characterize planetary signals, we built and used a custom pipeline, which we call the TESS trAnsiT findER, or TATER<sup>5</sup>. The pipeline

<sup>5</sup>.

searches for transit threshold crossing events (TCEs) in each *TESS* light curve and fits a transit model to each putative signal.

## Pre-search and Flattening Photometry

Our transit search was predicated on light curves produced by the *TESS* Science Processing Operations Center (SPOC) at NASA Ames Research Center, which also conducts its own photometric sweeps for planet candidates. SPOC conducts transit searches of the 2-min Pre-search Data Conditioning Simple Aperture Photometry (PDCSAP) light curves (Smith et al. 2012; Stumpe et al. 2012, 2014) with a wavelet-based, adaptive matched filter (Jenkins et al. 2010; Jenkins et al. 2020; Jenkins 2002) and for each TCE flagged, fits an initial limb-darkened model (Li et al. 2019) and conducts a suite of diagnostic tests (Twicken et al. 2018) to help make or break the planetary nature of the TCE.

The *TESS* Quick Look Pipeline (Huang et al. 2020a,b), or QLP, searches light curves from the full frame images (FFIs) of *TESS* using the Box Least Squares (BLS) algorithm (Kovács et al. 2002) and constructs its own diagnostic tests. Candidates passing the diagnostic tests and vetting are alerted as TOIs (Guerrero et al. 2021) on the online TOI catalog<sup>6</sup>. TOIs identified via SPOC and QLP are cross-referenced and compared to all TCEs identified by our own transit search algorithm, *TATER*.

*TATER* accessed and downloaded PDCSAP SPOC lightcurves from the MAST data archive. We defaulted to using 2-min cadence; we either used 2-min cadence photometry or otherwise binned 20-sec cadence observations up to 2-min. Although several targets were observed at higher cadence, 2-min cadence is often ideal for preserving transit detectability. Any observations with NaN or blank flux values were removed. Then, the light curve was flattened using a penalized spline with the `wotan` Python package (Hippke et al. 2019) with a break tolerance of 0.5 days and the maximum number of splines determined so as to assert a minimum knot spacing of 0.5 days. Nearly all known planets and planet candidates in our target sample had transit durations shorter than 0.5 days, thus preventing accidental removal of transit events through flattening. We flattened the light curve for each *TESS* sector separately and then stitched together the normalized light curves.

Our choice of knot spacing at 0.5 days was a reasonable choice for nearly our entire sample: the median transit duration of known planets and candidates in our sample is  $2.5^{+1.9}_{-1.1}$  h with a 95% confidence interval of (0.7, 8.0) h. As an additional check, we looked at TIC 55525572.01 (TOI 813.01), a sub-Jupiter ( $R_p = 7.18 \pm 0.45 R_\oplus$ ) and the planet with the third longest transit duration in our sample (13.6 h). We deemed the longest duration transit too shallow to detect (TOI 785.01,  $t_{\text{dur}} = 15.6$  h,  $R_p = 1.18 \pm 0.28 R_\oplus$ ) and the second longest transit duration unpredictable (TOI 5523.01,  $t_{\text{dur}} = 13.6$  h, singly transiting). We strongly detected TOI 813.01 in our transit search with a signal detection efficiency (SDE) of 17.7, where the SDE has become the standard test statistic for exoplanet detection. This demonstrates that *TATER* is able to detect transits even for unusually long transit durations.

---

<sup>6</sup>[tev.mit.edu/data/](http://tev.mit.edu/data/)

## Transit Search

TATER can operate using either BLS or the Transit Least Squares (TLS) algorithm (Hippke and Heller 2019). We use the `Astropy` Python package (Astropy Collaboration et al. 2013, 2018) implementation of BLS and the `tls` Python package developed by Hippke and Heller (2019).

BLS detects planets by convolving a normalized, phase-folded light curve with a box-shaped transit to calculate the SDE (Alcock et al. 2000). BLS then repeats this process for a grid of orbital periods, transit times, transit durations, and transit depths. A BLS periodogram can then be created by selecting the transit time, duration, and depth that maximizes SDE for a given period.

TLS is an alternative to the commonly used BLS algorithm. TLS is more sophisticated than BLS because it uses an astrophysically realistic transit model rather than a box as template for transit searches, including ingress and egress as well as limb darkening. Predictably, TLS usually outperforms BLS in transit signal detection (especially for smaller transit signals) but is also much more computationally intensive; TLS can compete with BLS in runtime at short periods and long cadences, but it also scales quadratically with the number of data points and runs slower on average when runtimes exceed hour timescales (Hippke and Heller 2019).

Once BLS or TLS is complete, if the SDE for a given period is sufficiently high, that signal can be classified as a threshold crossing event (TCE) and merit further investigation as a potential planet candidate. A “sufficiently high” SDE will vary depending on the preferred trade-off between false positive and false negatives, but Hippke and Heller (2019) found via synthetic light curve transit injection and recovery tests that  $SDE = 7$  corresponds to a false positive rate of  $\sim 1\%$ . Given our large sample size, such a false positive frequency would likely allow several false positives to slip through. However, as seen in Fig. 6 of Hippke and Heller (2019), this false positive frequency peaks between SDE value of 4 – 5 and drops off precipitously at higher SDE values. While a cumulative 1% of false positives exceeded an SDE of 7, only a fraction of those exceeded an SDE of 8, closer to only 0.1%; thus, we opted for a more conservative SDE cutoff of 8 for our planet search. Once we have identified a TCE with TATER the algorithm automatically masks the transit signal and repeats the search for additional TCEs above the SDE cutoff, finding multiple TCEs in 54% of searched systems.

For our purposes, in order to maximize the numbers of TCEs we could find, we ran TATER on all our systems with both BLS and TLS, counting as a TCE any detected signal that appeared with either algorithm (i.e. not necessarily both).

Out of 1814 TCEs detected (see Section 4.4), we found that 247 (14%) were detected with BLS alone, 1238 (68%) were detected with TLS alone, and 329 (18%) were detected with both algorithms. The high performance of TLS relative to BLS is to be expected, as TLS is able to detect smaller and less significant transit signals than BLS. When we subsequently vetted these TCEs in Section 4.4, we found that 25% (107/429) detected with BLS alone passed vetting, 28% (118/429) detected with TLS alone passed vetting, and 48% (204/429) detected with both algorithms passed vetting. It is no surprise that a higher proportion



of BLS-only TCEs passed vetting compared to TLS-only TCEs; TLS can typically detect smaller and less significant signals than BLS, which results in not only more detections at a given SDE but also more false positives that will fail vetting.

## Duplicate TCEs

Any pair of TCEs in a given system with periods closer than 3.5% were considered duplicates and they were consolidated so that only one was retained for vetting and analysis (whichever had a larger SDE). 3.5% was chosen as a conservative lower limit for period proximity based empirically on the closest orbital period pair known to date: Kepler-132 b and c have periods of 6.178 and 6.415 d (Rowe et al. 2014), proximate to within 3.7%<sup>7</sup>.

This duplicate cut removed 550 TCE signals with no apparent bias for short or long period signals. As a confidence check, we found that 70% of these removed duplicate signals had periods that were within 0.01% of the retained signal, and 89% of duplicate signals have period agreement better than 1%.

## TCE Sample

Our initial search of the target sample with TATER yielded a total of 2364 TCEs. However, excluding the 550 duplicate TCEs signals identified and described in Section 4.4 left 1814 unique TCEs. These TCEs were found around 746 stars in our target sample. As can be seen in Fig. 4.2, the vast majority of our TCEs are detected at short orbital periods ( $P < 10$  d).

## TCE Vetting

Using the `LEO-vetter` Python package (Kunimoto 2024), we vetted all 1814 TCE signals detected at  $SDE > 8$ , a conservative cut made relative to Hippke and Heller (2019) who found that  $SDE = 7$  corresponds to a false positive rate of  $\sim 1\%$ . `LEO-vetter` takes as input stellar parameters including radius, mass, density, effective temperature, surface gravity and corresponding uncertainties; the light curve including time series, unflattened fluxes, flattened fluxes, and flux uncertainties; signal properties including period, epoch, and duration. `LEO-vetter` then performs numerous tests to identify false alarms and false positives. Instrumental false alarms are identified through any of the following tests:

- Non-uniqueness: After conducting a model-shift uniqueness test (Thompson et al. 2018), the signal must be unique and strong when compared against the red noise, the strongest phased tertiary signal (i.e. excluding the primary transit signal and any secondary eclipse), and the strongest phased positive signal (i.e. the strongest signal due to a flux *increase*). 1081 TCEs failed this test.

---

<sup>7</sup>Lissauer et al. (2014) reports Kepler-132 is a binary and proposes planets b and c orbit different stellar components; if true, our 3.5% proximity limit is thus even more conservative.

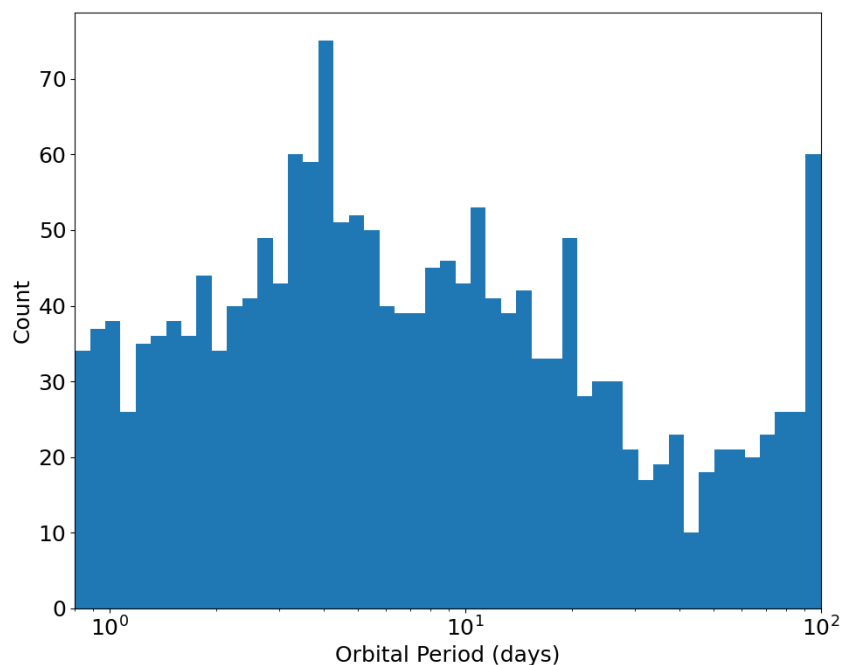


Figure 4.2: Histogram of the period distribution of the 1814 unique TCEs detected in our target sample with  $SDE > 8$ .

- Weak signals: The Multiple Event Statistic (MES, i.e. signal-to-noise ratio of the phased transit) must be  $> 9$ . 1079 TCEs failed this test.
- Bad fit: The reduced  $\chi^2$  for the transit model fit must be smaller than for a straight line fit. Further, `LEO-vetter` also requires that the Akaike Information Criterion (AIC) for the transit model must be such that  $AIC(\text{transit}) - AIC(\text{line}) \leq -20$ . 578 TCEs failed this test.
- Chases: The transit signal must not have too many nearby “chases”, i.e. nearby signals of comparable amplitude to the transit signal. Thompson et al. (2018) quantifies this metric so that no nearby significant signals yield a chase metric of 1 and a nearby signal identical to the transit yields a chase metric of 0. A median chase metric of  $< 0.8$  constitutes a failed test. This test is only conducted for signals with fewer than five transits. 329 TCEs failed this test.
- Bad transit shape: The average flux during transit should *decrease*, not increase during the transit event. 313 TCEs failed this test.
- Single event: The most significant Signal Event Statistic (SES) must not be more than

80% that of the MES. This test is only conducted for signals with fewer than five transits. 204 TCEs failed this test.

- Difference in mean and median: The distribution of transit depths as calculated from mean and median depth values must be consistent within  $1.5\sigma$ . 138 TCEs failed this test.
- Invalid transits: After bad transits are identified (defined as either not enough in-transit data,  $SES < 0$ , or reduced  $\chi^2 > 5$ ), there must be at least 2 remaining good transits. 137 TCEs failed this test.
- Noisiness: The baseline red noise ( $\sigma_r$ ) must be sufficiently small in comparison to the baseline white noise ( $\sigma_w$ ):  $\sqrt{N_{\text{transits}}}\sigma_r/\sigma_w < 4$ .  $N_{\text{transits}}$  is the number of observed transits,  $\sigma_w$  is the standard deviation of the flux and  $\sigma_r$  is the standard deviation of the MES amplitudes (Jenkins 2002). The baseline is all data outside the primary transit and the most significant secondary signal. 115 TCEs failed this test.
- Unphysical duration:  $a/R_*$  must be  $> 2$ , the best trapezoidal fit duration cannot be longer than half the period, and best transit fit duration cannot be shorter than half the trapezoidal fit duration. 110 TCEs failed this test.
- Sinusoidal: The best fit amplitude to a sinusoidal fit must not be significant at the  $10\sigma$  level or higher (i.e. sinusoidal amplitude uncertainty cannot be  $< 10\%$ ). This would indicate too much agreement with a sinusoidal model to conclusively rule it out. This test is only conducted for signals with  $P < 10$  days. 64 TCEs failed this test.
- Asymmetric: The transit duration before and after the transit midpoint (as determined from the transit ephemeris) cannot be discrepant by more than  $5\sigma$ . 8 TCEs failed this test.

Similarly, astrophysical false positives are identified when TCEs fail any of the following tests:

- Odd/even: The transit depth and epoch of odd versus even transits cannot be discrepant by more than  $3\sigma$  and  $10\sigma$ , respectively. 96 TCEs failed this test.
- Secondary: A secondary eclipse must not be too high in amplitude when compared against the red noise, the strongest phased tertiary signal (after the primary transit signal and any secondary eclipse), and the strongest phased positive signal (i.e. the strongest signal due a flux *increase*). The only exception is if the secondary eclipse signal is consistent with that of a planet. `LEO-vetter` defines these conditions as:  $\text{albedo} < 1$ ,  $R_p < 25 R_{\oplus}$ ,  $b < 0.95$ , and  $\delta_{\text{secondary}} < 0.1\delta_{\text{transit}}$ . 69 TCEs failed this test.
- Large: The transiting object cannot be larger than  $25 R_{\oplus}$ . 20 TCEs failed this test.

- V-shaped: The transit shape cannot be too V-shaped due to high impact parameter or large radius, with a requirement that  $b+R_p/R_* < 1.5$ . 2 TCEs failed this test.

A TCE only passed vetting if it did not fail any false alarm or false positive tests. TCEs that passed vetting were then promoted to planet candidates. Of the 1814 TCEs we detected, the `LEO-vetter` vetting package failed to complete vetting for 118 TCEs (6%), 1095 (60%) failed vetting as false alarms only, 79 (4%) failed vetting as false positives only, 93 (5%) failed vetting as both false alarms and false positives, and 429 (24%) passed all false alarm and false positive tests and were upgraded to planet candidates.

We also compared the input status of known TOIs (e.g. confirmed planet, planet candidate, or false positive) against the `LEO-vetter` output. A total of 739 TOIs were identified by TATER and fully processed through `LEO-vetter`, of which 428 (58%) passed vetting and the other 311 (42%) failed. Of these 739 TOIs, there were 323 confirmed planets, 331 planet candidates, and 85 false positives. Within these categories, `LEO-vetter` passed 209 of the 323 confirmed planets (65%), 193 of the 331 planet candidates (58%), and 26 of the 85 false positives (31%).

## An Application: TIC 281575427

To demonstrate how TATER detects planets and how `LEO-vetter` conducts planet candidate vetting, we present a representative system to detail the inputs, outputs, and procedures for planet detection and vetting. We selected TIC 281575427 (TOI-205) as our demonstration system. TOI-205 is an F star with  $M_* = 1.20 \pm 0.18 M_\odot$ ,  $R_* = 1.454 \pm 0.072 R_\odot$ , and  $T_{\text{eff}} = 6220 \pm 130$  K. The *TESS* SPOC pipeline originally identified a single TCE ( $P = 4.252984 \pm 0.000016$  d,  $R_p = 2.27 \pm 0.15 R_\oplus$ ). We detected the same TCE in the BLS iteration of our TATER pipeline, a  $4.252986^{+0.000074}_{-0.000073}$  d signal produced by a super-Earth candidate ( $R_p = 2.39^{+0.11}_{-0.10} R_\oplus$ ). The periodogram and transit model fit produced by TATER can be seen in Figs. 4.3 and 4.4. Our vetting of this TCE with `LEO-vetter` was successful, upgrading it to candidate status. Our `LEO-vetter` results can be seen in Fig. 4.5.

## TOI Validation

Once TCEs successfully passed vetting, we upgraded them to planet candidate status and subjected them to statistical validation. We conducted validation with TRICERATOPS (Giacalone and Dressing 2020; Giacalone et al. 2021), a Bayesian tool for vetting and statistical validation of *TESS* Objects of Interest (TOIs). In order to operate, TRICERATOPS needs only the TIC ID, the *TESS* sectors in which the target was observed, the best-fit orbital period, the phase-folded light curve centered on the transit, and target star properties. This tool uses the properties and positions of the target star and nearby stars, calculates the prior planetary occurrence probability as a function of orbital period from an empirical broken power law (Dong and Zhu 2013; Dressing and Charbonneau 2015; Howard et al. 2012; Mulders et al. 2015, 2018; Petigura et al. 2013) with a breakpoint at  $P = 10$  d, and similarly

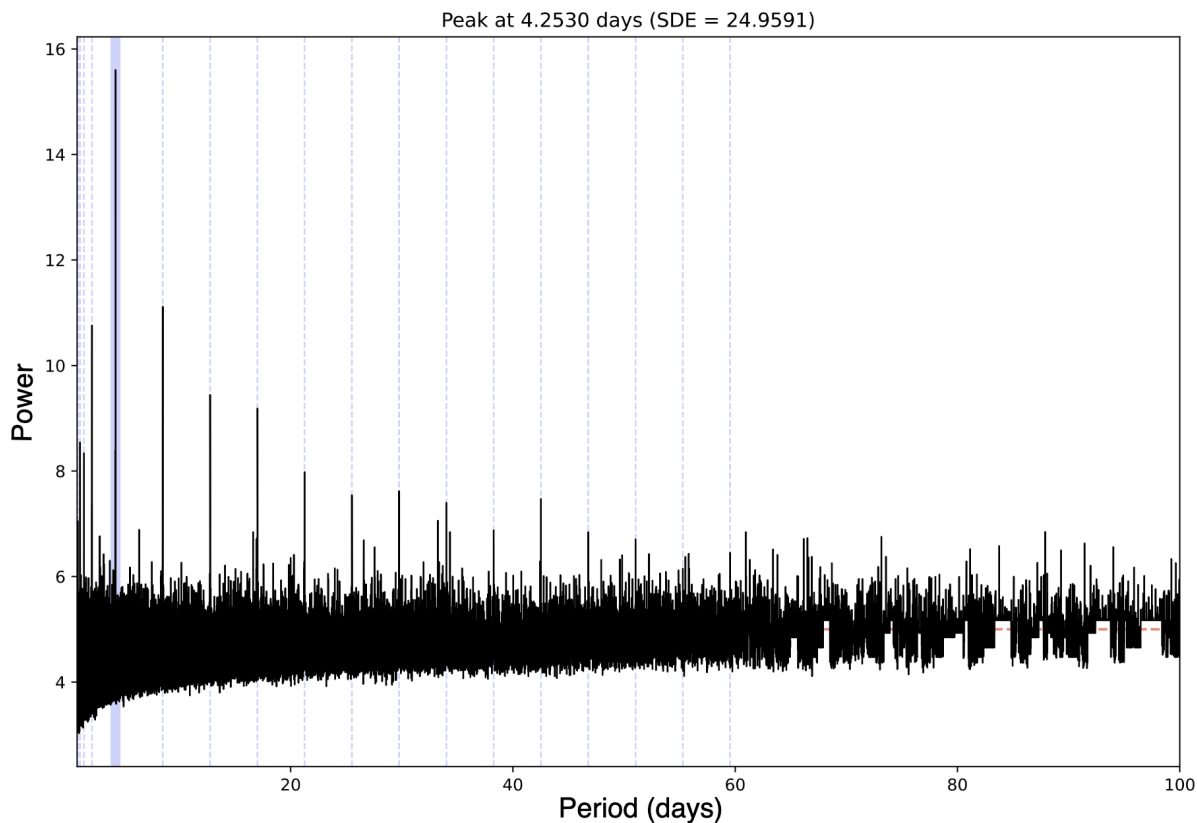


Figure 4.3: Example TATER periodogram of TIC 281575427 identifying a TCE with period of 4.252986 d (blue region). Aliases of the primary signal are located at vertical dashed blue lines and the horizontal red dashed line represents an SDE lower limit of 5. This TCE is a known planet candidate (TOI-205.01) and independently passed vetting with the `LEO-vetter` planet candidate vetting package (see Section 4.4 and Fig. 4.5).

calculates the prior eclipsing occurrence probability as a function of orbital period from another empirical broken power law (Kirk et al. 2016) with a breakpoint at  $P = 0.3$  d. These models of planet occurrence and stellar multiplicity are applied to a specific system and transit signal to quantify the relative likelihoods of the on-target transiting planet scenario and plausible false positive scenarios.

The planet radius must be smaller than  $8 R_{\oplus}$  in order for validation with `TRICERATOPS` to be valid. This is roughly the minimum radius for a brown dwarf (Burrows et al. 2011), and thus objects larger than this radius are extremely difficult to distinguish as planet or brown dwarf through photometry alone; RVs are typically also needed to estimate the mass (or an upper mass limit) and prove the object is low enough in mass to be planetary.

The likelihood of all false positive scenarios combined is the false positive probability

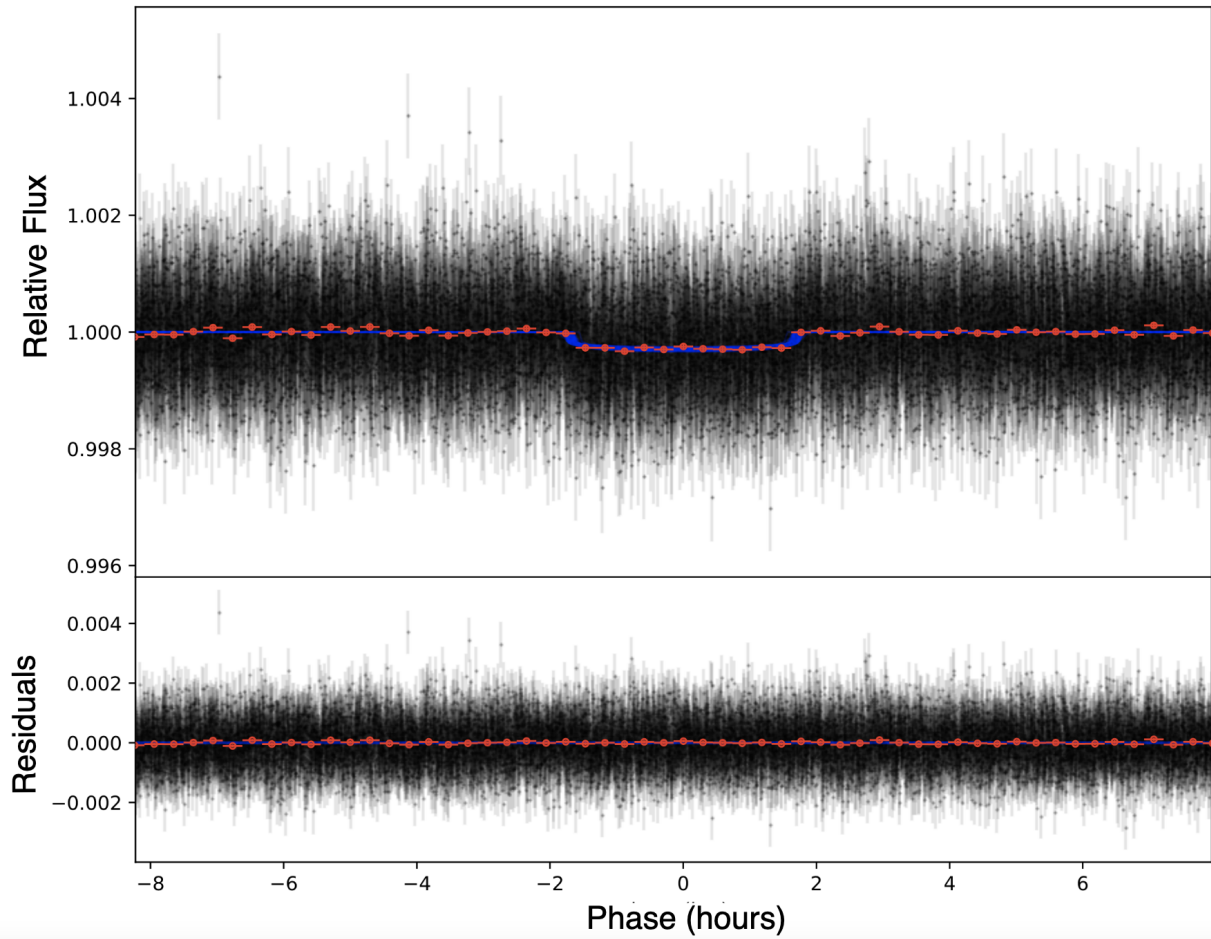


Figure 4.4: Example TATER transit model and residuals for the phased light curve of TIC 281575427. TATER detected a TCE with a period of 4.252986 d which we vetted and upgraded to candidate status with *LEO-vetter*. Black data points are the raw flux, red data points are binned flux, and the blue, overlapping lines are posterior samples of the transit model.

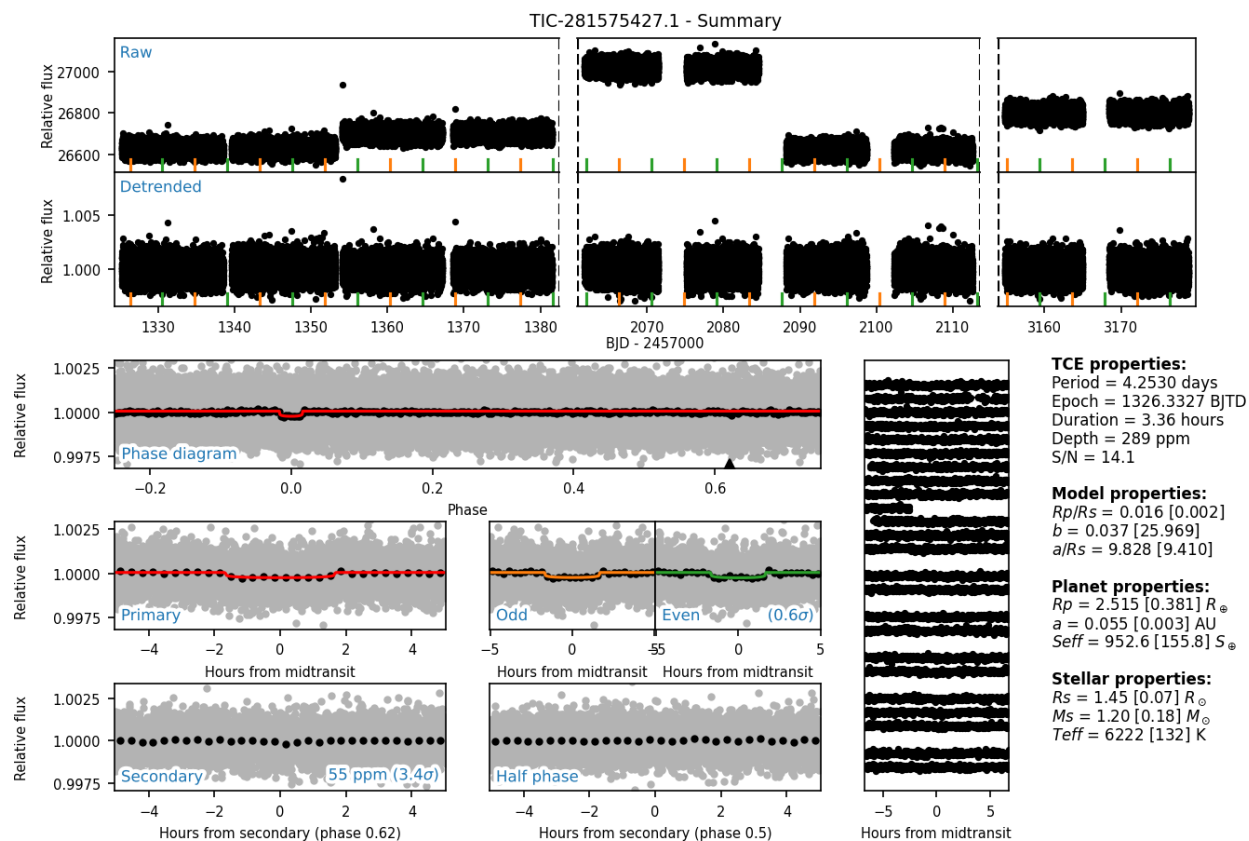


Figure 4.5: Example output of vetting for TIC 281575427 (TOI-205) with the planet vetting Python package `LEO-vetter`. The 4.252986 day signal being vetted is a candidate warm Neptune. The top two panels are the raw and normalized light curves, with identified transits marked in orange (odd transits) and green (even transits). The next panel below (on the left) is the phased light curve (with gray unbinned data points, black binned data points, red model line, and black triangle to denote the most significant secondary signal). The next row below includes the same phased light curve now focused exclusively in and near transit (left) and the light curve split into odd and even transits (right, with two subpanels plotting the odd transit model in orange, the even transit model in green, and the total discrepancy in odd/even transit depth noted). The bottom row includes the phased light curve near the most significant secondary signal (left, with signal depth and significance reported) and near phase = 0.5 (right). Right of these bottom three rows is a vertical panel plotting each transit separately. Finally, on the far right a table of TCE, model, planet, and stellar properties are reported.

(FPP). If all false positive scenario likelihoods are cumulatively low enough, the candidate is upgraded to a validated planet. Specifically, we use the default TRICERATOPS cutoff FPP of 0.015. Further, TRICERATOPS also requires that the nearby false positive probability (NFPP), i.e. the probability of the transit signal originating from a nearby resolved star, must be less than 0.001. We adopt the same requirements for validation in this work.

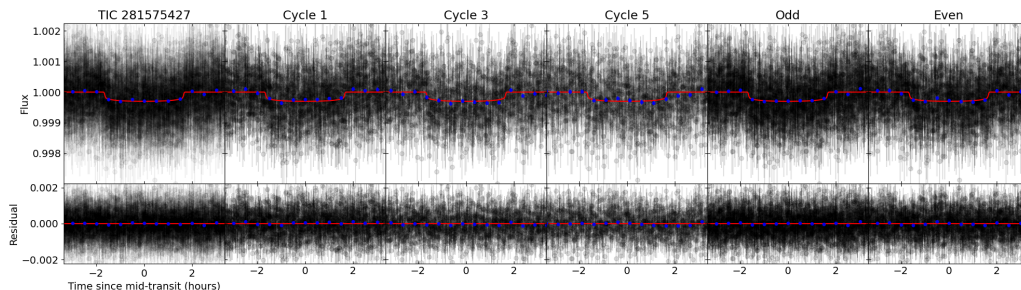


Figure 4.6: Phased light curves for TIC 281575427.

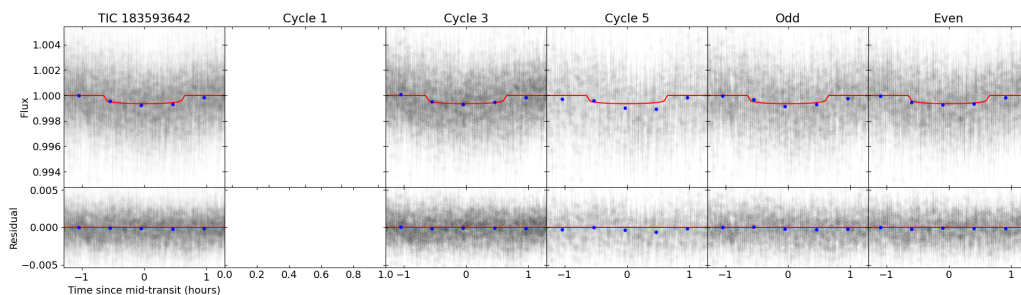


Figure 4.7: Phased light curves for TIC 183593642.

## 4.5 Results & Discussion

### Crossmatch to known TOIs

We compared our results against those of prior studies to characterize the performance of the TATER pipeline and its planet search algorithm. Because we selected our sample so that each target has at least one known planet or planet candidate, we could check whether we are detecting these known signals and assess what planetary radii and orbital periods are beyond the reach of TATER detection.



Table 4.2: Table of all TCEs detected with TATER (full table available for download)

TIC	TOI	Period (d)	$t_0$	$R_p$ ( $R_{\oplus}$ )	Transit depth	SDE	Vetted	Validated
1003831	564.01	1.6511500 $\pm$ 0.0000090	1518.2073 $\pm$ 0.0039	3.448 $\pm$ 0.095	0.000794 $\pm$ 0.000037	56.97	Y	N
1129033	398.01	1.3600370 $\pm$ 0.0000080	1410.9796 $\pm$ 0.0036	12.66 $\pm$ 0.22	0.0154 $\pm$ 0.0010	138.35	N	N
1528696	448.01	0.8820630 $\pm$ 0.0000050	1438.4015 $\pm$ 0.0028	6.03 $\pm$ 0.23	0.00499 $\pm$ 0.00038	74.12	Y	N
1528696		7.725 $\pm$ 0.064	1440.408 $\pm$ 0.066	2.2 $\pm$ 1.6	0.0006 $\pm$ 0.0010	9.35	N	N
1528696		8.769 $\pm$ 0.058	1441.251 $\pm$ 0.074	3.4 $\pm$ 1.9	0.0016 $\pm$ 0.0017	9.33	N	N
2527981		4.082 $\pm$ 0.061	2039.616 $\pm$ 0.070	4.2 $\pm$ 2.2	0.0035 $\pm$ 0.0049	10.78	N	N
2527981		4.712 $\pm$ 0.037	2036.459 $\pm$ 0.067	4.2 $\pm$ 3.0	0.0035 $\pm$ 0.0046	13.56	N	N
2527981		5.8476 $\pm$ 0.0044	2037.2091 $\pm$ 0.0075	13.69 $\pm$ 0.71	0.0361 $\pm$ 0.0034	16.97	N	N
2527981		10.307 $\pm$ 0.055	2037.705 $\pm$ 0.049	4.6 $\pm$ 2.2	0.0041 $\pm$ 0.0052	8.97	N	N
2670610		2.50487 $\pm$ 0.00017	1659.172 $\pm$ 0.018	2.23 $\pm$ 0.34	0.00031 $\pm$ 0.00014	8.32	N	N
2670610		13.479 $\pm$ 0.063	1656.943 $\pm$ 0.061	3.4 $\pm$ 0.8	0.00071 $\pm$ 0.00043	9.78	N	N
2760710		0.8028 $\pm$ 0.0044	1354.738 $\pm$ 0.072	1.04 $\pm$ 0.30	0.0016 $\pm$ 0.0009	8.87	N	N
2760710		2.089 $\pm$ 0.055	1355.291 $\pm$ 0.049	1.09 $\pm$ 0.38	0.0017 $\pm$ 0.0024	8.84	N	N
2760710		2.65188 $\pm$ 0.00022	1355.296 $\pm$ 0.017	1.27 $\pm$ 0.18	0.00232 $\pm$ 0.00091	8.2	N	N
4616072		2.125 $\pm$ 0.037	1469.624 $\pm$ 0.074	2.5 $\pm$ 1.3	0.00034 $\pm$ 0.00050	8.14	N	N
4616072		2.42711 $\pm$ 0.00013	1469.907 $\pm$ 0.016	3.25 $\pm$ 0.32	0.00058 $\pm$ 0.00033	9.28	N	N
4616072	466.01	4.187616 $\pm$ 0.00024	1469.0608 $\pm$ 0.0034	12.08 $\pm$ 0.16	0.00801 $\pm$ 0.00027	72.3	N	N
4616072		98.483 $\pm$ 0.064	1514.830 $\pm$ 0.072	3.2 $\pm$ 1.6	0.00057 $\pm$ 0.00075	11.07	N	N
4646810	461.01	56.4455 $\pm$ 0.0045	1430.838 $\pm$ 0.017	0.98 $\pm$ 0.49	0.00015 $\pm$ 0.00070	14.03	N	N
5109298		1.6184 $\pm$ 0.0009	2202.963 $\pm$ 0.011	7.40 $\pm$ 0.31	0.00093 $\pm$ 0.00015	13.18	N	N
5772442	979.01	1.1057 $\pm$ 0.0011	2230.077 $\pm$ 0.019	3.78 $\pm$ 0.70	0.000185 $\pm$ 0.00080	14.1	N	N
5868998	749.01	1.2710620 $\pm$ 0.000070	1572.4717 $\pm$ 0.0028	13.14 $\pm$ 0.25	0.0236 $\pm$ 0.0037	83.92	N	N
5868998		5.418 $\pm$ 0.039	1572.145 $\pm$ 0.068	2.8 $\pm$ 3.9	0.0011 $\pm$ 0.0017	8.81	N	N
5868998				2.8 $\pm$ 2.2	0.0011 $\pm$ 0.0030			

Table 4.3: Table of all vetted TOIs detected with TATER (full table available for download)

TIC	Period (d)	$t_0$	$R_p$ ( $R_{\oplus}$ )	$R_p/R_*$
175310067	11.284 <sup>+0.010</sup> <sub>-0.008</sub>	2240.2431 <sup>+0.0058</sup> <sub>-0.0057</sub>	8.56 <sup>+0.23</sup> <sub>-0.66</sub>	0.0511 <sup>+0.0040</sup> <sub>-0.0014</sub>
343648136	1.65420 <sup>+0.00060</sup> <sub>-0.00063</sub>	2362.1443 <sup>+0.0057</sup> <sub>-0.0060</sub>	3.71 <sup>+0.17</sup> <sub>-0.18</sub>	0.0243 <sup>+0.0012</sup> <sub>-0.0011</sub>
915110182	4.5238 <sup>+0.0017</sup> <sub>-0.0020</sub>	3017.090 <sup>+0.011</sup> <sub>-0.010</sub>	15.3 <sup>+3.0</sup> <sub>-4.2</sub>	0.171 <sup>+0.033</sup> <sub>-0.047</sub>

Table 4.4: Table of all planets we validate with TRICERATOPS.

TIC	TOI	Period (d)	$t_0$	$R_p$ ( $R_{\oplus}$ )	a (AU)	Newly Validated
89020549	132.01	2.109683 ± 0.000010	1326.9055 <sup>+0.0026</sup> <sub>-0.0015</sub>	3.32 <sup>+0.10</sup> <sub>-0.16</sub>	0.03119 <sup>+0.000030</sup> <sub>-0.00044</sub>	N
139285832	332.01	1.5541 <sup>+0.0017</sup> <sub>-0.0014</sub>	2063.222 <sup>+0.010</sup> <sub>-0.013</sub>	2.68 <sup>+0.28</sup> <sub>-0.26</sub>	0.025164 <sup>+0.000094</sup> <sub>-0.000065</sub>	N <sup>8</sup>
183593642	355.01	1.03731 <sup>+0.00036</sup> <sub>-0.00056</sub>	2088.421 <sup>+0.008</sup> <sub>-0.011</sub>	2.79 <sup>+0.15</sup> <sub>-0.18</sub>	0.02090 <sup>+0.000090</sup> <sub>-0.00029</sub>	Y
220029715	825.01	3.1853150 ± 0.0000050	1601.9350 <sup>+0.0019</sup> <sub>-0.0012</sub>	5.25 ± 0.13	0.03963 <sup>+0.000030</sup> <sub>-0.00015</sub>	N
234994474	134.01	1.4015220 ± 0.0000080	1326.0380 <sup>+0.0041</sup> <sub>-0.0018</sub>	1.368 ± 0.047	0.020500 <sup>+0.000028</sup> <sub>-0.000013</sub>	N
280437559	969.01	1.82372 <sup>+0.00072</sup> <sub>-0.00083</sub>	2230.1404 <sup>+0.0043</sup> <sub>-0.0050</sub>	2.88 <sup>+0.10</sup> <sub>-0.09</sub>	0.02543 <sup>+0.00020</sup> <sub>-0.000070</sub>	N
281575427	205.01	4.252986 <sup>+0.000074</sup> <sub>-0.000073</sub>	1326.333 <sup>+0.013</sup> <sub>-0.005</sub>	2.39 <sup>+0.11</sup> <sub>-0.10</sub>	0.054578 <sup>+0.000066</sup> <sub>-0.000073</sub>	Y
305424003	907.01	4.585043 <sup>+0.000063</sup> <sub>-0.000043</sub>	1631.6317 <sup>+0.0043</sup> <sub>-0.0047</sub>	8.8 <sup>+0.4</sup> <sub>-2.2</sub>	0.05742 <sup>+0.000050</sup> <sub>-0.00011</sub>	Y <sup>9</sup>
350153977	908.01	3.183768 <sup>+0.000090</sup> <sub>-0.000012</sub>	1629.7399 <sup>+0.0063</sup> <sub>-0.0021</sub>	2.900 <sup>+0.097</sup> <sub>-0.094</sub>	0.04178 <sup>+0.000030</sup> <sub>-0.00032</sub>	N
355703913	111.01	2.106160 <sup>+0.000021</sup> <sub>-0.000016</sub>	1326.1096 <sup>+0.0034</sup> <sub>-0.0028</sub>	7.35 <sup>+0.54</sup> <sub>-0.21</sub>	0.0316 <sup>+0.0012</sup> <sub>-0.0001</sub>	N
369455629	2199.01	3.376987 <sup>+0.000022</sup> <sub>-0.000035</sub>	2038.5064 <sup>+0.0022</sup> <sub>-0.0036</sub>	7.33 <sup>+0.25</sup> <sub>-0.70</sub>	0.04390 <sup>+0.000030</sup> <sub>-0.00016</sub>	N
403224672	141.01	1.0082480 ± 0.0000050	1325.5289 <sup>+0.0007</sup> <sub>-0.0011</sub>	1.51 <sup>+0.11</sup> <sub>-0.05</sub>	0.019931 <sup>+0.000011</sup> <sub>-0.0000070</sub>	N
421894914	1056.01	5.307978 <sup>+0.000071</sup> <sub>-0.000061</sub>	1326.068 <sup>+0.010</sup> <sub>-0.014</sub>	2.54 <sup>+0.12</sup> <sub>-0.11</sub>	0.06256 <sup>+0.00019</sup> <sub>-0.00013</sub>	Y

We crossmatched our detected TCEs to all the known candidates and planets in our target sample, in order to determine what fraction of the known candidates and planets could be detected as TCEs with TATER. As can be seen in Fig. 4.11, we recover the vast majority of known candidates and planets: approximately 89% are detected with an SDE > 8. If we lower the detection threshold to SDE = 5, the detection efficiency increases to 94%, but at the cost of thousands of additional TCEs detected at low significance and composed mostly of false positives.

## Newly validated planets

Our TATER planet detection pipeline, in concert with LEO-*vetter* (Kunimoto 2024), was able to detect hundreds of planet candidates. Of these candidates, we were able to use TRICERATOPS to statistically validate 4 new planets. All 4 of these newly validated planets were previously known planet candidates.

As can be seen in Fig. 4.10, the newly validated planets are all quite short in orbital

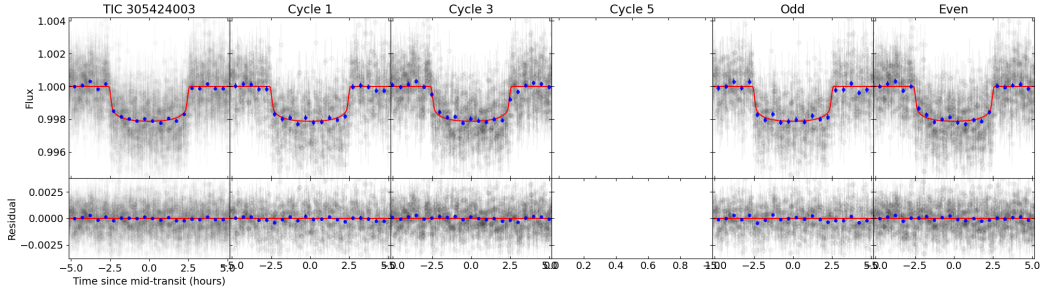


Figure 4.8: Phased light curves for TIC 305424003.

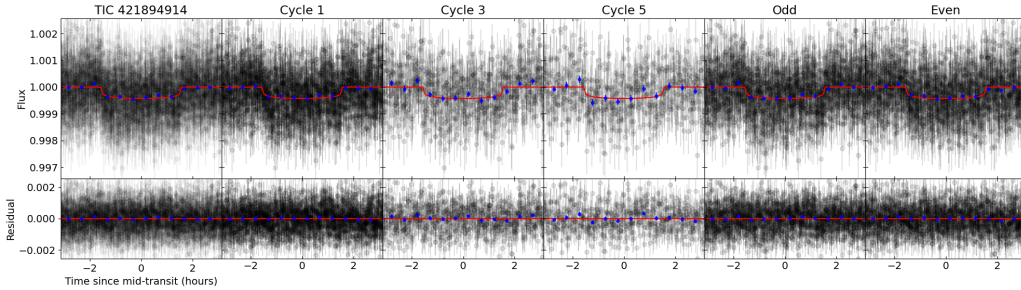


Figure 4.9: Phased light curves for TIC 421894914.

period (all have periods  $< 10$  d) but mostly moderate in size (only 1 of 4 is a sub-Jupiter, the remaining 3 are all sub-Neptunes). Our full list of detected TCEs is available in Table 4.2. Additionally, newly validated planets are available in Table 4.4. We discuss each newly validated planet in detail below.

### TIC 281575427 (TOI 205.01)

This 4.25 d planet ( $2.39_{-0.10}^{+0.11} R_{\oplus}$ ) orbits a F-type star ( $T_{\text{eff}} = 6220 \pm 130$  K,  $R_{*} = 1.454 \pm 0.072 R_{\odot}$ ,  $M_{*} = 1.20 \pm 0.18 M_{\odot}$ ,  $\log(g) = 4.192 \pm 0.087$ ). Difference image centroiding from SPOC data validation reports places the transit source within  $6.011''$  ( $1.63\sigma$ ) of the target star.

For this particular planet, there were already 2 HARPS spectra collected in 2018 ( $R = 115000$ , SNR per pixel  $\sim 90$  at 550 nm) which we used along with photometric values to estimate stellar parameters. We subjected published host star photometric values to AstroARIADNE, a stellar spectral energy distribution fitting code based on Vines and Jenkins (2022), and estimated that  $T_{\text{eff}} = 6335_{-37}^{+23}$  K,  $\log(g) = 4.06 \pm 0.05$ , and  $[\text{Fe}/\text{H}] = 0.03_{-0.03}^{+0.02}$ . Both photometric estimates of  $T_{\text{eff}}$  and  $\log(g)$  are in good agreement with the stellar values collected from the literature and used by TATER.

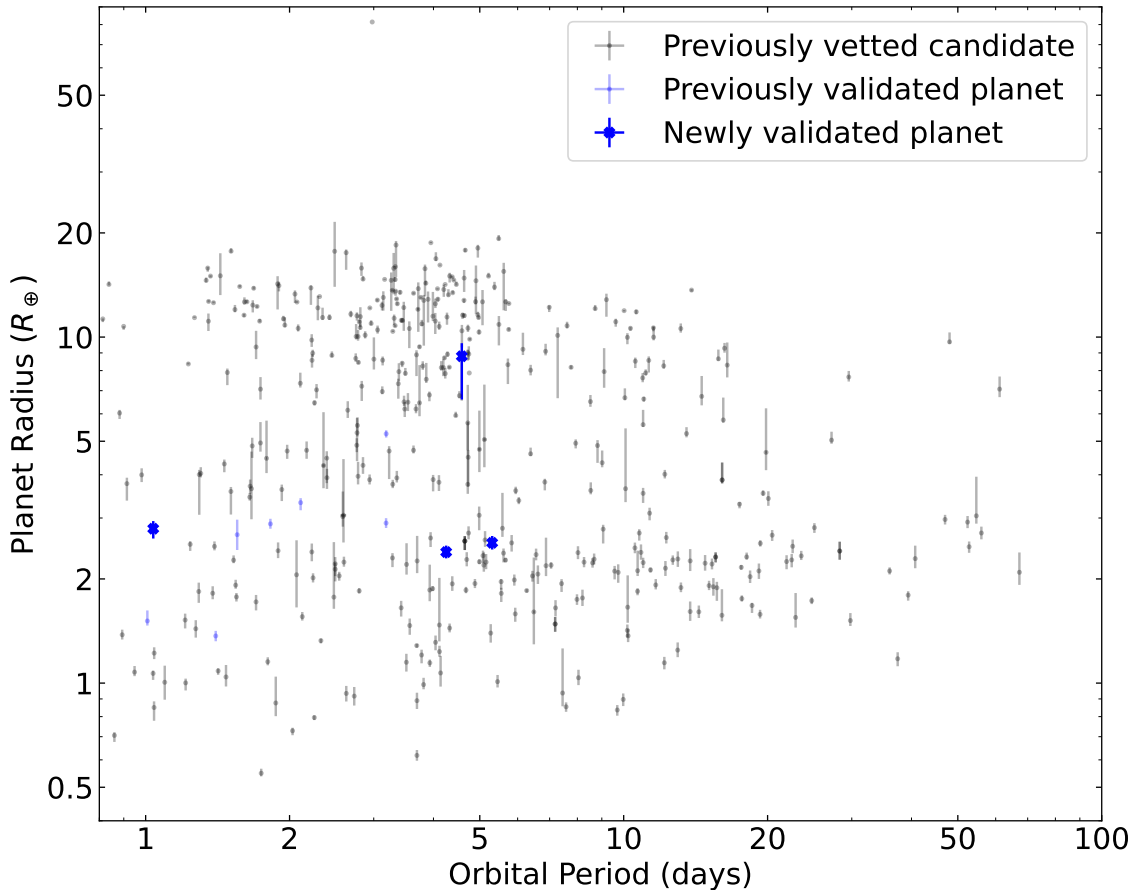


Figure 4.10: Period versus radius for all signals vetted or validated in this work. Black and blue points are candidates vetted with `LEO-vetter` and planets statistically validated with `TRICERATOPS`, respectively. Large, blue, bold points are validated planets that are new, meaning this work has validated them for the first time (Note: TOI 907.01 has been independently confirmed).

We next used the photometric results as inputs for synthesizing a spectrum based on Kurucz Atlas 12 models (Kurucz 1979). We compared these synthetic spectra against the 2 co-added HARPS spectra collected for this target in order to assess stellar parameters with SME (Piskunov and Valenti 2017; Valenti and Piskunov 1996). This spectroscopic fitting procedure yielded estimates of  $T_{\text{eff}} = 6330 \pm 150$  K,  $\log(g) = 4.17 \pm 0.25$ , and  $[\text{Fe}/\text{H}] = 0.18 \pm 0.09$ , all in good agreement with literature and photometric values.

Additionally, with SME we were able to determine that  $[\text{Mg}/\text{H}] = 0.19 \pm 0.06$  (at the 5160 – 5184 Å Mg triplet) and  $v \sin(i) = 13.5 \pm 0.7$  km s<sup>-1</sup>. This is assuming  $V_{\text{mic}} =$

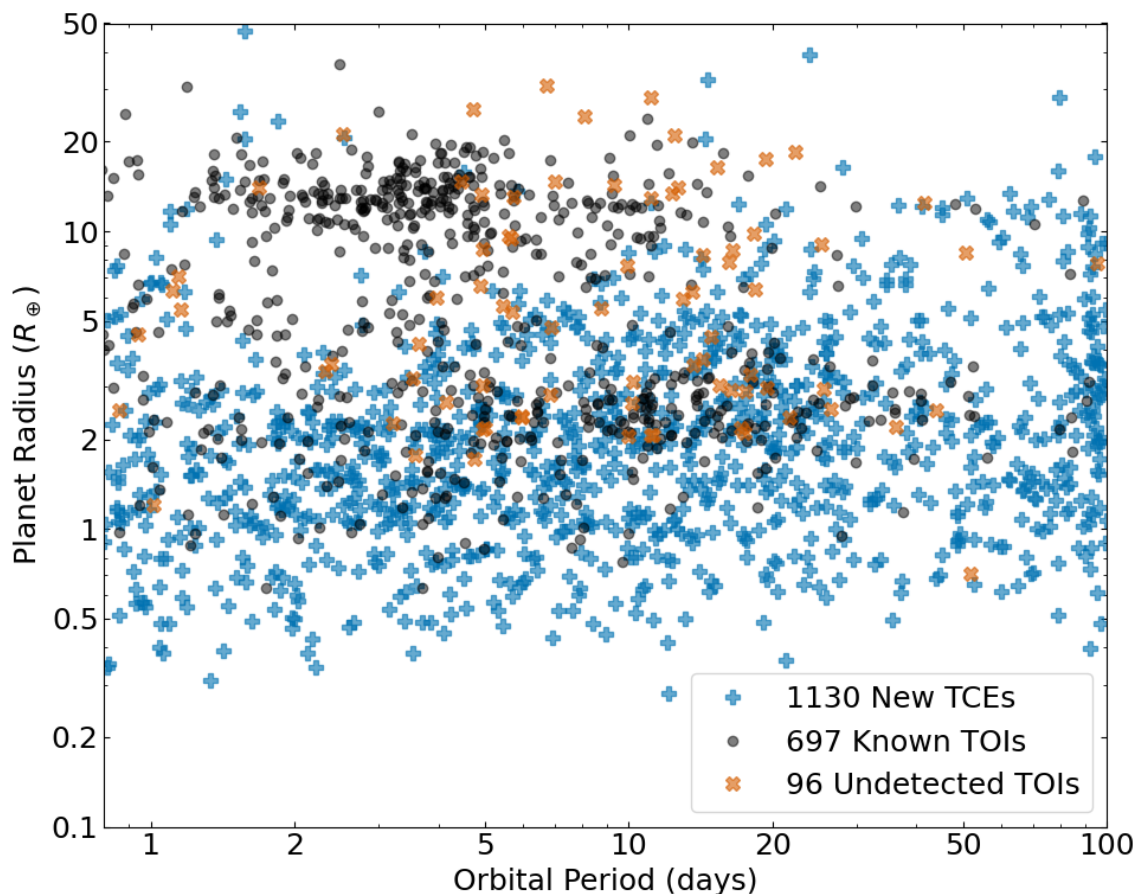


Figure 4.11: Period v. radius for all TCEs detected (or otherwise detectable) with TATER. New TCEs are black, while TCEs that match with known TOIs are blue. Also plotted in orange are additional known TOIs in our target systems that we were unable to detect with TATER.

$1.34 \pm 0.12 \text{ km s}^{-1}$  (Bruntt et al. 2010) and  $V_{\text{mac}} = 5.24 \pm 0.45 \text{ km s}^{-1}$  (Doyle et al. 2014).

We subjected this planet to modeling, vetting, and validation using photometry from *TESS* Cycle 1 (6 transits in Sector 1, 7 in Sector 2), Cycle 3 (5 transits in Sector 28, 4 transits in Sector 29), and Cycle 5 (5 transits in Sector 68).

We conducted statistical validation and determined a NFPP of  $2.74 \times 10^{-5}$  and FPP of  $2.78 \times 10^{-5}$ , thus validating the planet.

**TIC 183593642 (TOI 355.01)**

This 1.04 d planet ( $2.79_{-0.18}^{+0.15} R_{\oplus}$ ) orbits a F-type star ( $T_{\text{eff}} = 6050 \pm 130$  K,  $R_{*} = 1.317 \pm 0.066 R_{\odot}$ ,  $M_{*} = 1.13 \pm 0.15 M_{\odot}$ ). Difference image centroiding from SPOC data validation reports places the transit source within  $3.699''$  ( $0.81\sigma$ ) of the target star.

We subjected this planet to modeling, vetting, and validation using photometry from *TESS* Cycle 3 (18 transits in Sector 29, 22 transits in Sector 30) and Cycle 5 (17 transits in Sector 69). There was also 10-min cadence full frame image (FFI) photometry from Sectors 2 and 3 which we did not employ in our analysis.

We conducted statistical validation and determined a NFPP of  $2.42 \times 10^{-7}$  and FPP of  $4.35 \times 10^{-3}$ , thus validating the planet.

**TIC 305424003 (TOI 907.01)**

This 4.59 d planet ( $8.8_{-2.2}^{+0.4} R_{\oplus}$ ) orbits a F-type star ( $T_{\text{eff}} = 6220 \pm 130$  K,  $R_{*} = 2.060 \pm 0.092 R_{\odot}$ ,  $M_{*} = 1.20 \pm 0.17 M_{\odot}$ ). Difference image centroiding from SPOC data validation reports places the transit source within  $0.686''$  ( $0.25\sigma$ ) of the target star.

This target has also been independently confirmed via an RV mass measurement with the HARPS spectrograph (Neilsen et al. in prep; HARPS ESO programme ID 0103.C-0874). It is for this reason that we permit validation of this planet with TRICERATOPS; its radius may be larger than  $8 R_{\oplus}$ , but there are RV measurements that constrain the planetary mass and allow us to eliminate the possibility of a brown dwarf scenario.

We subjected this planet to modeling, vetting, and validation using photometry from *TESS* Cycle 1 (4 transits in Sector 12) and Cycle 3 (6 transits in Sector 39).

We conducted statistical validation and determined a NFPP of  $2.24 \times 10^{-14}$  and FPP of  $2.23 \times 10^{-14}$ , thus validating the planet.

**TIC 421894914 (TOI 1056.01)**

This 5.31 d planet ( $2.54_{-0.11}^{+0.12} R_{\oplus}$ ) orbits a F-type star ( $T_{\text{eff}} = 6120 \pm 120$  K,  $R_{*} = 1.370 \pm 0.063 R_{\odot}$ ,  $M_{*} = 1.16 \pm 0.16 M_{\odot}$ ). Difference image centroiding from SPOC data validation reports places the transit source within  $3.531''$  ( $1.06\sigma$ ) of the target star.

We subjected this planet to modeling, vetting, and validation using photometry from *TESS* Cycle 1 (6 transits in Sector 1, 6 in Sector 13), Cycle 3 (5 transits in Sector 27), and Cycle 5 (4 transits in Sector 67).

We conducted statistical validation and determined a NFPP of  $9.20 \times 10^{-4}$  and FPP of  $1.90 \times 10^{-3}$ , thus validating the planet.

## 4.6 Conclusion

In this paper, we analyzed a sample of 914 stars comprising every star observable during *TESS* Cycle 3 with at least one known planet or planet candidate in order to look for

additional planets with high cadence photometry. We developed a pipeline called TATER to search for transits in the photometry from each star using the BLS (Kovács et al. 2002) and TLS (Hippke and Heller 2019) search algorithms. We vetted any signals at SDE  $> 8$  (1814 total) with the LEO-vetter Python package (Kunimoto 2024). Then we subjected all candidates that passed vetting (435 total) to statistical validation with the TRICERATOPS Python package (Giacalone and Dressing 2020; Giacalone et al. 2021).

These efforts resulted in the validation of 13 planets; 4 of those have not been previously validated, and are thus new contributions to the known planet population. All 13 planets were previously known planet candidates, have orbital periods  $< 10$  d, and orbit F-type stars. Although we set out to find new planets in known planetary systems, all 13 of these newly validated planets were previously solitary planet candidates; thus, none of them have any known planetary siblings. Although these planets may truly be solitary, it is also quite possible another transit detection pipeline and/or additional photometry may reveal additional siblings.

One of the newly validated planets is a sub-Jupiter: TIC 305424003.01 (TOI 907.01,  $P = 4.59$  d,  $R_p = 8.8_{-2.2}^{+0.4} R_{\oplus}$ ); this planet also has a forthcoming independent mass confirmation (Neilsen et al. in prep; HARPS ESO programme ID 0103.C-0874). The other three newly validated planets are all sub-Neptunes: TIC 281575427.01 (TOI 205.01,  $P = 4.25$  d,  $R_p = 2.39_{-0.10}^{+0.11} R_{\oplus}$ ), TIC 183593642.01 (TOI 355.01,  $P = 1.04$  d,  $R_p = 2.79_{-0.18}^{+0.15} R_{\oplus}$ ), and TIC 421894914.01 (TOI 1056.01,  $P = 5.31$  d,  $R_p = 2.54_{-0.11}^{+0.12} R_{\oplus}$ ).

## Chapter 5

# Detection of H<sub>2</sub>O and CO<sub>2</sub> in the Atmosphere of the Hot Super-Neptune WASP-166b with JWST

We present and analyze James Webb Space Telescope (*JWST*) transmission spectroscopy observations of the hot super-Neptune, WASP-166b. Our proposed Small GO program involves observations with NIRISS SOSS Order-1 and NIRSpec BOTS G395M/F290LP with the aim of providing unprecedented insights into the key molecular features and formation pathway of WASP-166b. We use state-of-the-art data reduction tools like Ahsoka and **Eureka!** and atmospheric retrieval tools like POSEIDON and PLATON to determine the atmospheric composition of WASP-166b, explore formation scenarios, and thus investigate formation theories for the Hot Neptune Desert. We detect the presence of H<sub>2</sub>O (20.22 $\sigma$  significance) and CO<sub>2</sub> (4.90 $\sigma$ ) in the planet atmosphere, and report non-detections of SO<sub>2</sub>, NH<sub>3</sub>, and an observable cloud deck. We also find a high planetary metallicity ( $Z = 397^{+62}_{-54}$ ) and marginally substellar C/O ratio ( $C/O = 0.49^{+0.10}_{-0.16}$ ), which may suggest a formation pathway for WASP-166b that includes planetesimal accretion followed by core erosion or photoevaporation. These findings point to mechanisms that can create substellar C/O ratios and superstellar metallicities, like photoevaporation and core erosion, as important components of the formation of the Hot Neptune Desert.

### 5.1 Introduction

Although the current known exoplanet population has by now exceeded 5000, only a small fraction have had any constituents of their atmospheres measured. According to the NASA Exoplanet Archive (accessed 2024 Feb 2), only 235 of 5572 known exoplanets (< 5%) have



an observed planetary spectrum of 5 or more points. And yet, exoplanet atmospheres are quickly becoming one of the most fruitful areas of study for understanding planet formation, evolution, and demographics.

In this paper we present results from atmospheric investigations of WASP-166b, a hot super-Neptune ( $P = 5.44$  d,  $M_p = 32.1 \pm 1.6 M_\oplus$ ,  $R_p = 7.1 \pm 0.3 R_\oplus$ ). This planet is located at the edge of the Hot Neptune Desert, a region of parameter space at high insolation fluxes and intermediate planet radii that is extremely sparsely populated (see Fig. 5.1). WASP-166b is therefore part of a rare planet class and worthy of investigation to more fully understand the nature and formation mechanisms of the Hot Neptune Desert.

WASP-166b was originally detected via transit in photometry collected by the WASP survey over 2006 – 2012; it was then followed up with RV mass measurement and confirmation from CORALIE and HARPS over 2014 – 2018 Hellier et al. (2019). Then Bryant et al. (2020) analyzed additional transits of WASP-166b collected in February 2019 with the Next Generation Transit Survey (NGTS) and the Transiting Exoplanet Survey Satellite (*TESS*) in order to further refine the transit ephemeris and planet radius. The first report of an atmospheric constituent for WASP-166b came from Seidel et al. (2020) who reported a tentative ( $3.4\sigma$ ) detection of neutral sodium through ground-based HARPS transmission spectroscopy. This tentative detection was subsequently confirmed with additional ground-based transmission spectroscopy from ESPRESSO (Seidel et al. 2022), helping demonstrate the goodness of WASP-166b for additional atmospheric characterization. Doyle et al. (2022) also analyzed those same ESPRESSO observations, utilizing the reloaded Rossiter McLaughlin technique (Cegla et al. 2016) and measuring the sky-projected star-planet obliquity. They found the planet orbit to be well aligned with the stellar spin axis ( $\lambda = -15.52^{+2.85}_{-2.76}$  degrees), pointing toward planet formation within a protoplanetary disk. Further analysis of the same ESPRESSO observations (Lafarga et al. 2023) led to a tentative detection of water vapor and a suggestion of either low water abundance or high altitude clouds.

We present here our transmission spectroscopy analysis of WASP-166b with the goal of constraining molecular abundances, estimating the overall atmospheric metallicity, and determining the C/O ratio. These constraints allow us to investigate the formation pathway of WASP-166b in order to explore the origins of the Hot Neptune Desert.

In Section 5.2, we present our observations of WASP-166b. In Section 5.3, we discuss our data reduction procedure for both transits and corresponding *JWST* instruments. In Section 5.4, we conduct atmospheric retrievals and forward modeling on the reduced planetary spectrum. Then we present the results of our reduction and analysis in Section 5.5. Finally, we present our summary and conclusions in Section 5.6.

## 5.2 Observations

We obtained *JWST* transmission spectroscopy during two transits of WASP-166b. These observations were part of *JWST* Cycle 1 General Observer (GO) program 2062 (PI: Andrew Mayo, Co-PI: Dressing). The first observation was obtained on 31 Dec 2023 at 03:03 --

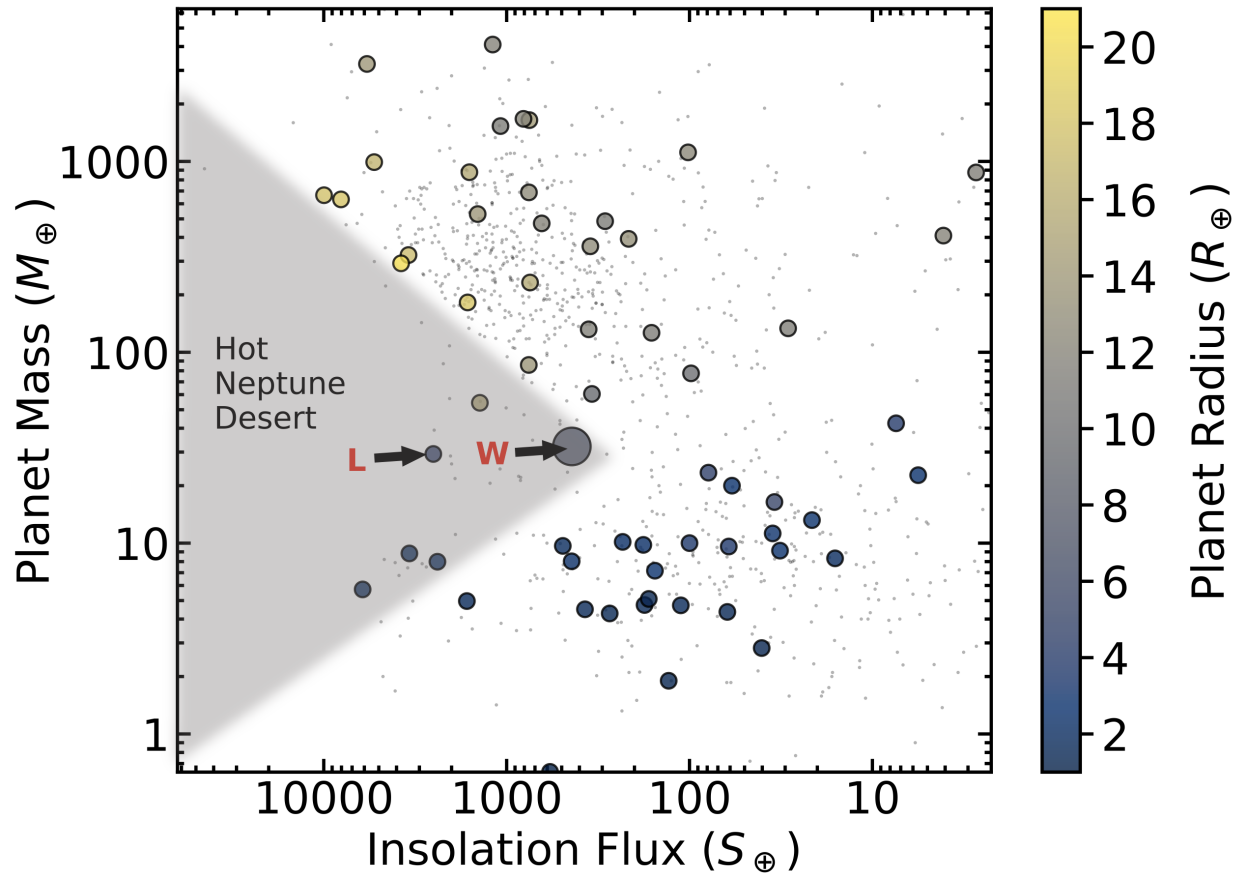


Figure 5.1: Insolation flux versus planet mass, with the Hot Neptune Desert labeled on the left. Small black dots are confirmed exoplanets; large dots colored by planet radius are confirmed planets with mass and radius uncertainties  $< 10\%$  and bright host stars ( $J < 9$ ). Our target is WASP-166b (“W”); LTT 9779b (“L”) is also shown and discussed later in the text (see Section 5.5).

Table 5.1: System parameters used in this paper. (1) Hellier et al. (2019), (2) Doyle et al. (2022).

Parameter	Value	Reference
WASP-166		
$M_*$ ( $M_\odot$ )	$1.19 \pm 0.06$	(1)
$R_*$ ( $R_\odot$ )	$1.22 \pm 0.06$	(1)
$T_{\text{eff}}$ (K)	$6050 \pm 50$	(1)
[Fe/H]	$0.19 \pm 0.05$	(1)
WASP-166b		
$P$ (days)	$5.44354215^{+0.00000307}_{-0.00000297}$	(2)
$t_0$ (BJD-2457000)	$1524.40869201^{+0.00030021}_{-0.00029559}$	(2)
$a$ (au)	$0.0668^{+0.0040}_{-0.0044}$	(2)
$i$ (deg)	$88.85^{+0.74}_{-0.94}$	(2)
$R_p$ ( $R_{\text{Jup}}$ )	$0.6155^{+0.0306}_{-0.0307}$	(2)
$M_p$ ( $M_{\text{Jup}}$ )	$0.101 \pm 0.005$	(1)
$T_{\text{eq}}$ (K)	$1270 \pm 30$	(1)

12:54 UTC with NIRISS, the Near Infrared Imager and Slitless Spectrograph (Albert et al. 2023; Doyon et al. 2023). It was collected in Single Object Slitless Spectroscopy (SOSS) mode (Order-1) covering a wavelength range of 0.9 to 2.8  $\mu\text{m}$  at a native Spectral Resolving Power (R) of  $\sim 650$  at 1.25  $\mu\text{m}$ .

The NIRISS SOSS science observation employed the GR700XD grism combined with the clear filter, making use of the SUBSTRIP96 subarray (2048 columns by 96 rows). The transit observations comprised 4836 integrations, with 2 groups per integration. Our effective exposure time during the observational window was 21413.808 s, yielding an effective integration time of 4.428 s (21413.808/4836). We added a recommended GR700XD/F277W exposure following our science exposure<sup>1</sup>, which included a total of 20 integrations, with 2 groups per integration.

The second observation was obtained on 16 Jan 2024 at 11:53 –– 21:01 UTC with NIRSpec, the Near Infrared Spectrograph (Birkmann et al. 2022; Böker et al. 2023; Espinoza et al. 2023; Jakobsen et al. 2022). It was collected in the Bright Object Time Series (BOTS) mode using the G395M grating and F290LP filter, covering a wavelength range from 2.80 to 5.18  $\mu\text{m}$  with  $R \sim 1000$  at 3.95  $\mu\text{m}$ .

The NIRSpec data was taken using the 1.6'' square aperture (S1600A1) with the SUB2048 subarray (2048 pixel columns by 32 rows on the NRS1 detector), and NRSRAPID readout pattern. Spectra were dispersed across approximately 1320-pixel columns of the subarray, with moderate curvature of the trace. The observation comprised a total of 8880 integrations

<sup>1</sup>See NIRISS SOSS recommended strategies at <https://jwst-docs.stsci.edu/>

taken in a single exposure, roughly centered around the 3.6 h transit. The observation was set up for maximum efficiency while remaining below an 80% full well threshold to avoid detector non-linearity. Due to the brightness of WASP-166 we used 3 groups per integration, resulting in an effective integration time of 2.706 s.

## 5.3 Analysis

Once our transit observations had been collected, we reduced the data from pixel-level data to planetary transmission spectra. In the following subsections we present and detail our data reduction procedures for the NIRISS SOSS and NIRSpec instruments.

### NIRISS SOSS Data Reduction

We used the *Ahsoka* pipeline (Louie et al. in prep) in our NIRISS SOSS analysis. The *Ahsoka* pipeline is comprised of six separate stages, and combines software modules from the *JWST* Science Calibration (Bushouse et al. 2023), *supreme-SPOON* (Feinstein et al. 2023; Radica et al. 2023), *nirHiss* (Feinstein et al. 2023), and *Eureka!* (Bell et al. 2022) pipelines. Additionally, we found that applying the *nirHiss* spectral box extraction routine to our data resulted in excessive scatter in our extracted stellar spectra. We therefore developed a custom optimal extraction routine for NIRISS SOSS data based on the procedures outlined in Horne (1986).

Below, we describe our application of *Ahsoka* detector-level and spectroscopic processing, as well as spectral extraction, to our WASP-166 b data in sections 5.3, 5.3, and 5.3. The output product from *Ahsoka* stage 3 is a time series of 1D (flux versus wavelength) stellar spectra. *Ahsoka* exclusively employs *Eureka!* to generate spectroscopic light curves, fit light curves, and produce the transmission spectrum (*Eureka!* Stages 4, 5, and 6). We describe our application of *Eureka!* to NIRISS SOSS stellar spectra in section 5.3.

#### *Ahsoka* Stage 1: Detector-level processing

We begin by downloading the *uncal.fits* (uncalibrated, pixel-level data) files from MAST, and then perform the following *jwst* pipeline<sup>2</sup> stage 1 detector-level<sup>3</sup> steps: `dq_init`, `saturation`, `superbias`, and `refpix`.

We next apply the *supreme-SPOON* group-level background subtraction and 1/f noise removal steps (Radica et al. 2023). The 1/f noise (Rauscher et al. 2014; Schlawin et al. 2020) is introduced during detector readout. As explained by Albert et al. (2023) and Radica et al. (2023), 1/f noise is one of the last noise sources affecting *JWST* near infrared

<sup>2</sup>[https://jwst-pipeline.readthedocs.io/en/latest/jwst/user\\_documentation/introduction.html](https://jwst-pipeline.readthedocs.io/en/latest/jwst/user_documentation/introduction.html)

<sup>3</sup>`calwebb_detector1`, see [https://jwst-pipeline.readthedocs.io/en/stable/jwst/pipeline/calwebb\\_detector1.html](https://jwst-pipeline.readthedocs.io/en/stable/jwst/pipeline/calwebb_detector1.html)

(NIR) detector data, and should therefore be one of the first noise sources removed, which in turn requires removal at the group level. During the 1/f noise removal step, we must mask or remove sources of flux that could bias our results, which include field star contaminants, target star flux, and Zodiacal light. The location of field star contaminants can be masked using the F277W exposure, while target star flux is masked by using the spectral trace.<sup>4</sup>

The **supreme-SPOON** background subtraction step operates by scaling the STScI background model<sup>5</sup> to group-level median frames of our observations. The 2 median frames (one for each group) are created from the out-of-transit integrations for each of the 2 groups (Radica et al. 2023). Scaling was performed in a small region in the lower left of our median frames unaffected by other flux sources, located at pixel locations:  $x \in [5,401]$ ,  $y \in [5,21]$ . In applying this step to our data, we found that Zodiacal light subtraction was unnecessary in the stage 1 group-level integrations. (The **supreme-SPOON** background subtraction step yielded a scale factor of 0 for both group-level median frames.) Figure 5.2 depicts the first (index 0) **refpix** integration frame for group 2 before and after the background subtraction step is applied.

We next apply the **supreme-SPOON** group-level 1/f noise subtraction algorithm, masking any field star contaminants (negligible for our data, see Figure 5.3) and spectral traces. Here, the noise-weighted average of each column in the group-level median frames is computed, and this is subtracted from each column of the raw image frames for each group. The final step in the 1/f noise subtraction algorithm is to add the background noise back into the image frames to ensure that additional steps in the **Ahsoka** pipeline are applied to the as-observed astrophysical images.<sup>6</sup>

The F277W filter blocks those wavelengths  $\lesssim 2.6 \mu\text{m}$ , and thus allows only the longest wavelengths of the order 1 spectrum to be dispersed upon the subarray. Additionally, the F277W exposure may be used to find the locations of any order 0 field star contaminants, since order 0 field star contaminants only appear at column pixel indices higher than  $\sim 700$  (Albert et al. 2023). The median image of our F277W integrations in Figure 5.3 indicates that our observations have no significant order 0 contaminants.

The **Ahsoka** detector-level reduction concludes with the following **jwst** pipeline steps: **linearity**, **jump**, **ramp\_fitting**, and **gain\_scale**. Since our NIRISS SOSS data only included 2 groups, the **jump** step was automatically skipped, as discussed in section 5.3.

## Ahsoka Stage 2: Spectroscopic processing

We next apply stage 2 spectroscopic processing<sup>7</sup> to our stage 1 output files, which are similar to the *rateints.fits* files used as inputs to our NIRSpec stage 2 processing (see §5.3). We begin with the following **jwst** pipeline steps: **assign\_wcs**, **srctype**, and **flat\_field**.

<sup>4</sup>See section 5.3 for a description of our procedures determining spectral trace location and width.

<sup>5</sup>See SOSS Background Observations at <https://jwst-docs.stsci.edu>.

<sup>6</sup>Refer to Radica et al. 2023 for additional details.

<sup>7</sup>`calwebb_spec2`, see [https://jwst-pipeline.readthedocs.io/en/latest/jwst/pipeline/calwebb\\_spec2.html](https://jwst-pipeline.readthedocs.io/en/latest/jwst/pipeline/calwebb_spec2.html)

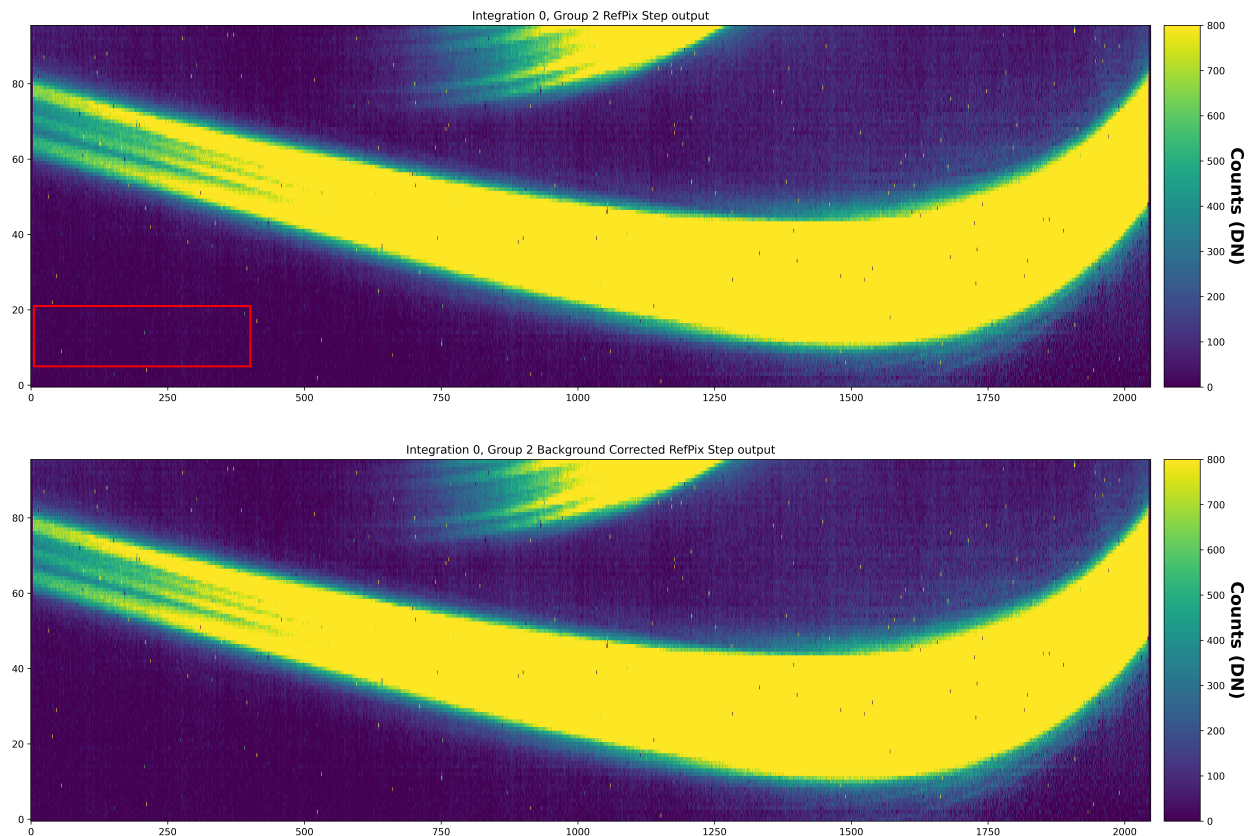


Figure 5.2: First (index 0) `refpix` integration frame for group 2 before and after the background subtraction step is applied. The box we used to scale the STScI background model is outlined in red.

We then again employ the `supreme-SPOON` background subtraction algorithm, using the same procedures and scaling region as with the detector-level process, except that only one median frame need be constructed during stage 2. Here, the computed background scaling factor was 0.76582.

We conclude Stage 2 with the `supreme-SPOON BadPix` custom cleaning step to flag and correct outlying/hot pixels (Radica et al. 2023). The `BadPix` step first creates a median frame using the out-of-transit integrations from the background subtraction step. Then, each pixel of the median frame is compared to surrounding pixels. Any pixel with a NaN or negative value, or that differs from surrounding pixels by more than  $5\sigma$ , is flagged. A mask records the locations of the flagged pixels on the NIRISS SOSS subarray, and flagged pixels are then replaced by the median value of surrounding pixels. Finally, the outlying/hot pixels (indicated by the mask) in each integration frame from the Stage 2 background subtraction step are replaced by the corresponding pixel values on the corrected median frame, which is

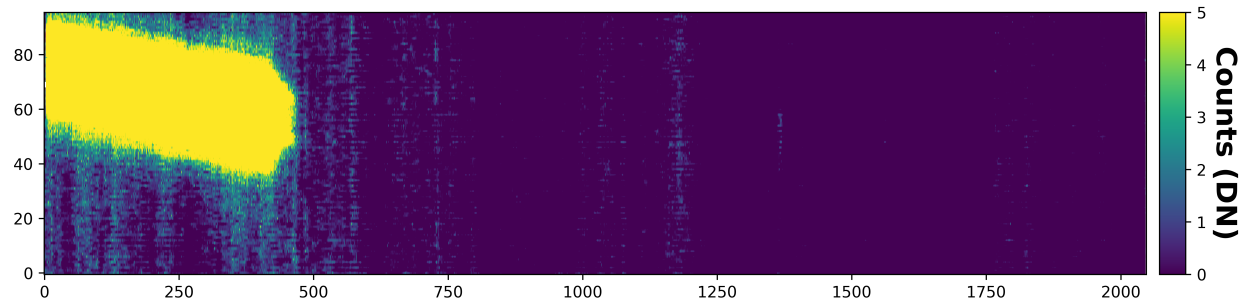


Figure 5.3: Median image of our F277W integrations. The F277W filter blocks those wavelengths  $\lesssim 2.6 \mu\text{m}$ , and thus allows only the longest wavelengths of the order 1 spectrum to be dispersed upon the subarray. The F277W exposure may be used to find the locations of any order 0 field star contaminants, which would appear as bright chevron shapes if present. Our observations have no significant order 0 contaminants.

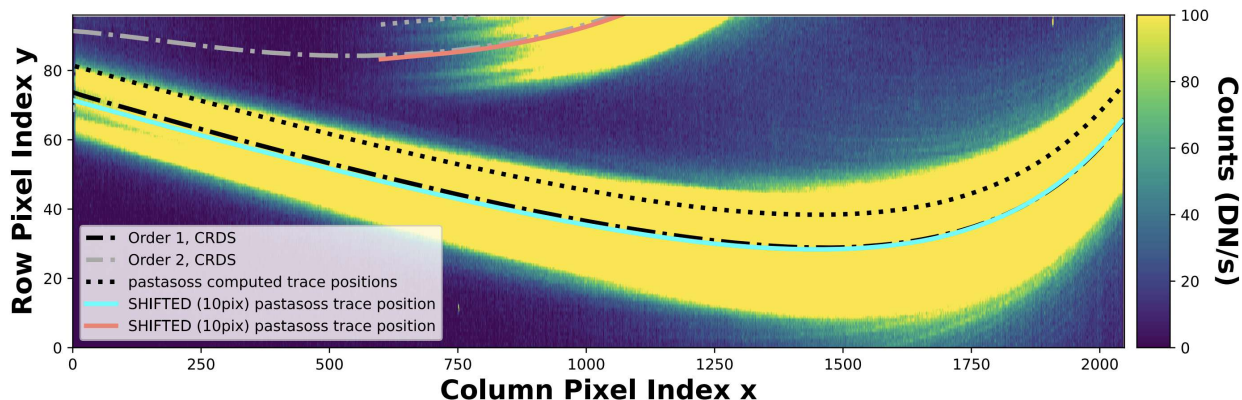


Figure 5.4: Comparison of the CRDS spectral trace, the `pastasoss`-derived spectral trace, and the `pastasoss` trace shifted by 10 pixels, all overplotted on our `BadPix` output frame from integration 0. We found that the `pastasoss` trace shifted by 10 pixels aligned best with our data.

scaled to the transit white light curve.

### Ahsoka Stage 3: Spectral extraction

The `Ahsoka` pipeline described by Louie et al. (in prep) produces a time series of 1D (flux versus wavelength) stellar spectra by applying the box extraction algorithm from `nirHiss` to the `BadPix` step output frames derived in Stage 2. `Ahsoka` employs the STScI-developed

`pastasoss` package<sup>8</sup> (Baines et al. 2023a,b) to determine the spectral trace position and wavelength solution. During observations, both the NIRISS SOSS spectral trace and wavelength solution are known to vary by a few pixels depending upon the precise position of the pupil wheel, which aligns the GR700XD grism with the optical path. The `pastasoss` package takes the pupil wheel position into account to determine the order 1 spectral trace position and wavelength solution to sub-pixel level accuracy.

Direct application of both the `pastasoss` package and `nirHiss` box extraction algorithm to our SUBSTRIP96 data were problematic. Below, we describe in turn how we overcame problems encountered with these two algorithms.

The `pastasoss` package was developed and tested on the SUBSTRIP256 subarray. We found that the `pastasoss`-derived trace was not centered upon the spectral trace of our SUBSTRIP96 data. Upon further investigation, we discovered that the order 1 spectrum for SUBSTRIP96 is shifted 10 pixels from the trace on SUBSTRIP256, as described by Albert et al. (2023). Figure 5.4 compares the CRDS spectral trace, the `pastasoss`-derived spectral trace, and the `pastasoss` trace shifted by 10 pixels, all overplotted on our `BadPix` output frame from integration 0. We found that the `pastasoss` trace shifted by 10 pixels aligned best with our data, and used that trace moving forward.

To apply the `nirHiss` box extraction algorithm to our data, we tested a variety of spectral extraction widths varying between 24 and 36 pixels, ultimately choosing a width of 30 pixels. To select the best extraction width, we computed the mean absolute deviation (MAD) for out-of-transit points in the raw white light curve produced from our data. We created the raw white light curve by summing the flux within the extraction width for all wavelengths, computing total flux for each of the 4836 integrations. We then normalized the flux for each integration by the median flux of the out-of-transit integrations. For this computation, we used integration indices [0,1750] and [4000,4835] as the out-of-transit points. Our extraction width of 30 pixels minimized out-of-transit MAD. Figure 5.5 shows the raw white light curve for the 30 pixel width box extraction.

Once the extraction width is determined, the `nirHiss` box extraction algorithm creates one stellar spectrum for each integration by summing the flux across the extraction width in each column. This provides a time series of 1D stellar spectra (flux versus wavelength). The extracted stellar spectra for all integrations are overplotted in Figure 5.6. Examination of the plot reveals an excessive number of outliers in our stellar spectra. We believe some of the outliers may be due to cosmic rays, which would normally be flagged during the *JWST* pipeline jump step, which was automatically skipped for our data since we only have 2 groups.

To deal with the outliers in our stellar spectra, we opted to create a custom optimal extraction routine for NIRISS SOSS data based upon the procedures outlined in Horne (1986).

---

<sup>8</sup><https://github.com/spacetelescope/pastasoss>



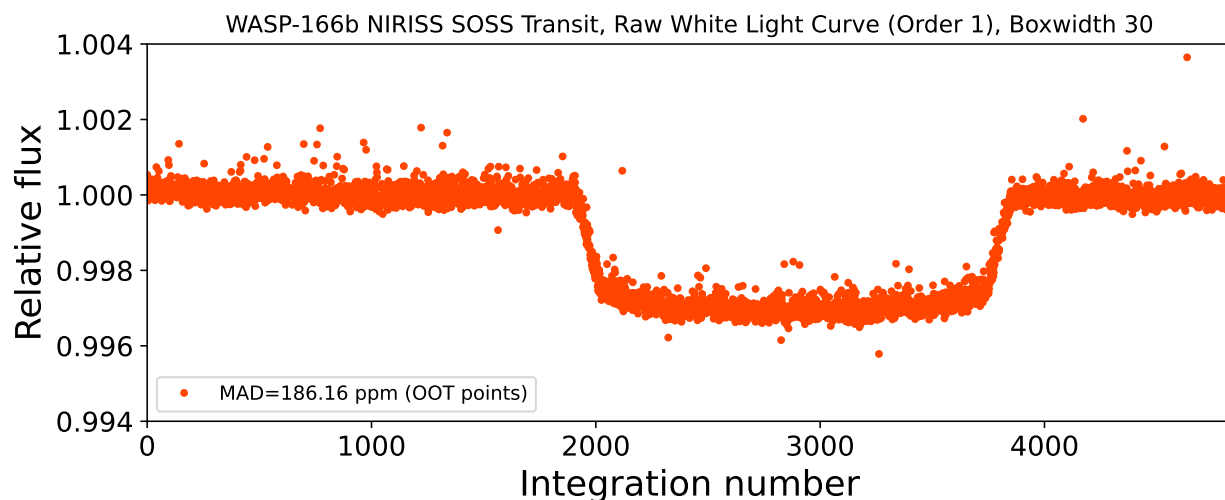


Figure 5.5: Raw white light curve for the 30 pixel width `nirHiss` box extraction. We normalized the flux for each integration by the median flux of the out-of-transit integrations. For this computation, we used integration indices [0,1750] and [4000,4835] as the out-of-transit points.

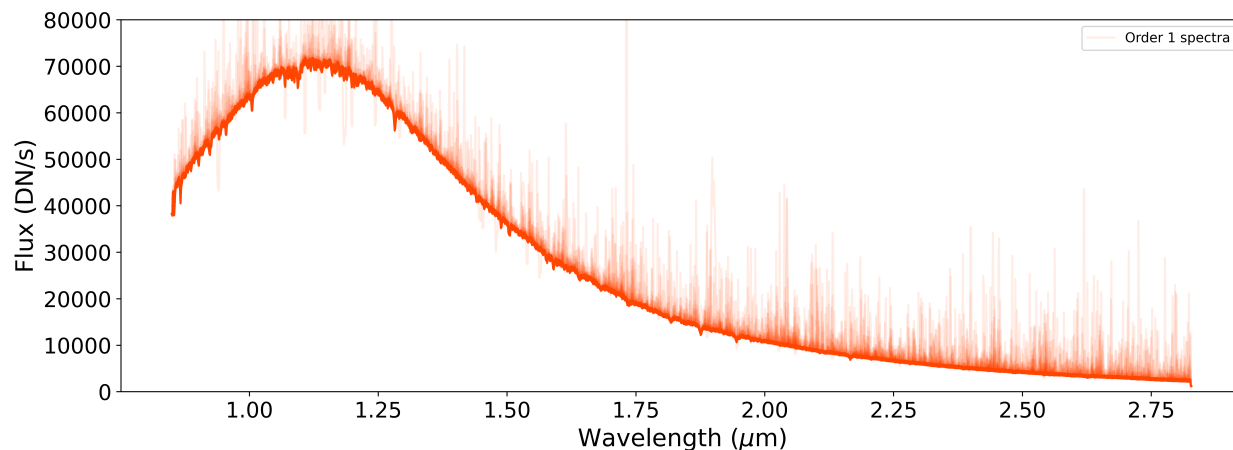


Figure 5.6: Extracted 1D stellar spectra (flux versus wavelength) overplotted for all integrations. Each stellar spectrum is plotted in partially transparent color ( $\alpha = 0.1$  in `matplotlib` plot), such that the most opaque region corresponds to the expected stellar spectrum, while the more transparent regions indicate outlying values of flux. We see an excessive number of outliers in our initially extracted stellar spectra, and thus opted to implement an optimal extraction routine.

**Ahsoka Stages 4, 5, 6: Eureka! application**

Our application of *Eureka!* to NIRISS SOSS was similar to that described for NIRSpec G395M stages 3, 4, and 5 (see §5.3, §5.3, and §5.3). In this section, we highlight the differences in our NIRISS SOSS analysis compared to NIRSpec.

We applied *Eureka!* stage 4 to both white light and spectroscopic light curves. For the spectroscopic light curves, we binned our time series of 1D stellar spectra into 100 evenly spaced channels across the NIRISS SOSS bandpass, from 0.83 to 2.81  $\mu\text{m}$ . For each light curve, we applied a box-car filter of 10 integrations in length and clipped any  $5\sigma$  outliers, performing 5 iterations of sigma clipping, removing  $<1.9\%$  of all integrations for any one light curve.

During *Eureka!* stage 4, we also computed quadratic limb darkening coefficients for each spectral channel using the ExoTiC-LD package<sup>9</sup> (Grant and Wakeford 2022).

We used *Eureka!* stage 5 to fit both white light and spectroscopic light curves. As with our NIRSpec analysis, we fixed the WASP-166b orbital parameters—period ( $P$ ), inclination ( $i_p$ ), semi-major axis ( $a/R_*$ ), eccentricity ( $e$ ), and argument of periapsis ( $\omega$ )—to the Hellier et al. 2019 and Doyle et al. 2022 values listed in Table 5.2 throughout our analysis.

Like our NIRSpec stage 5 analysis, we modeled the transit light curves using the *batman* package (Kreidberg 2015b), used a polynomial model with constant and linear coefficients  $c0$  and  $c1$  to model systematics, and employed a scatter multiplier to model white noise.

During our white light curve analysis, we fit for  $R_p/R_*$  using a wide normal distribution  $N(0.05177, 0.005)$  as a prior, and for  $t_0$  using the prior distribution  $N(60309.39051721021, 0.05)$ , which was estimated using literature values of period and  $t_0$ , combined with the known time of our observations. We fit for quadratic limb darkening coefficients on a uniform distribution  $U(0, 1)$  using the ExoTiC-LD coefficients computed in stage 4 as prior limb darkening values.

We used prior distributions on our systematic parameters of  $N(1.0, 0.05)$  for  $c0$  and  $N(0.0, 0.01)$  for  $c1$ , and we used a prior distribution of  $N(1.4, 2)$  for the scatter multiplier.

From the white light curve fit, we derived a central transit time  $t_0$  of  $60309.3909657_{-0.000046}^{+0.000046}$  BMJD<sub>TDB</sub>, which has an uncertainty of 3.9744 seconds. We fixed the central transit time to the median value of  $t_0$  during our spectroscopic fits. From the white light curve we saw no unusual events or substantial systematic trends (e.g. saturation, mirror tilt, High Gain Antenna move disturbance, etc.).

During our spectroscopic fits, we fit for all the same parameters *except* for  $t_0$ , which was fixed. Our prior distributions for all fit parameters were the same as those for our white light curve fits. In each spectral channel, we again used the ExoTiC-LD coefficients computed in stage 4 as prior limb darkening values.

As with the NIRSpec analysis, we did not manually clip any integrations, since we saw no evidence of failed or degraded integrations in the stage 4 2-D light curve.

We used the *emcee* (Foreman-Mackey et al. 2013) affine invariant Markov Chain Monte Carlo package (Goodman and Weare 2010) within the *Eureka!* pipeline for NIRISS SOSS

---

<sup>9</sup><https://exotic-ld.readthedocs.io/en/latest/>

stage 5 light curve fitting. For each of our `emcee` fits, we ran 1000 steps, discarding the first 500 as burn-in, using 200 walkers.

## NIRSpec Data Reduction

The primary tool we employed for our NIRSpec data reduction was `Eureka!` v0.10 (Bell et al. 2022). The full `Eureka!` data-reduction pipeline takes *JWST* time-series data through six stages, starting with the *uncal.fits* data (i.e. the raw detector pixel-level flux values) all the way through light curve fitting, and final generation of transmission spectra. The `Eureka!` pipeline has been used on many *JWST* atmospheric analyses and has produced reliable results (Ahrer et al. 2023; Alderson et al. 2023; JWST Transiting Exoplanet Community Early Release Science Team et al. 2023b; Lustig-Yaeger et al. 2023; Moran et al. 2023; Rustamkulov et al. 2023).

Throughout the data reduction process, our goal was to properly calibrate the data and minimize correlated or systematic noise without degrading or introducing bias. Our procedures for analysis of the NIRSpec WASP-166b data are discussed below.

Our data reduction procedure loosely followed the initial steps for `Eureka!` [V2], a customization of the `Eureka!` pipeline described and applied in Alderson et al. (2023) for their reduction of NIRSpec G395H two-detector observations. Our observations were made with the NIRSpec G395M (single detector) configuration. To the best of our knowledge a description of the data reduction procedure for G395M BOTS observations of exoplanet transmission spectroscopy has not previously been published. While the procedures for G395H reduction were a useful starting point, we tailored our procedures for G395M data.

### JWST Pipeline Stage 1: Detector-level processing

We started with the *rateints.fits* files (i.e. ramp-fitting calibrated flux values) available from the Mikulski Archive for Space Telescopes (MAST).<sup>10</sup> These files were generated by the default Stage 1 of the *JWST* Science Calibration Pipeline (*JWST* Pipeline, version 1.12.5)<sup>11</sup>. Stage 1 applies detector-level corrections to raw non-destructively read “ramps” from the uncalibrated *uncal.fits* data in order to produce 2-dimensional count rate (slope) images per exposure. The corrections made in this stage include detector dark current subtraction, identifying known bad pixels using the CRDS map, adjustments for detector non-linearity, dealing with cosmic ray hits, and many other effects.<sup>12</sup>

Kirk et al. (2024) has suggested that the default ‘jump’ detection step in the *JWST* Pipeline Stage 1 could be unreliable for small group numbers. The `jump` step will automatically skip execution if the input data contain less than 3 groups per integration.<sup>13</sup> As

<sup>10</sup>The data described here may be obtained from the MAST archive at <https://dx.doi.org/TBD>.

<sup>11</sup>[https://jwst-pipeline.readthedocs.io/en/latest/jwst/user\\_documentation/introduction.html](https://jwst-pipeline.readthedocs.io/en/latest/jwst/user_documentation/introduction.html)

<sup>12</sup>[https://jwst-pipeline.readthedocs.io/en/latest/jwst/pipeline/calwebb\\_detector1.html](https://jwst-pipeline.readthedocs.io/en/latest/jwst/pipeline/calwebb_detector1.html)

<sup>13</sup><https://jwst-pipeline.readthedocs.io/en/latest/jwst/jump/description.html>

our NIRSpec observation only used 3 groups per integration, we paid close attention to the effects of the jump step. However, we saw no evidence of systematics or large scatter in the transmission spectrum with the default `jump` step. We conducted a test case feeding the `uncal.fits` data through **Eureka!** Stage 1 while skipping the `jump` step and saw no difference between that and the default *JWST* Pipeline Stage 1 output `rateints.fits` files. The remaining reduction stages were processed through the **Eureka!** pipeline.

### **Eureka! Stage 2: Spectroscopic processing**

Starting with the `rateints.fits` files from MAST, we used **Eureka!** for Stage 2 processing. This stage continues the calibration process of Stage 1, with **Eureka!** serving essentially as a wrapper for the *JWST* Stage 2 pipeline. Based on Early Release Science (ERS) program literature (Ahrer et al. 2023; Alderson et al. 2023; JWST Transiting Exoplanet Community Early Release Science Team et al. 2023b; Lustig-Yaeger et al. 2023; Moran et al. 2023; Rustamkulov et al. 2023), we followed the default steps in this stage, with three exceptions. First and second, this stage typically performs flat-fielding and unit conversions; however, we skipped the `flat_field`<sup>14</sup>, and `phom`<sup>15</sup> steps as they result in a conversion to physical flux units that is not needed for our relative flux measurements. If included, these steps could potentially add noise depending on the accuracy of the latest detector flat fields provided by the Calibration References Data System (CRDS; our data uses version 11.17.5).<sup>16</sup> In addition, the small detector region that is affected by these steps can reduce the precision on background removal (May et al. 2023). None of the data-reduction pipelines used on the NIRSpec ERS program data described by Alderson et al. (2023), including **Eureka!**, performed a flat-field correction. As Alderson et al. (2023) explain: “the available flat fields were of poor quality and unexpectedly removed portions of the spectral trace.”

Third, we skipped the `extract_1d`<sup>17</sup> step since we are using **Eureka!** to perform an “Optimal” spectral extraction in the next stage (Rustamkulov et al. 2023).

### **Eureka! Stage 3: Spectral extraction**

Stage 3 of **Eureka!** begins with a background subtraction step, followed by “Optimal” spectral extraction (Horne 1986) after correcting the curvature of the spectral trace.

The relative position of the spectral trace on the detector is shown in Figure 5.7. Aligning the spectral trace is accomplished by determining the effective center of light in each detector column with a Gaussian fit and integer-shifting each column (standard operating procedure for **Eureka!**) in order to bring this effective peak to the central row of the subarray field.

For the column by column background subtraction we fitted and subtracted a flat median value from each column of the frames that were corrected for curvature, assessing the

<sup>14</sup><https://jwst-pipeline.readthedocs.io/en/latest/jwst/flatfield/index.html>

<sup>15</sup><https://jwst-pipeline.readthedocs.io/en/latest/jwst/phom/index.html>

<sup>16</sup><https://jwst-crds.stsci.edu/>

<sup>17</sup>[https://jwst-pipeline.readthedocs.io/en/latest/jwst/extract\\_1d/index.html](https://jwst-pipeline.readthedocs.io/en/latest/jwst/extract_1d/index.html)

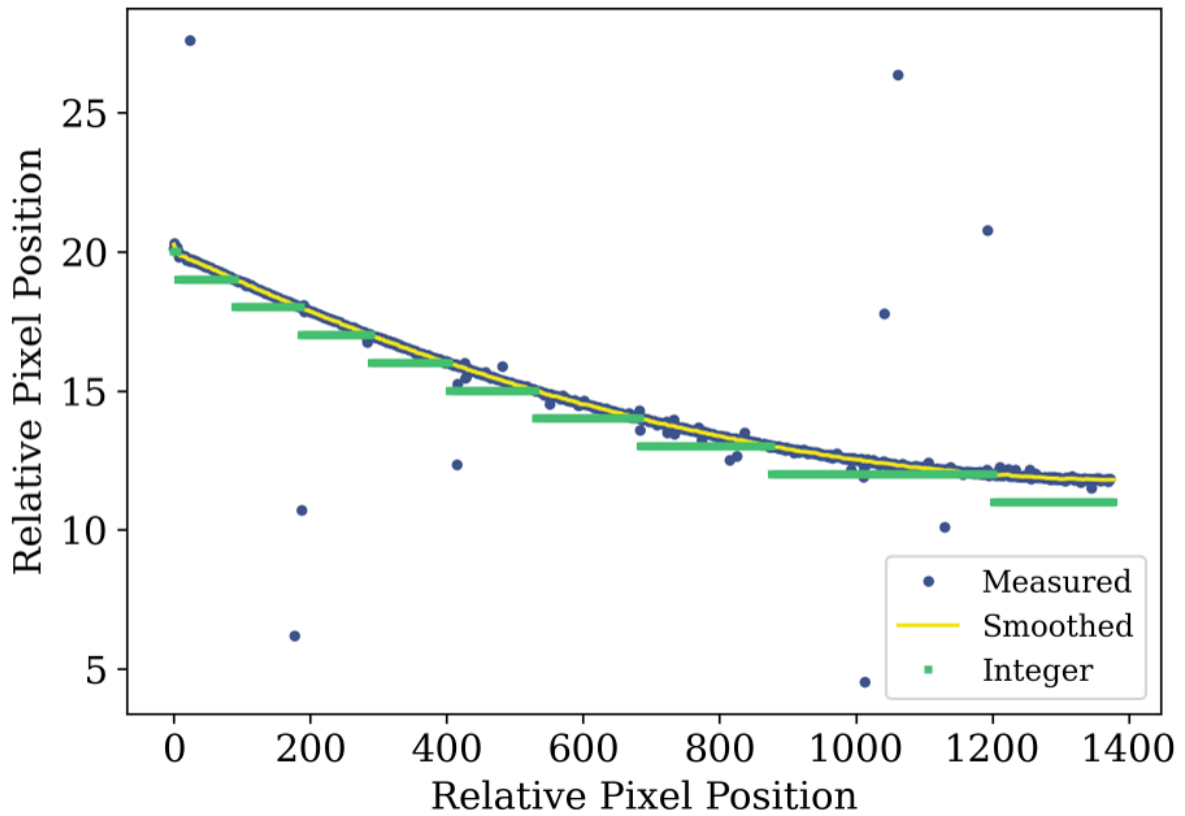


Figure 5.7: The measured, smoothed, and integer-rounded relative position of the spectral trace on the detector determined with the Eureka! atmospheric reduction pipeline (Bell et al. 2022). Significant curvature is evident.

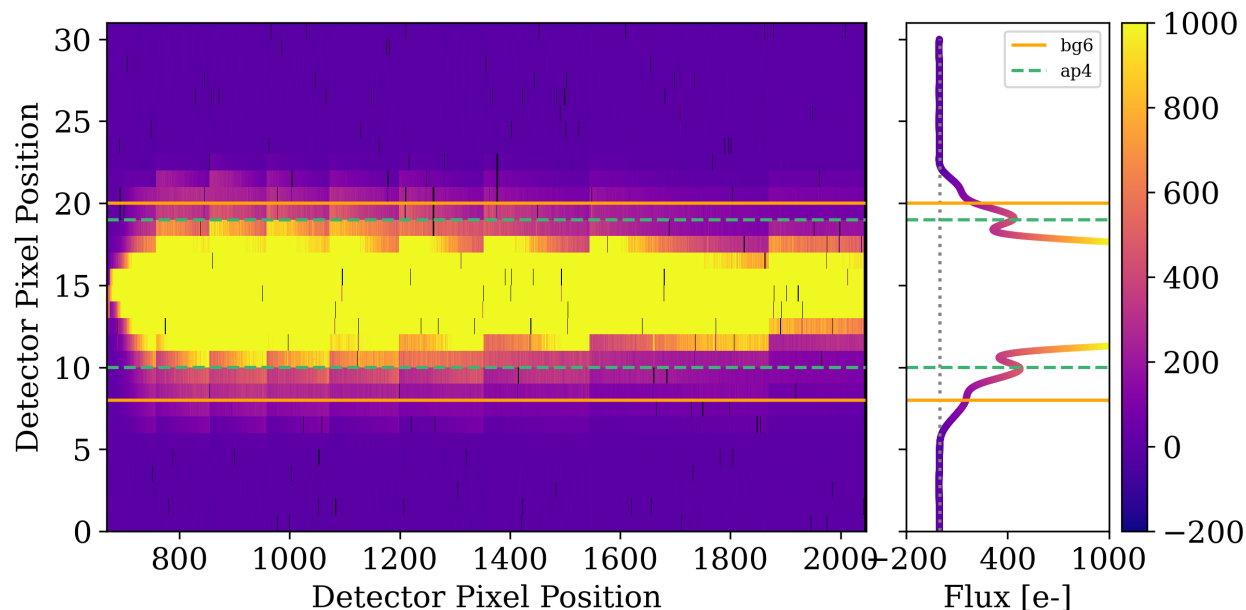


Figure 5.8: The aligned spectral trace and residual background are shown. The background region is outside the bg6 lines, and the spectral extraction aperture is inside the ap4 lines. Outlier pixels can be seen with certain bad pixels previously identified via the CRDS shown in black.

background median using only the pixels that were more than 6 pixels away from the middle row. We also applied a two-step outlier removal process in both time and space, with a  $10\sigma$  double-iteration rejection threshold for temporal outliers and a  $3\sigma$  threshold for spatial outliers, to eliminate the effects of cosmic ray events and prevent distortion from bad pixels in the background correction. We chose these thresholds based on published results that we have referenced, and our own trial and error to balance the background subtraction and filter out obvious outliers.

When constructing the median frame for “Optimal” spectral extraction, we employed an outlier rejection threshold of  $5\sigma$ . For spectral extraction, we used an aperture half-width of 4 pixels on both sides of the center pixel (for a total of 9 pixels, including the central pixel). During step 7 of “Optimal” spectral extraction (Eureka! ecf parameter “p7thresh”), as defined by Horne (1986), we used a spatial outlier rejection threshold value of  $15\sigma$ . No spectral smoothing was applied to the “Optimal” extraction profile. We ran various trial cases to determine the best combination of these background and extraction parameters to achieve the highest precision by minimizing background noise and maximizing extracted flux.

The aligned spectral trace and residual background are shown in Figure 5.8, with the boundaries outlined.

The result of the “Optimal” extraction process is shown for a single integration in Figure

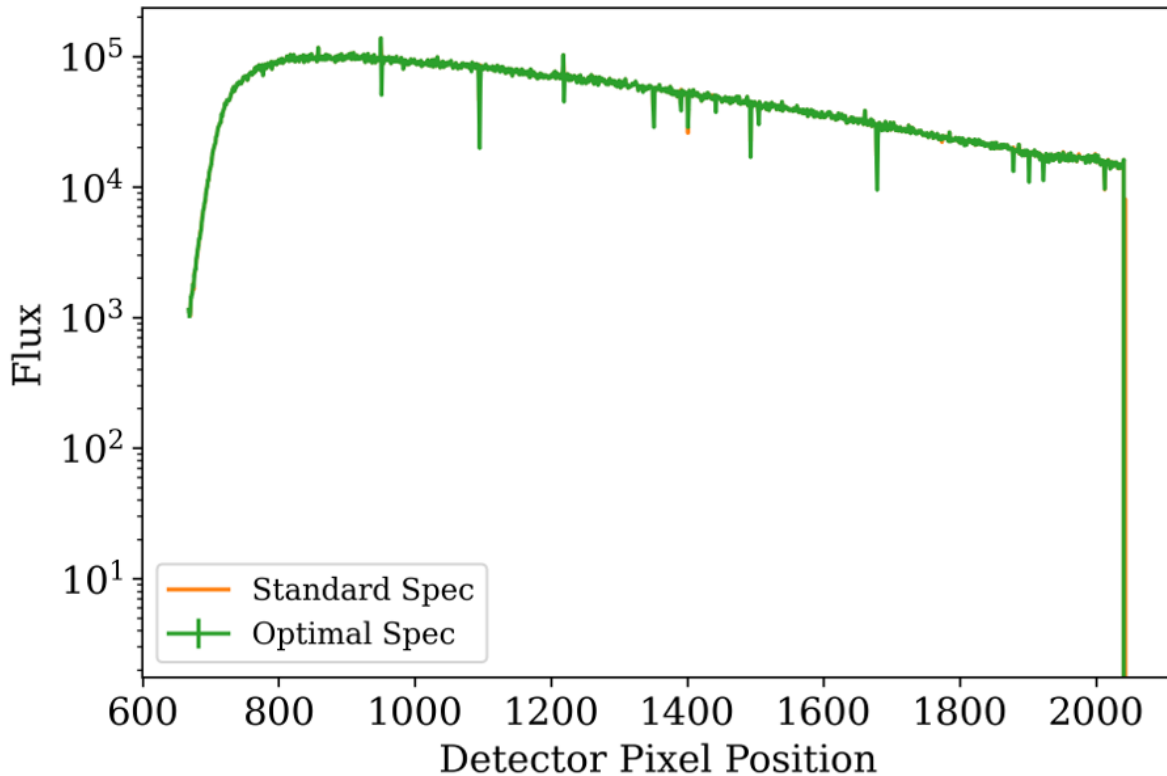


Figure 5.9: 1-D spectrum, with flux versus absolute pixel position for Integration 2. We use the “Optimal” spectrum (Horne 1986) shown in green, although it is almost an exact match to the Standard spectrum, shown in orange. The vertical spikes along the spectral profile indicate suspect pixel columns that were, in some cases, masked in Stage 4

5.9.

Stage 3 produces a time series of 1-D spectra (a 2-D light curve), first by pixel column, and then with the wavelength calibration applied.

#### Eureka! Stage 4: Spectroscopic light curves

Using outputs from the previous stage, **Eureka!** Stage 4 produces spectroscopic light curves by binning the time series of 1D spectra by wavelength. In addition, **Eureka!** generates a broadband (white) light curve. The package also performs sigma clipping of outlier integrations for each light curve at this stage.

Based on careful consideration of the flux level for each pixel across the spectral trace, and, in particular, evidence of bad pixel columns in the 2D light curves generated in Stage 3, we manually constructed a pixel column mask for those situations where the existing CRDS Data Quality (bad pixel) mask or other unmasked outlier pixels could have significantly impacted the fit and level of the inferred peak flux along a column. The final mask included 10 columns ( $\sim 0.8\%$  of the active columns). Our goal in building this mask was to improve the results for the affected wavelength channels, but not to introduce biases that could distort the final transmission spectrum.

For example, in the case of a fixed spectral resolving power ( $R = 100$ ), we extracted the flux from 2.80 to 5.17  $\mu\text{m}$ , splitting the light into 62 spectroscopic channels with bin width increasing in step with wavelength for equal resolution bins. For each light curve, we applied a box-car filter of 5 integrations in length and clipped any  $4\sigma$  outliers. We performed 20 iterations of sigma clipping in this manner. This procedure removed  $< 0.08\%$  of all integrations for any given light curve.

### Eureka! Stage 5: Light curve fitting

Stage 5 of Eureka! is generally concerned with fitting light curves, both broadband (white-light) and narrowband (spectroscopic). The focus, of course, is on determining the value of the transit depth with errors, across the usable wavelength range.

The orbital parameters of WASP-166b (see Table 5.1): period ( $P$ ), inclination ( $i_p$ ), semi-major axis ( $a/R_*$ ), eccentricity ( $e$ ), and argument of periapsis ( $\omega$ ), taken from recent literature (Doyle et al. 2022; Hellier et al. 2019) were calculated from a very high-quality dataset based on multiple transits, with multiple instruments, both ground, and space based. We fixed these parameters throughout our analysis.

We fit the white-light curve of our observation to determine the central transit time (Figure 5.10). The result was  $60325.72131^{+0.000037}_{-0.000035}$  BMJD-TDB (note uncertainty of  $< 4$  seconds) which we fixed to the median value for the analysis of our spectroscopic light curves. Similar to the NIRISS SOSS reduction, we saw no unusual events or substantial systematic trends in the white light curve (e.g. saturation, mirror tilt, High Gain Antenna move disturbance, etc.).

We used `batman` (Kreidberg 2015b) within the Eureka! framework to model the transit light curves.

Throughout our analysis of the white-light and spectroscopic light curves, we fit for the coefficients of our limb darkening model, following the guidance of Espinoza and Jordán (2016). We chose the Eureka! implementation of the widely used quadratic limb darkening model first described by Kopal (1950) and further discussed by Espinoza and Jordán (2015).

For all light curve fits, we kept the following as free parameters: the planet-star radius ratio ( $R_p/R_*$ ), a constant and linear photometric polynomial coefficient ( $c_0$  and  $c_1$ ), the centroid decorrelation parameters (coefficients for linear decorrelation against drift/jitter and PSF width in the spatial direction), and the scatter multiple (a multiplier to rescale



Table 5.2: Key parameter priors for the WASP-166b NIRSpec light curve fits with **Eureka!** (using **dynesty** for fitting).  $N(\mu, \sigma)$  stands for a normal distribution with mean  $\mu$  and std dev.  $\sigma$ ;  $U(a, b)$  stands for a uniform distribution between a and b. The physical and orbital parameter priors are from Hellier et al. (2019) and Doyle et al. (2022). The free white light curve central transit time  $t_{0\_wlc}$  prior was based on the time determined from examination of the **Eureka!** Stage 4 white light curve as well as estimates provided through the NASA Exoplanet Archive transit ephemeris service. The result of the white light curve fitting process gave us a high precision ( $< \pm 4$  sec) central transit time  $t_{0\_slc}$ , which we fixed for our analysis of the spectroscopic light curves.

Parameter	Prior
Physical & orbital parameters	
$R_p/R_*$	$N(0.05177, 0.01)$
$P$ (d)	5.44354215 (fixed)
$t_{0\_wlc}$ (BMJD-TDB)	$N(60325.72451, 0.005)$
$t_{0\_slc}$ (BMJD-TDB)	60325.72131 (fixed)
$i_p$ (deg)	88.85 (fixed)
$a/R_*$	11.83 (fixed)
$e$	0 (fixed)
$\omega$ (deg)	90 (fixed)
Limb-darkening coefficients (quadratic)	
$u1$	$U(0, 1)$
$u2$	$U(0, 1)$
Systematic variables	
$c0$	$N(1.0, 0.01)$
$c1$	$N(0.0, 0.01)$
Centroid decorrelation parameters	
$ypos$	$N(0.0, 0.10)$
$ywidth$	$N(0.0, 10.0)$
White noise parameter	
$scatter\ multiplier$	$N(1.1, 0.4)$

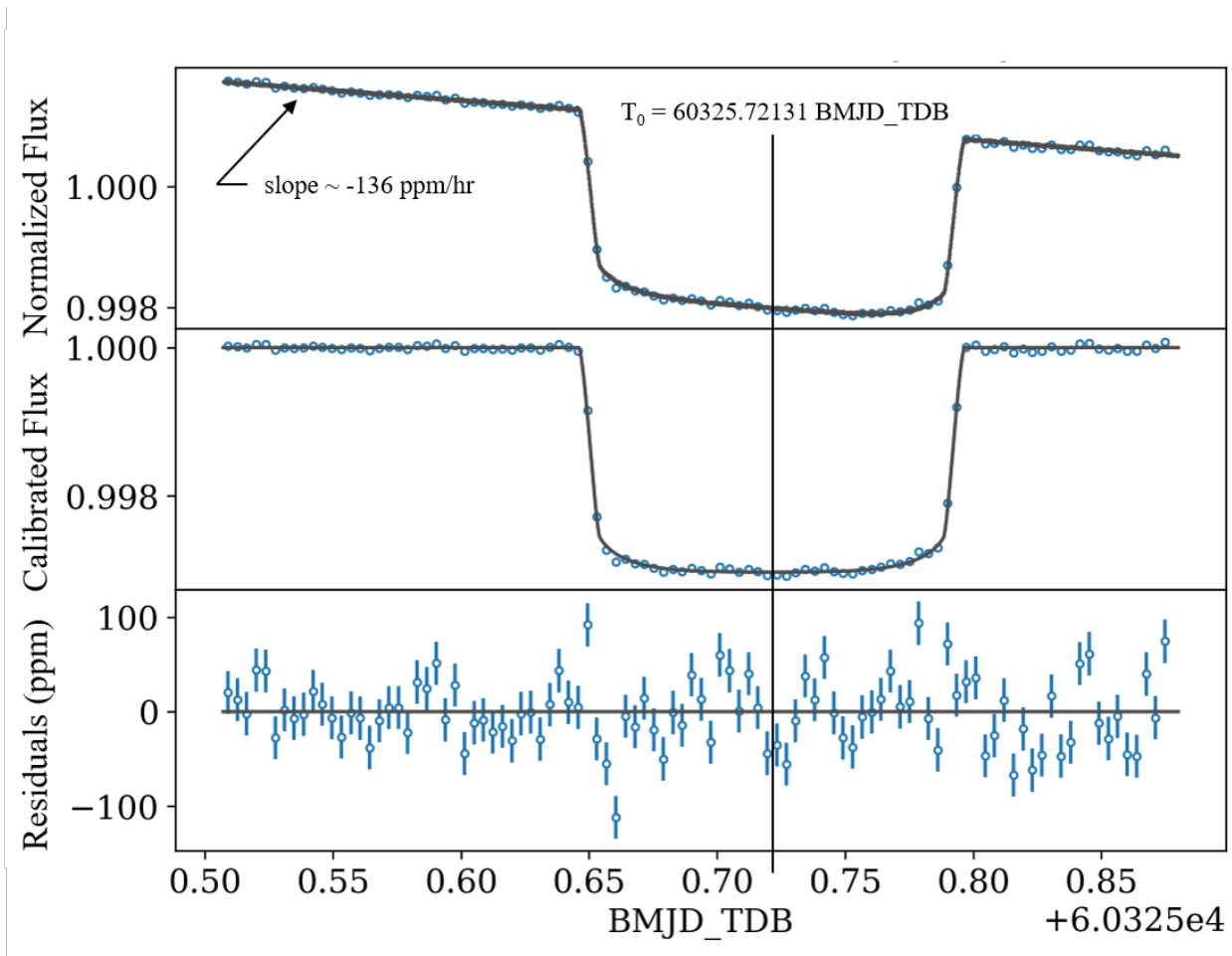


Figure 5.10: Broadband (white) light curve for WASP-166b, showing the fitted central transit time ( $T_0$ ), and showing the exposure-long downward linear trend in normalized flux ( $-136 \text{ ppm hr}^{-1}$ ). We saw no other indication of unusual events or trends in the light curve.

errors and produce a reduced chi-squared value of  $\sim 1.0$ ). Values for the fixed parameters, and prior bounds for the free parameters are shown in Table 5.2.

In our inspection of the 2-D light curves generated in Stages 3 and 4, we did not see any evidence of failed or degraded integrations, so we did not manually clip any integrations from the analysis in this stage.

All light curve fits were performed by the dynamic nested sampling package, **dynesty** (Speagle 2020) within the **Eureka!** pipeline framework and were run until convergence (using 500 live points and a  $\Delta \ln Z$  evidence tolerance of 0.001).

We saw evidence of an exposure-long slope ( $-136 \pm 1$  ppm per hour) in the normalized transit light curves (Figure 5.10). This is similar behavior to what was seen during the NIRSpec commissioning campaign reported by Espinoza et al. (2023). Evidence points to this being a detector-level effect. As of this writing, STScI has not determined the source of this trend, and is continuing to investigate. This slope is removed/flattened in the calibration process of Stage 5 and does not appear to affect our results. We otherwise saw no substantial systematic trends in the data.

### **Eureka! Stage 6: Transmission spectrum**

Stage 6, the final stage of **Eureka!**, creates and displays the planet spectrum in figure and table form using results from Stage 5.

We ran two full (pre-binned) data reduction cases for each instrument. First, we ran a full reduction for  $R = 100$ , which resulted in a total of 62 bins with bin size varying with wavelength. Second, we fixed the bin size to 10 pixels (bin width  $\sim 0.01797 \mu\text{m}$ ), for 132 bins and  $R \sim 221$  at  $3.95 \mu\text{m}$ . The purpose of this case was to provide a consistent set of data matched to a similarly binned (in wavelength) case for NIRISS to move forward into our atmospheric analysis phase.

May et al. (2023) have argued that using pre-binned data at the working resolution of the transmission spectral analysis is the best approach, rather than using the high-resolution data and separately binning it down to the working resolution post-binning. We choose to adopt this approach and use the pre-binned 10-pixel NIRSpec spectra for our downstream analysis.

We show excellent spectral precision with our reduced data. For the case of a constant 10 pixel bin size, we measure transit depth errors from 39 to 108 ppm over the wavelength range. A simulation using PandExo (Batalha et al. 2017) with this binning shows from 3 – 12% better performance than we show; however, according to Espinoza et al. (2023), PandExo likely is underestimating the actual errors by roughly 20%. Our realized precision exceeds the adjusted PandExo results.

## 5.4 Atmospheric Modeling and Retrieval Methods

We conduct atmospheric modeling and retrievals with two different modeling packages, POSEIDON (MacDonald 2023; MacDonald and Madhusudhan 2017) and PLATON (Zhang et al. 2019). We relied on POSEIDON for constraints of individual molecules and used PLATON to estimate the planetary C/O ratio and metallicity. Additionally, we used both POSEIDON and PLATON as tests to compare the goodness of both models against each other. In each subsection below we detail the inputs, assumptions, and processes that go into both atmospheric modeling packages.

### POSEIDON

The primary tool for our atmospheric characterization of WASP-166b was POSEIDON, a Python package for the modeling and analysis of exoplanet spectra. While POSEIDON has the capability to model 2-D and 3-D atmospheres, we focused, at least initially, on the 1-D case (the only atmospheric variation is in the radial direction). POSEIDON allows the characterization of atmospheres using both “free” and “equilibrium” chemistry. The simplifying assumption of chemical equilibrium can be convenient for providing an early estimation of the chemical composition of hot giant exoplanets such as WASP-166b.

POSEIDON models an atmosphere using a grid of pressure and temperature. We used a 100-layer grid, with a maximum pressure of 10 bars and a minimum pressure of  $10^{-9}$  bars. We used a relatively low minimum pressure to avoid clipping strong line cores and distorting our results<sup>19</sup>.

POSEIDON incorporates Rayleigh scattering and absorption from pair processes — collision-induced absorption (CIA) and free-free absorption consistent with the fill gasses (i.e. the dominant atmospheric constituents) that are present and other molecules specified in each model atmosphere considered (including for the complex equilibrium chemistry situation).

Before considering full retrievals, we experimented with a variety of forward models to gain insight into how the various model components (e.g. P-T profile, cloud treatment, trace gas list) can affect our transmission spectrum. This was a somewhat qualitative exercise, but it helped to narrow down the best candidate models for further retrieval analysis.

We considered both clear and cloudy conditions for our model atmospheres. Specifically for POSEIDON, we have used the simple “MacMad17” cloud model (MacDonald and Madhusudhan 2017) that is characterized by a fixed cloud “type” (e.g. opaque cloud deck) and a free cloud top pressure (“log P<sub>cloud</sub>”) parameter.

We explored both an isothermal pressure-temperature (P-T) profile and a two-parameter gradient profile. Usually, when considering transmission spectroscopy, an isothermal profile is a reasonable assumption (Greene et al. 2016; Guzmán-Mesa et al. 2020; Howe et al. 2017), however in some cases even small shifts in temperature in the pressure range probed by

---

<sup>19</sup>See POSEIDON High-Resolution Spectroscopy at <https://poseidon-retrievals.readthedocs.io>.

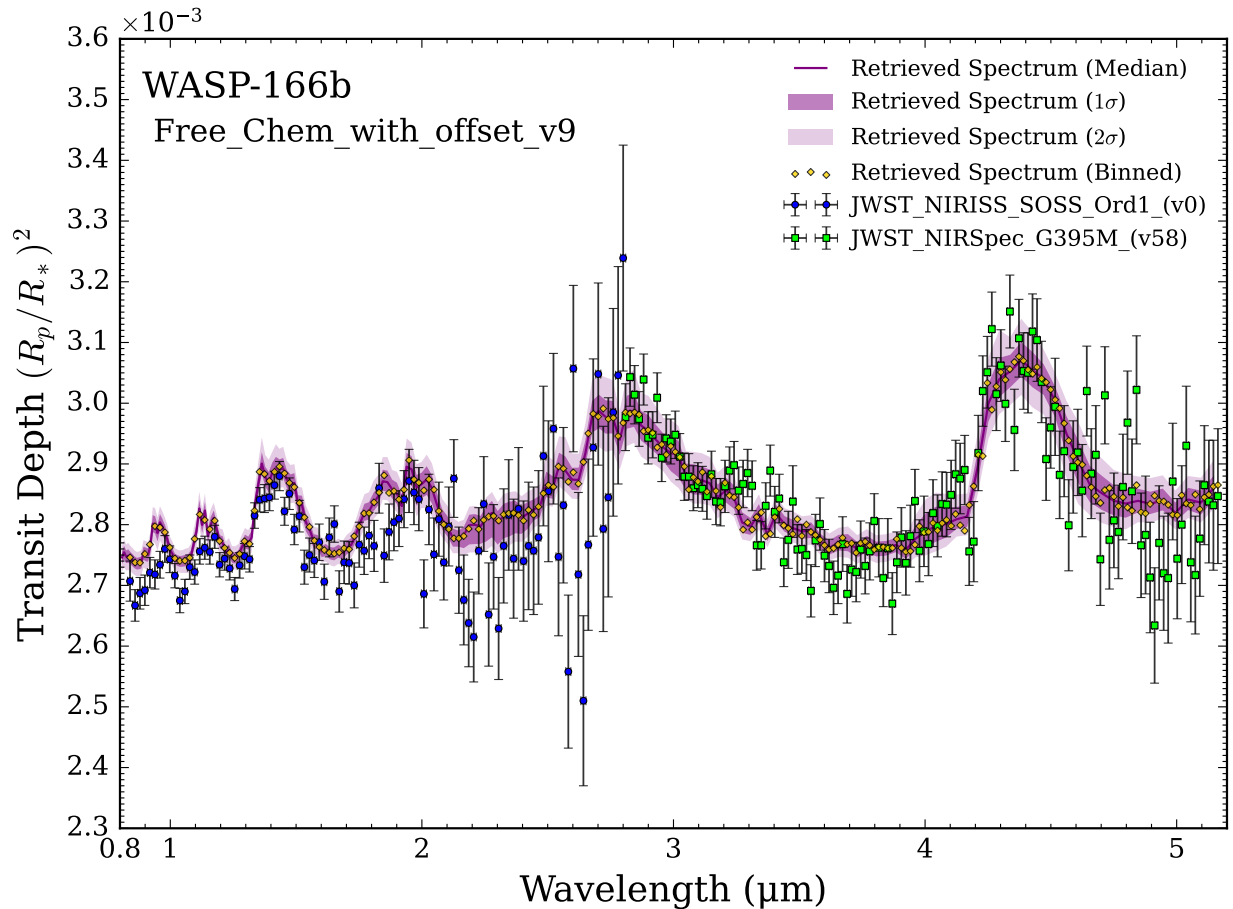


Figure 5.11: WASP-166b transmission spectrum from POSEIDON free chemistry retrieval, based on an early NIRISS data reduction, and later stage NIRSpec reduction. There is a retrieved transit depth offset between the instruments of 39 ppm; NIRISS data appears to be ‘relatively’ low by that amount. The data actuals have not been adjusted for the offset on the plot, but the retrieved spectrum has been. The results shown are using an ‘isothermal’ P-T model with an opaque cloud deck. Fill gasses, H<sub>2</sub> and He are present at the solar ratio. Trace gasses, H<sub>2</sub>O, CO<sub>2</sub>, SO<sub>2</sub>, and NH<sub>3</sub> are included in the model.

Table 5.3: Model parameters and prior distributions used in the atmospheric retrievals of WASP-166b.  $U(a,b)$  is the uniform distribution between values a and b, and  $N(\mu, \sigma^2)$  is the normal distribution with a mean  $\mu$  and variance  $\sigma^2$ . X are the various molecular species being considered (e.g. H<sub>2</sub>O). The POSEIDON reference pressure is 10 bars; for PLATON the reference pressure is 100 kPa.  $T_{eq}$  is the planetary equilibrium temperature.

Parameter	Symbol	Prior
<i>Free Chemistry (POSEIDON)</i>		
Planet radius at reference pressure (m)	R_p_ref	$U(0.55R_j, 0.63R_j)$
Temp (K); ‘isotherm’	T_iso	$U(600, 1500)$
Temp, max pressure (K); ‘gradient’	T_deep	$U(600, 1500)$
Temp, min pressure (K); ‘gradient’	T_high	$U(600, 1500)$
$\log(vmr_X)$ ( $\log(\text{bar})$ )	log_X	$U(-10, 1)$
$\log(\text{cloudtoppressure})$ ( $\log(\text{bar})$ )	log_P_cloud	$U(-7, 2)$
Dataset offset (ppm)	$\delta_{rel}$	$U(-250, 250)$
<i>Equilibrium Chemistry (POSEIDON)</i>		
Planet radius at reference pressure (m)	R_p_ref	$U(0.55R_j, 0.63R_j)$
Temp (K); ‘isotherm’	T_iso	$U(600, 1500)$
Temp, max pressure (K); ‘gradient’	T_deep	$U(600, 1500)$
Temp, min pressure (K); ‘gradient’	T_high	$U(600, 1500)$
Carbon/Oxygen ratio	C_to_O	$U(0.2, 2)$
$\log(\text{metallicity})^{18}$	log_Met	$U(-1, 4)$
$\log(\text{cloudtoppressure})$ ( $\log(\text{bar})$ )	log_P_cloud	$U(-7, 2)$
Dataset offset (ppm)	$\delta_{rel}$	$U(-250, 250)$
<i>Equilibrium Chemistry (PLATON)</i>		
Planet radius at reference pressure (m)	R_p_ref	$U(0.9R_p, 1.1R_p)$
Temp (K)	T	$U(0.5T_{eq}, 1.5T_{eq})$
Carbon/Oxygen ratio	C_to_O	$U(0, 1)$
$\log(\text{metallicity})$	log_Met	$U(-1, 3)$
$\log(\text{cloudtoppressure})$ ( $\log(\text{pascals})$ )	log_cloudtop_P	$U(-0.99, 5)$

transmission spectroscopy can have a significant effect on retrieved abundances (MacDonald and Madhusudhan 2017).

In our “free” chemistry retrievals we considered atmospheric abundances for a broad set of trace molecular constituents, including: H<sub>2</sub>O, CO<sub>2</sub>, CO, NH<sub>3</sub>, SO<sub>2</sub>, CH<sub>4</sub>, H<sub>2</sub>S, HCN, and C<sub>2</sub>H<sub>2</sub>. The remainder of the atmosphere in our models is composed of the fill gasses H<sub>2</sub> and He in a solar ratio; an appropriate assumption for planets ranging from Neptune to Jupiter in mass and radius and with equilibrium temperature less than 2000 K (D’Angelo et al. 2010; D’Angelo and Lissauer 2018; Heng 2017; MacDonald and Lewis 2022).

POSEIDON allows for the retrieval of small transit depth offsets between instrument data sets. We combine our NIRISS SOSS and NIRSpec G395M data for our retrieval analysis, including a systematic offset parameter ( $\delta_{rel}$ ) between the two instruments.

Table 5.3 lists the various model parameters, symbols, and prior distributions used in our retrievals for POSEIDON.

POSEIDON uses `MultiNest` (Feroz et al. 2009; Feroz et al. 2019) to sample the Bayesian evidence, and determine posterior distributions. `MultiNest` is used through its Python implementation `PyMultiNest` (Buchner 2016). As suggested by the POSEIDON documentation, we used 400 live points (which determines how finely the parameter space will be sampled) for our exploratory retrievals, and for our final published work we used 2000 live points.

POSEIDON provides information to judge the quality of the model fits, including  $\chi^2$  and reduced  $\chi^2$  values. In addition, it allows us to perform Bayesian model comparisons. For each retrieval case it generates the Bayesian evidence (Z) value which quantifies the quality of the model fit to the data. If we want to compare nested models (e.g. for a second model a particular molecule is removed from the first model’s free parameter list), POSEIDON has the facility to determine the Bayes factor and the “Equivalent” detection significance ( $\sigma$ ) of a particular free parameter.

We began the atmospheric characterization process of WASP-166b by performing recon retrievals with POSEIDON using free chemistry, testing various model/parameter scenarios.

For the retrievals, we fixed the system parameters to those shown in Table 5.1 and fit the free atmospheric model parameters presented in Table 5.3.

An example of a combined instrument, free chemistry retrieval with POSEIDON is shown in Figure 5.11. This is a case with an isothermal P-T profile, and an opaque cloud deck. We have included H<sub>2</sub>O, CO<sub>2</sub>, SO<sub>2</sub>, and NH<sub>3</sub> trace gasses in the model.

In conjunction with our retrieval studies, we have used forward modeling to examine the essential shape and character of spectral features resulting from various trace gasses. By considering spectra for these gasses individually, we can identify candidate molecules to include in further retrieval studies.

Thus far, our POSEIDON retrievals have yielded a very strong detection of H<sub>2</sub>O, at a significance level of 20.22 $\sigma$ . This detection significance is determined from the Bayesian evidence odds ratio between two models, with and without the molecule in question, H<sub>2</sub>O in this case. Similarly, we detected CO<sub>2</sub> with a significance of 4.90 $\sigma$ . The other molecules considered in our POSEIDON retrievals, SO<sub>2</sub> and NH<sub>3</sub>, were not detected with any significance relative to retrievals without each of these molecules.

## PLATON

In order to corroborate/confirm our POSEIDON “equilibrium” chemistry results we used the python package PLATON (Zhang et al. 2019), based on the well-known atmospheric modeling code, ExoTransmit (Kempton et al. 2017). Table 5.3 lists the various model parameters, symbols, and prior distributions used in our retrievals for PLATON.

We find that PLATON estimates a planetary metallicity of  $\log(Z) = 2.599 \pm 0.063$  ( $Z = 397^{+62}_{-54}$ ); WASP-166b is thus quite metal-rich, roughly 4 – 6x more so than Neptune, which has 71 – 100x solar metallicity (Karkoschka and Tomasko 2011).

PLATON also estimates a planetary C/O ratio of  $C/O = 0.49^{+0.10}_{-0.16}$ . By comparison, the host star WASP-166 has  $[C/H] = 0.15 \pm 0.09$  and  $[O/H] = 0.21 \pm 0.09$  from the Hypatia catalog (Hinkel et al. 2014), which yields  $[C/O] = [C/H] - [O/H] = -0.06 \pm 0.13$  and a resulting stellar C/O ratio of  $C/O = 0.87^{+0.29}_{-0.22}$ . Thus, although WASP-166b has a C/O ratio consistent with the Sun’s C/O ratio of 0.54 (Asplund et al. 2009), its C/O ratio is slightly substellar in relation to its host star, low by  $1.6\sigma$

## 5.5 Discussion

Our transmission spectroscopy analysis of WASP-166b yielded detections of H<sub>2</sub>O and CO<sub>2</sub> in the planet’s atmosphere and placed upper limits on the abundances of SO<sub>2</sub> and NH<sub>3</sub> as well as the upper altitude of any cloud deck that may be present. We compare these results to prior analyses of WASP-166b, explain the broader context of similar Hot Neptunes and the Hot Neptune Desert, and investigate how the atmospheric composition of WASP-166b informs our understanding of the planet’s formation and history pathway.

### Prior Atmospheric Observations of WASP-166b

The first study of the atmospheric composition of WASP-166b used HARPS transmission spectroscopy to detect neutral sodium (Seidel et al. 2020). Later, this detection was confirmed by ESPRESSO transmission spectroscopy (Seidel et al. 2022). Both studies focused on the Na I doublet at 588.9950 and 589.5924 nm. This doublet is extremely sensitive to even small quantities of sodium, and thus all prior sodium detections have been accomplished through the Na I doublet (Charbonneau et al. 2002, Redfield et al. 2008, Nikolov et al. 2016, Sing et al. 2016, Casasayas-Barris et al. 2017, Casasayas-Barris et al. 2019, Wyttenbach et al. 2017, Chen et al. 2018, Chen et al. 2020, Jensen et al. 2018, Deibert et al. 2019, Højmøller et al. 2019, Seidel et al. 2019, Cabot et al. 2020). Our observations, collected with the NIRISS SOSS and NIRSpec to provide wavelength coverage across 0.9 – 5.2  $\mu\text{m}$ , are thus entirely insensitive to sodium via this commonly used doublet. However, our results are consistent with that of Seidel et al. (2020) and Seidel et al. (2022) in that all three analyses point away from a flat transmission spectrum and toward a low or negligible cloud deck.

The same ESPRESSO transmission spectroscopy observations (2 transits from 2020 Dec and 2021 Feb) used to confirm sodium detection by Seidel et al. (2020) were subsequently



Table 5.4: Retrieved free parameter posterior median values from POSEIDON for selected cases. The P-T profile and Clouds define the particular parameterizations used for the retrieval cases. The remaining columns are the median values of the marginalized posterior distributions for the free parameters considered in each case. Beginning with Case 12, we reduced the minimum pressure of the model atmosphere grid from 10<sup>-6</sup> to 10<sup>-9</sup> bars.

ID	P-T profile	Clouds	$R_{p,ref}$ ( $R_J$ )	$T_{iso}$ (K)	$T_{high}$ (K)	$T_{deep}$ (K)	H <sub>2</sub> O (log vmr)	CO <sub>2</sub> (log vmr)	SO <sub>2</sub> (log vmr)	NH <sub>3</sub> (log vmr)	logPcloud (log bar)	$\delta_{rel}$ (ppm)
5	"gradient"	"deck"	0.560	-	659	1474	-1.86	-3.00	-5.58	-	-2.52	-41
9	"isothermal"	"deck"	0.570	865	-	-	-1.52	-2.85	-5.08	-4.07	-2.99	-39
12	"isothermal"	"cloud-free"	0.599	680	-	-	-1.24	-1.83	-7.02	-3.89	-	-50
13	"isothermal"	"cloud-free"	0.616	608	-	-	-	-	-	-	-	-79
14	"isothermal"	"cloud-free"	0.607	711	-	-	-0.81	-	-	-	-	-89
15	"isothermal"	"cloud-free"	0.602	784	-	-	-1.00	-1.52	-	-	-	-55
16	"isothermal"	"cloud-free"	0.601	814	-	-	-0.95	-1.56	-5.65	-	-	-51
17	"isothermal"	"cloud-free"	0.599	682	-	-	-1.23	-1.83	-6.95	-3.91	-	-50
18	"isothermal"	"deck"	0.595	724	-	-	-1.20	-1.99	-6.41	-3.81	-1.78	-47

Table 5.5: Detection significance of various atmospheric constituents based on POSEIDON with free chemistry. The “ $\sigma$  to baseline” column indicates the significance level at which each scenario is favored against the baseline, obtained by calculating the Bayes factor ( $\ln Z$ ). The “factor” column shows what individual molecule or model was added from the previous run (also bolded in the “Free parameters” column). The last column gives the single-factor detection significance. The offset between the instruments has been included as a free parameter for all scenarios. The fill gasses, H<sub>2</sub> and He are present in all cases at the solar ratio. The negligible  $\Delta\sigma$  for SO<sub>2</sub>, NH<sub>3</sub>, and clouds points to non-detections for all three components.

ID	Free parameters	$\ln Z$	$\sigma$ to baseline	factor	$\Delta\sigma$
13	Fill gasses (H <sub>2</sub> and He), isothermal P-T, cloud free (baseline)	1619.27 $\pm$ 0.16	–	–	–
14	<b>H<sub>2</sub>O</b> , isothermal P-T, and cloud free	1820.64 $\pm$ 0.17	20.22	H <sub>2</sub> O	20.22
15	H <sub>2</sub> O, <b>CO<sub>2</sub></b> , isothermal P-T, and cloud free	1931.50 $\pm$ 0.19	25.12	CO <sub>2</sub>	4.90
16	H <sub>2</sub> O, CO <sub>2</sub> , <b>SO<sub>2</sub></b> , isothermal P-T, and cloud free	1932.12 $\pm$ 0.19	25.14	SO <sub>2</sub>	0.02
17	H <sub>2</sub> O, CO <sub>2</sub> , SO <sub>2</sub> , <b>NH<sub>3</sub></b> , isothermal P-T, and cloud free	1934.27 $\pm$ 0.20	25.23	NH <sub>3</sub>	0.09
18	H <sub>2</sub> O, CO <sub>2</sub> , SO <sub>2</sub> , NH <sub>3</sub> , isothermal P-T, and <b>clouds</b>	1935.56 $\pm$ 0.20	25.28	clouds	0.05

also used to investigate the presence of water vapor and clouds in the atmosphere of WASP-166b. Lafarga et al. (2023) were able to strongly exclude scenarios with high water content and high pressure (low altitude) clouds that would yield the strongest water absorption signals, but they are also able to moderately exclude scenarios with low water content and low pressure (high altitude) clouds that would yield a non-detection. They find good fits to intermediate models containing either low water content and high cloud pressure or high water content with low cloud pressure, identifying a maximum likelihood near  $\log_{10}(\text{H}_2\text{O}) = -4$  and  $\log_{10}(\text{P}_{\text{cloud}}/\text{bar}) = 0$  (i.e. no cloud deck). Our results are consistent in that we do not detect the presence of clouds and also make a strong detection of H<sub>2</sub>O. However, our measured water abundance ( $\log_{10}(\text{H}_2\text{O}) = -1.2$ ) is relatively higher, which Lafarga et al. (2023) would argue suggests a corresponding low cloud pressure. However, Lafarga et al. (2023) also notes that they fix the temperature and scaling factor and also did not consider any other sources of opacity as we do; these simplifying assumptions may explain this slight inconsistency.

## Comparison to Hot Neptune LTT 9779b

Consulting the NASA Exoplanet Archive atmospheric spectroscopy table (accessed 2024 May 6), there is only one other planet in the Hot Neptune Desert that already has atmospheric characterization with JWST: LTT 9779b ( $M_p = 29.32 \pm 0.8 M_{\oplus}$ ,  $4.72 \pm 0.23 R_{\oplus}$ ,  $P = 0.792$  d; Jenkins et al. 2020). The locations of LTT 9779b, WASP-166b, and the Hot Neptune Desert can be seen in Fig 5.1. Radica et al. (2024) collected and analyzed a full phase curve and transit of WASP-166b with the NIRISS SOSS instrument ( $0.6 - 2.85 \mu\text{m}$ ) but found only muted spectral features. Although their findings were discrepant from a flat

transmission spectrum, they could not fully break the degeneracy between metallicity and cloud top pressure. By applying additional constraints on planetary metallicity through interior structure modeling, Radica et al. (2024) found that millibar pressure clouds in a H<sub>2</sub>O or CH<sub>4</sub> dominated atmosphere was the most likely scenario. Not only must the atmosphere of LTT 9779b withstand much more irradiation than that of WASP-166b (2500 S<sub>⊕</sub> versus 440 S<sub>⊕</sub>), the planet is also far smaller than WASP-166b (4.72±0.23 R<sub>⊕</sub> versus 7.1±0.3 R<sub>⊕</sub>) despite very similar planet masses, resulting in a smaller scale height and smaller spectral features. It is possible that LTT 9779b has only retained a thick atmosphere via the presence of a cloud deck that reduces the efficiency of atmospheric loss; meanwhile, the relatively lower stellar irradiation for WASP-166b may allow for a puffier atmosphere with fewer clouds without extreme atmospheric mass loss.

## The Formation of WASP-166b and the Hot Neptune Desert

The high planetary metallicity ( $Z = 397_{-54}^{+62}$ ) and substellar C/O ratio ( $C/O = 0.49_{-0.16}^{+0.10}$ ) of the atmosphere of WASP-166b shed light on plausible formation pathways for this planet. As discussed by Öberg et al. (2011), in situ planet formation and formation through gravitational instability should yield a stellar C/O ratio, with modifications to higher metallicity and lower C/O ratio (as seen for WASP-166b) indicative of “pollution” by planetesimal accretion after the gas accretion stage. Thiabaud et al. (2015) similarly find that superstellar C/O ratios are only attainable without planetary accretion and mixing of accreted solids with the envelope. Madhusudhan et al. (2017) echoed this result by finding that planetary core erosion can yield very high planetary metallicities and stellar or substellar C/O ratios, although photoevaporation could also play a role. Taking these results together, while it is still hard to clarify the exact formation pathway, WASP-166b fits the mold of a planet that attained a substellar C/O and high metallicity through a combination of planetesimal accretion, core erosion, or photoevaporation. However, our constraint on the C/O ratio is still marginally consistent with stellar and superstellar values that could arise without planetary accretion.

As WASP-166b is an usual planet residing within the Hot Neptune Desert, direct theories of how the planet formed necessarily also shed light on the formation mechanisms involved in the origin of the Hot Neptune Desert broadly. Although the extent and paucity of the Hot Neptune Desert have been well documented, its origins and mechanisms are less clear. Hot Neptune Desert origin theories generally invoke either planet migration or in situ formation. Maze et al. (2016) proposed that the desert upper boundary is an inner migration limit due to either photoevaporation (atmospheric loss) at high insolation fluxes or a gap in the inner protoplanetary disk during early planetary formation. Matsakos and Königl (2016) theorized the desert forms as planets undergo high-eccentricity migration followed by tidal circularization near their Roche limit. As for in situ theories, the lower desert boundary could be the result of planet cores forming after protoplanetary disk gas has dispersed (Helled et al. 2016; Lee and Chiang 2016; Rogers et al. 2011). Batygin et al. (2016) suggested that in situ hot super-Earth formation can lead to runaway gas accretion and create hot Jupiters, with hot Neptunes only forming under fine-tuned accretion conditions.

Our constraints on the formation mechanisms for WASP-166b do not yet reveal how much migration the planet underwent. However, our findings are highly consistent with planetesimal accretion followed by some degree of core erosion and/or photoevaporation. We cannot exclude any formation mechanisms for the Hot Neptune Desert through the analysis of a single planet, but theories that invoke photoevaporation (Mazeh et al. 2016) or can otherwise explain a marginally substellar or stellar C/O ratio with a high planetary metallicity are certainly worth exploring more thoroughly.

## 5.6 Conclusion

We present our atmospheric characterization of WASP-166b, a super-Neptune ( $P = 5.44$  d,  $M_p = 32.1 \pm 1.6 M_\oplus$ ,  $R_p = 7.1 \pm 0.3 R_\oplus$ ) located within the Hot Neptune Desert. We collected two total transit observations of the planet with JWST: one transit with NIRSpec BOTS G395M/F290LP ( $2.80 - 5.18 \mu\text{m}$ ) and one transit with NIRISS SOSS Order-1 ( $0.9 - 2.8 \mu\text{m}$ ) to achieve sufficient and complementary wavelength coverage.

We reduce these observations to planetary transmission spectra and conduct forward modeling and retrievals on the combined planetary spectrum in order to constrain the planet’s atmospheric constituents. We find the planet’s atmosphere contains abundances of H<sub>2</sub>O ( $20.22\sigma$  significance) and CO<sub>2</sub> ( $4.90\sigma$  significance). We also include SO<sub>2</sub> and NH<sub>3</sub> in our atmospheric models but do not significantly detect either molecule. We could not constrain or detect any cloud deck; if there is a cloud deck, our results point toward clouds below the observable region of the photosphere.

Puffy planets like WASP-166b are prime targets for detailed atmospheric analysis. Our transmission spectroscopy of WASP-166b yields meaningful constraints on molecular abundances, metallicity, and C/O ratio, thereby providing insight into the formation pathway and evolution of this low-density hot super-Neptune. The high planetary metallicity ( $Z = 397^{+62}_{-54}$ ) and slightly substellar C/O ratio (planetary  $C/O = 0.49^{+0.10}_{-0.16}$ , stellar  $C/O = 0.87^{+0.29}_{-0.22}$ ) of WASP-166b can be explained through planetesimal accretion followed by core erosion or photoevaporation. This in turn provides evidence that photoevaporation, or other mechanisms that allow for substellar C/O ratios and superstellar metallicities, play an important role in the formation of the Hot Neptune Desert. Collecting further atmospheric observations of additional Hot Neptunes will give us the insights necessary to better discriminate between the various formation models for the origin and nature of the Hot Neptune desert.

# Chapter 6

## Future Work

In this thesis I have presented new results across four papers, published and unpublished, that span several methods of exoplanet detection and characterization. My work from Chapters 2 and 3 corresponds to two published papers and focuses on measuring the masses of planets in the Kepler-538 and K2-136 systems. I present cutting edge methods of stellar activity mitigation and apply these to small RV signals within noisy data sets to detect and constrain small planet masses. Methods like those I use must continue to develop in order to keep up with better spectrographs producing higher quality RV observations. Improved stellar activity models applied to observations from next-generation spectrographs will open the field to smaller RV signals and allow for the detection of more Earth-like planets and planets orbiting more active stars. I explore the latter case more thoroughly in Chapter 3 by measuring the mass of K2-136c, now the smallest planet mass measurement ever made in an open cluster. This and future studies of other young open cluster planets will yield insights into planet evolution by providing snapshots of young, small planets. My work from Chapters 4 and 5 corresponds to two draft papers that will soon be submitted for publication. In Chapter 4 I collaborate in the development of a planet detection pipeline which I apply to high-cadence *TESS* photometry to search for new planets. I expand the known planet population by validating four short-period planets (one sub-Jupiter and three sub-Neptunes) that may be amenable to additional characterization including RV mass determination and atmospheric analysis. Finally, in Chapter 5 I present a study of WASP-166b, a puffy super-Neptune in the Hot Neptune Desert. By modeling the atmospheric constituents, the planetary metallicity, and the C/O ratio, I find evidence for H<sub>2</sub>O, CO<sub>2</sub>, substellar C/O ratio, and superstellar metallicity. These properties are consistent with some planetesimal accretion followed by core erosion or photoevaporation, lending plausibility to Hot Neptune Desert origin mechanisms like photoevaporation than can preserve substellar C/O and superstellar metallicity.

The work presented in this thesis opens up several avenues of interesting potential research that will become only more relevant and feasible as new observing programs commence and new telescopes and instruments come online. I have discussed the impact of current, ground-based RV surveys and space missions like *TESS* and JWST on future work extending beyond

this thesis; however, these current programs and instruments will in coming years be joined by next-generation instruments that will be even more powerful.

From the ground, there are already several extreme precision spectrographs operating with sensitivities well below  $1 \text{ m s}^{-1}$  such as EXPRES (Brewer et al. 2020), ESPRESSO (Pepe et al. 2021), KPF (Rubenzahl et al. 2023), and NEID (Schwab et al. 2016). New extreme precision spectrographs will also come online that will be able to compete with and outperform these contemporary instruments. For example, the G-CLEF spectrograph (Szentgyorgyi et al. 2016) commissioned for the Giant Magellan Telescope (GMT), with completion expected in the early 2030s. G-CLEF is expected to achieve RV sensitivity below  $50 \text{ cm s}^{-1}$  and has a goal to reach  $10 \text{ cm s}^{-1}$ .

The ArmazoNes high Dispersion Echelle Spectrograph (ANDES) spectrograph (Marconi et al. 2022) on the Extremely Large Telescope (ELT) is another planned spectrograph that will exceed current technical capabilities. Among its several scientific goals, ANDES is being designed in order to be able to probe the atmospheric composition of habitable, terrestrial planets.

Approaching  $10 \text{ cm s}^{-1}$  sensitivity will push our detection limits to smaller planets orbiting noisier stars at longer periods, yield more detections of potentially habitable, terrestrial worlds, and help complete the family portraits of many planetary systems. This will allow for more effective studies of the outer reaches of stellar systems, similar to our work on Kepler-538 in Chapter 2. It will also allow for larger and more comprehensive studies of planetary evolution. As discussed in our work on K2-136 (Chapter 3), young stars tend to be much more active than their older counterparts, making RV detections of young planets relatively difficult. Improved RV sensitivity in concert with sophisticated RV modeling and analysis techniques will help open the way to larger population studies of young planets orbiting young stars, a necessary regime for study in order to answer questions of planetary evolution.

Ground-based spectrographs are not all that will be pushed further in coming years. The *TESS* mission still has several years' worth of fuel remaining that can be used to carry on observations potentially into the 2030s. Just as with improved RV sensitivity, additional baselines via new *TESS* sector observations will pave the way for new *TESS* planet hunting projects like the results we present in Chapter 4, lead to further planet detections, and provide tighter constraints on currently known planets. In particular, *TESS* sensitivity will improve for longer-period planets, planets orbiting fainter stars, and planets orbiting stars that are noisier due their relative youth or old age.

*TESS* will be further aided by the upcoming PLATO mission, another space-based telescope designed to detect transiting planets orbiting bright stars (Rauer et al. 2014). PLATO is planned for launch in 2026 and is expected to detect thousands of transiting exoplanets, including an expected handful of terrestrial, habitable planets amenable to atmospheric characterization.

The Nancy Grace Roman telescope is expected to launch in May 2027 and will detect thousands of additional exoplanets via microlensing. Unlike detection methods like transits and RVs that become less effective at larger orbital separation, microlensing detection effi-

ciency peaks near a semi-major axis range of several AU. Thus, Roman will be more sensitive to the poorly understood outer reaches of planetary systems. Additionally, Roman is expected to detect thousands of transiting exoplanets. Wilson et al. (2023) predict a transiting planet yield between  $\sim 60,000$  and  $\sim 200,000$ , more than an order of magnitude larger than the total current known planet population. Further, Roman will have a coronagraph designed to achieve sufficient starlight suppression to characterize mature, large exoplanets in reflected light (Krist et al. 2023). Carrión-González et al. (2021) find there are already dozens of known planets that are optimistically amenable to direct imaging follow-up with the Roman coronagraph, including super-Earths like Tau Ceti e and f.

Opportunities will only improve for detailed planetary follow-up observations, especially atmospheric characterization. The JWST mission (Gardner et al. 2006, 2023), already the most powerful space telescope ever launched, will only continue to expand our understanding of exoplanet atmospheres. By providing unparalleled resolution and access to the near-infrared (NIR) and mid-infrared (MIR) between 1 and 10  $\mu\text{m}$ , JWST is far more sensitive than even Hubble to numerous common atmospheric molecules like  $\text{H}_2\text{O}$ ,  $\text{CO}$ ,  $\text{CO}_2$ ,  $\text{CH}_4$ , and  $\text{NH}_3$ .

Our current understanding of broad exoplanet demographic features like the Hot Neptune Desert is still very limited and nascent. Studies like our analysis of the atmosphere of WASP-166b in Chapter 5 are an important first step to constraining Hot Neptune formation, but individual Hot Neptune studies will need to give way to larger studies of multiple Hot Neptune atmospheres. Only JWST or other future (i.e. unbuilt) instruments will be sensitive to small enough exoplanet atmospheres to probe questions like this.

Another important telescope, planned for launch in the early 2040s, is the Habitable Worlds Observatory (HWO), a proposed space mission recommended by the 2020 Decadal Survey on Astronomy and Astrophysics (Astro2020<sup>1</sup>). This would be the first mission capable of performing atmospheric characterization of habitable, terrestrial exoplanets. It is therefore the first mission that may be capable of detecting (or at least placing statistical constraints on) the presence of biosignatures in habitable, rocky planet atmospheres.

---

<sup>1</sup>See the full survey at <https://www.nationalacademies.org/>

# Bibliography

- Ahrer, Eva-Maria et al. (Feb. 2023). “Early Release Science of the exoplanet WASP-39b with JWST NIRCam”. In: *Nature* 614.7949, pp. 653–658. DOI: 10.1038/s41586-022-05590-4. arXiv: 2211.10489 [astro-ph.EP].
- Aigrain, S. et al. (July 2015). “Testing the recovery of stellar rotation signals from Kepler light curves using a blind hare-and-hounds exercise”. In: *MNRAS* 450.3, pp. 3211–3226. DOI: 10.1093/mnras/stv853. arXiv: 1504.04029 [astro-ph.SR].
- Albert, Loïc et al. (July 2023). “The Near Infrared Imager and Slitless Spectrograph for the James Webb Space Telescope. III. Single Object Slitless Spectroscopy”. In: *PASP* 135.1049, 075001, p. 075001. DOI: 10.1088/1538-3873/acd7a3. arXiv: 2306.04572 [astro-ph.IM].
- Alcock, C. et al. (Oct. 2000). “The MACHO Project Large Magellanic Cloud Variable-Star Inventory. IX. Frequency Analysis of the First-Overtone RR Lyrae Stars and the Indication for Nonradial Pulsations”. In: *ApJ* 542.1, pp. 257–280. DOI: 10.1086/309530. arXiv: astro-ph/0005361 [astro-ph].
- Alderson, Lili et al. (Feb. 2023). “Early Release Science of the exoplanet WASP-39b with JWST NIRSpec G395H”. In: *Nature* 614.7949, pp. 664–669. DOI: 10.1038/s41586-022-05591-3. arXiv: 2211.10488 [astro-ph.EP].
- Asplund, Martin et al. (Sept. 2009). “The Chemical Composition of the Sun”. In: *ARA&A* 47.1, pp. 481–522. DOI: 10.1146/annurev.astro.46.060407.145222. arXiv: 0909.0948 [astro-ph.SR].
- Astropy Collaboration et al. (Oct. 2013). “Astropy: A community Python package for astronomy”. In: *A&A* 558, A33, A33. DOI: 10.1051/0004-6361/201322068. arXiv: 1307.6212 [astro-ph.IM].
- Astropy Collaboration et al. (Sept. 2018). “The Astropy Project: Building an Open-science Project and Status of the v2.0 Core Package”. In: *AJ* 156.3, 123, p. 123. DOI: 10.3847/1538-3881/aabc4f. arXiv: 1801.02634 [astro-ph.IM].
- Babusiaux, C. et al. (June 2023). “Gaia Data Release 3. Catalogue validation”. In: *A&A* 674, A32, A32. DOI: 10.1051/0004-6361/202243790. arXiv: 2206.05989 [astro-ph.SR].
- Bailer-Jones, C. A. L. et al. (Mar. 2021). “Estimating Distances from Parallaxes. V. Geometric and Photogeometric Distances to 1.47 Billion Stars in Gaia Early Data Release 3”. In: *AJ* 161.3, 147, p. 147. DOI: 10.3847/1538-3881/abd806. arXiv: 2012.05220 [astro-ph.SR].



- Baines, Tyler et al. (Nov. 2023a). “Characterization of the visit-to-visit Stability of the GR700XD Spectral Traces for NIRISS/SOSS Observations”. In: *arXiv e-prints*, arXiv:2311.07769, arXiv:2311.07769. DOI: 10.48550/arXiv.2311.07769. arXiv: 2311.07769 [astro-ph.IM].
- (Nov. 2023b). *Characterization of the visit-to-visit Stability of the GR700XD Wavelength Calibration for NIRISS/SOSS Observations*. Technical Report JWST-STScI-008571, 12 pages.
- Balucinska-Church, Monika and Dan McCammon (Dec. 1992). “Photoelectric Absorption Cross Sections with Variable Abundances”. In: *ApJ* 400, p. 699. DOI: 10.1086/172032.
- Baraffe, Isabelle et al. (May 2015). “New evolutionary models for pre-main sequence and main sequence low-mass stars down to the hydrogen-burning limit”. In: *A&A* 577, A42, A42. DOI: 10.1051/0004-6361/201425481. arXiv: 1503.04107 [astro-ph.SR].
- Barbato, D. et al. (Aug. 2018). “Exploring the realm of scaled solar system analogues with HARPS”. In: *A&A* 615, A175, A175. DOI: 10.1051/0004-6361/201832791. arXiv: 1804.08329 [astro-ph.EP].
- Barentsen, Geert et al. (Feb. 2019). *KeplerGO/lightkurve: Lightkurve v1.0b29*. DOI: 10.5281/zenodo.2565212. URL: <https://doi.org/10.5281/zenodo.2565212>.
- Barnes, J. R. et al. (Feb. 2005). “The dependence of differential rotation on temperature and rotation”. In: *MNRAS* 357.1, pp. L1–L5. DOI: 10.1111/j.1745-3933.2005.08587.x. arXiv: astro-ph/0410575 [astro-ph].
- Barnes, S. A. (Oct. 2010). “A Simple Nonlinear Model for the Rotation of Main-sequence Cool Stars. I. Introduction, Implications for Gyrochronology, and Color-Period Diagrams”. In: *ApJ* 722, pp. 222–234. DOI: 10.1088/0004-637X/722/1/222.
- Barnes, S. A. and Y.-C. Kim (Sept. 2010). “Angular Momentum Loss from Cool Stars: An Empirical Expression and Connection to Stellar Activity”. In: *ApJ* 721, pp. 675–685. DOI: 10.1088/0004-637X/721/1/675. arXiv: 1104.2350 [astro-ph.SR].
- Barragán, O. et al. (Nov. 2019). “Radial velocity confirmation of K2-100b: a young, highly irradiated, and low-density transiting hot Neptune”. In: *MNRAS* 490.1, pp. 698–708. DOI: 10.1093/mnras/stz2569. arXiv: 1909.05252 [astro-ph.EP].
- Barragán, O. et al. (Aug. 2022). “The young HD 73583 (TOI-560) planetary system: two 10- $M_{\oplus}$  mini-Neptunes transiting a 500-Myr-old, bright, and active K dwarf”. In: *MNRAS* 514.2, pp. 1606–1627. DOI: 10.1093/mnras/stac638. arXiv: 2110.13069 [astro-ph.EP].
- Batalha, N. E. and M. R. Line (Apr. 2017). “Information Content Analysis for Selection of Optimal JWST Observing Modes for Transiting Exoplanet Atmospheres”. In: *AJ* 153, 151, p. 151. DOI: 10.3847/1538-3881/aa5faa. arXiv: 1612.02085 [astro-ph.EP].
- Batalha, N. E. et al. (June 2017). “PandExo: A Community Tool for Transiting Exoplanet Science with JWST & HST”. In: *PASP* 129.6, p. 064501. DOI: 10.1088/1538-3873/aa65b0. arXiv: 1702.01820 [astro-ph.IM].
- Batalha, Natasha E. et al. (Nov. 2019). “The Precision of Mass Measurements Required for Robust Atmospheric Characterization of Transiting Exoplanets”. In: *ApJ* 885.1, L25, p. L25. DOI: 10.3847/2041-8213/ab4909. arXiv: 1910.00076 [astro-ph.EP].

- Batygin, Konstantin et al. (Oct. 2016). “In Situ Formation and Dynamical Evolution of Hot Jupiter Systems”. In: *ApJ* 829.2, 114, p. 114. DOI: 10.3847/0004-637X/829/2/114. arXiv: 1511.09157 [astro-ph.EP].
- Bell, Taylor J. et al. (2022). “Eureka!: An End-to-End Pipeline for JWST Time-Series Observations”. In: *Journal of Open Source Software* 7.79, p. 4503. DOI: 10.21105/joss.04503. URL: <https://doi.org/10.21105/joss.04503>.
- Benatti, S. et al. (Mar. 2017). “The GAPS Programme with HARPS-N at TNG. XII. Characterization of the planetary system around HD 108874”. In: *A&A* 599, A90, A90. DOI: 10.1051/0004-6361/201629484. arXiv: 1611.09873 [astro-ph.EP].
- Benatti, S. et al. (June 2021). “Constraints on the mass and on the atmospheric composition and evolution of the low-density young planet DS Tucanae A b”. In: *A&A* 650, A66, A66. DOI: 10.1051/0004-6361/202140416. arXiv: 2103.12922 [astro-ph.EP].
- Benneke, Björn et al. (July 2019a). “A sub-Neptune exoplanet with a low-metallicity methane-depleted atmosphere and Mie-scattering clouds”. In: *Nature Astronomy* 3, pp. 813–821. DOI: 10.1038/s41550-019-0800-5. arXiv: 1907.00449 [astro-ph.EP].
- Benneke, Björn et al. (Dec. 2019b). “Water Vapor and Clouds on the Habitable-zone Sub-Neptune Exoplanet K2-18b”. In: *ApJ* 887.1, L14, p. L14. DOI: 10.3847/2041-8213/ab59dc. arXiv: 1909.04642 [astro-ph.EP].
- Berger, T. A. et al. (Oct. 2018). “Revised Radii of Kepler Stars and Planets Using Gaia Data Release 2”. In: *ApJ* 866, 99, p. 99. DOI: 10.3847/1538-4357/aada83. arXiv: 1805.00231 [astro-ph.EP].
- Birkmann, S. M. et al. (May 2022). “The Near-Infrared Spectrograph (NIRSpec) on the James Webb Space Telescope. IV. Capabilities and predicted performance for exoplanet characterization”. In: *A&A* 661, A83, A83. DOI: 10.1051/0004-6361/202142592. arXiv: 2202.03309 [astro-ph.IM].
- Böker, T. et al. (Mar. 2023). “In-orbit Performance of the Near-infrared Spectrograph NIRSpec on the James Webb Space Telescope”. In: *PASP* 135.1045, 038001, p. 038001. DOI: 10.1088/1538-3873/acb846. arXiv: 2301.13766 [astro-ph.IM].
- Borucki, W. et al. (May 2008). “Finding Earth-size planets in the habitable zone: the Kepler Mission”. In: *Exoplanets: Detection, Formation and Dynamics*. Ed. by Y.-S. Sun et al. Vol. 249. IAU Symposium, pp. 17–24. DOI: 10.1017/S174392130801630X.
- Brandt, Timothy D. and Chelsea X. Huang (July 2015). “Bayesian Ages for Early-type Stars from Isochrones Including Rotation, and a Possible Old Age for the Hyades”. In: *ApJ* 807.1, 58, p. 58. DOI: 10.1088/0004-637X/807/1/58. arXiv: 1501.04404 [astro-ph.SR].
- Brewer, John M. et al. (Aug. 2020). “EXPRES. I. HD 3651 as an Ideal RV Benchmark”. In: *AJ* 160.2, 67, p. 67. DOI: 10.3847/1538-3881/ab99c9. arXiv: 2006.02303 [astro-ph.EP].
- Bruntt, H. et al. (July 2010). “Accurate fundamental parameters for 23 bright solar-type stars”. In: *MNRAS* 405.3, pp. 1907–1923. DOI: 10.1111/j.1365-2966.2010.16575.x. arXiv: 1002.4268 [astro-ph.SR].

- Bryant, Edward M. et al. (June 2020). “Simultaneous TESS and NGTS transit observations of WASP-166 b”. In: *MNRAS* 494.4, pp. 5872–5881. DOI: 10.1093/mnras/staa1075. arXiv: 2004.07589 [astro-ph.EP].
- Bryson, S. T. et al. (June 2017). *The Kepler Certified False Positive Table*. Tech. rep.
- Buchhave, L. A. et al. (June 2012). “An abundance of small exoplanets around stars with a wide range of metallicities”. In: *Nature* 486, pp. 375–377. DOI: 10.1038/nature11121.
- Buchner, Johannes (June 2016). *PyMultiNest: Python interface for MultiNest*. Astrophysics Source Code Library, record ascl:1606.005.
- Burrows, A. et al. (Dec. 1997). “A Nongray Theory of Extrasolar Giant Planets and Brown Dwarfs”. In: *ApJ* 491.2, pp. 856–875. DOI: 10.1086/305002. arXiv: astro-ph/9705201 [astro-ph].
- Burrows, Adam et al. (July 2011). “The Dependence of Brown Dwarf Radii on Atmospheric Metallicity and Clouds: Theory and Comparison with Observations”. In: *ApJ* 736.1, 47, p. 47. DOI: 10.1088/0004-637X/736/1/47. arXiv: 1102.3922 [astro-ph.SR].
- Burt, Jennifer A. et al. (Oct. 2020). “TOI-824 b: A New Planet on the Lower Edge of the Hot Neptune Desert”. In: *AJ* 160.4, 153, p. 153. DOI: 10.3847/1538-3881/abac0c. arXiv: 2008.11732 [astro-ph.EP].
- Bushouse, Howard et al. (Sept. 2023). *JWST Calibration Pipeline*. Zenodo. Version 1.12.0. DOI: 10.5281/zenodo.6984365.
- Cabot, Samuel H. C. et al. (May 2020). “Detection of neutral atomic species in the ultra-hot Jupiter WASP-121b”. In: *MNRAS* 494.1, pp. 363–377. DOI: 10.1093/mnras/staa748. arXiv: 2001.07196 [astro-ph.EP].
- Carrión-González, Ó. et al. (July 2021). “Catalogue of exoplanets accessible in reflected starlight to the Nancy Grace Roman Space Telescope. Population study and prospects for phase-curve measurements”. In: *A&A* 651, A7, A7. DOI: 10.1051/0004-6361/202039993. arXiv: 2104.04296 [astro-ph.EP].
- Casasayas-Barris, N. et al. (Dec. 2017). “Detection of sodium in the atmosphere of WASP-69b”. In: *A&A* 608, A135, A135. DOI: 10.1051/0004-6361/201731956. arXiv: 1710.06479 [astro-ph.EP].
- Casasayas-Barris, N. et al. (Aug. 2019). “Atmospheric characterization of the ultra-hot Jupiter MASCARA-2b/KELT-20b. Detection of CaII, FeII, NaI, and the Balmer series of H ( $H\alpha$ ,  $H\beta$ , and  $H\gamma$ ) with high-dispersion transit spectroscopy”. In: *A&A* 628, A9, A9. DOI: 10.1051/0004-6361/201935623. arXiv: 1905.12491 [astro-ph.EP].
- Cegla, H. M. et al. (Apr. 2016). “The Rossiter-McLaughlin effect reloaded: Probing the 3D spin-orbit geometry, differential stellar rotation, and the spatially-resolved stellar spectrum of star-planet systems”. In: *A&A* 588, A127, A127. DOI: 10.1051/0004-6361/201527794. arXiv: 1602.00322 [astro-ph.EP].
- Chambers, J. (Sept. 2018). “Planet Formation: An Optimized Population-synthesis Approach”. In: *ApJ* 865, 30, p. 30. DOI: 10.3847/1538-4357/aada09. arXiv: 1808.03293 [astro-ph.EP].

- Chaplin, W. J. et al. (Apr. 2019). “Filtering Solar-Like Oscillations for Exoplanet Detection in Radial Velocity Observations”. In: *AJ* 157.4, 163, p. 163. DOI: 10.3847/1538-3881/ab0c01. arXiv: 1903.00657 [astro-ph.SR].
- Charbonneau, D. et al. (Jan. 2000). “Detection of Planetary Transits Across a Sun-like Star”. In: *ApJ* 529, pp. L45–L48. DOI: 10.1086/312457. eprint: astro-ph/9911436.
- Charbonneau, D. et al. (Mar. 2002). “Detection of an Extrasolar Planet Atmosphere”. In: *ApJ* 568, pp. 377–384. DOI: 10.1086/338770. eprint: astro-ph/0111544.
- Chen, G. et al. (Aug. 2018). “The GTC exoplanet transit spectroscopy survey. IX. Detection of haze, Na, K, and Li in the super-Neptune WASP-127b”. In: *A&A* 616, A145, A145. DOI: 10.1051/0004-6361/201833033. arXiv: 1805.11744 [astro-ph.EP].
- Chen, G. et al. (Oct. 2020). “Detection of Na in WASP-21b’s lower and upper atmosphere”. In: *A&A* 642, A54, A54. DOI: 10.1051/0004-6361/202038661. arXiv: 2007.13429 [astro-ph.EP].
- Choi, Jieun et al. (June 2016). “Mesa Isochrones and Stellar Tracks (MIST). I. Solar-scaled Models”. In: *ApJ* 823.2, 102, p. 102. DOI: 10.3847/0004-637X/823/2/102. arXiv: 1604.08592 [astro-ph.SR].
- Ciardi, D. R. et al. (May 2015). “Understanding the Effects of Stellar Multiplicity on the Derived Planet Radii from Transit Surveys: Implications for Kepler, K2, and TESS”. In: *ApJ* 805, 16, p. 16. DOI: 10.1088/0004-637X/805/1/16. arXiv: 1503.03516 [astro-ph.EP].
- Ciardi, David R. et al. (Jan. 2018). “K2-136: A Binary System in the Hyades Cluster Hosting a Neptune-sized Planet”. In: *AJ* 155.1, 10, p. 10. DOI: 10.3847/1538-3881/aa9921. arXiv: 1709.10398 [astro-ph.EP].
- Collier Cameron, A. et al. (July 2019). “Three years of Sun-as-a-star radial-velocity observations on the approach to solar minimum”. In: *MNRAS* 487.1, pp. 1082–1100. DOI: 10.1093/mnras/stz1215. arXiv: 1904.12186 [astro-ph.SR].
- Cosentino, Rosario et al. (Sept. 2012). “HARPS-N: the new planet hunter at TNG”. In: *Ground-based and Airborne Instrumentation for Astronomy IV*. Vol. 8446. Society of Photo-Optical Instrumentation Engineers (SPIE) Conference Series, 84461V, p. 84461V. DOI: 10.1117/12.925738.
- Cosentino, Rosario et al. (July 2014). “HARPS-N @ TNG, two year harvesting data: performances and results”. In: *Ground-based and Airborne Instrumentation for Astronomy V*. Vol. 9147. Society of Photo-Optical Instrumentation Engineers (SPIE) Conference Series, 91478C, p. 91478C. DOI: 10.1117/12.2055813.
- Cretignier, M. et al. (Mar. 2022). “Stellar activity correction using PCA decomposition of shells”. In: *A&A* 659, A68, A68. DOI: 10.1051/0004-6361/202142435. arXiv: 2202.05902 [astro-ph.IM].
- Cunha, D. et al. (Feb. 2013). “Impact of stellar companions on precise radial velocities”. In: *A&A* 550, A75, A75. DOI: 10.1051/0004-6361/201220083. arXiv: 1212.2848 [astro-ph.EP].
- Cutri, R. M. et al. (June 2003). “VizieR Online Data Catalog: 2MASS All-Sky Catalog of Point Sources (Cutri+ 2003)”. In: *VizieR Online Data Catalog* 2246.

- D'Angelo, G. et al. (2010). "Giant Planet Formation". In: *Exoplanets*. Ed. by S. Seager, pp. 319–346. DOI: 10.48550/arXiv.1006.5486.
- D'Angelo, Gennaro and Jack J. Lissauer (2018). "Formation of Giant Planets". In: *Handbook of Exoplanets*. Ed. by Hans J. Deeg and Juan Antonio Belmonte, 140, p. 140. DOI: 10.1007/978-3-319-55333-7\_140.
- Deeg, Hans J. and Roi Alonso (2018). "Transit Photometry as an Exoplanet Discovery Method". In: *Handbook of Exoplanets*. Ed. by Hans J. Deeg and Juan Antonio Belmonte, 117, p. 117. DOI: 10.1007/978-3-319-55333-7\_117.
- Deibert, Emily K. et al. (Feb. 2019). "High-resolution Transit Spectroscopy of Warm Saturns". In: *AJ* 157.2, 58, p. 58. DOI: 10.3847/1538-3881/aaf56b. arXiv: 1812.02748 [astro-ph.EP].
- Demangeon, O. D. S. et al. (Sept. 2021). "Warm terrestrial planet with half the mass of Venus transiting a nearby star". In: *A&A* 653, A41, A41. DOI: 10.1051/0004-6361/202140728. arXiv: 2108.03323 [astro-ph.EP].
- Deming, D. et al. (Sept. 2009). "Discovery and Characterization of Transiting Super Earths Using an All-Sky Transit Survey and Follow-up by the James Webb Space Telescope". In: *PASP* 121, p. 952. DOI: 10.1086/605913. arXiv: 0903.4880 [astro-ph.EP].
- Deming, Drake et al. (Jan. 2024). "Precise Radial Velocities Using Line Bisectors". In: *AJ* 167.1, 34, p. 34. DOI: 10.3847/1538-3881/ad109f. arXiv: 2312.03068 [astro-ph.SR].
- Desidera, S. et al. (July 2023). "TOI-179: A young system with a transiting compact Neptune-mass planet and a low-mass companion in outer orbit". In: *A&A* 675, A158, A158. DOI: 10.1051/0004-6361/202244611. arXiv: 2210.07933 [astro-ph.EP].
- Dong, Subo and Zhaohuan Zhu (Nov. 2013). "Fast Rise of "Neptune-size" Planets (4-8  $R_{\oplus}$ ) from P  $\sim$ 10 to  $\sim$ 250 Days—Statistics of Kepler Planet Candidates up to  $\sim$ 0.75 AU". In: *ApJ* 778.1, 53, p. 53. DOI: 10.1088/0004-637X/778/1/53. arXiv: 1212.4853 [astro-ph.EP].
- Dotter, A. et al. (Sept. 2008). "The Dartmouth Stellar Evolution Database". In: *ApJS* 178, 89-101, pp. 89–101. DOI: 10.1086/589654. arXiv: 0804.4473.
- Dotter, Aaron (Jan. 2016). "MESA Isochrones and Stellar Tracks (MIST) 0: Methods for the Construction of Stellar Isochrones". In: *ApJS* 222.1, 8, p. 8. DOI: 10.3847/0067-0049/222/1/8. arXiv: 1601.05144 [astro-ph.SR].
- Douglas, S. T. et al. (July 2019). "K2 Rotation Periods for Low-mass Hyads and a Quantitative Comparison of the Distribution of Slow Rotators in the Hyades and Praesepe". In: *ApJ* 879.2, 100, p. 100. DOI: 10.3847/1538-4357/ab2468. arXiv: 1905.06736 [astro-ph.SR].
- Doyle, Amanda P. et al. (Nov. 2014). "Determining stellar macroturbulence using asteroseismic rotational velocities from Kepler". In: *MNRAS* 444.4, pp. 3592–3602. DOI: 10.1093/mnras/stu1692. arXiv: 1408.3988 [astro-ph.SR].
- Doyle, L. et al. (Oct. 2022). "The Hot Neptune WASP-166 b with ESPRESSO - I. Refining the planetary architecture and stellar variability". In: *MNRAS* 516.1, pp. 298–315. DOI: 10.1093/mnras/stac2178. arXiv: 2207.10127 [astro-ph.EP].

- Doyon, René et al. (Sept. 2023). “The Near Infrared Imager and Slitless Spectrograph for the James Webb Space Telescope. I. Instrument Overview and In-flight Performance”. In: *PASP* 135.1051, 098001, p. 098001. DOI: 10.1088/1538-3873/acd41b. arXiv: 2306.03277 [astro-ph.IM].
- Dressing, Courtney D. and David Charbonneau (July 2015). “The Occurrence of Potentially Habitable Planets Orbiting M Dwarfs Estimated from the Full Kepler Dataset and an Empirical Measurement of the Detection Sensitivity”. In: *ApJ* 807.1, 45, p. 45. DOI: 10.1088/0004-637X/807/1/45. arXiv: 1501.01623 [astro-ph.EP].
- Dumusque, X. et al. (Jan. 2011). “Planetary detection limits taking into account stellar noise. I. Observational strategies to reduce stellar oscillation and granulation effects”. In: *A&A* 525, A140, A140. DOI: 10.1051/0004-6361/201014097. arXiv: 1010.2616 [astro-ph.EP].
- Dumusque, X. et al. (Dec. 2014). “SOAP 2.0: A Tool to Estimate the Photometric and Radial Velocity Variations Induced by Stellar Spots and Plages”. In: *ApJ* 796.2, 132, p. 132. DOI: 10.1088/0004-637X/796/2/132. arXiv: 1409.3594 [astro-ph.SR].
- Dyrek, Achrène et al. (Jan. 2024). “SO<sub>2</sub>, silicate clouds, but no CH<sub>4</sub> detected in a warm Neptune”. In: *Nature* 625.7993, pp. 51–54. DOI: 10.1038/s41586-023-06849-0. arXiv: 2311.12515 [astro-ph.EP].
- Eastman, Jason (Oct. 2017). *EXOFASTv2: Generalized publication-quality exoplanet modeling code*. Astrophysics Source Code Library, record ascl:1710.003. ascl: 1710.003.
- Eastman, Jason et al. (Jan. 2013). “EXOFAST: A Fast Exoplanetary Fitting Suite in IDL”. In: *Publications of the Astronomical Society of the Pacific* 125, p. 83. DOI: 10.1086/669497. arXiv: 1206.5798 [astro-ph.IM].
- Eastman, Jason D. et al. (July 2019). “EXOFASTv2: A public, generalized, publication-quality exoplanet modeling code”. In: *arXiv e-prints*, arXiv:1907.09480, arXiv:1907.09480. DOI: 10.48550/arXiv.1907.09480. arXiv: 1907.09480 [astro-ph.EP].
- Espinoza, Néstor and Andrés Jordán (June 2015). “Limb darkening and exoplanets: testing stellar model atmospheres and identifying biases in transit parameters”. In: *MNRAS* 450.2, pp. 1879–1899. DOI: 10.1093/mnras/stv744. arXiv: 1503.07020 [astro-ph.EP].
- (Apr. 2016). “Limb darkening and exoplanets - II. Choosing the best law for optimal retrieval of transit parameters”. In: *MNRAS* 457.4, pp. 3573–3581. DOI: 10.1093/mnras/stw224. arXiv: 1601.05485 [astro-ph.EP].
- Espinoza, Néstor et al. (Jan. 2023). “Spectroscopic Time-series Performance of JWST/NIRSpec from Commissioning Observations”. In: *PASP* 135.1043, 018002, p. 018002. DOI: 10.1088/1538-3873/aca3d3. arXiv: 2211.01459 [astro-ph.EP].
- Feinstein, Adina D. et al. (Feb. 2023). “Early Release Science of the exoplanet WASP-39b with JWST NIRISS”. In: *Nature* 614.7949, pp. 670–675. DOI: 10.1038/s41586-022-05674-1. arXiv: 2211.10493 [astro-ph.EP].
- Fernández Fernández, Jorge and Peter J. Wheatley (May 2022). “X-ray irradiation of three planets around Hyades star K2 -136”. In: *Astronomische Nachrichten* 343.4, e10076, e10076. DOI: 10.1002/asna.20210076. arXiv: 2110.13754 [astro-ph.EP].

- Feroz, F. et al. (Oct. 2009). “MULTINEST: an efficient and robust Bayesian inference tool for cosmology and particle physics”. In: *MNRAS* 398, pp. 1601–1614. DOI: 10.1111/j.1365-2966.2009.14548.x. arXiv: 0809.3437.
- Feroz, Farhan et al. (Nov. 2019). “Importance Nested Sampling and the MultiNest Algorithm”. In: *The Open Journal of Astrophysics* 2.1, 10, p. 10. DOI: 10.21105/astro.1306.2144. arXiv: 1306.2144 [astro-ph.IM].
- Foreman-Mackey, Daniel et al. (Mar. 2013). “emcee: The MCMC Hammer”. In: *PASP* 125.925, p. 306. DOI: 10.1086/670067. arXiv: 1202.3665 [astro-ph.IM].
- Fortenbach, Charles D. and Courtney D. Dressing (May 2020). “A Framework For Optimizing Exoplanet Target Selection For The James Webb Space Telescope”. In: *PASP* 132.1011, 054501, p. 054501. DOI: 10.1088/1538-3873/ab70da. arXiv: 2002.01495 [astro-ph.EP].
- Fortney, J. J. et al. (Apr. 2007). “Planetary Radii across Five Orders of Magnitude in Mass and Stellar Insolation: Application to Transits”. In: *ApJ* 659.2, pp. 1661–1672. DOI: 10.1086/512120. arXiv: astro-ph/0612671 [astro-ph].
- Foster, G. et al. (May 2022). “Exoplanet X-ray irradiation and evaporation rates with eROSITA”. In: *A&A* 661, A23, A23. DOI: 10.1051/0004-6361/202141097. arXiv: 2106.14550 [astro-ph.EP].
- Fu, Guangwei et al. (Dec. 2022). “Water and an Escaping Helium Tail Detected in the Hazy and Methane-depleted Atmosphere of HAT-P-18b from JWST NIRISS/SOSS”. In: *ApJ* 940.2, L35, p. L35. DOI: 10.3847/2041-8213/ac9977. arXiv: 2211.13761 [astro-ph.EP].
- Fulton, B. J. and E. A. Petigura (Dec. 2018). “The California-Kepler Survey. VII. Precise Planet Radii Leveraging Gaia DR2 Reveal the Stellar Mass Dependence of the Planet Radius Gap”. In: *AJ* 156, 264, p. 264. DOI: 10.3847/1538-3881/aae828. arXiv: 1805.01453 [astro-ph.EP].
- Fulton, B. J. et al. (Sept. 2017). “The California-Kepler Survey. III. A Gap in the Radius Distribution of Small Planets”. In: *AJ* 154, 109, p. 109. DOI: 10.3847/1538-3881/aa80eb. arXiv: 1703.10375 [astro-ph.EP].
- Fulton, Benjamin J. et al. (Apr. 2018). “RadVel: The Radial Velocity Modeling Toolkit”. In: *PASP* 130.986, p. 044504. DOI: 10.1088/1538-3873/aaaaa8. arXiv: 1801.01947 [astro-ph.IM].
- Fűrész, G. (2008). “TRES”. In: *PhD thesis, University of Szeged, Hungary*.
- Gaia Collaboration and A. Vallenari (June 2022). “Gaia DR3: data release content and main properties”. In: *in prep*.
- Gaia Collaboration et al. (Nov. 2016). “The Gaia mission”. In: *A&A* 595, A1, A1. DOI: 10.1051/0004-6361/201629272. arXiv: 1609.04153 [astro-ph.IM].
- Gaia Collaboration et al. (Aug. 2018). “Gaia Data Release 2. Summary of the contents and survey properties”. In: *A&A* 616, A1, A1. DOI: 10.1051/0004-6361/201833051. arXiv: 1804.09365.

- Gaia Collaboration et al. (June 2021a). “Gaia Early Data Release 3. Summary of the contents and survey properties (Corrigendum)”. In: *A&A* 650, C3, p. C3. DOI: 10.1051/0004-6361/202039657e.
- Gaia Collaboration et al. (May 2021b). “Gaia Early Data Release 3. The Gaia Catalogue of Nearby Stars”. In: *A&A* 649, A6, A6. DOI: 10.1051/0004-6361/202039498. arXiv: 2012.02061 [astro-ph.SR].
- Gardner, Jonathan P. et al. (Apr. 2006). “The James Webb Space Telescope”. In: *Space Sci. Rev.* 123.4, pp. 485–606. DOI: 10.1007/s11214-006-8315-7. arXiv: astro-ph/0606175 [astro-ph].
- Gardner, Jonathan P. et al. (June 2023). “The James Webb Space Telescope Mission”. In: *PASP* 135.1048, 068001, p. 068001. DOI: 10.1088/1538-3873/acd1b5. arXiv: 2304.04869 [astro-ph.IM].
- Giacalone, Steven and Courtney D. Dressing (Feb. 2020). *triceratops: Candidate exoplanet rating tool*. Astrophysics Source Code Library, record ascl:2002.004. ascl: 2002.004.
- Giacalone, Steven et al. (Jan. 2021). “Vetting of 384 TESS Objects of Interest with TRICER-ATOPS and Statistical Validation of 12 Planet Candidates”. In: *AJ* 161.1, 24, p. 24. DOI: 10.3847/1538-3881/abc6af. arXiv: 2002.00691 [astro-ph.EP].
- Gibson, S. R. et al. (Aug. 2016). “KPF: Keck Planet Finder”. In: *Ground-based and Airborne Instrumentation for Astronomy VI*. Vol. 9908. Proc. SPIE, 990870, p. 990870. DOI: 10.1117/12.2233334.
- Gibson, S. R. et al. (July 2018). “Keck Planet Finder: preliminary design”. In: *Ground-based and Airborne Instrumentation for Astronomy VII*. Vol. 10702. Society of Photo-Optical Instrumentation Engineers (SPIE) Conference Series, 107025X, p. 107025X. DOI: 10.1117/12.2311565.
- Giles, Helen A. C. et al. (Dec. 2017). “A Kepler study of starspot lifetimes with respect to light-curve amplitude and spectral type”. In: *MNRAS* 472.2, pp. 1618–1627. DOI: 10.1093/mnras/stx1931. arXiv: 1707.08583 [astro-ph.SR].
- Goodman, Jonathan and Jonathan Weare (Jan. 2010). “Ensemble samplers with affine invariance”. In: *Communications in Applied Mathematics and Computational Science* 5.1, pp. 65–80. DOI: 10.2140/camcos.2010.5.65.
- Gossage, Seth et al. (Aug. 2018). “Age Determinations of the Hyades, Praesepe, and Pleiades via MESA Models with Rotation”. In: *ApJ* 863.1, 67, p. 67. DOI: 10.3847/1538-4357/aad0a0. arXiv: 1804.06441 [astro-ph.SR].
- Grant, David and Hannah R. Wakeford (Dec. 2022). *Exo-TiC/ExoTiC-LD: ExoTiC-LD v3.0.0*. Version v3.0.0. DOI: 10.5281/zenodo.7437681. URL: <https://doi.org/10.5281/zenodo.7437681>.
- Green, James C. et al. (Jan. 2012). “The Cosmic Origins Spectrograph”. In: *ApJ* 744.1, 60, p. 60. DOI: 10.1088/0004-637X/744/1/60. arXiv: 1110.0462 [astro-ph.IM].
- Greene, T. P. et al. (Jan. 2016). “Characterizing Transiting Exoplanet Atmospheres with JWST”. In: *ApJ* 817, 17, p. 17. DOI: 10.3847/0004-637X/817/1/17. arXiv: 1511.05528 [astro-ph.EP].



- Greene, Thomas P. et al. (June 2023). “Thermal emission from the Earth-sized exoplanet TRAPPIST-1 b using JWST”. In: *Nature* 618.7963, pp. 39–42. DOI: 10.1038/s41586-023-05951-7. arXiv: 2303.14849 [astro-ph.EP].
- Gregory, P. C. (Nov. 2007). “A Bayesian periodogram finds evidence for three planets in HD 11964”. In: *MNRAS* 381, pp. 1607–1616. DOI: 10.1111/j.1365-2966.2007.12361.x. arXiv: 0709.0970.
- Guerrero, Natalia M. et al. (June 2021). “The TESS Objects of Interest Catalog from the TESS Prime Mission”. In: *ApJS* 254.2, 39, p. 39. DOI: 10.3847/1538-4365/abefe1. arXiv: 2103.12538 [astro-ph.EP].
- Guzmán-Mesa, Andrea et al. (July 2020). “Information Content of JWST NIRSpec Transmission Spectra of Warm Neptunes”. In: *AJ* 160.1, 15, p. 15. DOI: 10.3847/1538-3881/ab9176. arXiv: 2004.10106 [astro-ph.EP].
- Hara, Nathan C. and Eric B. Ford (Mar. 2023). “Statistical Methods for Exoplanet Detection with Radial Velocities”. In: *Annual Review of Statistics and Its Application* 10.1, pp. 623–649. DOI: 10.1146/annurev-statistics-033021-012225. arXiv: 2308.00701 [astro-ph.IM].
- Hatzes, Artie P. et al. (Dec. 2000). “Evidence for a Long-Period Planet Orbiting  $\epsilon$  Eridani”. In: *ApJ* 544.2, pp. L145–L148. DOI: 10.1086/317319. arXiv: astro-ph/0009423 [astro-ph].
- Hayward, T. L. et al. (Jan. 2001). “PHARO: A Near-Infrared Camera for the Palomar Adaptive Optics System”. In: *PASP* 113, pp. 105–118. DOI: 10.1086/317969.
- Haywood, R. D. (Nov. 2015). “Hide and Seek: Radial-Velocity Searches for Planets around Active Stars”. PhD thesis. University of St Andrews. DOI: 10.5281/zenodo.35161.
- Haywood, R. D. et al. (Sept. 2014). “Planets and stellar activity: hide and seek in the CoRoT-7 system”. In: *MNRAS* 443, pp. 2517–2531. DOI: 10.1093/mnras/stu1320. arXiv: 1407.1044 [astro-ph.EP].
- Helled, Ravit et al. (Jan. 2016). “A possible correlation between planetary radius and orbital period for small planets”. In: *MNRAS* 455.1, pp. L96–L98. DOI: 10.1093/mnras/1/slv158. arXiv: 1510.04564 [astro-ph.EP].
- Hellier, Coel et al. (Sept. 2019). “WASP-166b: a bloated super-Neptune transiting a  $V = 9$  star”. In: *MNRAS* 488.3, pp. 3067–3075. DOI: 10.1093/mnras/stz1903. arXiv: 1811.05292 [astro-ph.EP].
- Heng, Kevin (2017). *Exoplanetary Atmospheres: Theoretical Concepts and Foundations*.
- Hinkel, Natalie R. et al. (Sept. 2014). “Stellar Abundances in the Solar Neighborhood: The Hypatia Catalog”. In: *AJ* 148.3, 54, p. 54. DOI: 10.1088/0004-6256/148/3/54. arXiv: 1405.6719 [astro-ph.SR].
- Hippke, Michael and René Heller (Mar. 2019). “Optimized transit detection algorithm to search for periodic transits of small planets”. In: *A&A* 623, A39, A39. DOI: 10.1051/0004-6361/201834672. arXiv: 1901.02015 [astro-ph.EP].
- Hippke, Michael et al. (Oct. 2019). “Wotan: Comprehensive Time-series Detrending in Python”. In: *AJ* 158.4, 143, p. 143. DOI: 10.3847/1538-3881/ab3984. arXiv: 1906.00966 [astro-ph.EP].

- Hoeijmakers, H. J. et al. (July 2019). “A spectral survey of an ultra-hot Jupiter. Detection of metals in the transmission spectrum of KELT-9 b”. In: *A&A* 627, A165, A165. DOI: 10.1051/0004-6361/201935089. arXiv: 1905.02096 [astro-ph.EP].
- Horne, K. (June 1986). “An optimal extraction algorithm for CCD spectroscopy.” In: *PASP* 98, pp. 609–617. DOI: 10.1086/131801.
- Howard, A. W. et al. (Oct. 2010). “The California Planet Survey. I. Four New Giant Exoplanets”. In: *ApJ* 721, pp. 1467–1481. DOI: 10.1088/0004-637X/721/2/1467. arXiv: 1003.3488 [astro-ph.EP].
- Howard, Andrew W. et al. (Aug. 2012). “Planet Occurrence within 0.25 AU of Solar-type Stars from Kepler”. In: *ApJS* 201.2, 15, p. 15. DOI: 10.1088/0067-0049/201/2/15. arXiv: 1103.2541 [astro-ph.EP].
- Howe, Alex R. et al. (June 2014). “Mass-radius Relations and Core-envelope Decompositions of Super-Earths and Sub-Neptunes”. In: *ApJ* 787.2, 173, p. 173. DOI: 10.1088/0004-637X/787/2/173. arXiv: 1402.4818 [astro-ph.EP].
- Howe, Alex R. et al. (Jan. 2017). “An Information-theoretic Approach to Optimize JWST Observations and Retrievals of Transiting Exoplanet Atmospheres”. In: *ApJ* 835.1, 96, p. 96. DOI: 10.3847/1538-4357/835/1/96. arXiv: 1612.01245 [astro-ph.EP].
- Huang, Chelsea X. et al. (Nov. 2020a). “Photometry of 10 Million Stars from the First Two Years of TESS Full Frame Images: Part I”. In: *Research Notes of the American Astronomical Society* 4.11, 204, p. 204. DOI: 10.3847/2515-5172/abca2e. arXiv: 2011.06459 [astro-ph.EP].
- (Nov. 2020b). “Photometry of 10 Million Stars from the First Two Years of TESS Full Frame Images: Part II”. In: *Research Notes of the American Astronomical Society* 4.11, 206, p. 206. DOI: 10.3847/2515-5172/abca2d.
- Izidoro, A. et al. (Feb. 2015). “Gas Giant Planets as Dynamical Barriers to Inward-Migrating Super-Earths”. In: *ApJ* 800, L22, p. L22. DOI: 10.1088/2041-8205/800/2/L22. arXiv: 1501.06308 [astro-ph.EP].
- Jakobsen, P. et al. (May 2022). “The Near-Infrared Spectrograph (NIRSpec) on the James Webb Space Telescope. I. Overview of the instrument and its capabilities”. In: *A&A* 661, A80, A80. DOI: 10.1051/0004-6361/202142663. arXiv: 2202.03305 [astro-ph.IM].
- Jenkins, J. M. et al. (Apr. 2010). “Overview of the Kepler Science Processing Pipeline”. In: *ApJ* 713, pp. L87–L91. DOI: 10.1088/2041-8205/713/2/L87. arXiv: 1001.0258 [astro-ph.EP].
- Jenkins, James S. et al. (Jan. 2020). “An ultrahot Neptune in the Neptune desert”. In: *Nature Astronomy* 4, pp. 1148–1157. DOI: 10.1038/s41550-020-1142-z. arXiv: 2009.12832 [astro-ph.EP].
- Jenkins, Jon M. (Aug. 2002). “The Impact of Solar-like Variability on the Detectability of Transiting Terrestrial Planets”. In: *ApJ* 575.1, pp. 493–505. DOI: 10.1086/341136.
- Jenkins, Jon M. et al. (Aug. 2016). “The TESS science processing operations center”. In: *Software and Cyberinfrastructure for Astronomy IV*. Ed. by Gianluca Chiozzi and Juan C. Guzman. Vol. 9913. Society of Photo-Optical Instrumentation Engineers (SPIE) Conference Series, 99133E, 99133E. DOI: 10.1117/12.2233418.

- Jensen, Adam G. et al. (Oct. 2018). “Hydrogen and Sodium Absorption in the Optical Transmission Spectrum of WASP-12b”. In: *AJ* 156.4, 154, p. 154. DOI: 10.3847/1538-3881/aadca7. arXiv: 1808.07010 [astro-ph.EP].
- Jin, Sheng et al. (Nov. 2014). “Planetary Population Synthesis Coupled with Atmospheric Escape: A Statistical View of Evaporation”. In: *ApJ* 795.1, 65, p. 65. DOI: 10.1088/0004-637X/795/1/65. arXiv: 1409.2879 [astro-ph.EP].
- Johns, M. et al. (Sept. 2012). “Giant Magellan Telescope: overview”. In: *Ground-based and Airborne Telescopes IV*. Vol. 8444. Proc. SPIE, 84441H, 84441H. DOI: 10.1117/12.926716.
- Jurgenson, C. et al. (Aug. 2016). “EXPRES: a next generation RV spectrograph in the search for earth-like worlds”. In: *Ground-based and Airborne Instrumentation for Astronomy VI*. Vol. 9908. Proc. SPIE, 99086T, 99086T. DOI: 10.1117/12.2233002. arXiv: 1606.04413 [astro-ph.IM].
- JWST Transiting Exoplanet Community Early Release Science Team et al. (Feb. 2023a). “Identification of carbon dioxide in an exoplanet atmosphere”. In: *Nature* 614.7949, pp. 649–652. DOI: 10.1038/s41586-022-05269-w. arXiv: 2208.11692 [astro-ph.EP].
- (Feb. 2023b). “Identification of carbon dioxide in an exoplanet atmosphere”. In: *Nature* 614.7949, pp. 649–652. DOI: 10.1038/s41586-022-05269-w. arXiv: 2208.11692 [astro-ph.EP].
- Kalirai, J. (July 2018). “Scientific discovery with the James Webb Space Telescope”. In: *Contemporary Physics* 59, pp. 251–290. DOI: 10.1080/00107514.2018.1467648. arXiv: 1805.06941 [astro-ph.IM].
- Karkoschka, Erich and Martin G. Tomasko (Jan. 2011). “The haze and methane distributions on Neptune from HST-STIS spectroscopy”. In: *Icarus* 211.1, pp. 780–797. DOI: 10.1016/j.icarus.2010.08.013.
- Kass, Robert E. and Adrian E. Raftery (1995). “Bayes Factors”. In: *Journal of the American Statistical Association* 90.430, pp. 773–795. DOI: 10.1080/01621459.1995.10476572. eprint: <https://www.tandfonline.com/doi/pdf/10.1080/01621459.1995.10476572>. URL: <https://www.tandfonline.com/doi/abs/10.1080/01621459.1995.10476572>.
- Kempton, E. M.-R. et al. (Apr. 2017). “Exo-Transmit: An Open-Source Code for Calculating Transmission Spectra for Exoplanet Atmospheres of Varied Composition”. In: *PASP* 129.4, p. 044402. DOI: 10.1088/1538-3873/aa61ef. arXiv: 1611.03871 [astro-ph.EP].
- Kempton, Eliza M. -R. et al. (Nov. 2018). “A Framework for Prioritizing the TESS Planetary Candidates Most Amenable to Atmospheric Characterization”. In: *PASP* 130.993, p. 114401. DOI: 10.1088/1538-3873/aadf6f. arXiv: 1805.03671 [astro-ph.EP].
- Kipping, D. M. (Nov. 2013a). “Efficient, uninformative sampling of limb darkening coefficients for two-parameter laws”. In: *MNRAS* 435, pp. 2152–2160. DOI: 10.1093/mnras/stt1435. arXiv: 1308.0009 [astro-ph.SR].
- (July 2013b). “Parametrizing the exoplanet eccentricity distribution with the Beta distribution”. In: *MNRAS* 434, pp. L51–L55. DOI: 10.1093/mnras1/slt075. arXiv: 1306.4982 [astro-ph.EP].

- Kirk, Brian et al. (Mar. 2016). “Kepler Eclipsing Binary Stars. VII. The Catalog of Eclipsing Binaries Found in the Entire Kepler Data Set”. In: *AJ* 151.3, 68, p. 68. DOI: 10.3847/0004-6256/151/3/68. arXiv: 1512.08830 [astro-ph.SR].
- Kirk, James et al. (Mar. 2024). “JWST/NIRCam Transmission Spectroscopy of the Nearby Sub-Earth GJ 341b”. In: *AJ* 167.3, 90, p. 90. DOI: 10.3847/1538-3881/ad19df. arXiv: 2401.06043 [astro-ph.EP].
- Kitchatinov, L. L. and S. V. Olemskoy (July 2012). “Differential rotation of main-sequence dwarfs: predicting the dependence on surface temperature and rotation rate”. In: *MNRAS* 423.4, pp. 3344–3351. DOI: 10.1111/j.1365-2966.2012.21126.x. arXiv: 1204.4261 [astro-ph.SR].
- Klein, Baptiste et al. (Mar. 2021). “Investigating the young AU Mic system with SPIRou: large-scale stellar magnetic field and close-in planet mass”. In: *MNRAS* 502.1, pp. 188–205. DOI: 10.1093/mnras/staa3702. arXiv: 2011.13357 [astro-ph.EP].
- Kopal, Z. (1950). “Detailed effects of limb darkening upon light and velocity curves of close binary systems”. In: *Harvard College Observatory Circular* 454, pp. 1–12.
- Kovács, G. et al. (Aug. 2002). “A box-fitting algorithm in the search for periodic transits”. In: *A&A* 391, pp. 369–377. DOI: 10.1051/0004-6361:20020802. eprint: astro-ph/0206099.
- Kreidberg, L. (Nov. 2015a). “batman: BASic Transit Model cALculationN in Python”. In: *PASP* 127, p. 1161. DOI: 10.1086/683602. arXiv: 1507.08285 [astro-ph.EP].
- Kreidberg, Laura (Nov. 2015b). “batman: BASic Transit Model cALculationN in Python”. In: *PASP* 127.957, p. 1161. DOI: 10.1086/683602. arXiv: 1507.08285 [astro-ph.EP].
- Krist, John E. et al. (Oct. 2023). “End-to-end numerical modeling of the Roman Space Telescope coronagraph”. In: *Journal of Astronomical Telescopes, Instruments, and Systems* 9, 045002, p. 045002. DOI: 10.1117/1.JATIS.9.4.045002. arXiv: 2309.16012 [astro-ph.IM].
- Kunimoto, Michelle (Apr. 2024). *LEO-vetter: Automated vetting for TESS planet candidates*. Astrophysics Source Code Library. ascl: 2404.026.
- Kurucz, R. (1993). “ATLAS9 Stellar Atmosphere Programs and 2 km/s grid.” In: *ATLAS9 Stellar Atmosphere Programs and 2 km/s grid. Kurucz CD-ROM No. 13. Cambridge, Mass.: Smithsonian Astrophysical Observatory, 1993*. 13.
- Kurucz, R. L. (May 1979). “Model atmospheres for G, F, A, B, and O stars.” In: *ApJS* 40, pp. 1–340. DOI: 10.1086/190589.
- (1992). “Model Atmospheres for Population Synthesis”. In: *The Stellar Populations of Galaxies*. Ed. by B. Barbuy and A. Renzini. Vol. 149. IAU Symposium, p. 225.
- Lafarga, M. et al. (May 2023). “The hot Neptune WASP-166 b with ESPRESSO - III. A blue-shifted tentative water signal constrains the presence of clouds”. In: *MNRAS* 521.1, pp. 1233–1252. DOI: 10.1093/mnras/stad480. arXiv: 2302.04794 [astro-ph.EP].
- Lammer, H. et al. (Apr. 2014). “Origin and loss of nebula-captured hydrogen envelopes from ‘sub’- to ‘super-Earths’ in the habitable zone of Sun-like stars”. In: *MNRAS* 439.4, pp. 3225–3238. DOI: 10.1093/mnras/stu085. arXiv: 1401.2765 [astro-ph.EP].

- Lee, E. J. and E. Chiang (Feb. 2016). “Breeding Super-Earths and Birthing Super-puffs in Transitional Disks”. In: *ApJ* 817, 90, p. 90. DOI: 10.3847/0004-637X/817/2/90. arXiv: 1510.08855 [astro-ph.EP].
- Li, Jie et al. (Feb. 2019). “Kepler Data Validation II-Transit Model Fitting and Multiple-planet Search”. In: *PASP* 131.996, p. 024506. DOI: 10.1088/1538-3873/aaf44d. arXiv: 1812.00103 [astro-ph.IM].
- Lienhard, F. et al. (July 2022). “Multi-mask least-squares deconvolution: extracting RVs using tailored masks”. In: *MNRAS* 513.4, pp. 5328–5343. DOI: 10.1093/mnras/stac1098. arXiv: 2204.13556 [astro-ph.EP].
- Lindgren, L. et al. (Aug. 2018). “Gaia Data Release 2. The astrometric solution”. In: *A&A* 616, A2, A2. DOI: 10.1051/0004-6361/201832727. arXiv: 1804.09366 [astro-ph.IM].
- Lissauer, Jack J. et al. (Mar. 2014). “Validation of Kepler’s Multiple Planet Candidates. II. Refined Statistical Framework and Descriptions of Systems of Special Interest”. In: *ApJ* 784.1, 44, p. 44. DOI: 10.1088/0004-637X/784/1/44. arXiv: 1402.6352 [astro-ph.EP].
- Lithwick, Yoram et al. (Dec. 2012). “Extracting Planet Mass and Eccentricity from TTV Data”. In: *ApJ* 761.2, 122, p. 122. DOI: 10.1088/0004-637X/761/2/122. arXiv: 1207.4192 [astro-ph.EP].
- Livingston, John H. et al. (Mar. 2018). “Three Small Planets Transiting a Hyades Star”. In: *AJ* 155.3, 115, p. 115. DOI: 10.3847/1538-3881/aaa841. arXiv: 1710.07203 [astro-ph.EP].
- Lopez, E. D. and K. Rice (Oct. 2018). “How formation time-scales affect the period dependence of the transition between rocky super-Earths and gaseous sub-Neptunes and implications for  $\eta_{\oplus}$ ”. In: *MNRAS* 479, pp. 5303–5311. DOI: 10.1093/mnras/sty1707.
- Lopez, Eric D. and Jonathan J. Fortney (Oct. 2013). “The Role of Core Mass in Controlling Evaporation: The Kepler Radius Distribution and the Kepler-36 Density Dichotomy”. In: *ApJ* 776.1, 2, p. 2. DOI: 10.1088/0004-637X/776/1/2. arXiv: 1305.0269 [astro-ph.EP].
- (Sept. 2014). “Understanding the Mass-Radius Relation for Sub-neptunes: Radius as a Proxy for Composition”. In: *ApJ* 792.1, 1, p. 1. DOI: 10.1088/0004-637X/792/1/1. arXiv: 1311.0329 [astro-ph.EP].
- Lopez, Eric D. et al. (Dec. 2012). “How Thermal Evolution and Mass-loss Sculpt Populations of Super-Earths and Sub-Neptunes: Application to the Kepler-11 System and Beyond”. In: *ApJ* 761.1, 59, p. 59. DOI: 10.1088/0004-637X/761/1/59. arXiv: 1205.0010 [astro-ph.EP].
- Lustig-Yaeger, Jacob et al. (Nov. 2023). “A JWST transmission spectrum of the nearby Earth-sized exoplanet LHS 475 b”. In: *Nature Astronomy* 7, pp. 1317–1328. DOI: 10.1038/s41550-023-02064-z. arXiv: 2301.04191 [astro-ph.EP].
- MacDonald, Ryan J. (Jan. 2023). “POSEIDON: A Multidimensional Atmospheric Retrieval Code for Exoplanet Spectra”. In: *The Journal of Open Source Software* 8, 4873, p. 4873. DOI: 10.21105/joss.04873.

- MacDonald, Ryan J. and Nikole K. Lewis (Apr. 2022). “TRIDENT: A Rapid 3D Radiative-transfer Model for Exoplanet Transmission Spectra”. In: *ApJ* 929.1, 20, p. 20. DOI: 10.3847/1538-4357/ac47fe. arXiv: 2111.05862 [astro-ph.EP].
- MacDonald, Ryan J. and Nikku Madhusudhan (Aug. 2017). “HD 209458b in new light: evidence of nitrogen chemistry, patchy clouds and sub-solar water”. In: *MNRAS* 469.2, pp. 1979–1996. DOI: 10.1093/mnras/stx804. arXiv: 1701.01113 [astro-ph.EP].
- Madhusudhan, Nikku et al. (Oct. 2014). “Toward Chemical Constraints on Hot Jupiter Migration”. In: *ApJ* 794.1, L12, p. L12. DOI: 10.1088/2041-8205/794/1/L12. arXiv: 1408.3668 [astro-ph.EP].
- Madhusudhan, Nikku et al. (Aug. 2017). “Atmospheric signatures of giant exoplanet formation by pebble accretion”. In: *MNRAS* 469.4, pp. 4102–4115. DOI: 10.1093/mnras/stx1139. arXiv: 1611.03083 [astro-ph.EP].
- Madhusudhan, Nikku et al. (Oct. 2023). “Carbon-bearing Molecules in a Possible Hycean Atmosphere”. In: *ApJ* 956.1, L13, p. L13. DOI: 10.3847/2041-8213/acf577. arXiv: 2309.05566 [astro-ph.EP].
- Mahadevan, S. et al. (July 2010). “The Habitable Zone Planet Finder: A proposed high-resolution NIR spectrograph for the Hobby Eberly Telescope to discover low-mass exoplanets around M dwarfs”. In: *Ground-based and Airborne Instrumentation for Astronomy III*. Vol. 7735. Proc. SPIE, 77356X, p. 77356X. DOI: 10.1117/12.857551. arXiv: 1007.3235 [astro-ph.IM].
- Mahadevan, S. et al. (July 2014). “The Habitable-zone Planet Finder: A status update on the development of a stabilized fiber-fed near-infrared spectrograph for the for the Hobby-Eberly telescope”. In: *Ground-based and Airborne Instrumentation for Astronomy V*. Vol. 9147. Proc. SPIE, 91471G, 91471G. DOI: 10.1117/12.2056417.
- Mahadevan, Suvrath et al. (Sept. 2012). “The habitable-zone planet finder: a stabilized fiber-fed NIR spectrograph for the Hobby-Eberly Telescope”. In: *Ground-based and Airborne Instrumentation for Astronomy IV*. Ed. by Ian S. McLean et al. Vol. 8446. Society of Photo-Optical Instrumentation Engineers (SPIE) Conference Series, 84461S, 84461S. DOI: 10.1117/12.926102. arXiv: 1209.1686 [astro-ph.EP].
- Malavolta, L. et al. (May 2017). “The Kepler-19 System: A Thick-envelope Super-Earth with Two Neptune-mass Companions Characterized Using Radial Velocities and Transit Timing Variations”. In: *AJ* 153, 224, p. 224. DOI: 10.3847/1538-3881/aa6897. arXiv: 1703.06885 [astro-ph.EP].
- Malavolta, L. et al. (Mar. 2018). “An Ultra-short Period Rocky Super-Earth with a Secondary Eclipse and a Neptune-like Companion around K2-141”. In: *AJ* 155, 107, p. 107. DOI: 10.3847/1538-3881/aaa5b5. arXiv: 1801.03502 [astro-ph.EP].
- Mamajek, Eric E. and Cameron P. M. Bell (Dec. 2014). “On the age of the  $\beta$  Pictoris moving group”. In: *MNRAS* 445.3, pp. 2169–2180. DOI: 10.1093/mnras/stu1894. arXiv: 1409.2737 [astro-ph.SR].
- Mandel, K. and E. Agol (Dec. 2002). “Analytic Light Curves for Planetary Transit Searches”. In: *ApJ* 580, pp. L171–L175. DOI: 10.1086/345520. eprint: astro-ph/0210099.

- Mann, A. W. et al. (Jan. 2019). “How to Constrain Your M Dwarf. II. The Mass-Luminosity-Metallicity Relation from 0.075 to 0.70 Solar Masses”. In: *ApJ* 871, 63, p. 63. DOI: 10.3847/1538-4357/aaf3bc. arXiv: 1811.06938 [astro-ph.SR].
- Mann, Andrew W. et al. (Feb. 2016). “Zodiacal Exoplanets in Time (ZEIT). I. A Neptune-sized Planet Orbiting an M4.5 Dwarf in the Hyades Star Cluster”. In: *ApJ* 818.1, 46, p. 46. DOI: 10.3847/0004-637X/818/1/46. arXiv: 1512.00483 [astro-ph.EP].
- Mann, Andrew W. et al. (Jan. 2018). “Zodiacal Exoplanets in Time (ZEIT). VI. A Three-planet System in the Hyades Cluster Including an Earth-sized Planet”. In: *AJ* 155.1, 4, p. 4. DOI: 10.3847/1538-3881/aa9791. arXiv: 1709.10328 [astro-ph.EP].
- Marconi, A. et al. (Aug. 2022). “ANDES, the high resolution spectrograph for the ELT: science case, baseline design and path to construction”. In: *Ground-based and Airborne Instrumentation for Astronomy IX*. Ed. by Christopher J. Evans et al. Vol. 12184. Society of Photo-Optical Instrumentation Engineers (SPIE) Conference Series, 1218424, p. 1218424. DOI: 10.1117/12.2628689.
- Martin, D. Christopher et al. (Jan. 2005). “The Galaxy Evolution Explorer: A Space Ultraviolet Survey Mission”. In: *ApJ* 619.1, pp. L1–L6. DOI: 10.1086/426387. arXiv: astro-ph/0411302 [astro-ph].
- Martín, Eduardo L. et al. (Mar. 2018). “The Lithium Depletion Boundary and the Age of the Hyades Cluster”. In: *ApJ* 856.1, 40, p. 40. DOI: 10.3847/1538-4357/aaaeb8. arXiv: 1802.07155 [astro-ph.SR].
- Masuda, Kento and Daniel Tamayo (Nov. 2020). “Revisiting the Architecture of the KOI-89 System”. In: *AJ* 160.5, 224, p. 224. DOI: 10.3847/1538-3881/abb8cd. arXiv: 2009.06850 [astro-ph.EP].
- Matsakos, Titos and Ariele Königl (Mar. 2016). “On the Origin of the Sub-Jovian Desert in the Orbital-period-Planetary-mass Plane”. In: *ApJ* 820.1, L8, p. L8. DOI: 10.3847/2041-8205/820/1/L8. arXiv: 1603.00414 [astro-ph.EP].
- May, E. M. et al. (Dec. 2023). “Double Trouble: Two Transits of the Super-Earth GJ 1132 b Observed with JWST NIRSpec G395H”. In: *ApJ* 959.1, L9, p. L9. DOI: 10.3847/2041-8213/ad054f. arXiv: 2310.10711 [astro-ph.EP].
- Mayo, Andrew W. et al. (Mar. 2018). “275 Candidates and 149 Validated Planets Orbiting Bright Stars in K2 Campaigns 0-10”. In: *AJ* 155.3, 136, p. 136. DOI: 10.3847/1538-3881/aaadff. arXiv: 1802.05277 [astro-ph.EP].
- Mayo, Andrew W. et al. (Oct. 2019). “An 11 Earth-mass, Long-period Sub-Neptune Orbiting a Sun-like Star”. In: *AJ* 158.4, 165, p. 165. DOI: 10.3847/1538-3881/ab3e2f. arXiv: 1908.08585 [astro-ph.EP].
- Mayor, M. and D. Queloz (Nov. 1995). “A Jupiter-mass companion to a solar-type star”. In: *Nature* 378, pp. 355–359. DOI: 10.1038/378355a0.
- Mayor, M. et al. (Dec. 2003). “Setting New Standards with HARPS”. In: *The Messenger* 114, pp. 20–24.
- Mazeh, T. et al. (May 2016). “Dearth of short-period Neptunian exoplanets: A desert in period-mass and period-radius planes”. In: *A&A* 589, A75, A75. DOI: 10.1051/0004-6361/201528065. arXiv: 1602.07843 [astro-ph.EP].

- Mégevand, D. et al. (July 2010). “ESPRESSO: projecting a rocky exoplanet hunter for the VLT”. In: *Ground-based and Airborne Instrumentation for Astronomy III*. Vol. 7735. Proc. SPIE, 77354Y, 77354Y. DOI: 10.1117/12.856656.
- Moran, Sarah E. et al. (May 2023). “High Tide or Riptide on the Cosmic Shoreline? A Water-rich Atmosphere or Stellar Contamination for the Warm Super-Earth GJ 486b from JWST Observations”. In: *ApJ* 948.1, L11, p. L11. DOI: 10.3847/2041-8213/acb9c. arXiv: 2305.00868 [astro-ph.EP].
- Morbideilli, A. (Mar. 2018). “Accretion Processes”. In: *arXiv e-prints*. arXiv: 1803.06708 [astro-ph.EP].
- Mortier, A. et al. (Sept. 2013). “New and updated stellar parameters for 71 evolved planet hosts. On the metallicity-giant planet connection”. In: *A&A* 557, A70, A70. DOI: 10.1051/0004-6361/201321641. arXiv: 1307.7870 [astro-ph.EP].
- Mortier, A. et al. (Dec. 2014). “Correcting the spectroscopic surface gravity using transits and asteroseismology. No significant effect on temperatures or metallicities with ARES and MOOG in local thermodynamic equilibrium”. In: *A&A* 572, A95, A95. DOI: 10.1051/0004-6361/201424537. arXiv: 1410.1310 [astro-ph.SR].
- Morton, T. D. (Mar. 2015). *isochrones: Stellar model grid package*. Astrophysics Source Code Library. ascl: 1503.010.
- Morton, T. D. et al. (May 2016). “False Positive Probabilities for all Kepler Objects of Interest: 1284 Newly Validated Planets and 428 Likely False Positives”. In: *ApJ* 822, 86, p. 86. DOI: 10.3847/0004-637X/822/2/86. arXiv: 1605.02825 [astro-ph.EP].
- Mousis, Olivier et al. (June 2020). “Irradiated Ocean Planets Bridge Super-Earth and Sub-Neptune Populations”. In: *ApJ* 896.2, L22, p. L22. DOI: 10.3847/2041-8213/ab9530. arXiv: 2002.05243 [astro-ph.EP].
- Mulders, Gijs D. et al. (Jan. 2015). “A Stellar-mass-dependent Drop in Planet Occurrence Rates”. In: *ApJ* 798.2, 112, p. 112. DOI: 10.1088/0004-637X/798/2/112. arXiv: 1406.7356 [astro-ph.EP].
- Mulders, Gijs D. et al. (July 2018). “The Exoplanet Population Observation Simulator. I. The Inner Edges of Planetary Systems”. In: *AJ* 156.1, 24, p. 24. DOI: 10.3847/1538-3881/aac5ea. arXiv: 1805.08211 [astro-ph.EP].
- Mullally, F. et al. (Apr. 2015). “Planetary Candidates Observed by Kepler. VI. Planet Sample from Q1–Q16 (47 Months)”. In: *ApJS* 217, 31, p. 31. DOI: 10.1088/0067-0049/217/2/31. arXiv: 1502.02038 [astro-ph.EP].
- Nardiello, D. et al. (Aug. 2021). “A PSF-based Approach to TESS High quality data Of Stellar clusters (PATHOS) - IV. Candidate exoplanets around stars in open clusters: frequency and age-planetary radius distribution”. In: *MNRAS* 505.3, pp. 3767–3784. DOI: 10.1093/mnras/stab1497. arXiv: 2105.09952 [astro-ph.EP].
- NASA Exoplanet Science Institute (2020). *Planetary Systems Table*. DOI: 10.26133/NEA12. URL: <https://catcopy.ipac.caltech.edu/doi/doi.php?id=10.26133/NEA12>.
- Nikolov, Nikolay et al. (Dec. 2016). “VLT FORS2 Comparative Transmission Spectroscopy: Detection of Na in the Atmosphere of WASP-39b from the Ground”. In: *ApJ* 832.2, 191, p. 191. DOI: 10.3847/0004-637X/832/2/191. arXiv: 1610.01186 [astro-ph.EP].



- Noyes, R. W. et al. (Apr. 1984). “Rotation, convection, and magnetic activity in lower main-sequence stars.” In: *ApJ* 279, pp. 763–777. DOI: 10.1086/161945.
- Núñez, Alejandro et al. (Feb. 2024). “The Factory and the Beehive. V. Chromospheric and Coronal Activity and Its Dependence on Rotation in Praesepe and the Hyades”. In: *ApJ* 962.1, 12, p. 12. DOI: 10.3847/1538-4357/ad117e. arXiv: 2311.18690 [astro-ph.SR].
- Öberg, Karin I. et al. (Dec. 2011). “The Effects of Snowlines on C/O in Planetary Atmospheres”. In: *ApJ* 743.1, L16, p. L16. DOI: 10.1088/2041-8205/743/1/L16. arXiv: 1110.5567 [astro-ph.GA].
- Osborn, Ares et al. (Nov. 2023). “TOI-332 b: a super dense Neptune found deep within the Neptunian desert”. In: *MNRAS* 526.1, pp. 548–566. DOI: 10.1093/mnras/stad2575. arXiv: 2308.12137 [astro-ph.EP].
- Owen, J. E. and Y. Wu (Sept. 2017). “The Evaporation Valley in the Kepler Planets”. In: *ApJ* 847, 29, p. 29. DOI: 10.3847/1538-4357/aa890a. arXiv: 1705.10810 [astro-ph.EP].
- Penny, Matthew T. et al. (Mar. 2019). “Predictions of the WFIRST Microlensing Survey. I. Bound Planet Detection Rates”. In: *ApJS* 241.1, 3, p. 3. DOI: 10.3847/1538-4365/aafb69. arXiv: 1808.02490 [astro-ph.EP].
- Pepe, F. et al. (Jan. 2021). “ESPRESSO at VLT. On-sky performance and first results”. In: *A&A* 645, A96, A96. DOI: 10.1051/0004-6361/202038306. arXiv: 2010.00316 [astro-ph.IM].
- Perryman, M. et al. (Dec. 2014). “Astrometric Exoplanet Detection with Gaia”. In: *ApJ* 797, 14, p. 14. DOI: 10.1088/0004-637X/797/1/14. arXiv: 1411.1173 [astro-ph.EP].
- Perryman, M. A. C. et al. (Mar. 1998). “The Hyades: distance, structure, dynamics, and age”. In: *A&A* 331, pp. 81–120. arXiv: astro-ph/9707253 [astro-ph].
- Petigura, E. A. et al. (Nov. 2013). “Prevalence of Earth-size planets orbiting Sun-like stars”. In: *Proceedings of the National Academy of Science* 110, pp. 19273–19278. DOI: 10.1073/pnas.1319909110. arXiv: 1311.6806 [astro-ph.EP].
- Petigura, E. A. et al. (Feb. 2018). “The California-Kepler Survey. IV. Metal-rich Stars Host a Greater Diversity of Planets”. In: *AJ* 155, 89, p. 89. DOI: 10.3847/1538-3881/aaa54c. arXiv: 1712.04042 [astro-ph.EP].
- Piskunov, Nikolai and Jeff A. Valenti (Jan. 2017). “Spectroscopy Made Easy: Evolution”. In: *A&A* 597, A16, A16. DOI: 10.1051/0004-6361/201629124. arXiv: 1606.06073 [astro-ph.IM].
- Powell, Diana et al. (Feb. 2024). “Sulfur dioxide in the mid-infrared transmission spectrum of WASP-39b”. In: *Nature* 626.8001, pp. 979–983. DOI: 10.1038/s41586-024-07040-9.
- Predehl, P. and J. H. M. M. Schmitt (Jan. 1995). “X-raying the interstellar medium: ROSAT observations of dust scattering halos.” In: *A&A* 293.
- Press, William H. et al. (1992). *Numerical recipes in FORTRAN. The art of scientific computing*.
- Queloz, D. et al. (Nov. 2001). “No planet for HD 166435”. In: *A&A* 379, pp. 279–287. DOI: 10.1051/0004-6361:20011308. eprint: astro-ph/0109491.
- Quirrenbach, Andreas et al. (Dec. 2020). “The CARMENES M-dwarf planet survey”. In: *Ground-based and Airborne Instrumentation for Astronomy VIII*. Ed. by Christopher

- J. Evans et al. Vol. 11447. Society of Photo-Optical Instrumentation Engineers (SPIE) Conference Series, 114473C, p. 114473C. DOI: 10.1117/12.2561380.
- Radica, Michael et al. (Sept. 2023). “Awesome SOSS: transmission spectroscopy of WASP-96b with NIRISS/SOSS”. In: *MNRAS* 524.1, pp. 835–856. DOI: 10.1093/mnras/stad1762. arXiv: 2305.17001 [astro-ph.EP].
- Radica, Michael et al. (Feb. 2024). “Muted Features in the JWST NIRISS Transmission Spectrum of Hot Neptune LTT 9779b”. In: *ApJ* 962.1, L20, p. L20. DOI: 10.3847/2041-8213/ad20e4. arXiv: 2401.15548 [astro-ph.EP].
- Rajpaul, V. et al. (Sept. 2015). “A Gaussian process framework for modelling stellar activity signals in radial velocity data”. In: *MNRAS* 452, pp. 2269–2291. DOI: 10.1093/mnras/stv1428. arXiv: 1506.07304 [astro-ph.EP].
- Rasmussen, C. E. and C. K. I. Williams (2006). *Gaussian Processes for Machine Learning*.
- Rauer, H. et al. (Nov. 2014). “The PLATO 2.0 mission”. In: *Experimental Astronomy* 38.1-2, pp. 249–330. DOI: 10.1007/s10686-014-9383-4. arXiv: 1310.0696 [astro-ph.EP].
- Rauscher, Bernard J. et al. (Aug. 2014). “New and Better Detectors for the JWST Near-Infrared Spectrograph”. In: *PASP* 126.942, p. 739. DOI: 10.1086/677681.
- Raymond, S. N. et al. (May 2009). “Planet-Planet Scattering Leads to Tightly Packed Planetary Systems”. In: *ApJ* 696, pp. L98–L101. DOI: 10.1088/0004-637X/696/1/L98. arXiv: 0903.4700 [astro-ph.EP].
- Raymond, Sean N. and Alessandro Morbidelli (Jan. 2022). “Planet Formation: Key Mechanisms and Global Models”. In: *Demographics of Exoplanetary Systems, Lecture Notes of the 3rd Advanced School on Exoplanetary Science*. Ed. by Katia Biazzo et al. Vol. 466. Astrophysics and Space Science Library, pp. 3–82. DOI: 10.1007/978-3-030-88124-5\_1. arXiv: 2002.05756 [astro-ph.EP].
- Rayner, J. T. et al. (Mar. 2003). “SpeX: A Medium-Resolution 0.8–5.5 Micron Spectrograph and Imager for the NASA Infrared Telescope Facility”. In: *PASP* 115.805, pp. 362–382. DOI: 10.1086/367745.
- Rayner, John T. et al. (Sept. 2004). “Four years of good SpeX”. In: *Ground-based Instrumentation for Astronomy*. Ed. by Alan F. M. Moorwood and Masanori Iye. Vol. 5492. Society of Photo-Optical Instrumentation Engineers (SPIE) Conference Series, pp. 1498–1509. DOI: 10.1117/12.551107.
- Redfield, Seth et al. (Jan. 2008). “Sodium Absorption from the Exoplanetary Atmosphere of HD 189733b Detected in the Optical Transmission Spectrum”. In: *ApJ* 673.1, p. L87. DOI: 10.1086/527475. arXiv: 0712.0761 [astro-ph].
- Richey-Yowell, Tyler et al. (Feb. 2019). “HAZMAT. V. The Ultraviolet and X-Ray Evolution of K Stars”. In: *ApJ* 872.1, 17, p. 17. DOI: 10.3847/1538-4357/aafa74. arXiv: 1901.00502 [astro-ph.SR].
- Ricker, G. R. et al. (Jan. 2015). “Transiting Exoplanet Survey Satellite (TESS)”. In: *Journal of Astronomical Telescopes, Instruments, and Systems* 1.1, 014003, p. 014003. DOI: 10.1117/1.JATIS.1.1.014003.

- Rigby, Jane et al. (Apr. 2023). “The Science Performance of JWST as Characterized in Commissioning”. In: *PASP* 135.1046, 048001, p. 048001. DOI: 10.1088/1538-3873/acb293. arXiv: 2207.05632 [astro-ph.IM].
- Roettenbacher, Rachael M. (Oct. 2021). “The Impact of Stellar Activity on Our Ability to Detect Exoplanets”. In: *The Star-Planet Connection*, 25, p. 25. DOI: 10.5281/zenodo.5627381.
- Rogers, Leslie A. et al. (Sept. 2011). “Formation and Structure of Low-density exo-Neptunes”. In: *ApJ* 738.1, 59, p. 59. DOI: 10.1088/0004-637X/738/1/59. arXiv: 1106.2807 [astro-ph.EP].
- Rowe, Jason F. et al. (Mar. 2014). “Validation of Kepler’s Multiple Planet Candidates. III. Light Curve Analysis and Announcement of Hundreds of New Multi-planet Systems”. In: *ApJ* 784.1, 45, p. 45. DOI: 10.1088/0004-637X/784/1/45. arXiv: 1402.6534 [astro-ph.EP].
- Rubenzahl, Ryan A. et al. (Dec. 2023). “Staring at the Sun with the Keck Planet Finder: An Autonomous Solar Calibrator for High Signal-to-noise Sun-as-a-star Spectra”. In: *PASP* 135.1054, 125002, p. 125002. DOI: 10.1088/1538-3873/ad0b30. arXiv: 2311.05129 [astro-ph.IM].
- Rustamkulov, Z. et al. (Feb. 2023). “Early Release Science of the exoplanet WASP-39b with JWST NIRSpec PRISM”. In: *Nature* 614.7949, pp. 659–663. DOI: 10.1038/s41586-022-05677-y. arXiv: 2211.10487 [astro-ph.EP].
- Sanders, G. H. (June 2013). “The Thirty Meter Telescope (TMT): An International Observatory”. In: *Journal of Astrophysics and Astronomy* 34, pp. 81–86. DOI: 10.1007/s12036-013-9169-5.
- Santos, N. C. et al. (June 2014). “The HARPS search for southern extra-solar planets. XXXV. The interesting case of HD 41248: stellar activity, no planets?” In: *A&A* 566, A35, A35. DOI: 10.1051/0004-6361/201423808. arXiv: 1404.6135 [astro-ph.EP].
- Sanz-Forcada, J. et al. (Aug. 2011). “Estimation of the XUV radiation onto close planets and their evaporation”. In: *A&A* 532, A6, A6. DOI: 10.1051/0004-6361/201116594. arXiv: 1105.0550 [astro-ph.EP].
- Scargle, J. D. (Dec. 1982). “Studies in astronomical time series analysis. II - Statistical aspects of spectral analysis of unevenly spaced data”. In: *ApJ* 263, pp. 835–853. DOI: 10.1086/160554.
- Schlawin, Everett et al. (Nov. 2020). “JWST Noise Floor. I. Random Error Sources in JWST NIRCам Time Series”. In: *AJ* 160.5, 231, p. 231. DOI: 10.3847/1538-3881/abb811. arXiv: 2010.03564 [astro-ph.IM].
- Schmitt, Joseph R. et al. (Nov. 2014). “Planet Hunters. VII. Discovery of a New Low-mass, Low-density Planet (PH3 C) Orbiting Kepler-289 with Mass Measurements of Two Additional Planets (PH3 B and D)”. In: *ApJ* 795.2, 167, p. 167. DOI: 10.1088/0004-637X/795/2/167. arXiv: 1410.8114 [astro-ph.EP].
- Schwab, C. et al. (Aug. 2016). “Design of NEID, an extreme precision Doppler spectrograph for WIYN”. In: *Ground-based and Airborne Instrumentation for Astronomy VI*. Vol. 9908. Proc. SPIE, 99087H, 99087H. DOI: 10.1117/12.2234411.

- Seager, S. and G. Mallén-Ornelas (Mar. 2003). “A Unique Solution of Planet and Star Parameters from an Extrasolar Planet Transit Light Curve”. In: *ApJ* 585, pp. 1038–1055. DOI: 10.1086/346105. eprint: astro-ph/0206228.
- Seager, S. et al. (Nov. 2007). “Mass-Radius Relationships for Solid Exoplanets”. In: *ApJ* 669.2, pp. 1279–1297. DOI: 10.1086/521346. arXiv: 0707.2895 [astro-ph].
- Seidel, J. V. et al. (Mar. 2019). “Hot Exoplanet Atmospheres Resolved with Transit Spectroscopy (HEARTS). II. A broadened sodium feature on the ultra-hot giant WASP-76b”. In: *A&A* 623, A166, A166. DOI: 10.1051/0004-6361/201834776. arXiv: 1902.00001 [astro-ph.EP].
- Seidel, J. V. et al. (Sept. 2020). “Hot Exoplanet Atmospheres Resolved with Transit Spectroscopy (HEARTS). V. Detection of sodium on the bloated super-Neptune WASP-166b”. In: *A&A* 641, L7, p. L7. DOI: 10.1051/0004-6361/202038497. arXiv: 2007.01783 [astro-ph.EP].
- Seidel, J. V. et al. (June 2022). “The hot Neptune WASP-166 b with ESPRESSO II: confirmation of atmospheric sodium”. In: *MNRAS* 513.1, pp. L15–L19. DOI: 10.1093/mnras/1/slac027. arXiv: 2203.04494 [astro-ph.EP].
- Seifahrt, Andreas et al. (Aug. 2022). “MAROON-X: the first two years of EPRVs from Gemini North”. In: *Ground-based and Airborne Instrumentation for Astronomy IX*. Ed. by Christopher J. Evans et al. Vol. 12184. Society of Photo-Optical Instrumentation Engineers (SPIE) Conference Series, 121841G, 121841G. DOI: 10.1117/12.2629428. arXiv: 2210.06563 [astro-ph.IM].
- Sing, D. K. et al. (Jan. 2016). “A continuum from clear to cloudy hot-Jupiter exoplanets without primordial water depletion”. In: *Nature* 529, pp. 59–62. DOI: 10.1038/nature16068. arXiv: 1512.04341 [astro-ph.EP].
- Skrutskie, M. F. et al. (Feb. 2006). “The Two Micron All Sky Survey (2MASS)”. In: *AJ* 131, pp. 1163–1183. DOI: 10.1086/498708.
- Smith, Jeffrey C. et al. (Sept. 2012). “Kepler Presearch Data Conditioning II - A Bayesian Approach to Systematic Error Correction”. In: *PASP* 124.919, p. 1000. DOI: 10.1086/667697. arXiv: 1203.1383 [astro-ph.IM].
- Snedden, C. A. (1973). “Carbon and Nitrogen Abundances in Metal-Poor Stars.” PhD thesis. THE UNIVERSITY OF TEXAS AT AUSTIN.
- Sousa, S. G. et al. (Feb. 2011). “Spectroscopic characterization of a sample of metal-poor solar-type stars from the HARPS planet search program. Precise spectroscopic parameters and mass estimation”. In: *A&A* 526, A99+. DOI: 10.1051/0004-6361/201015646. arXiv: 1012.1528 [astro-ph.SR].
- Sousa, S. G. et al. (Apr. 2015). “Homogeneous spectroscopic parameters for bright planet host stars from the northern hemisphere. The impact on stellar and planetary mass”. In: *A&A* 576, A94, A94. DOI: 10.1051/0004-6361/201425227. arXiv: 1503.02443 [astro-ph.SR].
- Sousa, Sérgio G. (2014). “ARES + MOOG: A Practical Overview of an Equivalent Width (EW) Method to Derive Stellar Parameters”. In: *Determination of Atmospheric Parameters of B*, pp. 297–310. DOI: 10.1007/978-3-319-06956-2\_26.

- Sozzetti, A. et al. (Aug. 2007). “Improving Stellar and Planetary Parameters of Transiting Planet Systems: The Case of TrES-2”. In: *ApJ* 664, pp. 1190–1198. DOI: 10.1086/519214. arXiv: 0704.2938.
- Speagle, Joshua S. (Apr. 2020). “DYNESTY: a dynamic nested sampling package for estimating Bayesian posteriors and evidences”. In: *MNRAS* 493.3, pp. 3132–3158. DOI: 10.1093/mnras/staa278. arXiv: 1904.02180 [astro-ph.IM].
- Stefansson, Gudmundur et al. (Oct. 2020). “The Habitable Zone Planet Finder Reveals a High Mass and Low Obliquity for the Young Neptune K2-25b”. In: *AJ* 160.4, 192, p. 192. DOI: 10.3847/1538-3881/abb13a. arXiv: 2007.12766 [astro-ph.EP].
- Struve, O. (Oct. 1952). “Proposal for a project of high-precision stellar radial velocity work”. In: *The Observatory* 72, pp. 199–200.
- Stumpe, Martin C. et al. (Sept. 2012). “Kepler Presearch Data Conditioning I—Architecture and Algorithms for Error Correction in Kepler Light Curves”. In: *PASP* 124.919, p. 985. DOI: 10.1086/667698. arXiv: 1203.1382 [astro-ph.IM].
- Stumpe, Martin C. et al. (Jan. 2014). “Multiscale Systematic Error Correction via Wavelet-Based Bandsplitting in Kepler Data”. In: *PASP* 126.935, p. 100. DOI: 10.1086/674989.
- Sun, L. et al. (Apr. 2019). “Kepler-411: a four-planet system with an active host star”. In: *A&A* 624, A15, A15. DOI: 10.1051/0004-6361/201834275. arXiv: 1902.09719 [astro-ph.EP].
- Szentgyorgyi, Andrew et al. (Aug. 2016). “The GMT-Consortium Large Earth Finder (G-CLEF): an optical Echelle spectrograph for the Giant Magellan Telescope (GMT)”. In: *Ground-based and Airborne Instrumentation for Astronomy VI*. Ed. by Christopher J. Evans et al. Vol. 9908. Society of Photo-Optical Instrumentation Engineers (SPIE) Conference Series, 990822, p. 990822. DOI: 10.1117/12.2233506.
- Tamayo, Daniel et al. (Aug. 2020). “Predicting the long-term stability of compact multiplanet systems”. In: *Proceedings of the National Academy of Science* 117.31, pp. 18194–18205. DOI: 10.1073/pnas.2001258117. arXiv: 2007.06521 [astro-ph.EP].
- Tayar, Jamie et al. (Mar. 2022). “A Guide to Realistic Uncertainties on the Fundamental Properties of Solar-type Exoplanet Host Stars”. In: *ApJ* 927.1, 31, p. 31. DOI: 10.3847/1538-4357/ac4bbc. arXiv: 2012.07957 [astro-ph.EP].
- Taylor, B. J. (Dec. 2006). “The Benchmark Cluster Reddening Project. I. Reddening Values for the Hyades, Coma, and Praesepe”. In: *AJ* 132, pp. 2453–2468. DOI: 10.1086/508610.
- The LUVVOIR Team (Sept. 2018). “The LUVVOIR Mission Concept Study Interim Report”. In: *arXiv e-prints*. arXiv: 1809.09668 [astro-ph.IM].
- Thiabaud, A. et al. (Feb. 2015). “Gas composition of the main volatile elements in protoplanetary discs and its implication for planet formation”. In: *A&A* 574, A138, A138. DOI: 10.1051/0004-6361/201424868.
- Thompson, S. E. et al. (Apr. 2018). “Planetary Candidates Observed by Kepler. VIII. A Fully Automated Catalog with Measured Completeness and Reliability Based on Data Release 25”. In: *ApJS* 235, 38, p. 38. DOI: 10.3847/1538-4365/aab4f9. arXiv: 1710.06758 [astro-ph.EP].

- Torres, Guillermo (Feb. 1999). “Substellar Companion Masses from Minimal Radial Velocity or Astrometric Information: a Monte Carlo Approach”. In: *PASP* 111.756, pp. 169–176. DOI: 10.1086/316313.
- Torres, Guillermo et al. (Oct. 2012). “Improved Spectroscopic Parameters for Transiting Planet Hosts”. In: *ApJ* 757.2, 161, p. 161. DOI: 10.1088/0004-637X/757/2/161. arXiv: 1208.1268 [astro-ph.SR].
- Tsantaki, M. et al. (July 2013). “Deriving precise parameters for cool solar-type stars. Optimizing the iron line list”. In: *A&A* 555, A150, A150. DOI: 10.1051/0004-6361/201321103. arXiv: 1304.6639 [astro-ph.SR].
- Twicken, Joseph D. et al. (June 2018). “Kepler Data Validation I—Architecture, Diagnostic Tests, and Data Products for Vetting Transiting Planet Candidates”. In: *PASP* 130.988, p. 064502. DOI: 10.1088/1538-3873/aab694. arXiv: 1803.04526 [astro-ph.EP].
- Udry, S. et al. (Nov. 2014). “Exoplanet Science with the European Extremely Large Telescope. The Case for Visible and Near-IR Spectroscopy at High Resolution”. In: *ArXiv e-prints*. arXiv: 1412.1048 [astro-ph.EP].
- Valenti, J. A. and N. Piskunov (Sept. 1996). “Spectroscopy made easy: A new tool for fitting observations with synthetic spectra.” In: *A&AS* 118, pp. 595–603.
- Van Eylen, V. et al. (Oct. 2018). “An asteroseismic view of the radius valley: stripped cores, not born rocky”. In: *MNRAS* 479, pp. 4786–4795. DOI: 10.1093/mnras/sty1783. arXiv: 1710.05398 [astro-ph.EP].
- Vanderburg, A. and J. A. Johnson (Oct. 2014). “A Technique for Extracting Highly Precise Photometry for the Two-Wheeled Kepler Mission”. In: *PASP* 126, p. 948. DOI: 10.1086/678764. arXiv: 1408.3853 [astro-ph.IM].
- Vanderburg, A. et al. (Jan. 2016). “Planetary Candidates from the First Year of the K2 Mission”. In: *ApJS* 222, 14, p. 14. DOI: 10.3847/0067-0049/222/1/14. arXiv: 1511.07820 [astro-ph.EP].
- Vanderburg, Andrew et al. (Aug. 2019). “TESS Spots a Compact System of Super-Earths around the Naked-eye Star HR 858”. In: *ApJ* 881.1, L19, p. L19. DOI: 10.3847/2041-8213/ab322d. arXiv: 1905.05193 [astro-ph.EP].
- Vines, Jose I. and James S. Jenkins (Apr. 2022). “ARIADNE: Measuring accurate and precise stellar parameters through SED fitting”. In: *MNRAS*. DOI: 10.1093/mnras/stac956. arXiv: 2204.03769 [astro-ph.SR].
- Vogt, S. S. et al. (June 1994). “HIRES: the high-resolution echelle spectrometer on the Keck 10-m Telescope”. In: *Instrumentation in Astronomy VIII*. Ed. by D. L. Crawford and E. R. Craine. Vol. 2198. Proc. SPIE, p. 362. DOI: 10.1117/12.176725.
- Wilson, Robert F. et al. (Nov. 2023). “Transiting Exoplanet Yields for the Roman Galactic Bulge Time Domain Survey Predicted from Pixel-level Simulations”. In: *ApJS* 269.1, 5, p. 5. DOI: 10.3847/1538-4365/acf3df. arXiv: 2305.16204 [astro-ph.EP].
- Wolfgang, Angie et al. (July 2016). “Probabilistic Mass-Radius Relationship for Sub-Neptune-Sized Planets”. In: *ApJ* 825.1, 19, p. 19. DOI: 10.3847/0004-637X/825/1/19. arXiv: 1504.07557 [astro-ph.EP].

- Wright, Edward L. et al. (Dec. 2010). “The Wide-field Infrared Survey Explorer (WISE): Mission Description and Initial On-orbit Performance”. In: *AJ* 140.6, pp. 1868–1881. DOI: 10.1088/0004-6256/140/6/1868. arXiv: 1008.0031 [astro-ph.IM].
- Wright, Nicholas J. et al. (Sept. 2018). “The stellar rotation-activity relationship in fully convective M dwarfs”. In: *MNRAS* 479.2, pp. 2351–2360. DOI: 10.1093/mnras/sty1670. arXiv: 1807.03304 [astro-ph.SR].
- Wytttenbach, A. et al. (June 2017). “Hot Exoplanet Atmospheres Resolved with Transit Spectroscopy (HEARTS). I. Detection of hot neutral sodium at high altitudes on WASP-49b”. In: *A&A* 602, A36, A36. DOI: 10.1051/0004-6361/201630063. arXiv: 1702.00448 [astro-ph.EP].
- Xie, Ji-Wei (Feb. 2014). “Transit Timing Variation of Near-resonance Planetary Pairs. II. Confirmation of 30 Planets in 15 Multiple-planet Systems”. In: *ApJS* 210.2, 25, p. 25. DOI: 10.1088/0067-0049/210/2/25. arXiv: 1309.2329 [astro-ph.EP].
- Yang, Jia-Yi et al. (Apr. 2020). “Occurrence and Architecture of Kepler Planetary Systems as Functions of Stellar Mass and Effective Temperature”. In: *AJ* 159.4, 164, p. 164. DOI: 10.3847/1538-3881/ab7373. arXiv: 2002.02840 [astro-ph.EP].
- Zacharias, N. et al. (Feb. 2013). “The Fourth US Naval Observatory CCD Astrograph Catalog (UCAC4)”. In: *AJ* 145.2, 44, p. 44. DOI: 10.1088/0004-6256/145/2/44. arXiv: 1212.6182 [astro-ph.IM].
- Zechmeister, M. and M. Kürster (Mar. 2009). “The generalised Lomb-Scargle periodogram. A new formalism for the floating-mean and Keplerian periodograms”. In: *A&A* 496, pp. 577–584. DOI: 10.1051/0004-6361:200811296. arXiv: 0901.2573 [astro-ph.IM].
- Zeng, L. and D. Sasselov (Mar. 2013). “A Detailed Model Grid for Solid Planets from 0.1 through 100 Earth Masses”. In: *PASP* 125, p. 227. DOI: 10.1086/669163. arXiv: 1301.0818 [astro-ph.EP].
- Zeng, L. et al. (Mar. 2016a). “Mass-Radius Relation for Rocky Planets Based on PREM”. In: *ApJ* 819, 127, p. 127. DOI: 10.3847/0004-637X/819/2/127. arXiv: 1512.08827 [astro-ph.EP].
- (Mar. 2016b). “Mass-Radius Relation for Rocky Planets Based on PREM”. In: *ApJ* 819, 127, p. 127. DOI: 10.3847/0004-637X/819/2/127. arXiv: 1512.08827 [astro-ph.EP].
- Zeng, L. et al. (Dec. 2017). “Exoplanet Radius Gap Dependence on Host Star Type”. In: *Research Notes of the American Astronomical Society* 1.1, 32, p. 32. DOI: 10.3847/2515-5172/aa9ed9. arXiv: 1712.05458 [astro-ph.EP].
- Zeng, Li et al. (Oct. 2018). “Survival function analysis of planet size distribution with Gaia Data Release 2 updates”. In: *MNRAS* 479.4, pp. 5567–5576. DOI: 10.1093/mnras/sty1749. arXiv: 1806.11234 [astro-ph.EP].
- Zhang, Michael et al. (Mar. 2019). “Forward Modeling and Retrievals with PLATON, a Fast Open-source Tool”. In: *PASP* 131.997, p. 034501. DOI: 10.1088/1538-3873/aaf5ad. arXiv: 1811.11761 [astro-ph.EP].
- Zhang, Michael et al. (Feb. 2024). “GJ 367b Is a Dark, Hot, Airless Sub-Earth”. In: *ApJ* 961.2, L44, p. L44. DOI: 10.3847/2041-8213/ad1a07. arXiv: 2401.01400 [astro-ph.EP].

- Zieba, Sebastian et al. (Aug. 2023). “No thick carbon dioxide atmosphere on the rocky exoplanet TRAPPIST-1 c”. In: *Nature* 620.7975, pp. 746–749. DOI: 10.1038/s41586-023-06232-z. arXiv: 2306.10150 [astro-ph.EP].